TESIS DE LA UNIVERSIDAD DE ZARAGOZA

2025 316

Ilenia Serra

Understanding the molecular basis of industrially relevant biocatalysts: an electron paramagnetic resonance investigation of chlorite dismutases

Director/es
García Rubio, Inés
Van Doorslaer, Sabine

ISSN 2254-7606

Prensas de la Universidad Universidad Zaragoza

Universidad de Zaragoza
Servicio de Publicaciones

ISSN 2254-7606

Universidad Zaragoza
1542

Tesis Doctoral

UNDERSTANDING THE MOLECULAR BASIS OF INDUSTRIALLY RELEVANT BIOCATALYSTS: AN ELECTRON PARAMAGNETIC RESONANCE INVESTIGATION OF CHLORITE DISMUTASES

Autor

Ilenia Serra

Director/es

García Rubio, Inés
Van Doorslaer, Sabine

UNIVERSIDAD DE ZARAGOZA
Escuela de Doctorado

5-Bioquímica y Biología Molecular

2023

University of Antwerp

FACULTY OF SCIENCE

Understanding the molecular basis of industrially relevant biocatalysts: an electron paramagnetic resonance investigation of chlorite dismutases

---

Inzicht in de moleculaire basis van industrieel relevante biokatalysatoren: een elektronen paramagnetische resonantie studie van chlorietdismutasen

PhD thesis submitted for the degree of
Doctor in Science
at the University of Antwerp to be defended by

Ilenia Serra

Supervisors:
Prof. Dr. Sabine Van Doorslaer
Prof. Dr. Inés García-Rubio

Antwerp, 2023

FACULTAD DE CIENCIAS
DEPARTAMENTO DE BIOQUÍMICA Y BIOLOGÍA MOLECULAR

Understanding the molecular basis of industrially relevant biocatalysts: an electron paramagnetic resonance investigation of chlorite dismutases

---

Comprensión de las bases moleculares de biocatalizadores relevantes para la industria: investigación de clorito dismutasas mediante resonancia paramagnética electrónica

PhD thesis submitted for the degree of
Doctor in Biochemistry and Molecular Biology
at the University of Zaragoza to be defended by

Ilenia Serra

Supervisors:
Prof. Dr. Sabine Van Doorslaer
Prof. Dr. Inés García-Rubio

Antwerp, 2023

Jury members

Internal Doctoral Committee Chair
Prof. Dr. Christian Johannessen, University of Antwerp

Internal Doctoral Committee Members
Prof. Dr. Ir. Sammy Verbruggen, University of Antwerp
Prof. Dr. Ir. Yann Sterckx, University of Antwerp

External Jury Members
Prof. Dr. Marilena Di Valentin, University of Padova
Prof. Dr. Olav Schiemann, University of Bonn

Promotors
Prof. Dr. Sabine Van Doorslaer, University of Antwerp
Prof. Dr. Inés García-Rubio, University of Zaragoza

Disclaimer

Ai miei genitori, che mi sostengono sempre, comunque vada

To my parents, who always support me, no matter what

Acknowledgments

It was exactly the day before my 25th birthday when I received the communication that I was selected for the PARACAT project and I would have to move to Belgium in the next couple of months to start my PhD. I remember thinking it couldn't have been a better birthday gift! And yet, after four years, two new 'home' countries, learning two new languages and encountering a handful of different cultures from all over the world, it is only *now* that I can fully understand to which extent my PhD has been a life-changing experience. Beside the science, this period of my life was filled with personal enrichment that originated from the opportunity to connect and dialogue with so many valuable people. I would like to thank everyone I met on the way of this PhD journey, my mentors, my friends, my colleagues and even all the people with whom I exchanged only a few minutes of conversation, because all of you helped me become the person I am today.

Sabine, thank you for giving me the opportunity to join your lab. Among many, I learnt from you a very important lesson about modesty in science: that one should always be careful about the finest detail, but also know when it's time to stop, when there's nothing more to claim. Now I understand that even if my best effort doesn't lead to a revolutionary breakthrough, it will be an important drop in the vast sea of scientific knowledge. **Inés**, your warm welcome in Zaragoza was the best I could receive to start my "Spanish chapter"! Working with you has been a pleasure: thank you for your seemingly infinite patience and your supportive presence in the lab. Apart from the science, I learnt from you that behind a scientist there's always a *person*, with all that life brings along. Sabine and Inés, both of you are inspiring persons. Thank you for all the constructive discussions and for entrusting me during these years. I am grateful I had the chance to learn from two outstanding scientists like you are.

Next, I am sincerely grateful to all my PhD **jury members** for reading this thesis manuscript and giving their valuable remarks, which definitely had an impact on the quality of this work.

Daniel, without the *tons* of chlorite dismutase that you expressed and purified for me, I wouldn't be here writing these lines! Thank you for the amazing collaboration and for your help in the lab during my months at BOKU. A big thank also to prof. **Christian Obinger** and all the people in the group for the fruitful meetings and feedback during the course of my PhD. Next, I would like to express my gratitude to **Leonid** and prof. **Alexander Schnegg** for welcoming me in Mulheim and giving me

the opportunity to enrich this work with interesting experiments. A special mention to my collaborators from Spain, **Pablo** and prof. **Nunilo Cremades**, for the nice outcome of our joint efforts. Even if not presented in this thesis, I am glad I could contribute to such an interesting project. I take the opportunity to also thank **Pauline** and prof. **Ange Mouithys**, from the University of Liege. Perhaps we didn't obtain all the hoped results, but it was a pleasure to work with you (and fight together against the misbehaving spectrometer!).

Dear friends and colleagues from the **PARACAT** project, we shared a lot in the past years. We went on this adventure together and we knew we could count on each other, understanding each other's challenges for being at the same stage of our path. It felt a bit like being high-school mates, didn't it? We had moments of fun, moments of frustration, moments of hard work, moments of relax. But in the end, here we are, closing this chapter of our lives, going separate ways. I wish to all of you the best for your future.

I won't be able to stress enough how important my colleagues from the Building N have been in making my workplace such a welcoming and pleasant environment. From the old guard of the formerly-BIMEF group: **Kevin**, **Zainab** and **Niels**, I couldn't have been happier to have you as my *bio-EPR* mentors. You were such patient and helpful colleagues, and I am truly grateful for that. **Vincent**, your energy and science enthusiasm are contagious. Always sparkling with new ideas, yet being very pragmatic, your pieces of advice have been precious to me. **Momo**, you are one of my dearest friends in Antwerp. Countless chats, hang-out moments and super nice trips together will be among the sweetest memories of my PhD. **Melissa** and **Ivan**, room 2.14 was definitely more vibrant when you were around, and, Melissa, it's really nice to have you back in the group: hopefully you'll manage to also *tame* our new machines! **Andrea**, we witnessed together the change of times and the formation of the new TSM^2 group. In the sacred role of *meme master*, you brightened so many of these Belgian rainy days giving me a reason to smile and laugh, thank you! **Lore**, you are such an energic girl and I love your storytelling skills: I always look forward to seeing you popping up in my office with some weird new gossips! **Robine**, my 'baby', it was a pleasure to introduce you to *the ways of EPR*. You're sweet but determined at the same time, which is an amazing quality: keep going like that! From the NANOrOPT group of past and present: **Sofie**, not only a 'real professor' (:P) and superpowered scientist, but also a warm-hearted person to rely on. I'm happy for all the good moments we shared, let that strong woman in you always shine! **Salomé**, if I felt welcomed from the very first day, it's thanks to you! Counting on your support and friendship meant a lot to me. **Miles**, whether you believe it or not, I have finally *grown up*. Your wisdom, but mostly your jokes, won't be forgotten. Ducksiem… Oh wait, I mean, **Maksiem**: I think I said it all. 

Aina, always very well organized, proactive, enthusiastic in conversation, what more could I expect from my 'younger twin'? Lunch breaks are not the same when you're not around! **Vini**, we've known each other for less than two years, but I feel we're friends of a lifetime. Thank you for being there: my final years of PhD wouldn't have been so nice without an amazing friend like you. I would like to also thank **Paul**, **Ivan**, **Alexander** and **Federico** for being always available to help in the lab and for the nice chats over several university receptions. From the international community of the first floor: **Shabab**, **Alice**, **Michele**, and **Domenico**, thanks for the many occasions to hang out and have fun together! To all the people who have passed by the Building N, for long or for short, whom I didn't specifically mention: even if we didn't spend much time together, thank you for being 'part of the family' and bringing along your good vibes.

Ritwik, you opened my eyes and my heart. I hope I will always be able to take care of you as much as you have been doing with me until today. *Āmi tōmākē bhālōbāsi*.

A special thanks to my best friends from Italy, **Eli**, **Marty**, **Pedu**, **Leo**, **Enrica** and the girls from **DanzArte** for always being there for me despite the distance, despite the pandemic, despite the floods. Friends like you are an invaluable treasure.

Un grazie speciale ai miei migliori amici in Italia, Eli, Marty, Pedu, Leo, Enrica e le ragazze di DanzArte per esserci sempre stati per me, nonostante la distanza, nonostante la pandemia, nonostante l'alluvione. Avere amici come voi è una ricchezza inestimabile.

Finally, my deepest gratitude goes to my **mum** and **dad**, to whom this thesis is dedicated. Like the poet Kahlil Gibran said, *you are the bow,* and I am *the living arrow* you have sent forth. I wouldn't have reached this goal without your unconditioned love and constant encouragement. I love you so much.

Infine, la mia più profonda gratitudine va a mia mamma e mio papà, ai quali dedico questa tesi. Come disse il poeta Kahlil Gibran, voi siete l'arco *e io* la freccia vivente *che avete scoccato lontano. Non avrei raggiunto questo traguardo senza il vostro amore incondizionato e il vostro costante incoraggiamento. Vi voglio bene, tantissimo.*

Ilenia Serra

August 2023

Contents

List of Abbreviations

List of Amino Acids

Symbol	Short name	Full name
A	Ala	Alanine
R	Arg	Arginine
N	Asn	Asparagine
D	Asp	Aspartic acid
C	Cys	Cysteine
Q	Gln	Glutamine
E	Glu	Glutamic acid
G	Gly	Glycine
H	His	Histidine
I	Ile	Isoleucine
L	Leu	Leucine
K	Lys	Lysine
M	Met	Methionine
F	Phe	Phenylalanine
P	Pro	Proline
S	Ser	Serine
U	Sec	Selenocysteine
T	Thr	Threonine
W	Trp	Tryptophan
Y	Tyr	Tyrosine
V	Val	Valine

Abbreviations

BCA	bicinchoninic acid
CCD	central composite design
***C*Cld**	chlorite dismutase from *Cyanothece* sp. PCC7425
Cld	chlorite dismutase
CLEAs	cross-linked enzyme aggregates
CLECs	cross-linked enzyme crystals

CPO	chloroperoxidase
CT	charge-transfer
CW	continuous-wave
***Da*Cld**	chlorite dismutase from *Dechloromonas aromatica*
DFT	density-functional theory
DQ	double-quantum
DSC	differential scanning calorimetry
DyP	dye-decolorizing peroxidase
ECD	electronic circular dichroism
***Ec*DyP**	dye-decolorizing peroxidase from *Escherichia coli*
EDL	ejection delay line
***Efe*B**	exogenous iron uptake peroxidases B
ENDOR	electron nuclear double resonance
EPR	electron paramagnetic resonance
ESE	electron-spin-echo
ESEEM	electron spin echo envelope modulation
FID	free induction decay
FT	Fourier transformation
Hb	hemoglobin
HNTs	halloysite nanotubes
HRP	peroxidase from horseradish
HS	high-spin
HYSCORE	hyperfine sublevel correlation spectroscopy
IPTG	isopropyl thiogalactosidase
***Kp*DyP**	dye-decolorizing peroxidase from *Klebsiella pneumoniae*
LPO	lactoperoxidase
LS	low-spin
MaCld	chlorite dismutase from *Magnetospirillum* sp.
***Ma*Pgb**	protoglobin from *Methanosarcina acetivorans*
Mb	myoglobin
MCF	macroporous siliceous foams
MD	molecular dynamics

MNP	2-methyl-2-nitrosopropane
MPD	2-methyl-2,4-pentanediol
MPO	myeloperoxidase
NADH	nicotinamide adenine dinucleotide
***Nd*Cld**	chlorite dismutase from *Candidatus "Nitrospira defluvii"*
NiR	nitrite reductase
NMR	nuclear magnetic resonance
NOS	nitric oxide synthase
NP	nitrophorin
NQI	nuclear quadrupole interaction
NQR	nuclear quadrupole resonance
PAA	peroxyacetic acid
PcrAB	perchlorate reductase
PCRB	perchlorate-reducing bacteria
PDB	protein data bank
PMS	phenazine methosulfate
RFQ	rapid freeze-quench
RNS	reactive nitrogen species
ROS	reactive oxygen species
SQ	single-quantum
***Tc*DyP**	dye-decolorizing peroxidase from *Thermomonospora curvata*
TIP	"temperature-independent" buffer
WT	wild-type
ZFS	zero-field splitting

Being single is cool if you're an electron!

Dear scientist and non-scientist friends, here's a brief explanation of my 4-years research work in less than 400 (simple) words. Enjoy!

Do physics and chemistry seem just a bunch of nerdy mathematical gibberish? What if I tell you that after reading this, you'll know a bit of both without seeing a single number? First, take an onion: if the nucleus of an atom is its central core, the electrons occupy its layers. How they do it, is a bit more complicated.

Imagine electrons as passengers boarding a train. The first person finds a comfortable place to sit, the second person chooses the furthest seat, the third one the same and so on until no seats are left. Eventually, the latecomers will sit close to strangers even if they feel a bit uncomfortable. In a similar manner, even if they don't really like to stay close to each other, electrons find a compromise and roam around the nucleus in *pairs*. Simple, right?

Yet some electrons, just as with us, cannot give up a solitary life, and remain *unpaired*. Which doesn't mean they aren't active! Sometimes, so desperate to find a companion, they kidnap electrons from other molecules that come their way, becoming very dangerous! You've probably heard about the *free radicals*; their bad reputation precedes their name. But did you know that the same unpaired electrons which form these free radicals can also be useful, if not essential, for our health and everyday life, when they are placed in the right spot?

Small but mighty

In the chemistry of life, enzymes are the tiny machines which keep all living organisms functioning properly. Because they're often way more efficient than any man-designed process, we want to use them for novel purposes which go beyond their biological role. Enzymes are already employed in household goods, food processing and production of pharmaceuticals, to cite a few. In my research, I study an exciting enzyme, called *chlorite dismutase*, which degrades toxic compounds and produces oxygen. Guess what? This enzyme won't do its job without unpaired electrons, but there's more. With the right techniques, we can use these unpaired electrons as little spies to better understand how this enzyme works and develop sustainable technologies for the future. Surprised? I hope so. Believe it or not, without a single line of math, you've just learnt how cool physics and chemistry can shape the world around you. *Bravo*!

Summary

Chlorite dismutases (Clds) are heme *b*-containing oxidoreductases of bacterial origin which degrade chlorite (ClO_2^-) to form chloride (Cl^-) and molecular oxygen (O_2). This unique enzymatic activity was originally found in perchlorate- and chlorate-reducing bacteria (PCRBs), where Clds act as scavenging systems for the toxic chlorite produced during the respiration. Interestingly, the Cld activity was later identified in non-PCRBs, such as in nitrite-oxidizing bacteria and cyanobacteria. In these organisms, the physiological role of chlorite dismutases is still not completely elucidated. In addition to their intriguing reactivity – the formation of an O-O bond was formerly described only for oxygenic organisms and in a methano-oxidizing bacterium – chlorite dismutases raised interest for their potential industrial applications, such as in the field of bioremediation, construction of biosensors and as a tool to improve aeration in bioreactors, to cite a few. In this work, I principally focused on the study of the dimeric chlorite dismutase from *Cyanothece* sp. PCC7425 (*C*Cld) to gain insights into different enzyme properties, including the role of key amino acids in the heme surroundings, modes of ligand binding and mechanistic details. The ultimate goal was to reach a comprehensive understanding of these systems in the view of possible future industrial applications. Although the integration of different approaches was necessary to elucidate the investigated aspects, in my work I treated the subject mainly from a spectroscopic point of view. The project can be viewed as a combination of three main research questions: i) the role(s) of a conserved arginine residue situated at the distal side of the heme iron and the impact of its flexibility on different enzyme properties; ii) the mechanism of substrate binding and the influence of the arginine in this aspect; iii) the nature of the intermediate states formed during the catalytic cycle and their dependency on pH. Exploiting the paramagnetic nature of the ferric heme iron, either in the resting state of the enzyme, or upon ligand binding and in reaction with the substrate(s), electron paramagnetic resonance (EPR) spectroscopy was chosen as a principal approach to address these questions.

In Chapter 1, I will give a broad introduction on the proteins investigated in this work, including a general description of heme systems, followed by a more detailed discussion on globins, heme peroxidases and chlorite dismutases. In Chapter 2, the main techniques used will be treated from a theoretical point of view. An overview of the principles behind the recombinant production of proteins will be given. Next, optical and EPR spectroscopies will be treated in detail. The principles of stopped-flow UV-vis spectroscopy and Rapid Freeze-Quench will be explained as well.

Chapter 3 focuses on the application of EPR spectroscopy to heme proteins and more specifically to heme enzymes with potential industrial usage as biocatalysts. A description of the most relevant oxidation and spin states of the heme iron will be presented, followed by a discussion on the catalytically relevant Compound I, an intermediate state found in many peroxidase enzymatic cycles. Finally, some successful examples of the use of EPR spectroscopy for the study of these enzymes will be provided.

In Chapter 4 I present the results of a systematic study on the interplay of buffers and cryoprotectants in the preparation of samples for low-temperature EPR spectroscopy. For this work, the well-known myoglobin was chosen as a model system and its ability to undergo an alkaline transition in presence of different combination of buffers and glassing agents was assessed by optical and EPR spectroscopy. This study highlights the importance of tailoring the experimental conditions to the system of interest to avoid data misinterpretation.

Chapter 5 focuses on the impact of the flexibility of the conserved arginine in *C*Cld, which was shown to be able to adopt different orientations, either pointing towards the heme or towards the substrate entry channel. Through site-directed mutagenesis, the variants Q74V and Q74E of *C*Cld were created, where the glutamine 74, normally hydrogen-bonded to arginine 127, was exchanged to either a valine or a glutamate in order to alter the flexibility of the arginine itself. Together with structural and biochemical methods, an EPR pH-dependency analysis of the wild-type and variants highlighted the effects of the altered arginine flexibility on the alkaline transition of *C*Cld and on the mode of binding of an OH^- group, showing differences in the profile of both high-spin and low-spin iron at pH ≥ 9.

These findings led to the hypothesis that the arginine, and its flexibility, could have a decisive role in very first step of the catalytic activity, *i.e.,* the binding of the substrate, which is extensively investigated in Chapters 6 and 7. Initially, due to the fast reactivity of chlorite dismutases with their natural substrate, nitrite (NO_2^-) was employed as a substrate analogue in order to form a stable complex. The NO_2^--bound forms of the wild-type *C*Cld, Q74 variants and two additional variants, in which the conserved arginine was mutated to either alanine or lysine (R127A, R12K), were investigated by X-ray crystallography, molecular dynamics (MD) simulations and EPR spectroscopy (both in continuous-wave and pulsed mode). While the crystal structures exclusively showed nitrite binding through one of the oxygen atoms (*O*-nitrito mode), both MD simulations and EPR spectroscopy suggested that the binding through the nitrogen atom could also occur (*N*-nitro mode). In particular, in Chapter 7 an in-depth HYSCORE analysis of NO_2^--bound

myoglobin and wild-type *C*Cld is presented, providing a spectroscopic fingerprint for the *O*-nitrito binding mode in the myoglobin model and preliminary evidence for an *N*-nitro coordination mode in *C*Cld.

Next, in Chapter 8, the short-lived intermediate states formed during the reaction of *C*Cld with either chlorite or hypochlorite are investigated with a rapid freeze-quench (RFQ) method combined with EPR spectroscopy. In the reaction with hypochlorite, RFQ-EPR revealed the signature of an amino-acid based-radical, possibly representing Compound I*, the decay product of Compound I in the absence of an electron donor. On the other hand, in the reaction with chlorite a prominent EPR signal was detected and assigned to a chlorine dioxide radical ($ClO_2^{\bullet}$), an off-pathway product likely derived from the high concentration of chlorite in the reaction mixture. Thanks to these findings, new insights were obtained on the reactivity of the candidate intermediate Compound I, its dependency on pH and on the presence of external electron donors.

To conclude, Chapter 9 is focused on enzyme immobilization for industrial applications. A general overview of the principal immobilization techniques will be given and the most common pitfalls in protocol optimization for industrial scale-up will be presented. Finally, the preliminary results of few immobilization experiments carried out with horseradish peroxidase and *C*Cld will be discussed, highlighting the importance of tuning the experimental conditions such as pH, buffer composition, initial protein concentration or pre-treatment of the support for the success of the immobilization protocol.

I will summarize the main outcomes of this work in Chapter 10 and I will discuss their relevance in the context of chlorite dismutase (and heme protein in general) research. A general perspective on the remaining open questions and future work will close this thesis manuscript.

Samenvatting

Chlorietdismutasen (Clds) zijn heem-*b*-bevattende oxidoreductases van bacteriële oorsprong die chloriet (ClO_2^-) afbreken tot chloride (Cl^-) en moleculaire zuurstof (O_2). Deze unieke enzymatische activiteit werd oorspronkelijk ontdekt in perchloraat- en chloraatreducerende bacteriën (PCRBs), waar Clds fungeren als *scavenging* systeem voor het giftige chloriet dat tijdens de celrespiratie wordt geproduceerd. Interessant is dat de Cld-activiteit later werd geïdentificeerd in niet-PCRBs, zoals in nitrietoxiderende bacteriën en cyanobacteriën. In deze organismen is de fysiologische rol van chlorietdismutasen nog steeds niet volledig opgehelderd. Naast hun intrigerende reactiviteit - de vorming van een O-O-binding was voorheen alleen beschreven voor zuurstofrijke organismen en in een methaanoxiderende bacterie - wekten chlorietdismutasen belangstelling op voor hun potentiële industriële toepassingen, zoals op het gebied van bioremediatie, de bouw van biosensoren en als hulpmiddel om de beluchting in bioreactoren te verbeteren, om er enkele te noemen. In dit werk heb ik mij voornamelijk gericht op de studie van het dimeer chlorietdismutase van *Cyanothece* sp. PCC7425 (*C*Cld) om inzicht te krijgen in verschillende enzymeigenschappen, waaronder de rol van belangrijke aminozuren in de heemomgeving, manieren van ligandbinding en mechanistische details. Het uiteindelijke doel was te komen tot een volledig begrip van deze systemen met het oog op mogelijke toekomstige industriële toepassingen. Hoewel de integratie van verschillende benaderingen noodzakelijk was om de onderzochte aspecten op te helderen, heb ik het onderwerp in mijn werk voornamelijk vanuit spectroscopisch oogpunt behandeld. Het project kan worden gezien als een combinatie van drie belangrijke onderzoeksvragen: i) de rol(len) van een geconserveerd arginine-residu gelegen aan de distale zijde van het heemijzer en de invloed van de flexibiliteit ervan op verschillende enzymeigenschappen; ii) het mechanisme van substraatbinding en de invloed van het arginine in dit aspect; iii) de aard van de tussenliggende toestanden gevormd tijdens de katalytische cyclus en hun afhankelijkheid van pH. Door gebruik te maken van de paramagnetische aard van het ferrisch heemijzer, hetzij in de rusttoestand van het enzym, hetzij na binding van het ligand en in reactie met het (de) substraat(en), werd elektronenparamagnetische resonantie (EPR)-spectroscopie gekozen als voornaamste benadering om deze vragen te beantwoorden.

In Hoofdstuk 1 geef ik een brede inleiding over de in dit werk onderzochte eiwitten, inclusief een algemene beschrijving van heemsystemen, gevolgd door een meer gedetailleerde bespreking van globines, heemperoxidases en chlorietdismutases. In Hoofdstuk 2 worden de belangrijkste gebruikte technieken theoretisch

behandeld. Er wordt een overzicht gegeven van de principes achter de recombinante productie van eiwitten. Vervolgens worden optische en EPR-spectroscopieen in detail behandeld. Ook de principes van *stop-flow* UV-vis spectroscopie en de *Rapid Freeze-Quench* methode worden toegelicht.

Hoofdstuk 3 richt zich op de toepassing van EPR spectroscopie op heemeiwitten en meer specifiek op heemenzymen met potentieel industrieel gebruik als biokatalysator. Een beschrijving van de meest relevante oxidatie- en spintoestanden van het heemijzer zal worden gegeven, gevolgd door een bespreking van het katalytisch relevante *Compound I*, een tussentoestand die in veel enzymatische cycli van peroxidasen wordt aangetroffen. Tenslotte worden enkele succesvolle voorbeelden gegeven van het gebruik van EPR-spectroscopie voor de studie van deze enzymen.

In Hoofdstuk 4 presenteer ik de resultaten van een systematisch onderzoek naar de wisselwerking tussen buffers en cryoprotectanten bij de voorbereiding van monsters voor EPR-spectroscopie bij lage temperatuur. Voor dit werk werd het bekende myoglobine gekozen als modelsysteem en de alkalische overgang werd beoordeeld in aanwezigheid van verschillende combinaties van buffers en glasvormende middelen m.b.v. optische en EPR-spectroscopie. Deze studie benadrukt het belang van het aanpassen van de experimentele omstandigheden aan het bestudeerde eiwitsysteem om verkeerde interpretatie van de gegevens te voorkomen.

Hoofdstuk 5 richt zich op de invloed van de flexibiliteit van het geconserveerde arginine in *C*Cld. Via gerichte mutagenese werden de varianten Q74V en Q74E van *C*Cld gecreëerd, waarbij de glutamine 74, die normaal gesproken een waterstofbrug vormt met arginine 127, werd vervangen door een valine of een glutamaat om de flexibiliteit van het arginine zelf te veranderen. Samen met structurele en biochemische methoden bracht een EPR-pH-afhankelijkheidsanalyse van het wild-type en de varianten de effecten van de gewijzigde argineneflexibiliteit op de alkalische overgang van *C*Cld en op de wijze van binding van een OH^--groep aan het licht, waarbij verschillen in het profiel van zowel hoog-spin als laag-spin ijzer bij pH ≥ 9 werden aangetoond.

Deze bevindingen leidden tot de hypothese dat het arginine en zijn flexibiliteit een beslissende rol spelen in de allereerste stap van de katalytische activiteit, namelijk de binding van het substraat, die uitgebreid wordt onderzocht in Hoofdstuk 6 en 7. Vanwege de snelle reactiviteit van chlorietdismutases met hun natuurlijk substraat werd aanvankelijk nitriet (NO_2^-) gebruikt als substraatanaloog om een stabiel

complex te vormen. De NO_2^--gebonden vormen van het wild-type *C*Cld, Q74-varianten en twee andere varianten, waarin het geconserveerde arginine was vervangen door alanine of lysine (R127A, R12K), werden onderzocht met X-stralenkristallografie, moleculaire dynamica (MD)-simulaties en EPR-spectroscopie (zowel in *continuous wave*- als in gepulste modus). Hoewel de kristalstructuren een overwicht van nitrietbinding via een van de zuurstofatomen lieten zien (O-nitrito-modus), suggereerden zowel MD-simulaties als EPR-spectroscopie dat de binding via het stikstofatoom ook zou kunnen plaatsvinden (N-nitro-modus). Met name in Hoofdstuk 7 wordt een diepgaande HYSCORE-analyse van NO_2^--gebonden myoglobine en wild-type *C*Cld gepresenteerd, die een spectroscopische vingerafdruk oplevert voor de O-nitrito-bindingsmodus in het myoglobinemodel en voorlopig bewijs voor een N-nitro-coördinatiemodus in *C*Cld.

Vervolgens worden in Hoofdstuk 8 de kortlevende tussentoestanden onderzocht die worden gevormd tijdens de reactie van *C*Cld met chloriet of hypochloriet met een snelle freeze-quench (RFQ)-methode in combinatie met EPR-spectroscopie. In de reactie met hypochloriet onthulde RFQ-EPR de signatuur van een op aminozuren gebaseerd radicaal, dat mogelijk staat voor *Compound I**, het vervalproduct van *Compound I* in afwezigheid van een elektrondonor. Anderzijds werd in de reactie met chloriet een prominent EPR-signaal gedetecteerd en toegewezen aan een chloordioxideradicaal ($ClO_2^\bullet$), een afgeleide product dat waarschijnlijk afkomstig is van de hoge concentratie chloriet in het reactiemengsel. Dankzij deze bevindingen werden nieuwe inzichten verkregen in de reactiviteit van het kandidaattussenproduct *Compound I*, zijn afhankelijkheid van de pH en van de aanwezigheid van externe elektronendonoren.

Tot slot is Hoofdstuk 9 gericht op enzymimmobilisatie voor industriële toepassingen. Er wordt een algemeen overzicht gegeven van de belangrijkste immobilisatietechnieken en de meest voorkomende valkuilen bij de optimalisatie van protocollen voor industriële opschaling. Tenslotte zullen de voorlopige resultaten van enkele immobilisatie-experimenten met mierikswortelperoxidase en *C*Cld worden besproken, waarbij het belang wordt benadrukt van het afstemmen van de experimentele condities zoals pH, buffersamenstelling, initiële eiwitconcentratie of voorbehandeling van de drager voor het succes van het immobilisatieprotocol. In Hoofdstuk 10 zal ik de belangrijkste resultaten van dit werk samenvatten en hun relevantie voor het onderzoek naar chlorietdismutase (en heemeiwitten in het algemeen) bespreken. Een algemeen perspectief op de resterende open vragen en toekomstig werk zal dit manuscript afsluiten.

Resumen

Las proteínas llamadas clorito-dismutasas (Clds) son oxidorreductasas de origen bacteriano que contienen un grupo hemo de tipo *b* y degradan el clorito (ClO_2^-) para formar cloruro (Cl^-) y oxígeno molecular (O_2). Esta actividad enzimática única se encontró originalmente en bacterias reductoras de perclorato y clorato (PCRBs), donde las Clds actúan como sistemas de eliminación del clorito tóxico producido durante la respiración. Curiosamente, la actividad de las Clds se identificó más tarde también en bacterias no PCRB, como las nitrito-oxidantes y las cianobacterias. En estos organismos, la función fisiológica de las clorito-dismutasas aún no está completamente determinada. Además de su reactividad inusual (la formación de un enlace O-O sólo se había descrito anteriormente en organismos oxigénicos y en una bacteria metano-oxidante), las clorito-dismutasas han suscitado interés por sus posibles aplicaciones industriales, por ejemplo en el campo de la biorremediación, la construcción de biosensores y como herramienta para mejorar la aireación en biorreactores, por citar algunas. En este trabajo, me he centrado principalmente en el estudio de la clorito-dismutasa dimérica de *Cyanothece* sp. PCC7425 (*C*Cld) para profundizar en diferentes propiedades de la enzima, incluidas la función de los aminoácidos clave en el entorno del hemo, los modos de unión del ligando y los detalles mecanísticos de la reacción. El objetivo último es alcanzar una comprensión exhaustiva de estos sistemas con vistas a posibles futuras aplicaciones industriales. Aunque la integración de distintos enfoques esa necesaria para dilucidar los aspectos investigados, en mi trabajo he tratado el tema principalmente desde un punto de vista espectroscópico. El proyecto puede verse como una combinación de tres cuestiones principales de la investigación: i) la función, o funciones, de un residuo conservado de arginina, Arg127, situado en el lado distal del grupo hemo y el impacto de su flexibilidad en diferentes propiedades de la enzima; ii) el mecanismo de unión del sustrato así como la influencia de la arginina en esta cuestión; iii) la naturaleza de los estados intermedios formados durante el ciclo catalítico y su dependencia del pH. Debido a la naturaleza paramagnética del hemo, ya sea en el estado de reposo de la enzima, tras la unión del ligando, o después de la reacción con el sustrato o sustratos, se eligió la espectroscopia de resonancia paramagnética electrónica (EPR) como enfoque principal para abordar estas cuestiones.

En el Capítulo 1 se hace una amplia introducción sobre las proteínas investigadas en este trabajo, incluyendo una descripción general de los sistemas hemo, seguida de una discusión más detallada sobre globinas, hemo peroxidasas y clorito-dismutasas. En el Capítulo 2, se tratarán desde un punto de vista teórico las

principales técnicas utilizadas y se dará una visión general de los principios en los que se basa la producción recombinante de proteínas. A continuación, se tratarán en detalle las espectroscopias óptica y EPR. También se explicarán los principios de la espectroscopia UV-vis *stopped-flow* y de la técnica de *rapid freeze-quench*.

El capítulo 3 se centra en la aplicación de la espectroscopia EPR a las proteínas hemo y, más concretamente, a las enzimas hemo con potencial uso industrial como biocatalizadores. En él se presentará una descripción de los estados de oxidación y espín más relevantes del hierro hemínico, seguida de una discusión sobre el *Compound I*, un estado intermedio catalíticamente relevante que se encuentra en muchos ciclos enzimáticos de peroxidasas. Por último, se ofrecerán algunos ejemplos exitosos del uso de la espectroscopia EPR para el estudio de estas enzimas.

En el capítulo 4 se presentan los resultados de un estudio sistemático sobre la interacción de tampones y crioprotectores en la preparación de muestras para espectroscopia EPR a baja temperatura. Para este trabajo, se eligió la conocida proteína mioglobina como sistema modelo y se evaluó su capacidad para experimentar una transición alcalina en presencia de diferentes combinaciones de tampones y agentes vitrificantes mediante espectroscopia óptica y EPR. Este estudio destaca la importancia de adaptar las condiciones experimentales al sistema de interés para evitar interpretaciones erróneas de los datos.

El capítulo 5 se centra en el impacto de la flexibilidad de la arginina conservada en la *C*Cld, que se demostró capaz de adoptar diferentes orientaciones, ya sea apuntando hacia el hemo o hacia el canal de entrada del sustrato. Mediante un enfoque basado en *site-directed mutagenesis*, se crearon los mutantes Q74V y Q74E de *C*Cld, en las que la glutamina 74, normalmente unida por un puente de hidrógeno a la arginina 127, se cambió por una valina o un glutamato para alterar la flexibilidad de la propia arginina. Junto con métodos estructurales y bioquímicos, un análisis de EPR dependiente del pH tanto de la enzima nativa como de los mutantes puso de relieve el impacto de la flexibilidad alterada de la arginina en la transición alcalina de la *C*Cld y en el modo de unión de un grupo OH^-, mostrando diferencias en el espectro del hierro de alto y bajo espín a pH ≥ 9.

Estos hallazgos condujeron a la hipótesis de que la arginina, y su movilidad, podrían tener una función decisiva en el primer paso de la actividad catalítica, es decir, la unión del sustrato, que se investiga ampliamente en los capítulos 6 y 7. Inicialmente, debido a la rápida reactividad de las clorito-dismutasas con su sustrato natural, se empleó el nitrito (NO_2^-) como análogo del sustrato para formar un complejo estable. Las formas unidas a NO_2^- de la *C*Cld nativa, las variantes Q74 y dos variantes

adicionales, en las que la arginina conservada se cambió por alanina o lisina (R127A, R12K), se investigaron mediante cristalografía de rayos X, simulaciones de dinámica molecular (MD) y espectroscopia EPR tanto en modo de onda continua como pulsado. Aunque las estructuras cristalinas muestran la unión del nitrito a través de uno de los átomos de oxígeno (modo *O*-nitrito), tanto las simulaciones MD como la espectroscopia EPR sugieren que también podía producirse la unión a través del átomo de nitrógeno (modo *N*-nitro). En particular, en el Capítulo 7 se presenta un análisis HYSCORE en profundidad de la mioglobina unida a NO_2^- y de la *C*Cld nativa, proporcionando una huella espectroscópica del modo de unión *O*-nitrito en el modelo de mioglobina y pruebas preliminares de un modo de coordinación *N*-nitro en la *C*Cld.

A continuación, en el Capítulo 8, se investigan los estados intermedios de vida corta que se forman durante la reacción de la *C*Cld con clorito o hipoclorito mediante un método de *rapid freeze-quench* (RFQ) combinado con espectroscopia EPR. En la reacción con hipoclorito, la RFQ-EPR reveló la huella de un radical localizado en un aminoácido, posiblemente el llamado *Compound I**, producto de la desintegración del intermedio reactivo, *Compound I,* en ausencia de un donante de electrones. Por otro lado, en la reacción con clorito se detectó una señal EPR prominente que se asignó a un radical de dióxido de cloro (ClO_2^-), un producto fuera de ruta probablemente derivado de la alta concentración de clorito en la mezcla de reacción. Gracias a estos hallazgos, se obtuvieron nuevos conocimientos sobre la reactividad del intermedio *Compound I*, su dependencia del pH y de la presencia de donantes de electrones exógenos.

Para concluir, el Capítulo 9 se centra en la inmovilización de enzimas para aplicaciones industriales. En él, se da una visión general de las principales técnicas de inmovilización y se presentarán los escollos más comunes en la optimización de protocolos para el escalado industrial. Por último, se discuten los resultados preliminares de algunos de estos experimentos de inmovilización llevados a cabo con las proteínas *horseradish peroxidase* y la *C*Cld, destacando la importancia de ajustar las condiciones experimentales como el pH, la composición del tampón, la concentración inicial de proteína o el pretratamiento del soporte para el éxito del protocolo de inmovilización.

En el capítulo 10 se resumen los principales resultados de este trabajo y se discute su relevancia en el contexto de la investigación de las clorito-dismutasas y de las hemo proteínas en general. El manuscrito de esta tesis se cierra con una perspectiva general sobre las cuestiones pendientes y los trabajos futuros.

Chapter 1

General introduction

Abstract

In this general introduction, a detailed description of heme proteins from a structural and biochemical point of view is provided.

First, the heme group and its relevance in biological systems are introduced. Then, the main features of globins, with a focus on the model heme protein myoglobin, are briefly discussed. It follows a comprehensive description of heme peroxidases, among which the peroxidase from horseradish, by far the most extensively studied, is here presented in terms of structure and catalytic activity. The main heme peroxidase superfamilies are then introduced according to the most recent phylogenetic classification. A more extended description is provided for the sub-families of dye-decolorizing peroxidases and chlorite dismutases, the latter being the central subject of this work. Finally, a section is dedicated to the applications of heme peroxidases, and chlorite dismutases in particular, in the field of industrial biocatalysis. Established usages and possible novel applications are discussed.

As more extensively explained at the end of this Chapter, the main goal of this thesis is the investigation of chlorite dismutase by applying a spectrum of different techniques, in order to gain mechanistic insights for potential applications in bioremediation and other industrial fields.

1.1 Heme proteins

1.1.1 The heme group

Evolution demonstrated that the diverse and complex spectrum of (bio)chemical reactions which characterizes the very essence of living organisms would have not been achieved with the sole use of organic compounds. Instead, Nature found its way to address many biological tasks with the exploitation of metal ions, among which, iron undoubtedly plays the most important role. Iron is the second most abundant metal on Earth after aluminum, but differently from the latter, it has redox properties which facilitate electron transfer and acid-base processes essential for life. Therefore, it is not surprising that living beings evolved means to make good use of it, though facing some challenges. On the one hand, the amount of insoluble – and thus difficult to uptake – Fe^{3+} (in the form of hydroxides or hydrated iron oxides) progressively increased in the sea water after the appearance of oxygen-generating photosynthetic organisms, ca 3 billion years ago. Secondly, harmful reactive oxygen species (ROS) can be formed in presence of free Fe^{2+}, through the pathways known as Fenton and Haber-Weiss reactions [1]. In this sense, the use of coordination complexes which could keep iron (and other metals) in a "safe" and yet convenient configuration is a remarkable example of Nature's ability to develop one strategy for multiple purposes. With time, living organisms learned how to tune the coordination chemistry of iron in order to modulate the Fe^{3+}/Fe^{2+} redox potential and therefore perform the most varied biological reactions, spanning from oxygen transport and storage to electron transfer, but also sensing, cellular signaling, biosynthesis and gene regulation [2].

The variety and versatility of metal complexes in biology fascinated many researchers over the years and keeps fostering investigations in many fields of Science, from fundamental biochemistry to bioinspired synthetic chemistry. A milestone in porphyrin research is certainly the synthesis of protoporphyrin IX and hemin in 1929 by Hans Fischer, at that time Professor of Organic Chemistry at the Technical University of Munich, for which he received the Nobel Prize in 1930 [3]. Protoporphyrin IX is a key point in the synthesis of functional porphyrins since it is where the synthetic pathways of heme and chlorophyll diverge. When ferrous iron (Fe^{2+}) is inserted in this structure, heme *b* (also referred to as ferri- or iron-protoporphyrin IX) is created. The core structure of heme *b*, which is common to other porphyrins, is that of a tetrapyrrole (**Figure 1.1**) where several conjugated double bonds are responsible for its characteristic UV-vis absorption spectrum (Chapter 2, section 2.2.1). In addition to that, heme *b* possesses four methyl groups, two vinyl groups (at the α-side) and two propionate groups (at the γ-side) as substituents of the peripheric carbons. Further modifications of this molecule give

rise to a variety of heme structures (such as heme *a*, heme *o*, heme *c*...) [2] whose detailed discussion ranges out the scope of the present study. Therefore, I will simply refer to heme when indicating heme *b* throughout the document.

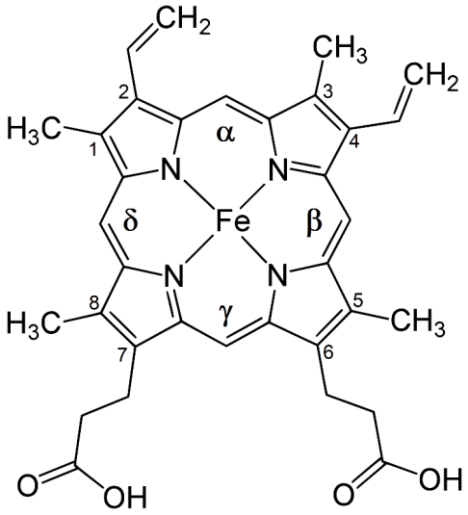

Figure 1.1 *Structure of heme b. Note that the scheme was represented independently of the redox state of the Fe ion.*

Numerous proteins, including the well-known myoglobin and hemoglobin but also enzymes such as cytochromes P450 (P450s) and heme peroxidases contain a heme prosthetic group. The ability of these systems to perform such a varied spectrum of reactions depends on numerous factors, including the polarity and the accessibility of the heme pocket, the interconversion between different oxidation states of the iron, but also heme distortions (*e.g.* ruffling and saddling) [4]. In heme proteins, the nature of the axial ligands plays a key role in the modulation of the iron reduction potential. Common endogenous ligands for the heme iron are amino acids such as histidine, methionine, and cysteine. Normally, one of these residues occupies at least one of the iron axial coordination positions and it is commonly known as the "proximal" (or 5^{th}) ligand. In some cases, the "distal"(or 6^{th}) position is occupied by another amino acid to give a hexacoordinated heme iron, most frequently with a bi-His or His-Met configuration, *e.g.* in many cytochromes [2]. Otherwise, an exogeneous compound can act as distal ligand, as in the case of ferric horse-heart myoglobin or certain P450s, where this role is exerted by a weakly-bound water molecule [5]. Finally, examples of pentacoordinate heme, where the 6^{th} coordination position is vacant and available to react with external substrates, include chloroperoxidases [6] and nitric oxide synthases (NOS) [7]. Along with the striking variability in heme protein functions goes the absence of a common scaffold for

heme binding. Indeed, the most diverse protein folds are observed for heme-containing proteins. In the next sections the main structural and biochemical highlights of the systems investigated in this work will be discussed in detail.

1.1.2 Globins

Globins are small heme-containing proteins that span across all six kingdoms of life. They are named after the Latin term *globus*, "sphere", for their ball-like shape which is arranged in the highly conserved tertiary motif known as the globin fold. In the *classical* globin fold, typical of vertebrate globins, eight α-helices, connected by short loops, are disposed in a characteristic 3-over-3 sandwich structure (**Figure 1.2**) and labelled with letter A to H from the N-terminus to the C-terminus. This fold includes a pocket where the heme prosthetic group resides. Differently from their structure, the primary sequence of globins is not fully conserved, but there is a strictly conserved histidine at the 8th position of the F helix (F8His), that binds the iron heme at the proximal side [8].

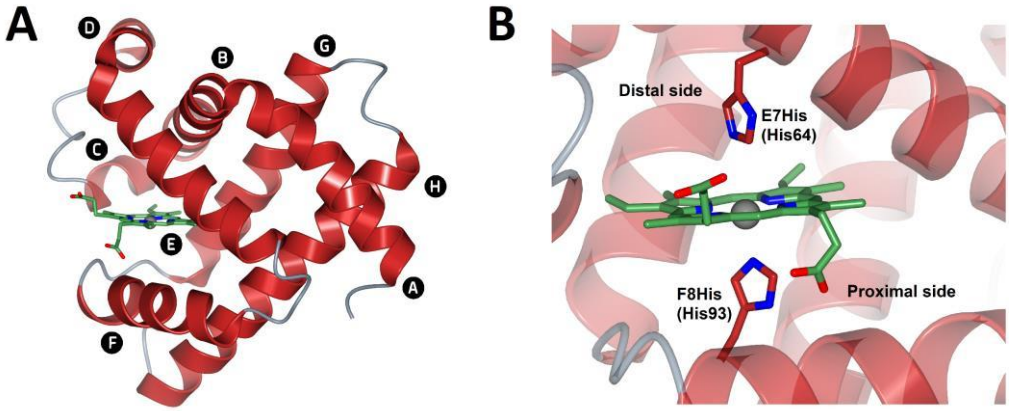

Figure 1.2 *Crystal structure of myoglobin from horse heart depicted in ribbon representation (PDB: 5D5R [8]* ***A)*** *The typical 3-over-3 sandwich fold is shown. The labelling of the eight α-helices follows the conventional globin nomenclature. The heme group is represented in green sticks with porphyrin nitrogen atoms and propionate oxygen atoms highlighted in blue and red, respectively.* ***B)*** *Magnification of the heme pocket. The conserved F8His coordinates the heme at the proximal side, while at the distal side E7His plays an important role as H-bond donor, helping the stabilization of the O_2 molecule upon binding. The specific amino acid nomenclature for horse heart myoglobin is indicated between parenthesis.*

The occurrence of globins in virtually all kingdoms of life became evident with the development of high-throughput methods for genome sequencing which boosted evolutionary studies and soon led to the definition of a "globin superfamily". Despite numerous and diverse functions are now described for globins, they are assumed to have evolved from a common ancestor which could have been present on Earth as early as 4 billion years ago. Primordial globins may have had a role in the response of anaerobic organisms to an increasingly oxidative atmosphere. Therefore, early functions could likely include O_2 scavenging, sensing, and reactions with other diatomic gaseous ligands such as nitric oxide (NO) and carbon monoxide (CO). The role of O_2 transport and storage would have probably happened only at a later time, with the emergence of multicellular organisms [9, 10]. Nowadays, the most extensively investigated globins are undoubtedly vertebrate hemoglobin (Hb) and myoglobin (Mb) for their oxygen-related functions and for being recently linked to NO metabolism and ROS scavenging [8]. In this work, myoglobin is used as a model heme protein for (i) the calibration of a Rapid Freeze-Quench (RFQ) setup (Section 2.3.4), (ii) studying the interplay of different buffers and cryoprotectants for low-temperature Electron Paramagnetic Resonance (EPR) spectroscopy (Chapter 4), and (iii) nitrite (NO_2^-) binding experiments (Chapter 7). Therefore, a detailed discussion of this system is provided.

1.1.2.1 Myoglobin

Myoglobin is the reservoir of dioxygen in muscle tissue, being principally found in striated muscles (*e.g.* heart and skeletal) but also to a minor extent in smooth muscles and endothelial cells [8]. The structure of Mb is the first protein structure to be resolved by X-ray crystallography. It consists of a single polypeptide chain of 160 amino-acid residues arranged in a *classic* globin fold, with a molecular weight of ~ 17.600 Da. The heme cofactor is positioned in a rather hydrophobic pocket and it is held in place by non-covalent interactions. As shown in **Figure 1.2 B**, at the proximal side, F8His (His93) coordinates the heme iron, while at the distal side E7His (His64) modulates the binding of O_2 and other exogenous ligands as explained more in detail in [11]. Inside the cells, the ferrous heme iron (Fe^{2+}) of myoglobin can reversely bind O_2 with a higher affinity than hemoglobin. This facilitates the extraction of oxygen from the blood, in addition to the cooperative effects which drive oxygen binding and release in Hb [8]. However, the oxidation to the Fe^{3+} state generates the so-called aquomet (or sometimes simply referred to as met-) myoglobin, incapable of oxygen binding. Here, a water molecule (from this the name *aquo*) sits at the 6th distal position. When Mb is extracted from muscle tissues and purified for research purposes, it gets oxidized by the oxygen present in the atmosphere and therefore it assumes the conformation of aquomet Mb, and eventually undergoes denaturation.

Apart from the well characterized O_2-related functions, it is now known that Mb possesses a range of additional physiological roles, most importantly linked to the NO metabolism. It has been demonstrated that oxygenated myoglobin (oxy-Mb) converts toxic NO to nitrate (NO_3^-) thanks to its dioxygenase activity [12]. Secondly, deoxygenated myoglobin (deoxy-Mb) can exploit its nitrite reductase activity and form NO from nitrite (NO_2^-) thus mediating a vasodilatation process which is independent of the activity of nitrite oxide synthase enzyme [13]. In terms of affinity and rate of ligand binding, E7His plays a fundamental role. It has been shown that this residue can discriminate O_2 from CO by the fact that the former binds to the heme with an angle of ~ 60°, while the latter binds to it perpendicularly [14, 15]. The same amino acid is also involved in determining the binding mode of NO_2^-, as demonstrated by crystallographic studies (**Figure 1.3**). The crystal structure of wild-type (WT) aquomet Mb from horse heart in the presence of NO_2^- revealed that this ligand coordinates the ferric heme iron through a *O*-nitrito binding mode (**Figure 1.3 A & C**) [16]. Not long after, the same authors conducted a site-directed mutagenesis study in which they replaced His64 (E7His) with a valine, thus removing an important H-bond donor at the heme distal side [17]. The crystal structure of the H64V mutant in presence of NO_2^- exhibited a *N*-nitro binding mode (**Figure 1.3 B & D**), with a rather long Fe-N(nitrite) bond distance of 2.6 Å which indicates that electrostatic interactions are responsible for holding the ligand in place. Chapter 7 will provide the reader with an in-depth spectroscopic analysis of the nitrite-bound form of aquomet Mb and its relevance in ligand-binding studies of chlorite dismutases.

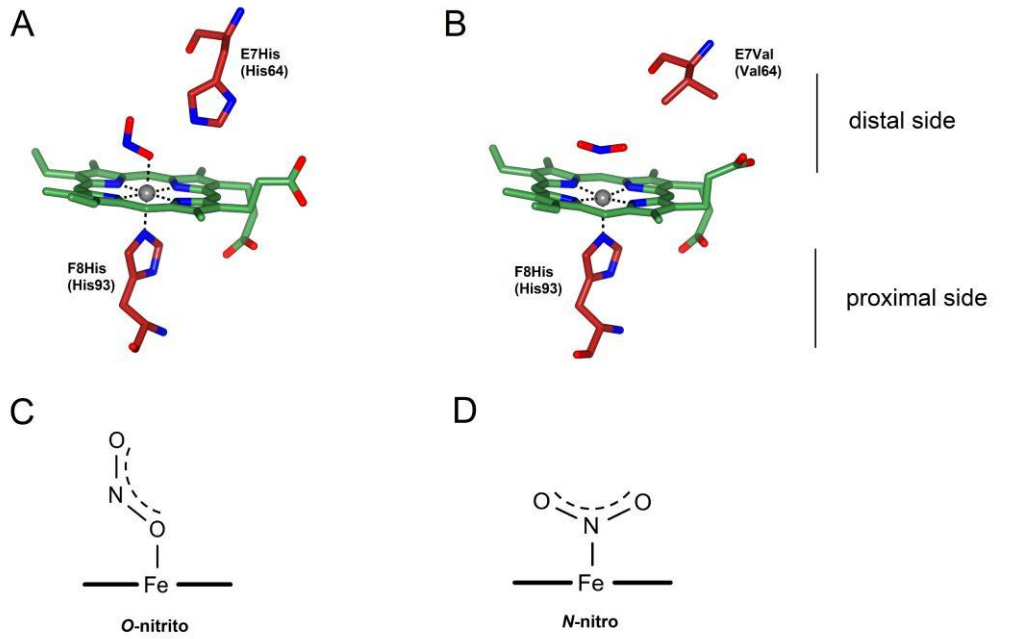

Figure 1.3 *3D view of the active-sites of wild-type* ***(A)*** *and H64V* ***(B)*** *variants of horse heart myoglobin binding NO_2^-. For clarity, only the heme group and two most relevant amino acids are displayed in stick representation, while the heme iron is depicted as a grey sphere. When the H-bond donor His64 is present, the preferred coordination mode for nitrite is via O-nitrito binding* ***(C)****. Alternatively, when His64 is replaced by a valine residue, nitrite orientation suggests a N-nitro binding mode* ***(D)****.*

1.1.3 Heme peroxidases

Peroxidases are ubiquitous enzymes which are found in all forms of life. Their appearance on Earth dates back to primordial times (ca 2.3 – 2.4 billion years ago) when they most likely served as an antioxidative stress response for both prokaryotic and eukaryotic organisms which needed to adapt to the increasing concentration of dioxygen in the atmosphere. The majority of known peroxidases use a heme group as redox cofactor, most frequently of the *b* type, to catalyze hydrogen peroxide (H_2O_2)-mediated oxidations of a multitude of substrates. **Scheme 1.1** represents the classic peroxidase cycle. Briefly, H_2O_2 oxidizes the ferric iron of the resting state to an Fe(IV) oxoferryl and a π-cation porphyrin radical intermediate, a protein state which is commonly referred to as Compound I (**Scheme 1.1 step 1**), formally two oxidizing equivalents above the resting state. Next, a one-electron donor (AH) gets oxidized to its radical form ($A^{\bullet}$), mediating the

formation of the oxoferryl species known as Compound II, one oxidizing equivalent above the resting state (**Scheme 1.1 step 2**). The oxidation of a second AH molecule finally brings back the enzyme to the resting state (**Scheme 1.1 step 3**) [18, 19].

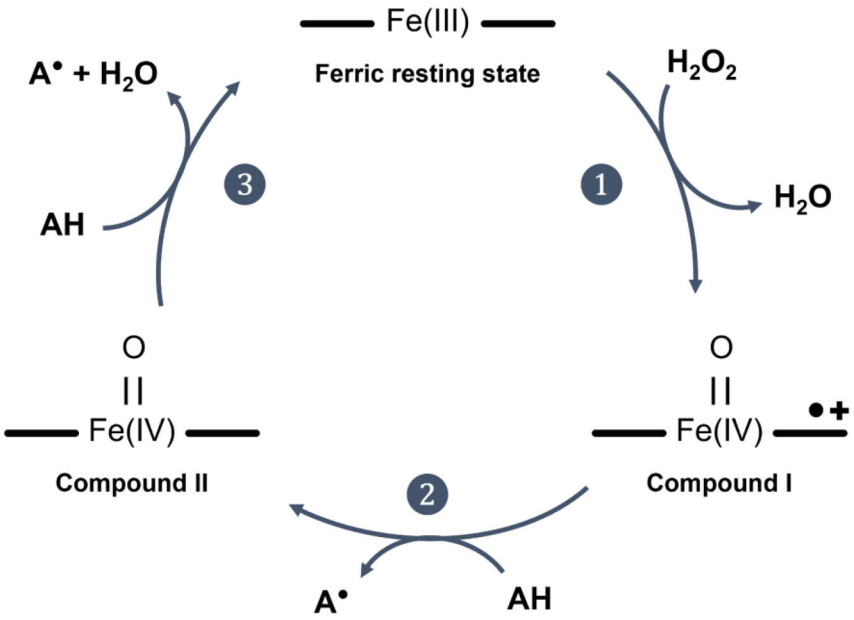

Scheme 1.1 *Peroxidase catalytic cycle*

The first reaction of a peroxidase enzyme was observed by Louis Antoine Planche in 1810. Planche found out that samples of guaiac resin turned to a vivid blue color when in contact with the roots of the horseradish plant (*Armoracia rusticana*) [20]. The term "peroxidase", however, was coined much later towards the end of the 19th century, and it was not before the 1950s that the presence of multiple variants of the peroxidase enzyme in the horseradish and other plants roots were identified and described [21]. To these horseradish proteins, which possessed different structure or different biophysical properties but performed the same catalytic reaction, was given the name of *isozymes* (or *isoenzymes*) [22]. In 1977, 42 horseradish peroxidase (HRP) isoenzymes were detected, of which only seven were later biochemically characterized [23]. To date, 28 genes coding for natural HRP isoenzymes are available in public databases, of which C1A is definitely the best studied [21]. The interest in HRP boosted between the late 1980s and the 1990s with the development of molecular biology diagnostic kits, but later followed a decline. Only recently, also thanks to the discovery of new naturally occurring

isoenzymes, HRP gained renewed attention for possible biotechnological applications including biocatalysis and bioremediation.

Overall, HRP C is a globular protein with a prevalence of α-helices and a short β-sheet region (**Figure 1.4 A**) [24]. Although still nowadays the preferred method for large-scale production of HRP relies on extraction and purification from the horseradish roots, the first crystal structure of HRP isoenzyme C was obtained from a protein recombinantly expressed in *E. coli* in a non-glycosylated form [25]. Previous efforts in obtaining crystals suitable for X-ray diffraction were hampered by the large heterogeneity in glycosylation patterns. Indeed, the surface of HRP C contains several N-glycosylation sites and the total carbohydrate content falls between 18 and 22 % depending on the enzyme preparation. Other important features comprise four disulfide bridges between cysteine residues and two different types of metal centers. At the center of the molecule, right in between two domains referred to as "proximal" and "distal" , resides a heme *b* prosthetic group. The iron heme is coordinated by a proximal histidine (His170) and by the four pyrrole nitrogens (**Figure 1.4 B**). The 6th axial coordination position is free and available to bind H_2O_2 during turnover. In addition to hydrogen peroxide, distal amino acids Arg38 and His42 facilitate the binding and stabilization of other molecules such as CO, cyanide (CN^-), fluoride (F^-) and azide (N_3^-). Finally, the two calcium atoms, located at the opposite sides of the heme pocket, are essential for the structural integrity and thermal stability of the enzyme [26].

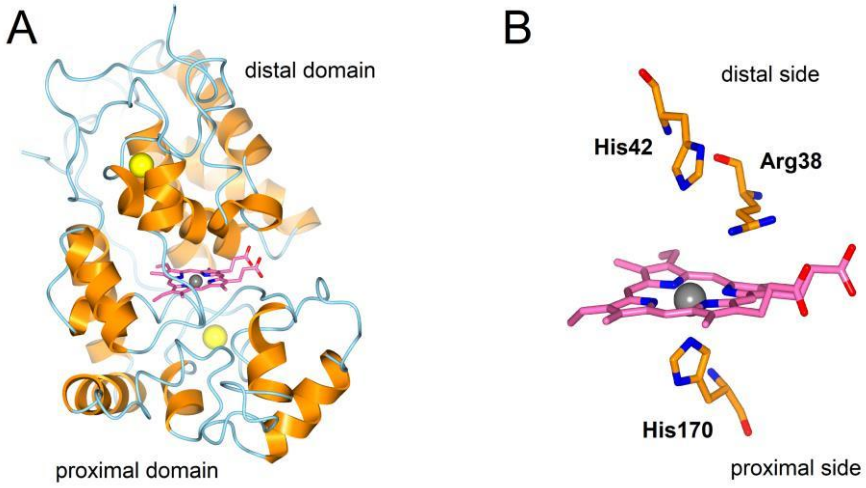

Figure 1.4 *Crystal structure of HRP isoenzyme C in cartoon representation* ***(A)*** *and magnification of the heme site in sticks representation* ***(B)*** *(PDB: 1H5A* [24]*). Calcium atoms are depicted as yellow spheres, while the heme iron as a grey sphere. In the zoom-in, the key amino acid residues are highlighted.*

As many other peroxidases, HRP is able to react with a variety of reducing compounds. Common substrates include aromatic phenols, phenolic acids, amines and sulfonates. Because of this promiscuous character, it is difficult to distinguish the *real* substrate(s) (*i.e.* the physiological substrate(s)) from all the molecules which can practically interact with these enzymes. As a result, the physiological role of many known peroxidases, including HRP, is still under discussion. While certain peroxidases seem to have H_2O_2 scavenging as sole function (*e.g.* some bacterial and mitochondrial peroxidases [19]), in other cases the activated substrate takes part in further reactions. For instance, the formation of radicals upon the reaction of HRP with phenols and amines suggests their participation in cross-linking processes for the synthesis of biopolymers [26]. In addition to the classical peroxidase activity, catalase-, cyclooxygenase- and peroxygenase-like activities have been described for some representatives of this enzyme macro-group [19]. Finally, some peroxidases perform reactions which are attractive for industrial applications, such as epoxidations, hydroxylations and sulfoxydations [27]. The following sections will provide the reader with an overview of peroxidase classification, with a focus on the peroxidase-chlorite dismutase superfamily. Given the complexity and diversity of the peroxidase macro group, here I only report a brief summary of the main superfamilies. The interested reader is referred to [19] for a comprehensive description of the phylogenetic and structural relationships between the different heme peroxidases groups. At the end of this chapter, the potential use of chlorite dismutases as industrial biocatalysts will be contextualized in the broader frame of industrial applications of heme peroxidases.

1.1.3.1 Peroxidase-catalase superfamily

To date, the peroxidase-catalase superfamily counts the highest number of deposited sequences in gene and protein databases. Members of this superfamily are found across the domains of Bacteria, Archaea and Eukarya, being distributed in the latter in the kingdoms of Plants, Fungi, Protozoa, Chromista and Metazoan. Of this superfamily, only *catalase-peroxidase* representatives show a high *catalase* activity, meaning that they can use an additional H_2O_2 molecule as a 2-electron donor to yield dioxygen. The typical fingerprints of this superfamily are the distal amino-acid triad Arg-Trp/Phe-His and the proximal triad is His-Trp/Phe-Asp, while the overall structure is mainly globular and rich in α-helices. In-depth phylogenetic analysis revealed a clear subdivision in three structural classes, which were given the names of Family I, II and III, whose detailed discussion exceeds the scope of this work. Noteworthy, HRP belongs to Family III, together with several plant secretory peroxidases whose main function is believed to be related to the oxidation of lignin precursors and secondary metabolites [19].

1.1.3.2 Peroxidase-cyclooxygenase superfamily

Members of the peroxidase-cyclooxygenase superfamily are present in all domains of life and are distributed in seven main families. Generally, they are multidomain proteins with one peroxidase domain constituted in prevalence by α-helices. A particularity of this superfamily is that the prosthetic group is covalently linked to the protein by two ester bonds with conserved Asp and Glu residues. As a consequence, the distorted heme confers these peroxidases unique spectral and redox properties. Signature features of this superfamily include a distal catalytic histidine neighbored by two aspartate residues. At the proximal side, the coordinating histidine is H-bonded to an asparagine. Among its representatives, the peroxidase-cyclooxygenase superfamily contains short bacterial *peroxicins* (Family V) which are shown to have ancestral origins. Family VI instead comprises well-known animal peroxidases, including myeloperoxidase (MPO) and lactoperoxidase (LPO). Finally, the members of Family VII are observed both in bacteria and in several animal phyla, with the particular sub-group of α-cyclooxygenase being evolved in such a way that oxygenation of fatty acids is the main physiological activity in contrast to a reduced peroxidase activity [19].

1.1.3.3 Peroxidase-peroxygenase superfamily

Representatives of the peroxidase-peroxygenase superfamily possess the unique ability to incorporate a peroxide-derived oxygen into substrate molecules. They are also distinct from the other superfamilies by the presence of a cysteine residue replacing the coordinating histidine at the proximal side of the heme iron. The exceptional range of activities which characterize these peroxidases includes oxidation of organic and inorganic halides, one-electron oxidations, hydroxylations, epoxidations and dealkylations. For a long time, chloroperoxidase (CPO) from the ascomycetous fungus *Leptoxyphium fumago* was at the center of research interest [28]. Despite new members have been later identified and characterized, the peroxidase-peroxygenase superfamily remains the one with the smallest number of members known to date, but it is clear that many more representatives are yet to be discovered [19].

1.1.3.4 Peroxidase-chlorite dismutase superfamily

This peroxidase superfamily was originally proposed as a grouping of three different protein families on the basis of common structural features in spite of a generally low sequence similarity [29]. It was named CDE from the families of Chlorite dismutases (Clds), Dye-decolorizing peroxidases (DyPs), and exogenous iron uptake peroxidases B (EfeBs) [30, 31], although renaming became necessary after the EfeB members were actually found to be part of the DyPs family. The main

structural element which brings together the representatives of these superfamily is the heme-binding scaffold. The architecture of the active site of chlorite dismutases and dye-decolorizing peroxidases shows indeed a surprising similarity despite their different reactivities. Both enzymes possess a fully conserved arginine at the distal site of the heme group and DyPs present an additional aspartate residue. At the proximal side, the iron is always coordinated by a conserved histidine, which in turn is bound to a glutamate or to an aspartate in Clds and DyPs, respectively. The peroxidase-chlorite dismutase superfamily was later identified as a small component of a much larger "α + β barrel" structural superfamily, whose characteristics and diverse functionalities have been extensively discussed in a recent review [32]. The subdivision of the peroxidase-chlorite dismutase superfamily comprises four distinct DyPs families, four Cld-like clades and two functional Clds clades. Whereas DyPs mainly exhibit the classic peroxidase reaction (see **Scheme 1.1**) and functional Clds efficiently degrade chlorite in chloride and molecular oxygen, the Cld-like representatives show neither of the two activities. The common ancestor of this superfamily probably resides in the DyP-subfamily A whose members are found in facultative anaerobic bacteria. These enzymes later evolved to give more complex DyP-subfamilies C and D, the former found in proteobacteria, actinobacteria and cyanobacteria, while the latter belonging to fungi phyla. A different pathway might have led to the appearance of shorter DyP-B peroxidases, which constitute the most divergent subfamily, and eventually to the evolution of chlorite dismutases. In fact, Clds are thought to be derived from DyP-B peroxidases through partial deletions and modifications of ancestral DyP genes [19].

1.1.4 Dye-decolorizing peroxidases (DyPs)

In contrast to other families of peroxidases, the history of DyPs research is relatively young. The first description of the activity of dye-decolorizing peroxidases was given in 1999 when a strain of the fungus *Geotrichum candidum* was used to decolorize molasses and an anthraquinone dye in shaken flasks (from here the name "dye-decolorizing") [33]. The original classification in the four families A, B, C and D (*vide supra*) is based on primary sequence homology. However, with the progressive discovery of new representatives in a great variety of organisms and with the most diverse functionalities, the need for an updated classification which could better explain the structure-function relationship in these enzymes emerged. Therefore, in 2015 a new classification based on tertiary structure alignments was proposed: class A was renamed as P (primitive), class B as I (intermediate), while classes C and D were joint in a single class V (adVanced) [34]. The core of DyPs is a "α + β barrel" subunit (**Figure 1.5**), common to all the enzymes belonging to this family. The heme pocket is recognized to be the binding site of hydrogen peroxide, however the binding site of other substrates must be located away from the heme

region, whose restrictive arrangement would prevent the entering of bulky substrates like synthetic dyes [35]. Several studies suggest that the catalysis might ultimately occur at the surface of the enzyme, where an electron can be delivered *via* a long-range electron transfer from the heme distal side [36–38]. Notably, beyond the classic peroxidase cycle, several additional catalytic activities were described for DyPs, including hydrolase [39], deferrochelatase [31] and oxidase [40]. Because of their diverse spectrum of substrates and activities, the physiological roles of DyPs are still under discussion. Fungal DyPs from Class V (formerly DyP-D) are thought to be involved in a parasitism mechanism since they are active towards natural anthraquinone compounds produced by plants as a defence against fungal infection [41]. Other representatives of Class V, both from bacteria and basidiomycetes, have been shown to be able to degrade lignin, even though it remains to be determined whether this constitutes the primary activity of these enzymes [42, 43]. Finally, an interesting additional function of certain DyPs is their ability to associate with encapsulin, a protein used by bacteria to create intracellular nano-compartments. Thanks to this association, DyPs from *Mycobacterium tuberculosis* and other pathogens are able to elude the host immune system assault [44]. It is evident from these examples that many aspects of the dye-decolorizing peroxidases family remain to be elucidated and that new insights will open ways for the development of novel biotechnological solutions. On the same line, the striking similarities between the heme pocket of DyPs and Clds intrigued many researchers in the last two decades and fostered studies which aimed at finding the structural determinants responsible for the different enzymatic

activities. I will now discuss in detail the current knowledge on chlorite dismutases, which constitute the main object of study of this work.

1.1.5 Chlorite dismutases (Clds)

Not long before the discovery of DyPs, in 1996 Ginkel and co-workers described a heme *b*-containing enzyme performing an unusual biochemical reaction. They gave it the name of chlorite dismutase for its ability to decompose chlorite (ClO_2^-) in chloride (Cl^-) and molecular oxygen (O_2) [45]. The enzyme was isolated from the facultative anaerobic bacterium *Azospira oryzae*, which respires perchlorate (ClO_4^-) in the absence of oxygen. Perchlorate-reducing bacteria, or PCRBs, can utilize perchlorate or chlorate (ClO_3^-) as final electron acceptors in their respiratory chain in anaerobic conditions. Thus, the enzyme chlorite dismutase is used by these organisms to remove ClO_2^- which is produced intracellularly as a consequence of their metabolism [46, 47]. Although the first chlorite dismutases were identified in PCRBs [45, 48–51], soon after homologous enzymes were found in bacteria which do not reduce perchlorate. Clds representatives were isolated from nitrite-oxidizing bacteria such as "*Candidatus* Nitrospira defluvii" [52] and *Nitrobacter winogradskyi* [53], but also more recently in cyanobacteria [54]. Despite evolutionary studies suggest an ancient origin of the Cld genes, the presence of chlorite in the environment is attributed mostly to relatively recent human activity [46, 47]. This raised some questions about the possible physiological role of Clds in non-perchlorate-reducing bacteria, which is still under discussion.

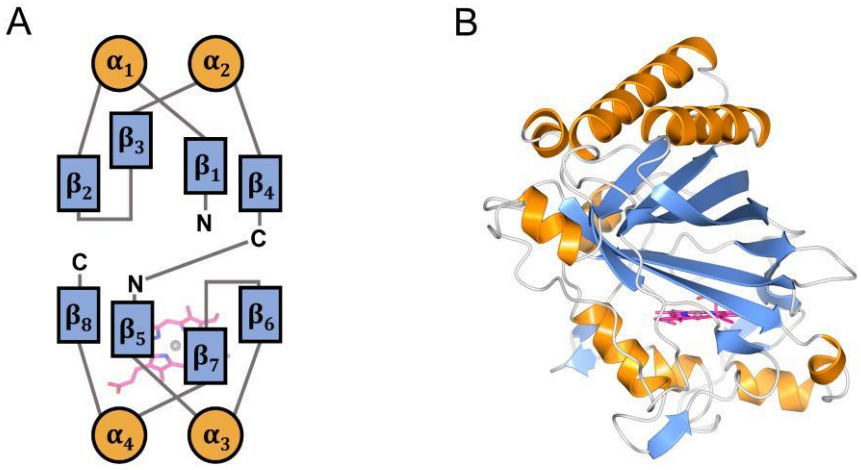

Figure 1.5 *Schematic* ***(A)*** *and ribbon* ***(B)*** *representation of an "α + β barrel" subunit. The scheme in (A) is reproduced from* [67]*. The structure of Klebsiella pneumoniae dye-decolorizing peroxidase (KpDyP, PDB: 6KFS) was used to generate the figure in (B).*

From a structural point of view, Clds belong to a big superfamily of porphyrin-binding "α + β barrel" proteins, together with DyPs and EfeBs [32]. According to the most recent classification, Clds are divided in two clades, namely clade I (or "long Clds") comprising mostly pentameric representatives (**Figure 1.6 A**), and clade II (or "short Clds") containing dimeric enzymes (**Figure 1.6 B**) [19]. Clade I subunits consist of two ferredoxin-like folds, each one composed of a total of four antiparallel β-strands flanked on one side by two α-helices. In these enzymes the C-terminal fold is responsible for heme-binding. Clade II Clds lack the α-helices of the N-terminal fold, being therefore significantly shorter than clade I members. Nevertheless, the structure of clade II enzymes is almost completely superimposable with the C-terminal fold of clade I Clds and similarly able to bind the heme prosthetic group (**Figure 1.6 C**). Notably, also the active site arrangement is practically identical in the two clades (**Figure 1.6 D**). A fully conserved histidine coordinates the ferric heme iron at the proximal side. The imidazolate character of this residue is enhanced by an extended H-bonding network which includes a glutamate, a lysine and two tryptophan residues [55]. At the distal side, a loosely bound water molecule is found as sixth axial ligand, keeping the iron in high-spin configuration, at least at acidic and neutral pH conditions. On the same side of the heme, a fully conserved arginine sits in an otherwise completely hydrophobic environment. Site-directed mutagenesis investigations suggest that this residue is catalytically relevant and essential to prevent the chlorine species transiently formed during the catalytic cycle to escape the active site and damage the protein moiety (*vide infra*) [55–58]. A particular feature of this arginine residue is its flexibility, which is demonstrated by its appearance in two distinct conformations in different crystal structures of Clds. More specifically, while in clade I Clds the arginine sidechain points preferentially toward the heme iron ("IN" conformation) [59–61], in the short clade II Clds, it is always oriented away from the heme, pointing toward the substrate entry channel ("OUT" conformation) [53, 55]. This reflects an important difference

Figure 1.6 *Structural arrangements of clade I and clade II chlorite dismutases.* ***(A)*** *Pentameric (clade I) Cld from Magnetospirillum sp. (PDB: 5A12) (MaCld) in violet cartoon representation;* ***(B)*** *Dimeric (clade II) Cld from Cyanothece sp. PCC7425 (PDB: 5MAU) (CCld) in gold cartoon representation; in both structures heme cofactors are shown as blue sticks and iron ions as grey spheres.* ***(C)*** *Overlay of the monomers from MaCld (violet) and CCld (gold): CCld lacks the N-terminal α-helices, being considerably shorter than MaCld. Nonetheless, the C-terminal domain is almost superimposable in the two enzymes;* ***(D)*** *Overlay of the active sites of MaCld (violet) and CCld (gold), where the arrangement of the key amino-acid residues is shown: in MaCld, Arg183 points toward the heme iron ("IN" conformation), while in CCld the corresponding Arg127 points away from the heme ("OUT" conformation) as a result of its H-bonds with the conserved Gln74. Water molecules in the active site are omitted for clarity.*

between clade I and clade II Clds, which is the presence of an additional conserved glutamine in the latter, H-bonded to the catalytic arginine and therefore responsible for modulating its flexibility [55].

Despite the name chlorite dismutase, the oxidoreduction performed by these enzymes is not *per se* a dismutation, which would require a species to be converted in two different ones with higher and lower oxidation states, respectively. In the Cld reaction a dioxygen molecule is produced from chlorite, implying the formation of a covalent O-O bond. Besides the water-splitting complex of photosystem II, only

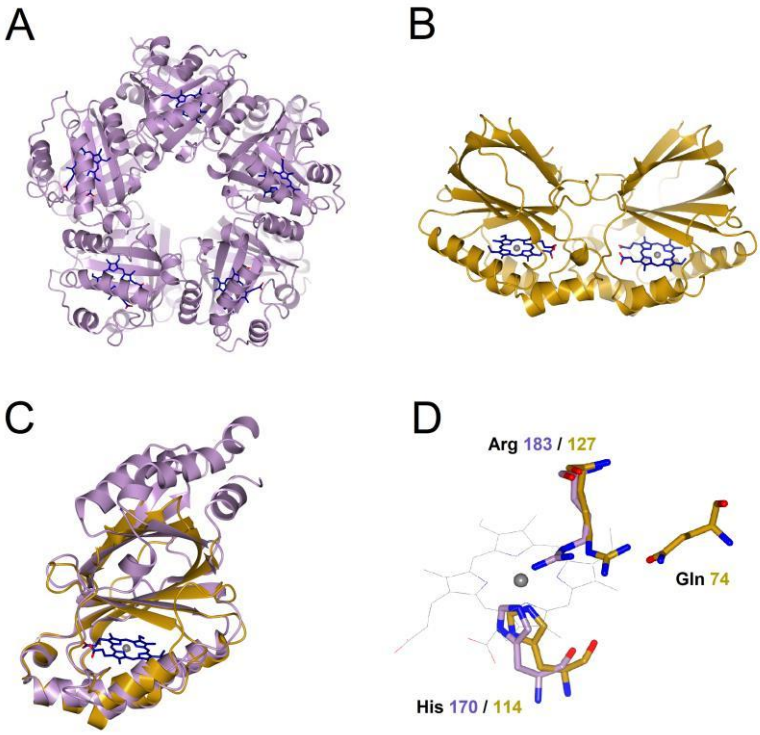

chlorite dismutases and an enzyme from a methane-oxidizing bacterium are known to catalyze such reaction, to date [62]. The observation of a 1:1 stoichiometry between chlorite and the produced dioxygen, as well as ^{18}O-labelling studies, confirmed that the oxygen atoms of O_2 derive from a single chlorite molecule [50, 63]. Some open questions remain, however, concerning the nature of the catalytic intermediates formed in the reaction cycle. After the binding of the substrate chlorite to form an Fe(III)-chlorite complex (**Scheme 1.2, Reaction 1**), two principal routes have been proposed on the basis of experimental and computational data. In the first case, the chlorite molecule would be heterolytically cleaved to give an oxoiron(IV) species with a delocalized π-cation porphyrin radical

(Compound I) and a hypochlorite (ClO^-) intermediate (**Scheme 1.2**, **Reaction 2A**). Otherwise, the ClO_2^- anion would undergo homolytic cleavage to form the oxoiron(IV) species referred to as Compound II and a chlorine monoxide radical ($ClO^\bullet$) (**Scheme 1.2**, **Reaction 2B**). The heterolytic cleavage would be followed by a rebound mechanism of the hypochlorite intermediate (**Scheme 1.2**, **Reaction 3A**), while in the case of the homolytic pathway, the nucleophilic attack of $ClO^\bullet$ to the ferryl species would occur (**Scheme 1.2, Reaction 3B**). In both cases, the final step would be the release of the products chloride and dioxygen (**Scheme 1.2, Reaction 4**). Initially, spectroscopic evidence of compound I formation upon reaction with chlorite or peroxyacetic acid supported the heterolytic cleavage pathway [63–65]. By contrast, computational studies highlighted that the energy barriers would be significantly lower in the case of a homolytic cleavage [66].

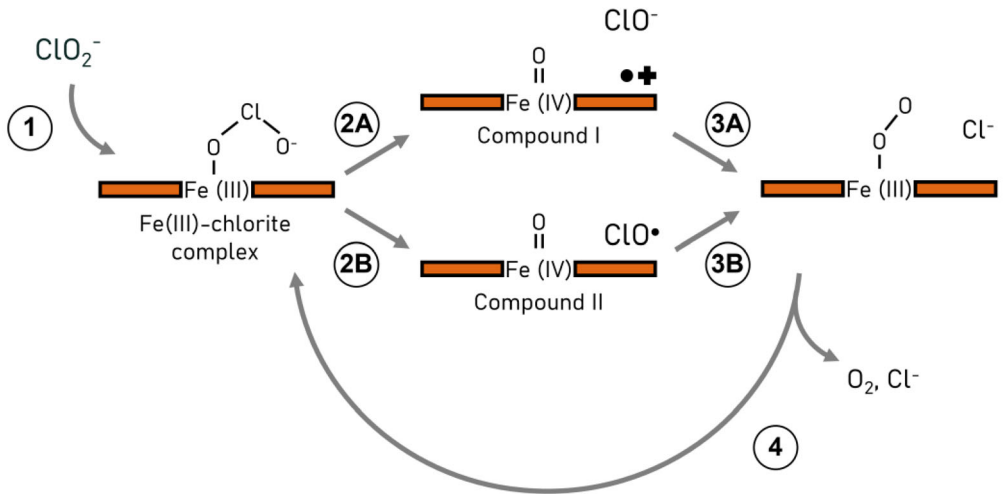

Scheme 1.2 *Proposed catalytic pathways for chlorite dismutases.*

The difficulties in determining the exact nature of the catalytic intermediates stem from their rather unclear spectral features observed by stopped-flow UV-vis experiments and their dependency on pH, whose origin has not been completely elucidated until today [67]. Due to the paramagnetic nature of the ferric resting state, Compound I and chlorine radical intermediates, EPR spectroscopy poses itself as a technique of choice for the investigation of these systems. However, while the time scale of chlorite dismutases turnover can be accessed to a certain extent with conventional stopped-flow experiments, EPR often requires working at cryogenic temperatures, especially when paramagnetic transition-metal ions need to be

detected and characterized. Therefore, specific methodological solutions which allow the freeze-quenching of the enzymatic reaction in the (sub) millisecond time scale are needed. RFQ approaches and their combination with EPR spectroscopy will be treated in detail in Chapter 2 (section 2.3.4), while Chapter 8 will illustrate the application of the RFQ technique to study the interaction of the Cld from *Cyanothece* sp. PCC7425 (*C*Cld) with ClO_2^- and ClO^-. Likewise, the most recently proposed catalytic mechanism(s) will be discussed more extensively in Chapter 8 in order to contextualize the mechanistic insights into chlorite dismutase reactivity obtained by RFQ-EPR experiments.

1.1.6 Industrial application of heme peroxidases

Sustainability, circular economy, environmental footprint are terms that we hear more and more often in the media, being at the center of environmental activists' campaigns or highlighted as priorities in societal policies. The concept of *green chemistry* emerged as a response to the Pollution Prevention Act of 1990 and quickly developed in the nineties with the organization of several international meetings and the institution of networks, in both U.S and Europe, dedicated to the topic [68]. The green chemistry approach was concretized by Paul Anastas and John Warner in 1998 with the publication of the notorious "12 principles" in their book *Green Chemistry: Theory and Practice*, which provided clear guidelines for future research. The first principle, known as "principle of prevention", affirms that "it is better to prevent waste than to treat or clean up waste after it has been created" and it can be considered as the achievement to obtain by applying the good practices described in their *manifesto*. These include the design of safer chemicals, the use of less hazardous solvents, the minimization of energy requirements, the employment of catalysts over stoichiometric reagents and the development of products which can be degraded to innocuous components at the end of their life [69]. With this approach in mind, it is not surprising that the field of biocatalysis, *i.e.* the use of biological molecules or entire organisms to catalyze chemical reactions, gained more and more attention in the last decades. In particular, enzymes arouse a great interest because of their high performances in mild conditions (*e.g.* aqueous solvents, neutral pH, moderate temperature...), their high substrate specificity and their regio- and/or stereoselectivity. Nowadays, examples of well-consolidated applications of enzymes as biocatalysts span across several industrial sectors, with pharmaceutics, food and beverages, detergents and textile manufacturing being among the most famous ones [70].

Peroxidases constitute perhaps the most versatile enzyme superfamily in terms of industrial usage. Among these, the fungal CPO and the plant HRP are well-known to catalyze important reactions for the production of chiral building blocks, such as the oxidation of olefins (CPO) and sulfides (both CPO and HRP). HRP can also catalyze radical-initiated polymerization reactions, by directly oxidizing the monomeric substrate or by inducing the formation of a free radical onto an initiator molecule. This kind of polymerization of phenolic compounds is used to obtain structured polymers such as thermoplastic or thermoresistant resins [27]. Moreover, HRP has been at the center of numerous studies in the field of biosensor construction. The term *biosensor*, according to the International Union of Pure and Applied Chemistry (IUPAC), refers to a device which consists of a biological component in close contact with a physicochemical transducer [71]. The transducer converts a biological signal (*e.g.* a conformational change, or an increased or decreased enzymatic activity) into a quantitative and measurable signal, normally electric, thermal, or optical, which is directly proportional to the concentration of the analyte of interest. Examples of analytes which can be detected by HRP-based sensors clearly include hydrogen peroxide, but also neurotransmitters such as adrenaline and dopamine, pharmaceuticals, phenols, and heavy metals, to cite a few [27].

Along with the development of more sustainable approaches, there is a recognized need for innovative solutions to address the environmental impact of current technologies. In this sense, bioremediation represents a promising field for the removal of xenobiotic pollutants from air, water, or soil. Peroxidases are good candidates for the catalysis of bioremediation reactions thanks to their activity toward a broad range of substrates and their high redox potential, even though the cost of their production and their relative instability in operation conditions constitute until now a major bottleneck for their application on a large scale. The main use of peroxidase in bioremediation processes is based on the oxidation of toxic compounds including petroleum hydrocarbons, halogenated molecules, and some of the so-called “emerging pollutants” such as pharmaceuticals and other household and hospital chemicals. The formation of free radicals during the peroxidase cycle is exploited to trigger a cascade reaction which will eventually generate less hazardous or more easily degradable derivatives [27].

Since their discovery, chlorite dismutases have also been considered as potential industrial enzymes to be applied in the field of bioremediation [72–74]. In fact, despite being a common component in detergents and pesticides, ClO_2^- has been recently associated to cellular toxicity and concerns about its increased concentrations in the environment have been raised [75]. To date, the applicability of Clds in the industrial sector is still limited by the absence of optimized protocols for a large-scale recombinant production and by the lack of a full understanding of

their reaction mechanism. Among the unresolved questions are the nature of the catalytic intermediates, as mentioned before, but also the strict dependency of the catalytic efficiency on pH and the irreversible inactivation after a certain number of turnovers [49, 50, 65]. In any case, bioremediation is not the only application that has been proposed for chlorite dismutases. A lysate from the perchlorate reducing bacterium *Dechloromonas agitata* has been used to develop an enzymatic bioassay to detect ClO_4^- in environmental samples. Briefly, the lysate is mixed with nicotinamide adenine dinucleotide (NADH) and phenazine methosulfate (PMS). The activity of perchlorate reductase (PcrAB) and Cld contained in the lysate ultimately produces dioxygen which in turn reacts with PMS. Finally, the latter mediates the oxidation of NADH, which is followed spectroscopically [76]. Other examples of industrial usage of Cld include hygiene control and aeration enhancement in bioreactors. In the first case, heterologous expression of Cld in non-PCRB allows the generation of chlorite-resistant strains able to survive a cost-effective chlorite treatment for the removal of contaminant species. The potentiality of this approach is demonstrated by the presence of a recently deposited patent in U.S. [77]. Similarly, Cld-expressing organisms could facilitate dioxygen generation and mass transfer in large-scale bioreactors [76]. One of the most recent applications of chlorite dismutases is the production of dioxygen *inside* human cells proposed by Markhard *et. al.* [78]. The authors developed an *in vitro* methodology which comprises the heterologous expression of a pentameric Cld in HeLa cells (an immortalized tumoral cell line) and the supply of sodium chlorite to the same cells for it to be transformed in molecular oxygen by the Cld. Although they propose their technology to have applications in alleviating hypoxia-mediated diseases or in supporting existing cellular therapies, the toxicity of chlorite and the irreversible inactivation of Clds remain drawbacks difficult to overcome.

1.2 Goal of the thesis

The present work is principally focused on the study of the dimeric chlorite dismutase from *Cyanothece sp.* PCC7425, taken as a representative of the clade II subdivision. The project aims at gaining insights into different properties of the enzyme, including the role of key amino acids in the heme surroundings, ligand binding features and mechanistic details to reach a comprehensive understanding of these systems in the view of possible future industrial applications. Although the integration of different approaches is necessary to elucidate the investigated aspects, in this thesis the subject will be addressed mainly from a spectroscopic point of view.

The details of the applied methods, which include optical, EPR and RFQ-EPR spectroscopies will be illustrated in Chapter 2. A brief overview of the principles of protein recombinant expression will be given as well. Next, Chapter 3 will highlight the potentiality of paramagnetic systems in biocatalysis, with a focus on heme proteins.

The main challenges of performing EPR spectroscopy of heme proteins at cryogenic temperatures will be discussed in Chapter 4. Here, I will present the findings of a systematic study conducted in the frame of this project and focused on the interplay of common biological buffers and cryoprotectants in the preparation of samples for low-temperature EPR of heme proteins. After that, in Chapters 5, 6, 7 and 8 I will report the main findings on the biochemical and biophysical features of *C*Cld obtained during the course of this project. In Chapter 9, after a general introduction on the rationale of protein immobilization methods for industrial usage, preliminary data on the incorporation of HRP and *C*Cld in different supports will be discussed. In Chapter 10, I will summarize the contents of this thesis and discuss the main outcomes.

In appendices A and B the supporting material to Chapters 4 and 7 will be given. Finally, in appendix C the reader will find a brief summary of two side projects in which I have been involved.

Chapter 2

Methods

Abstract

In this Chapter, I describe the methods used in my doctoral project. Section 2.1 contains the basic concepts related to the production and purification of recombinant proteins. The specific protocols used for the preparation of the chlorite dismutase samples used in this work are described in detail in the publications from which each chapter is redrafted. Moreover, Chapter 6 contains a brief description of the procedure that I used to recombinantly produce the chlorite dismutase variant R127K.

Sections 2.2 and 2.3 focus on the main spectroscopic techniques used for the characterization of the proteins investigated in this work, namely UV-vis and EPR spectroscopies. Stopped-flow UV-vis spectroscopy, mainly carried out by our collaborators at the Die Universität für Bodenkultur in Vienna (BOKU), is also briefly introduced. At the end of the Chapter, I give an overview of the principal RFQ techniques combined with EPR spectroscopy for the study of short-lived enzymatic intermediates. Next, I provide an in-depth description of the RFQ setup used in this work and the theory of the calibration procedure.

2.1 Recombinant protein production

The technology of recombinant DNA constitutes a revolution in the field of biochemistry. In the past, the only way to isolate proteins was that of extracting them from their original source, which obviously suffered from limitations such as low availability of the protein of interest in the native organism or hazards related to the manipulation of dangerous species. The advent of recombinant DNA technology made possible the standardization of safer and more efficient protocols to produce proteins on a larger scale, which rely on the utilization of the DNA replication, transcription, and translation machinery of a "host" organism for the synthesis of the molecule of interest. Recombinant DNA techniques mimic the natural phenomenon of genetic recombination observed in all living beings (breakage and rejoining of DNA fragments) to create novel and unique combinations of genetic material [79–82]. In this section, a general overview of the principal steps needed to obtain a recombinant protein, graphically illustrated in **Figure 2.1A**, will be given.

Recombinant DNA manipulation is based on the use of *vectors*, DNA molecules which can autonomously replicate in a suitable host organism. *Plasmids*, *i.e.* circular DNA molecules found in bacteria as accessory chromosomes, are frequently used as vectors. Briefly, a DNA fragment containing the gene of interest is cut from the original genome with the use of specific enzymes called *restriction enzymes*, which can recognize and cut specific DNA sequences, producing partially single-stranded filaments, commonly referred to as "sticky ends". The name derives from the fact that when the same enzymes are used to cut open the vector, complementary single-stranded filaments with a high affinity for the ends of the target gene, will be produced. Finally, the insertion of the target will be performed with the aid of a *ligase* enzyme, which catalyzes the formation of the phosphodiester bonds between the DNA bases. Once the recombinant DNA vector is ready, it has to be transformed (*i.e.* transferred) into a suitable host organism. The most used organism in gene cloning techniques is by far the bacterium *Escherichia coli*, of which several strains of relatively low biohazard have been selected and optimized to this purpose. Nonetheless, yeasts and animal cells can be used as host organisms as well [79–81].

The target gene is amplified in the transformed cells through the process of DNA replication and it is passed to the progeny when the bacterium multiplies. It is important to note that not all vectors are *expression* vectors. While the process of gene amplification is normally carried out with *cloning* vectors, the actual protein production requires the cloning of the gene in a second type of vector containing some essential elements for the successful expression of the protein in the final host system. These include a promoter and a terminator sequence to initiate and stop

the transcription, respectively, but also a ribosome binding site and a start and stop codon which will regulate the translation process (**Figure 2.1B**). Nowadays, most of expression vectors for prokaryotic systems such as *E. coli*, contain *inducible promoter* sequences, meaning that the actual production of the protein is suppressed in the host organism until a synthetic *inducer*, such as isopropyl thiogalactosidase (IPTG), is added to the cell culture at a determined level of cell growth. Expression vectors often contain a "tag" sequence, attached to either the N-terminal or the C-terminal of the polypeptide, which allow easy one-step purification of the recombinant protein based on affinity chromatography. However, despite the procedural advantages, it has to be noted that the tag sequence might alter the conformation and thus the biochemical properties of the expressed protein. In this case, removal of the tag, by chemical or enzymatic cleavage, may be necessary [80, 82].

Once the host organism has synthetized the protein, the following steps might differ depending on the location of the expressed protein (cytoplasm, periplasm, or extracellular environment). For a common cytoplasmic expression, the cells are generally harvested by centrifugation, then disrupted by sonication to obtain a crude extract. If the protein possesses an affinity tag, the crude extract is directly loaded onto an affinity chromatography column and with just one-step purification, a good degree of purity is normally achieved. However, in most cases it is advisable to carry out a second purification step through size-exclusion chromatography which will not only allow to remove potential contaminants retained because of unspecific binding to the affinity column, but also to discriminate the eventual presence of aggregates or different multimeric forms of the protein of interest.

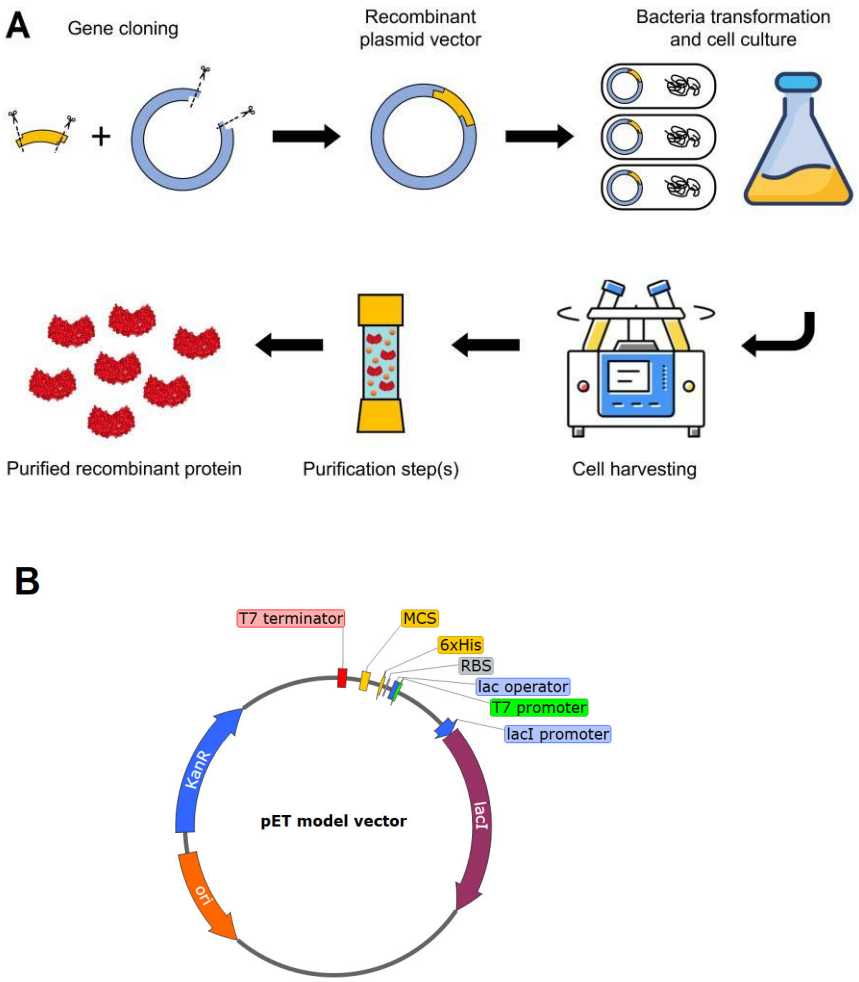

Figure 2.1 (A) *Conceptual illustration of recombinant protein production and* ***(B)*** *essential elements of an expression vector of the pET series.* ***(A)*** *The gene target is cut from the native genome with selected restriction enzymes which are likewise used to open the expression vector. After ligation, the recombinant vector is obtained, which is used to transform competent bacterial cells. The cells are cultivated and protein expression is induced at a determined extent of cell growth. The cells are harvested and sonicated to obtain a crude extract which will subsequentially follow one or multiple steps of purification until a protein sample with the desired degree of purity is obtained.* ***(B)*** *A model of expression vector containing the essential elements: an origin or replication (ori), a multiple cloning site (MCS) where the target gene is inserted; a lac operator, promoter and inhibitor for inducible protein expression; a T7 transcription factor promoter and terminator, a ribosome binding site (RBS), a sequence for Kanamicyn resistance and a 6-hisitidine affinity tag for easy one-step protein purification.*

2.2 Optical spectroscopy

2.2.1 UV-visible absorption spectroscopy in protein science

UV-visible (UV-vis) absorption spectroscopy is a widely used analytical technique based on the interaction of molecules with the electromagnetic radiation in the near-ultraviolet (150–400 nm) and visible (400–800 nm) range. Upon irradiation at determined wavelengths, the electrons are promoted from the ground state to an excited state. Therefore, to obtain the UV-vis spectrum of a chosen chromophore, the absorbance (in arbitrary units) is recorded as a function of the wavelength of the incident light. Since the absorption profile depends not only on the nature of the optically-active center but also on its chemical environment, UV-vis spectroscopy can be very useful to investigate different aspects of biological macromolecules, including oxidation states, ligand-binding, and catalysis. Moreover, this technique is routinely applied in (bio)chemical labs for the determination of protein concentration. Indeed, according to the Lambert-Beer law (Equation 2.1), the concentration of a solute is, within a certain range, linearly correlated to its absorbance at a selected wavelength [83].

$$A(\lambda) = \log\left({}^{I_0}/_{I}\right) = \varepsilon(\lambda) \cdot C \cdot l \qquad (2.1)$$

Here, A is the absorption at the wavelength λ, I_0 and I the intensities of the incident and transmitted light, respectively, ε the molar extinction coefficient (M^{-1} cm^{-1}) at the wavelength λ, C the molar concentration (M) of the solute and l the optical path length (cm).

Proteins generally show a maximum of absorption around 280 nm, which is due to aromatic amino acids such as phenylalanine, tyrosine and tryptophane [84]. In the particular case of heme proteins, the characteristic pattern of a porphyrin absorption spectrum is observed, whose bands position depends on the charge of the metal center, the nature of the ligands and the substituents of the prosthetic group. A simple UV-vis spectrum can reveal detailed information on the active-site of a heme protein, including the redox and spin state of the iron, but also the binding of an external ligand or signs of heme degradation. **Figure 2.2** depicts the UV-vis spectra of the model heme protein myoglobin at neutral pH or in presence of either sodium dithionite or sodium azide (NaN_3), where the changes in the oxidation and spin state of the heme iron are highlighted.

Described in the four-orbital model of Gouterman [85], this absorption profile originates from the electronic transitions between the two highest occupied

molecular orbitals (HOMO) and the two lowest unoccupied molecular orbitals (LUMO) in the highly delocalized π-system of the porphyrin ring. The strong absorption in the near-UV region (400 - 430 nm) is commonly referred to as Soret band, while the less intense peaks in the visible range are known as Q-bands (or α and β peaks) and typically fall between 500 and 650 nm. In high-spin (HS) ferric heme proteins, an additional charge transfer (CT) band around 650 nm can be observed. The absorption bands of some well-known heme systems in different spin and oxidation states, as well as those of some peroxidases of interest in the context of this work are reported in **Table 2.1**.

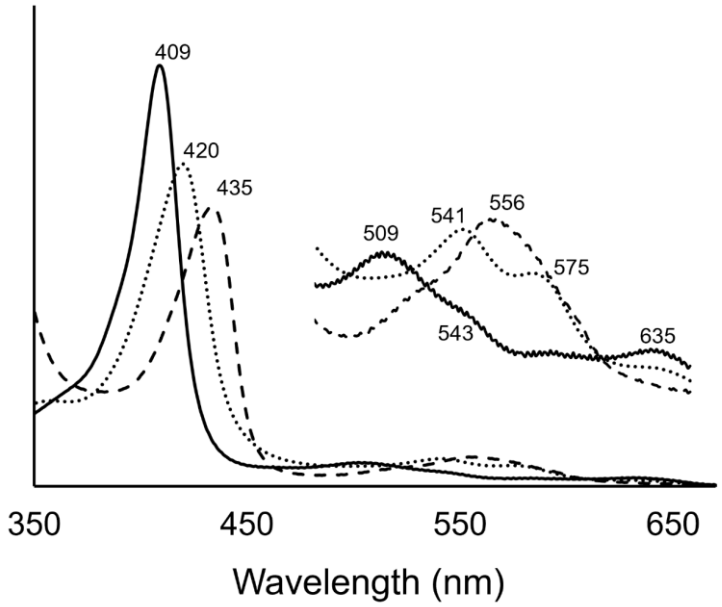

Figure 2.2 *UV-vis absorption spectra of horse heart myoglobin in 50 mM TRIS-HCl buffer pH 7.0 (solid), in presence of a 50-fold molar excess of NaN_3 (dotted) and in presence of an excess of sodium dithionite (dashed).The region from 470 nm to 650 nm is magnified in the inset for better visualization of the Q-bands. All the characteristic absorption bands are indicated in the figure. HS Fe(III) myoglobin presents a Soret band at 409 nm; the addition of NaN_3 causes a shift to 420 nm accompanied by hypochromicity which reflects the conversion to a low-spin (LS) Fe(III) state due to the ligation of N_3^- to the heme iron; differently, sodium dithionite acts a reducing agent, so the shift of the Soret band to 435 and the further hypochromicity represent the change in the redox state of the heme iron from a Fe(III) to a Fe(II) state.*

System	Type	Soret	α	β	CT	Ref.
hhMb	Ferric HS	409	509	543	635	This work
hhMb – NaN_3	Ferric LS	420	541	575	-	This work
hhMb - dithionite	Ferrous LS	435	520	556	-	This work
HRP	Ferric HS	403	498	-	640	[86]
HRP	Compound I	400	525	577	-	[86]
HRP	Compound II	420	527	555	-	[86]
MPO	Ferric HS	428	500	570	620	[87]
*Kp*DyP	Ferric HS	405	507	539	640	[88]
*Kp*DyP	Compound I	397	-	648		[88]
*Kp*DyP	Compound II	427	517	555	-	[88]

Table 2.1 *Typical UV-vis absorption bands of model heme systems and peroxidases of interest. The values for different spin and oxidation states of the heme iron are reported. hhMb, horse heart myoglobin; HRP, Horseradish peroxidase; MPO, human myeloperoxidase; KpDyP, Klebsiella pneumoniae dye-decolorizing peroxidase.*

2.2.2 Stopped-flow UV-vis spectroscopy

By means of UV-vis spectroscopy enzymatic turnovers can be investigated as well, provided that the time scale of the reaction is accessible with the available instrumentation setup. For very fast enzymatic reactions, a stopped-flow device is used in combination with a conventional UV-vis spectrometer, facilitating the observation of intermediate states formed in the time range of milliseconds. In a standard stopped-flow system, two syringes are loaded with the reagents solutions (*i.e.* the enzyme and its substrate) before a chosen volume of both reactants is rapidly pushed through a mixer, where the reaction is initiated. In few milliseconds the mixture enters a measurement cell and the flow is instantaneously stopped. In this way, part of the solution is trapped inside the measurement cell and the proceeding of the reaction is followed spectroscopically [89]. The stopped-flow technique is very useful to study pre-steady state reaction kinetics, as during the experiment it is not only possible to record the full UV-vis spectrum, but also the single time traces of the absorbance at specific wavelengths, which represent the formation (or the consumption) of a certain species. For pseudo-first order reactions, *i.e.* bimolecular reactions in which one the two reagents is in large excess, the fitting of the single time traces gives an *observed* rate constant (k_{obs}) in s^{-1}, which can be used to calculate the *apparent* rate constant (k_{app} or k') in $M^{-1}\ s^{-1}$ by repeating the experiment with different amounts of the substrate (**Figure 2.3**). With this approach it is possible to investigate the rate of formation and conversion of intermediate states, as well as the binding of an external ligand. Additional information can be obtained by studying the kinetics of a particular reaction at different pH values, but also by combining this approach with other techniques such as site-directed mutagenesis, in order to understand which are the critical residues involved in a determined enzymatic process and how they might impact the enzyme functionality.

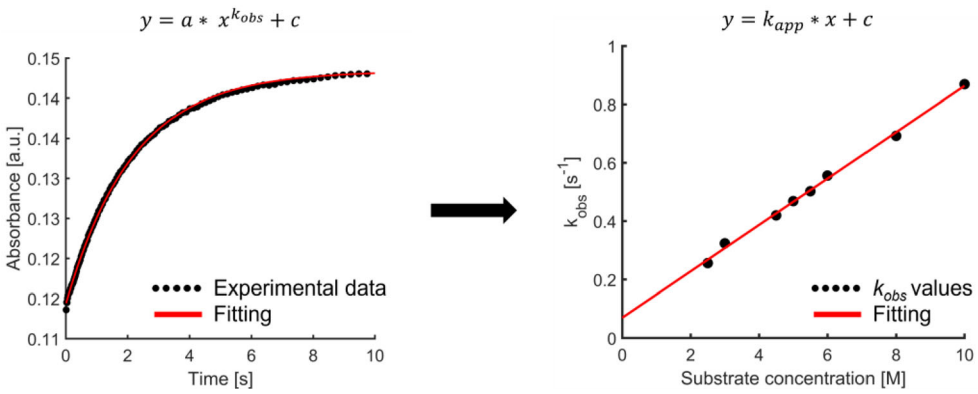

Figure 2.3 *Illustration of the data analysis procedure for the extraction of k_{app} of a pseudo-first order reaction, from a stopped flow experiment. The curve fitting of the time trace at a specific wavelength, which represent the formation of the product in a simple [A] → [B] process, gives a k_{obs} value for a determined concentration of the substrate. By repeating the experiment at distinct substrate concentrations, different k_{obs} values are obtained. Finally, the apparent rate constant k_{app} can be calculated from the linear fit of k_{obs} vs the substrate concentration.*

2.3 Electron paramagnetic resonance spectroscopy

EPR is a spectroscopic technique which allows the investigation of paramagnetic systems, with one or more unpaired electrons. A non-exhaustive list of these systems includes organic and inorganic radicals, transition-metal ions, certain molecular gases and, most importantly for this work, biological samples. Compared to the vast majority of diamagnetic systems, it is understandable that the limited number of existing paramagnetic species makes EPR appear as a "niche" technique. However, this apparent limitation readily turns into the advantage of having a highly selective and sensitive tool to focus on the system of interest without major background issues. Like a very precise magnifying glass, EPR spectroscopy provides insights in the electronic properties of the paramagnet and its close-by environment. With the investigation of different magnetic interactions, it is possible to obtain details on local symmetry, electron density, nature of surrounding nuclei, dynamics, and spin concentration, to cite a few. In the following sections, an introduction to the EPR technique will be given and the most relevant aspects related to its application to biological systems will be discussed. For more information, the interested reader is referred to the textbooks and review papers used as a base for this chapter [90–92].

2.3.1 Fundamentals

Electrons possess an intrinsic property called *spin* which provides them with a magnetic dipole moment. In most cases, electrons occur in pairs, therefore their net moment is zero. However, systems containing unpaired electrons possess a net spin moment which allow them to interact with an external magnetic field. In the 1920s, the experiments of Stern and Gerlach demonstrated the quantized nature of the electron spin, while the electron spin resonance phenomenon was observed for the first time in the 1940s by Zavoisky [93].

The electron spin is characterized by an intrinsic angular momentum $\boldsymbol{S}$, a vector whose magnitude is quantized in units of $\hbar S(S+1)$, with S being the electron spin quantum number. By projecting $\boldsymbol{S}$ onto an axis conventionally taken collinear with the direction of an external magnetic field, one obtains m_s, the electron magnetic quantum number, which can assume only $2S+1$ discrete values between $-S$ and S. Therefore, an electron with $S = ½$ has only two possible spin states corresponding to $m_s = +½$ and $m_s = -½$, which are denoted as "spin-up" (or α-spin) and "spin-down" (or β-spin). In the absence of a magnetic field, the two spin states are degenerate (*i.e.* they have the same energy) and the electron has the same probability of being in either of the two. Considering the electron as a particle of mass m_e and charge e, its intrinsic angular momentum generates a magnetic dipole moment ($\boldsymbol{\mu}_s$), which is related to the gyromagnetic ratio (γ) by:

$$\boldsymbol{\mu}_s = -\gamma \boldsymbol{S}\hbar \tag{2.2}$$

$$= -g_e \frac{e\hbar}{2m_e}\boldsymbol{S} \tag{2.3}$$

$$= -g_e\beta_e\boldsymbol{S} \tag{2.4}$$

In this equation, g_e is the free electron g-factor (≈ 2.0023) and β_e the Bohr magneton (9.274×10^{-24} J T^{-1}). The interaction Hamiltonian ($\mathcal{H}$) of the electron magnetic moment in an external magnetic field ($\boldsymbol{B_0}^T$) is described by:

$$\mathcal{H} = -\boldsymbol{\mu}_s \cdot \boldsymbol{B_0}^T = g_e\beta_e \boldsymbol{S} \cdot \boldsymbol{B_0}^T \tag{2.5}$$

As a convention, the z-component of the electron magnetic moment (μ_z) is chosen to be parallel to the direction of the external magnetic field (B_0), therefore Eq. 2.5 results in the energy (E):

$$E = g_e\beta_e m_s B_0 = \pm ½\, g_e\beta_e B_0 \tag{2.6}$$

At a given B_0, the solutions of Eq. 2.6 represent two states of different energy, where the lowest energy β-spin state corresponds to μ_z being parallel aligned to the direction of B_0, and the higher energy α-spin state corresponds to μ_z having an anti-parallel alignment with B_0. The splitting of the electron spin energy levels in a magnetic field is called *Zeeman effect*, after the Dutch physicist Pieter Zeeman, who received the Nobel Prize in 1902 for his studies on the influence of magnetism on light irradiation phenomena. **Figure 2.4** represents the Zeeman effect and the principle of the continuous-wave (CW) EPR experiment. In CW-EPR, the paramagnetic sample is placed in a homogeneous magnetic field of increasing magnitude and it is continuously irradiated with microwaves of a fixed frequency. When the energy splitting induced by the applied field matches the energy quantum of the irradiating microwaves ($h\nu$), the resonance condition is satisfied and absorption occurs, generating an EPR line. As far as the instrumentation is concerned, the standard EPR spectrometers operate at ~ 9.5 GHz (commonly referred to as X-band) in combination with electromagnets which can generate fields up to 1.5 T. An additional oscillation is applied to the external field, typically at a frequency of 100 kHz, resulting in the oscillation of the detector output at the same frequency and giving rise to a first derivative profile of the absorption curve. Through phase-sensitive detection, the signal channel selects the output signals which oscillate at the same frequency of a reference arm signal, resulting in a great improvement of signal-to-noise ratios.

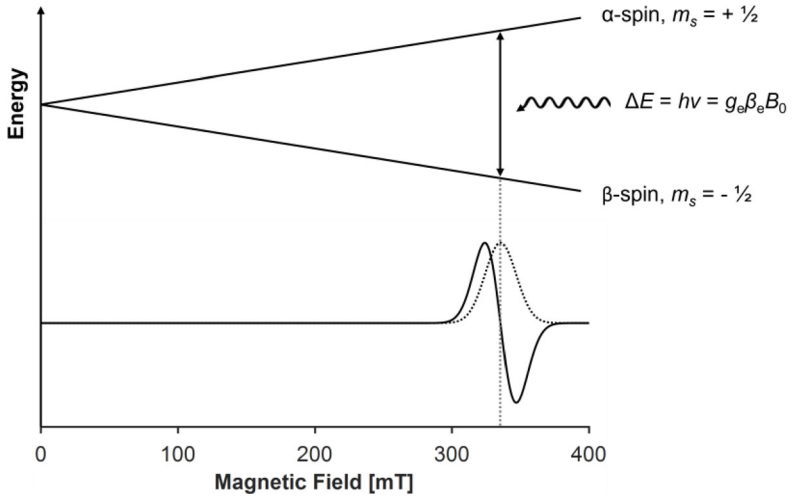

Figure 2.4 *According to the Zeeman effect, when an unpaired electron is placed in a homogeneous magnetic field of increasing magnitude, the difference between the energy levels of the two spin manifolds (α and β) increases linearly. When the energy gap matches the energy quantum carried by the microwaves with fixed frequency, absorption occurs (dotted line). Note that in CW-EPR the signal is normally recorded as a first derivative (solid line). Figure adapted from* [90].

2.3.2 The spin Hamiltonian

As it may appear obvious, the Zeeman effect is not the only factor influencing an EPR spectrum. A more rigorous description of the several magnetic interactions accessible by EPR spectroscopy is given by the spin Hamiltonian, a simplified version of the Hamiltonian operator which defines the total energy of a system. The spin Hamiltonian $\mathcal{H}$ given below considers only the interactions of a paramagnetic system with electron spin $\boldsymbol{S}$ and nuclear spin $\boldsymbol{I}$:

$$\mathcal{H} = \mathcal{H}_{\mathrm{EZ}} + \mathcal{H}_{\mathrm{NZ}} + \mathcal{H}_{\mathrm{HF}} + \mathcal{H}_{\mathrm{NQ}} + \mathcal{H}_{\mathrm{ZFS}} \tag{2.7}$$

In the following sections, each term of the spin Hamiltonian will be shortly explained to provide the reader with the basic tools to understand and interpret the spectra presented in this work.

2.3.2.1 The electron Zeeman interaction

In the previous paragraphs the interaction of a free unpaired electron with an external magnetic field was briefly introduced. However, in a more realistic situation the electron is part of a molecular system, which confers it not only a spin angular momentum $\boldsymbol{S}$, but also an orbital angular momentum $\boldsymbol{L}$. Spin-orbit coupling derives from the interaction between the magnetic dipole moment $\boldsymbol{\mu}_{\mathrm{s}}$ and the magnetic moment generated by the angular momentum $\boldsymbol{L}$. The combination of the spin-orbit term and Eq. 2.5 can be formally rewritten as:

$$\mathcal{H}_{\mathrm{EZ}} = \beta_{\mathrm{e}}\, \boldsymbol{B_0}^{\mathrm{T}} \cdot \boldsymbol{g} \cdot \boldsymbol{S} \tag{2.8}$$

with the $\boldsymbol{g}$ tensor, a 3×3 matrix in mathematical terms, defined as:

$$\boldsymbol{g} = \begin{bmatrix} g_{xx} & g_{xy} & g_{xz} \\ g_{yx} & g_{yy} & g_{yz} \\ g_{zx} & g_{zy} & g_{zz} \end{bmatrix} \tag{2.9}$$

Normally, each paramagnetic system is described by the three principal g values of the diagonalized tensor (Eq. 2.10), which correspond to its principal axes. Notably, the frame of the $\boldsymbol{g}$ tensor does not always coincide with the molecular frame, therefore three Euler angles are used to describe the relative orientations between the different frames.

$$\boldsymbol{g} = \begin{bmatrix} g_{xx} & 0 & 0 \\ 0 & g_{yy} & 0 \\ 0 & 0 & g_{zz} \end{bmatrix} \tag{2.10}$$

In a fast motion regime (*i.e.* at room temperature and non-viscous solutions), the $\boldsymbol{g}$ anisotropy is averaged by the rapid thumbling of the molecules and a $g_{iso} = (g_x + g_y + g_z)/3$ is sufficient to describe the Zeeman interaction. However, in powders and in frozen solutions all the molecules are fixed in different orientations and each molecule gives rise to single lines that appear at different magnetic field positions. The resulting EPR spectrum, also known as "powder spectrum" (**Figure 2.5**), is the sum of all these contributions. The absorption spectrum is characterized by turning points at the positions of the principal *g* values, which appear as distinct lines in the signal recorded as first derivative.

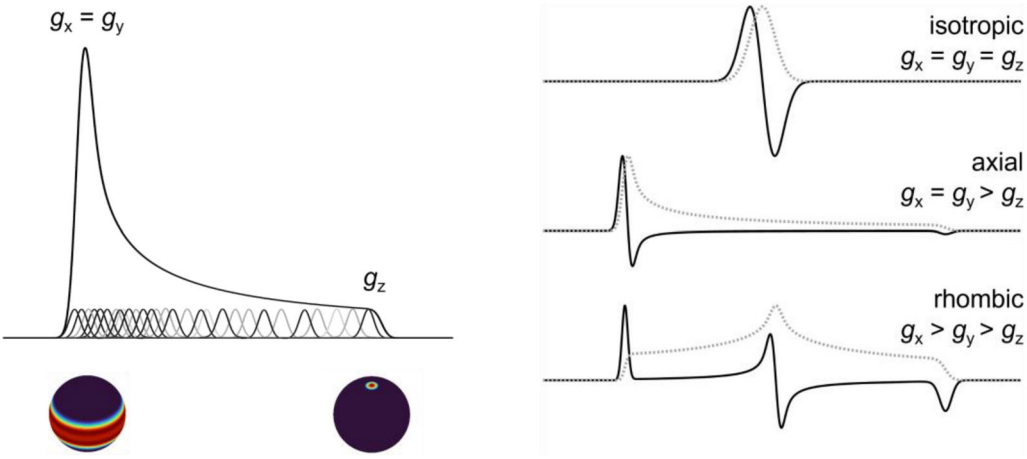

Figure 2.5 *Illustration of an axial powder spectrum in absorption mode (left) and exemplary solid-state CW EPR spectra with different* $\boldsymbol{g}$ *tensor geometries (right), represented in absorption (dotted grey) and first derivative (solid black) modes. A powder spectrum arises from all the contributions of the excited orientations at each magnetic field position. The symmetry of the* $\boldsymbol{g}$ *tensor is defined isotropic, axial or rhombic according to the relative magnitudes of the principal g values.*

2.3.2.2 The nuclear Zeeman interaction

Nuclear spins can generate a magnetic moment $\boldsymbol{\mu}_N$ which is related to the nuclear spin angular momentum $\boldsymbol{I}$ by the proportionality factor g_N and the nuclear magneton β_N according to Eq. 2.11:

$$\boldsymbol{\mu}_N = g_N \beta_N \boldsymbol{I} \tag{2.11}$$

A description similar to the one of the electron Zeeman effect can be applied to nuclear spins systems. The nuclear Zeeman levels for a nucleus with the *z*-component of the nuclear magnetic moment collinear with the direction of the external magnetic field B_0, are expressed by:

$$E_{NZ} = -m_I g_N \beta_N B_0 \tag{2.12}$$

which follows from:

$$\mathcal{H}_{NZ} = \beta_N \boldsymbol{B_0}^T \cdot g_N \cdot \boldsymbol{I} \tag{2.13}$$

with B_0 parallel to the z-axis.

The transition between nuclear Zeeman levels is known as nuclear magnetic resonance (NMR). Because of the selection rules in CW-EPR ($\Delta m_s = 1, \Delta m_I = 0$), NMR transitions are observable only with pulsed EPR techniques (see section 2.3.3). However, the interaction of unpaired electrons with nuclei possessing $I > 0$ gives rise to an additional hyperfine interaction, whose effect can be also observed, in certain cases, in CW-EPR spectra.

2.3.2.3 The hyperfine interaction

An unpaired electron in the proximity of a nucleus with $I > 0$ interacts with its magnetic dipole moment resulting in a further splitting of the energy levels. This effect, known as hyperfine interaction, is independent of the external magnetic field, unlike the Zeeman interaction.

The Hamiltonian consists of two parts, namely the *anisotropic* ($\mathcal{H}_{dip}$) and the isotropic ($\mathcal{H}_F$) components:

$$\mathcal{H}_{\mathrm{HF}} = \mathcal{H}_{dip} + \mathcal{H}_{\mathrm{F}} \tag{2.14}$$

$\mathcal{H}_{\mathrm{dip}}$ is derived from the classical description of the dipolar magnetic field by introducing the spin operators $\boldsymbol{S}^{\mathrm{T}}$ and $\boldsymbol{I}$ for the interacting magnetic moments:

$$\mathcal{H}_{\mathrm{dip}} = \boldsymbol{S}^{\mathrm{T}} \cdot \boldsymbol{T} \cdot \boldsymbol{I} = \frac{\mu_0}{4\pi} g_e \beta_e g_{\mathrm{N}} \beta_{\mathrm{N}} \left[\frac{3\left(\boldsymbol{S}^{\mathrm{T}} \cdot \boldsymbol{r}\right)\left(\boldsymbol{r}^{\mathrm{T}} \cdot \boldsymbol{I}\right)}{r^5} - \frac{\boldsymbol{S}^{\mathrm{T}} \cdot \boldsymbol{I}}{r^3} \right] \tag{2.15}$$

While the anisotropic (dipolar) hyperfine depends on the relative orientation and distance of between the electron and nuclear magnetic moments, in the isotropic case (r = 0) a spatial overlap of the magnetic moments (Fermi contact) occurs and the dipolar interaction becomes independent of $\boldsymbol{r}$. The Fermi contact interaction ($\mathcal{H}_{\mathrm{F}}$) is limited to s-orbitals or orbitals with partial s-character, for which the wavefunction is non-zero at the nucleus ($\psi_0(r = 0) \neq 0$):

$$\mathcal{H}_{\mathrm{F}} = a_{\mathrm{iso}} \boldsymbol{S}^{\mathrm{T}} \cdot \boldsymbol{I} \tag{2.16}$$

In Eq. 2.16 the term a_{iso} represents the isotropic hyperfine coupling constant, which is proportional to the s-electron spin density at the nucleus $|\psi_0(0)|^2$, according to:

$$a_{\mathrm{iso}} = \frac{2\mu_0}{3} g_e \beta_e g_{\mathrm{N}} \beta_{\mathrm{N}} |\psi_0(0)|^2 \tag{2.17}$$

Finally, the Hamiltonian describing the hyperfine interaction can be generalized as follows:

$$\mathcal{H}_{\mathrm{HF}} = \mathcal{H}_{\mathrm{dip}} + \mathcal{H}_{\mathrm{F}} = \boldsymbol{S}^{\mathrm{T}} \cdot \boldsymbol{A} \cdot \boldsymbol{I} \tag{2.18}$$

where $\boldsymbol{A}$ is the hyperfine tensor, comprising both the isotropic and the anisotropic components.

In practice, the hyperfine interaction results in a further splitting of the EPR spectra in several lines. In a system where an unpaired electron interacts with a nucleus of spin I, there are $2I + 1$ energy levels for each m_s value, giving rise to $2I + 1$ EPR transitions (remember the selection rules $|\Delta m_s| = 1$, $|\Delta m_I| = 0$). When the electron interacts with N equivalent nuclei, the number of transitions increases to $2NI + 1$. In liquids, the rapid tumbling of the molecules averages out the anisotropic component of the hyperfine interaction and the isotropic coupling gives rise to well-resolved

splitting (**Figure 2.6**). However, in the solid state such as in powders or in frozen solutions, unresolved anisotropic hyperfine lines are one of the major causes of inhomogeneous broadening of the CW-EPR lines. Resolving the small hyperfine couplings which are hidden under a broad CW line is nowadays possible with advanced pulsed EPR techniques, providing great insights into the chemical surrounding of the paramagnetic center.

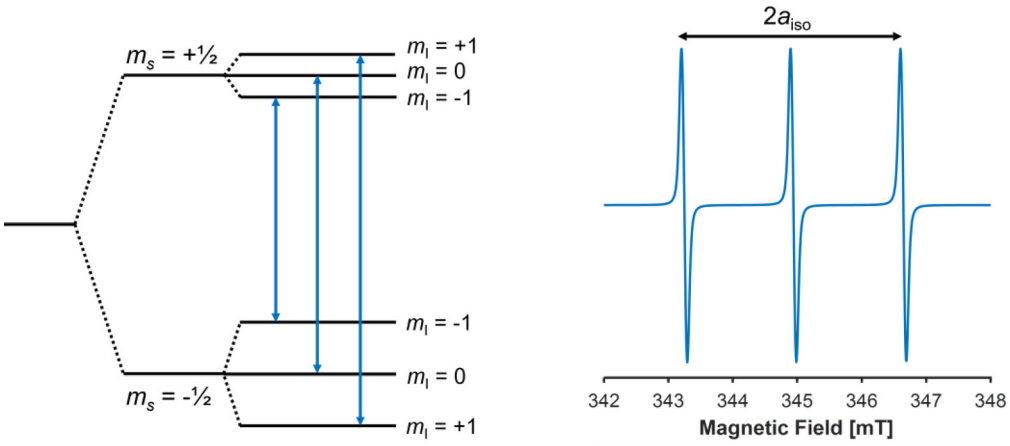

Figure 2.6 Left: *the energy level diagram for a S = ½, I = 1 spin system showing the electron and nuclear Zeeman levels and the allowed EPR transitions as blue arrows. The figure represents the case in which the hyperfine constant is > 0 and the hyperfine term is larger that the nuclear Zaeeman term.* ***Right:*** *the simulation of the CW-EPR spectrum of a nitroxide spin label in fast motion regime, where one unpaired electron interacts with a* ^{14}N *nucleus with I = 1. The three lines of the EPR spectrum have equal intensity and are equally spaced by* a_{iso}.

2.3.2.4 The nuclear quadrupole interaction

The internal structure of a nucleus with $I > ½$ is responsible for the deviation of its charge distribution from a spherical to an ellipsoid symmetry, which is directly proportional to the magnitude of the nuclear quadrupole moment Q. The electron distribution in the immediate vicinity of the nucleus generates an electric-field gradient which tends to orient this non-spherical charge distribution. This effect is known as nuclear quadrupole interaction (NQI) and it is described by the Hamiltonian term:

$$\mathcal{H}_{\mathrm{NQ}} = \boldsymbol{I}^{\mathrm{T}} \cdot \boldsymbol{P} \cdot \boldsymbol{I} \tag{2.19}$$

where $\boldsymbol{P}$ is the nuclear quadrupole tensor, a 3×3 symmetric and traceless matrix. In its principal axis system, $\boldsymbol{P}$ is a diagonal matrix of the form:

$$\boldsymbol{P} = \begin{bmatrix} P_x & 0 & 0 \\ 0 & P_y & 0 \\ 0 & 0 & P_z \end{bmatrix} = \begin{bmatrix} K(-1+\eta) & 0 & 0 \\ 0 & K(-1-\eta) & 0 \\ 0 & 0 & 2K \end{bmatrix} \tag{2.20}$$

where K is defined as:

$$K = \frac{e^2qQ/h}{4I(2I-1)} \tag{2.21}$$

e^2qQ/h being the quadrupole coupling constant (in MHz) and I the nucleus spin quantum number. The quantity e^2qQ is composed of two contributions arising from the quadrupole moment (eQ, isotope-specific) and from the electric-field gradient (eq), respectively. The Hamiltonian in the principal axis frame of $\boldsymbol{P}$ can be expressed as:

$$\mathcal{H}_{\mathrm{NQ}} = K\left[(3I_z^2 - I^2) + \eta\left(I_x^2 - I_y^2\right)\right] \tag{2.22}$$
$$= P_xI_x^2 + P_yI_y^2 + P_zI_z^2 \tag{2.23}$$

The convention in EPR and NMR is that $|P_x| \leq |P_y| \leq |P_z|$, therefore the parameter η, called asymmetry and defined as $(P_x - P_y)/P_z$, can assume only values in the range $0 \leq \eta \leq 1$. Despite the involvement of the nuclear spin in the Hamiltonian representation of the NQI, it is important to remember that this effect is purely electrostatic. Moreover, in CW-EPR spectra the nuclear quadrupole interaction is expected to have moderate and hardly detectable effects, which do not include additional splitting, but rather small shifts of the hyperfine lines. However, the spectra of pulsed EPR experiments such as HYSCORE and ENDOR can be affected to first order by the NQI (see section 2.3.3.3).

2.3.2.5 The zero-field splitting

The zero-field splitting (ZFS) phenomenon occurs in systems which possess multiple unpaired electrons (S > ½). Its name is due to the fact that in the absence of an external magnetic field, the ground states of a system with S > ½, characterized by different $|m_s|$ values, will have different energies. The ZFS arises

from two main contributions, namely the spin-spin coupling, *i.e.* the direct dipolar interaction between unpaired electrons, and the spin-orbit coupling (section 2.3.2.1). In the *d* block transition-metal ions, such as the ferric high-spin iron of heme proteins, the primary contribution comes from the spin-orbit coupling and the CW-EPR spectra of these system is highly impacted by the ZFS, as it will be discussed in Chapter 3 in more details. The Hamiltonian for the zero-field splitting is analogous to the one of the NQI, having the form:

$$\mathcal{H}_{\mathrm{ZFS}} = \boldsymbol{S}^{\mathrm{T}} \cdot \boldsymbol{D} \cdot \boldsymbol{S} \tag{2.24}$$

where $\boldsymbol{D}$ is the symmetric and traceless dipolar tensor. In the principal axis frame, $\boldsymbol{D}$ can be expressed as:

$$\boldsymbol{D} = \begin{bmatrix} D_x & 0 & 0 \\ 0 & D_y & 0 \\ 0 & 0 & D_z \end{bmatrix} = \begin{bmatrix} -(1/3)D + E & 0 & 0 \\ 0 & -(1/3)D - E & 0 \\ 0 & 0 & (2/3)D \end{bmatrix} \tag{2.25}$$

and the relative Hamiltonian becomes:

$$\mathcal{H}_{\mathrm{ZFS}} = D\left[S_z^2 - \frac{1}{3}S(S+1)\right] + E\left(S_x^2 - S_y^2\right) \tag{2.26}$$

$$= D_x S_x^2 + D_y S_y^2 + D_z S_z^2 \tag{2.27}$$

From Eq. 2.25 one can immediately derive the relations:

$$D = \frac{3}{2}D_z \tag{2.28}$$

$$E = \frac{1}{2}(D_x - D_y) \tag{2.29}$$

D and E are known as the tetragonal and rhombic zero-field splitting parameters, respectively. The ratio E/D, known as rhombicity, is commonly reported in the literature of EPR on heme proteins (and high-spin system in general) and it can assume the values between 0 and $\frac{1}{3}$ due to the convention $|D_x| \leq |D_y| \leq |D_z|$.

2.3.3 Pulsed EPR spectroscopy

CW-EPR is very useful to get initial information on the system of interest. For instance, in the case of heme proteins, the g values which characterize HS and LS Fe(III) species are often considered as "fingerprints" for specific active site geometries, ligand binding or transient intermediate states. However, CW-EPR suffers from some limitations, mostly related to the impossibility of resolving small interactions such as dipolar couplings between electron spins or hyperfine couplings between an unpaired electron and nearby magnetic nuclei (see section 2.3.2.3). Pulsed EPR spectroscopy allows to overcome these limitations by dramatically increasing the resolution of the spin Hamiltonian interactions. Differently from CW-EPR, where the sample is continuously irradiated with low-power microwaves, in pulsed EPR the microwaves are sent to the sample as short pulses of high-power. There exists a variety of pulsed EPR techniques which are used to manipulate the spin system and then record their response to magnetization as a transient emission (*e.g.* free induction decay, spin echo). In the following section, the effect of the microwave pulses on a paramagnetic system will be treated with a classical picture. For a more rigorous quantum-mechanical description, the reader is referred to [90–92]. Later, a brief introduction on the pulsed techniques used in this work will be provided.

2.3.3.1 Pulses and spins

In a paramagnetic system, a subset of spins with nearly identical resonance frequency is called a "spin packet" and it is characterized by a vectorial magnetic moment. The magnetization $\boldsymbol{M}$ is the vector sum (per unit volume) of the individual magnetic moments and at thermal equilibrium it is parallel to the z-direction of the external magnetic field, $\boldsymbol{B}_0$ ($\boldsymbol{M} = \boldsymbol{M}_0$). In this condition, $\boldsymbol{M}$ does not change over time. When a magnetic field oscillating at a frequency equal to the pulse microwave frequency, is applied perpendicular to the z-axis, $\boldsymbol{M}$ is tilted away. For the effect of the external magnetic field $\boldsymbol{B}_0$, $\boldsymbol{M}$ immediately starts to precess around the z-axis with the Larmor frequency (ω_L), according to the classical torque equation:

$$\frac{d\boldsymbol{M}}{dt} = -\gamma(\boldsymbol{B}_0 + \boldsymbol{B}_1(t)) \times \boldsymbol{M} \tag{2.29}$$

where γ is the gyromagnetic ratio of the spin and $\boldsymbol{B}_1(t)$ is the linearly-polarized magnetic field component of the irradiating microwave, which is perpendicular to the z-axis and time-dependent.

$$\boldsymbol{B}_1(t) = \cos\left(\omega_{MW}{}^t\right) \tag{2.30}$$

For a simpler description of the system, one can consider a frame of reference, the so-called *rotating frame*, which rotates around the z-axis with the (angular) microwave frequency, ω_{MW}. In the rotating frame we will only consider one time-independent component of $\boldsymbol{B}_1$, ω_1, and $\Delta\omega$ which describes the off-set between the resonance frequency of the spins and the frequency of the rotating frame. The relation between $\boldsymbol{B}_1$ and ω_1 is given by:

$$\omega_1 = \gamma \boldsymbol{B}_1 \tag{2.31}$$

While $\Delta\omega$ is defined as:

$$\Delta\omega = \omega_{\mathrm{L}} - \omega_{\mathrm{MW}} \tag{2.32}$$

When $\Delta\omega = 0$, *i.e.* when the spin packet is on resonance with the applied MW, the magnetization vector is only affected by $\boldsymbol{B}_1$. More specifically, the effect of a MW pulse is that of rotating $\boldsymbol{M}$ around the axis corresponding to the phase of the MW irradiation, either the x- or the y-axis in the rotating frame. The flip angle depends on the strength of the magnetic field $\boldsymbol{B}_1$ and on the duration of the applied pulse t_p, according to Eq. 2.33:

$$\theta = \omega_1 t_p = \gamma B_1 t_p \tag{2.33}$$

In the simplest case of a single MW pulse with flip angle of 90°, a transient signal called free induction decay (FID) is generated. After the magnetization vector is flipped to the (x,y)-plane by a $\pi/2$ pulse, the spins – initially having the same phase – start to precess around the z-axis with their individual resonance off-sets $\Delta\omega$. This gives rise to the FID, which loses intensity as the spins get dephased and relaxed during the precession (**Figure 2.7, a-c**). The magnetization vector finally returns to its equilibrium state following specific relaxation processes, namely the longitudinal or T_1 relaxation, which describes the relaxation of $\boldsymbol{M}_0$ along the z-axis due to spin-lattice interactions, and the transversal or T_2 relaxation, which describes the spins dephasing in the (x,y)-plane due to spin-spin interactions.

2.3.3.2 The Hahn spin echo

Due to its very short life-time caused by fast electron relaxations T_1 and T_2, an FID is often undetectable with common EPR spectrometers, whose detectors possess a protective technical deadtime of ~ 96 ns. The next simplest pulsed experiment that can be performed is the generation of a Hahn echo through a 2-pulse sequence, as illustrated in **Figure 2.7**. After the first pulse with flip angle $\theta = \pi/2$, the spins are

left to dephase for a certain time τ and then a second pulse with flip angle $\theta = \pi$ is sent. The second pulse flips all the dephasing spins by π, so that they are situated again on the transversal plane. This time, the spins with the highest dephasing frequency will be behind the ones with slower dephasing, so that they can catch each other and refocus, after a second time τ. This results in an emission signal called Hahn echo (also primary echo or 2-pulse echo) which is no other than a combination of an "inverted" FID in the first half and a regular FID in the second half.

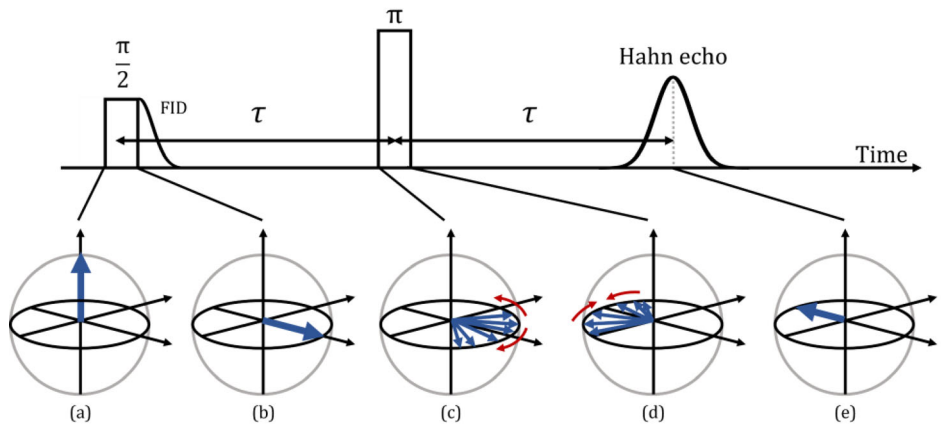

Figure 2.7 *Schematic representation of the 2-pulse sequence generating a Hahn echo. a) At equilibrium the magnetization vector* ***M*** *(blue arrow) is aligned with the z-axis of the external magnetic field; b) the* $\pi/2$ *pulse flips the magnetization to the (x,y)-plane; c) and d) the spins which are dephasing on the (x,y)-plane are flipped by the second pulse* π *after a time = τ so that they can refocus; e) after a second time = τ, when the magnetization vector is built again, the Hahn echo signal is emitted. Note that in this representation, the effect of the longitudinal relaxation is omitted for simplicity.*

The 2-pulse sequence is at the basis of several more advanced pulsed experiments. An immediate application, which represents an alternative to CW-EPR, is to record the Hahn echo, with a fixed τ, as a function of the applied magnetic field. This experiment is known as Electron Spin Echo (ESE)-Detected EPR and it results in an "absorption-like" spectrum which allows to better detect broad lines not always visible with CW-EPR. On the other hand, because of nuclear modulation effects on the echo amplitude, spectral distortions might be generated. The Hahn echo sequence is also used for relaxation time measurements, as in inversion recovery experiments for the calculation of T_1, or in spin-echo decay experiments to measure T_2.

2.3.3.3 ESEEM spectroscopy

Electron spin echo envelope modulation (ESEEM) spectroscopy comprises a number of techniques which aim at determining nuclear frequencies in paramagnetic systems, being particularly suited to detect weakly-coupled nuclei. In the ESEEM experiment, the echo generated by a particular sequence of MW pulses is recorded as a function of one or more evolution times between the pulses. Appropriate pulse sequences will modulate the echo amplitude, leading to one- or two-dimensional time-domain signals. By applying Fourier transformation (FT), the modulating nuclear frequencies can be obtained and the Hamiltonian parameters of the coupled nuclei can be extracted by spectral simulations.

Two-pulse ESEEM The 2-pulse sequence of the form $\pi/2 - \tau - \pi - \tau - echo$ was already introduced before to describe the generation of a Hahn echo. Differently from the ESE-Detected EPR experiment, in this case the decay of the primary echo in function of τ is followed in the time domain at a fixed magnetic field position. In addition to the decay caused by relaxation effects, the echo will be modulated with the nuclear frequencies of the nuclei coupled to the unpaired electron(s). The values of these frequencies can be extracted from the signal in the frequency domain obtained by FT. One drawback of this technique is that extra peaks due to the combinations of frequencies will appear after FT, making the interpretation of a system with multiple magnetic nuclei difficult since the number of lines will increase dramatically. Another limitation is given by the fact the echo decay mainly depends on electron spin-spin relaxation (T_2), which is usually very fast. The modulation can thus be observed for a very limited time, resulting in significant line broadening after FT.

Three-pulse ESEEM One way to overcome the T_2 limitation is that of adding a third pulse to generate a so-called stimulated echo. The 3-pulse ESEEM sequence is given by $\pi/2 - \tau - \pi/2 - T - \pi/2 - \tau - echo$ (**Figure 2.8a**) where in addition to the evolution time τ, an extra inter-pulse time T is present where the spins relax more slowly. Here, the echo decay depends on the nuclear T_2, which is essentially on the same order of magnitude of the electron T_1, resulting in narrower lines in the frequency domain and better spectral resolution. Another advantage of 3-pulse ESEEM is that, in presence of multiple magnetic nuclei, it yields combinations of nuclear frequencies only within one m_s manifold, generating a less crowded spectrum. There are, however, some drawbacks. In the simplest experiment T is varied while τ is constant, but specific combinations of τ and nuclear frequencies will give the so-called "blind spots". For this reason it is advisable to perform a 2D experiment where the 3-pulse ESEEM is recorded at different τ values, although this

might be time-consuming. Finally, phase cycling is also necessary to remove unwanted echoes, adding extra experimental time.

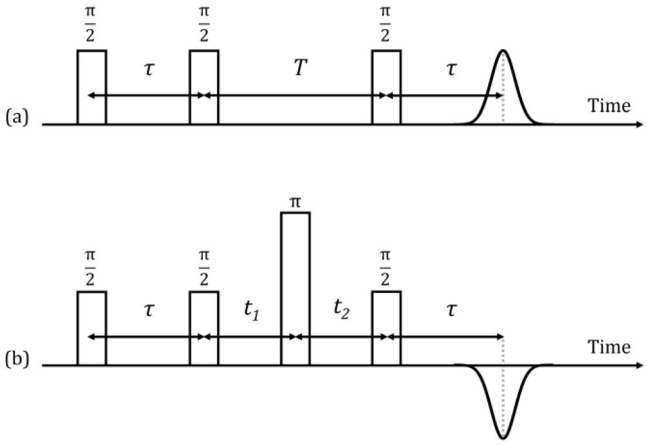

Figure 2.8 *Schematic representation of the 3-pulse (a) and the 4-pulse (HYSCORE) (b) sequences.*

HYSCORE The Hyperfine Sublevel Correlation Spectroscopy (HYSCORE) is a 4-pulse technique with sequence $\pi/2 - \tau - \pi/2 - t_1 - \pi - t_2 - \pi/2 - \tau - echo$ (**Figure 2.8b**). HYSCORE is a 2D experiment where the evolution times t_1 and t_2 are independently varied. After FT, the resulting spectrum in the frequency domain will show cross peaks which correlate the nuclear frequencies in the α and β electron spin manifolds. The quadrants are normally referred to as (+,+) and (-,+) according to the sign of ν_1, while the quadrants with negative ν_2 are generally omitted since they contain the same information. The (+,+)-quadrant contains the signals from weakly-coupled nuclei, *i.e.* with the hyperfine coupling (A) smaller than twice the Larmor frequency (ν_L). Conversely, the (-,+)-quadrant contains signals from strongly-coupled nuclei, *i.e.* with $A > 2\nu_L$ (**Figure 2.9a**). In a disordered system, such as in frozen solutions, the peaks are not usually sharp and well-defined, but more often stretched in ridges. This is due to the sum of all the different molecular orientations excited for the particular field value at which the experiment is performed (see **Figure 2.5**). Moreover, for a system with high-spin coupled nuclei ($I \geq 1$) the number of cross peaks can increase significantly because of the larger number of possible nuclear transitions. **Figure 2.9b** shows a simulated HYSCORE spectrum of a S = ½, I = 1 system where, for each m_s manifold, two single-quantum (SQ) and one double-quantum (DQ) nuclear transitions can occur and contribute to the spectrum. The analysis of the DQ cross-peaks (Eq. 2.34) can be very useful to obtain first input values for spectral simulation.

$$\nu_{\alpha,\beta}^{\mathrm{DQ}} = 2\sqrt{\left(\nu_{\mathrm{L}} \pm \frac{A}{2}\right)^2 + \left(\frac{e^2qQ}{4h}\right)^2\left(3+\eta_p^2\right)} \tag{2.34}$$

In this equation, A is the hyperfine coupling in frequency units for the given magnetic field, while e^2qQ/h and η are the quadrupole coupling constant and the asymmetry parameter, respectively already introduced in section 2.3.2.4. Because of the limitation $0 \leq \eta \leq 1$, the hyperfine coupling and the boundaries for the quadrupole coupling can be estimated. It is important to remember that the great increase in spectral resolution due to the addition of a second dimension is counterbalanced by some disadvantages. Analogously to 3-pulse ESEEM, HYSCORE suffers from blind spots effects and it is therefore recommended to perform the experiment at different τ values. Phase cycling and the exploration of different magnetic field positions for orientation selection might also increase the experimental time significantly.

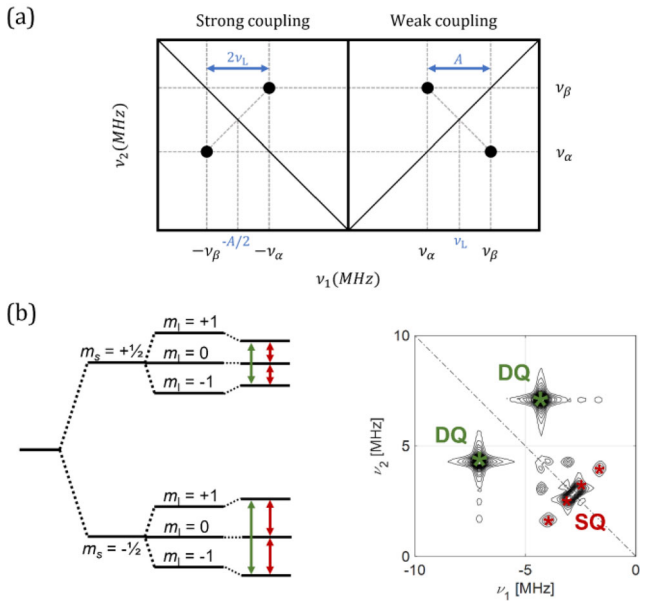

Figure 2.9 *Basics of the HYSCORE experiment.* ***(a)*** *Schematic illustration of a HYSCORE spectrum for an S = ½ , I = ½ system with cross peaks appearing either in the (+,+)- or the (-,+)- quadrant according to strong or weak hyperfine coupling, respectively. A is the hyperfine coupling constant at the chosen magnetic field position and ν_L is the Larmor frequency.* ***(b)*** *Energy levels for an unpaired electron interacting with an I = 1 nucleus, showing the single-quantum and double-quantum transitions in red and green, respectively (left) and a simulated HYSCORE spectrum for an electron strongly coupled to a ^{14}N nucleus (I = 1), where the single- and double-quantum transitions are indicated (right).*

2.3.4 Rapid Freeze-Quench EPR

2.3.4.1 Introduction and scope of the technique

In the study of enzymatic reactions, the characterization of short-lived intermediate states can provide useful mechanistic insights. During their turnover, enzymes containing paramagnetic centers (*e.g.* heme enzymes) undergo transient spin and/or redox state changes which could be ideally investigated by EPR. However, the EPR signal from transition-metal ions, such as the iron in heme systems, can be observed only at cryogenic temperatures due to fast relaxation processes. For this reason, an issue emerges in the preparation of samples for EPR spectroscopy in case of fast reacting species. Normally, the reactants are mixed in a standard Eppendorf tube, transferred into the EPR tube (or capillary for high-frequency experiments) and flash frozen in liquid nitrogen. This procedure can take from a few seconds to minutes, but surely cannot be performed in milliseconds, which is frequently the time scale of enzymatic reactions. To overcome this experimental limitation, the technique of RFQ was introduced. The concept is analogous to the stopped-flow technique (see section 2.2.2) but in this case, after the mixing phase, the sample is sprayed in the form of a fine jet from an ejection nozzle into a cryogenic bath or onto a cold metallic surface. The goal is to quench the reaction by freezing, in the shortest time possible. Despite the simplicity of the idea, in practice the use and optimization of the freeze-quench technique is not trivial. Several factors impact the achievable freezing time, the reproducibility of the experiment and the quality of the prepared sample.

2.3.4.2 Rapid freeze-quench in the literature

The rapid freeze-quench technique was first developed in the 1960s [94, 95]. In 1974, Ballou and Palmer provided a detailed description of a freeze-quench device suitable for aqueous solutions and their subsequent investigation by EPR spectroscopy [96]. In their system an electric motor was coupled to a flywheel which eventually allowed the linear movement of the syringes containing the reagents solutions. The sample was frozen in a bath of cold isopentane at a temperature of ca -140 °C, contained into an EPR sampling tube. Already from the early works, some criticalities emerged. Soon it became clear that many technical aspects, such as the flow rate or the diameter of the ejection nozzle, had a great influence on quality of the obtained sample. The main issues appeared to be the homogeneity of the frozen particles and the packing efficiency inside the EPR tube. Ballou and Palmer reported a loss of intensity of the EPR signal of the freeze-quenched sample, compared to a standard freezing method, presumably due to a packing efficiency of only about 50-70%, which hampered the significancy of their

calculated quenching time. As commercial instrumentation made its appearance in the 1990s, RFQ gained more popularity in enzyme research. Different sample collection systems were adapted to be coupled to NMR [95], EPR [97] and Mössbauer [98] spectroscopies, even though the freezing method was still based on fast spraying into a bath of cold isopentane (or propane). In 2000 Ollerich *et al.* presented a method for collecting the freeze-quenched sample in a way that it could be sequentially investigated by EPR and Resonance Raman spectroscopies [99]. They focused their work on the well-known binding reaction of azide (N_3^-) to ferric myoglobin (Mb) which was already considered as a standard for the calibration of RFQ devices introduced earlier (section 2.3.4.4). While their device and freezing method were essentially similar to the ones already described in literature, the group of Ollerich is perhaps the first to raise awareness on the limited reliability of the quenching time calibration procedure, after the very early studies. They highlighted the struggle to obtain a good packing efficiency and reproducibility, which reflected on the poor fitting of the calibration curve obtained by EPR experiments.

In the attempt to overcome the limitations of the commercial setups and to achieve a faster freezing, several research groups started to design and build "home-made" RFQ devices. A new approach, first introduced by Tanaka and colleagues [100] and later followed by Lin *et al.* [101], was based on spraying the sample directly on the surface of rotating metal disks (made out of copper or silver) partially submerged in liquid nitrogen. In this way, a fine powder of frozen sample particles was directly transferred by the rotating disk into the liquid nitrogen underneath. In combination with the use of high-performance sub-millisecond micro-mixers, this method provided quenching times of ~ 50 - 200 μs. A more sophisticated solution was later developed by Cherepanov and de Vries [102] who described a microsecond freeze-hyperquenching device and reported a total quenching time of ~ 130 μs. In their system, HPLC-grade pumps and tubing are used to apply high-pressures and obtain flows with high linear rate. The reagents are injected into a tangential micro-mixer which guarantees a mixing time < 20 μs and efficiently mixes viscous aqueous solutions. Both the mixer and the collection system are mounted in a low-pressure chamber to maintain the jet speed between the mixer and the freezing medium constant. A small jet diameter and a high jet speed allow a freezing time < 30 μs.

One of the major drawbacks in the application of the freeze-quench technique to biological samples is the typically high amount of sample needed per single experiment, which results from inefficient sample collection and packing. The coupling of RFQ with high-frequency EPR (*e.g.* W-band, ~ 94 GHz) might represent a solution, since the amount of sample needed for this kind of experiment is definitely smaller than for the conventional X-band measurements (~ 2 to 4 μL,

against 80-100 µL). In 2004 Schünemann and colleagues reported the first application of RFQ to high-frequency EPR with the use of a commercial device coupled to a home-made sample collection system adapted to the fragile W-band EPR capillaries [103]. In another application from Manzerova *et al.* [104], several innovative parts were designed and assembled. First, the ejection nozzle consisted in a metal tube bent at a 90° angle having 25 drilled holes, 100 µm in diameter, to break the stream into independent jets of high kinetic energy. Secondly, the freezing method based on the work of Tanaka and co-workers and Lin and co-workers [100, 101], was upgraded with the use of a copper-beryllium alloy for the rotating disk, to retain the thermal conductivity of copper and having at the same time a more resistant material to abrasive scratching. An ingenious way to scrape the frozen powder off the disks was employed by bringing single-edged blades into contact with the rotating wheels. Finally, an adapted packing stage was designed to fill the small capillaries necessary for D-band EPR (~ 140 GHz). A similar approach has been used by Kaufmann *et al.* [105] for preparing freeze-quenched samples for W-band EPR, but with their setup it was possible to collect samples quenched at different times in a single freezing experiment. It is clear from the presented examples that despite many uses of RFQ and instrumentational developments have been described so far, it remains a challenging technique. In the following sections a description of the RFQ setup used in this work is provided and the main aspects of the instrument calibration are discussed.

2.3.4.3 RFQ setup from BioLogic

In this study a device from BioLogic was used, consisting of an SFM-2000 stopped-flow unit and an MPS-70 controller unit, combined with a Freeze-Quench sample collector adapted for EPR tubes (**Figure 2.10 A**) [106]. The use of a commercial instrumentation provides the advantage of having a guaranteed standard performance and reproducibility. On the other hand, introducing customized parts to improve the functionality of the setup is not straightforward, due to the material and spatial limitations of a preset design. In this work, only the cooling system was in-house designed and optimized (**Figure 2.10 B**). Briefly, the sample is frozen in a bath of cold isopentane in which a teflon funnel is immersed and connected to a standard X-band EPR tube. The isopentane is refrigerated by a flow of cold nitrogen gas which passes through a copper coil which is in turn connected to a second coil immerged in a bath of liquid N_2, responsible for cooling down the N_2 gas. By regulating the flow of the N_2 gas and the level of the liquid N_2, it is possible to control the temperature of the isopentane. With this setup, the lowest working temperature is of ~ -130 °C, since below this temperature the isopentane becomes viscous and eventually freezes. In this RFQ setup, the pumps pushing the solutions in the system are driven by independent stepping-motors, which guarantee an almost linear movement of the syringes. The flow rate can be controlled through the BIOKINE

software by adjusting the time and the volume of solution per shot. A waste collection system is also integrated in the setup to discard the aged solution sitting in the mixing chamber before the freshly-mixed sample is collected. The RFQ setup can be operated in continuous or interrupted mode. In the first case, after the mixing, the sample is pushed through an "ejection delay line" (EDL) of a known volume and immediately sprayed into the cryogenic bath. Differently, in the interrupted mode, an additional ageing time is added after the mixing phase, before pushing the sample out of the system. By varying the flow rate, the ageing time, and the volume of the EDL (different interchangeable EDLs are provided with the instrumentation), it is possible to freeze the sample at different "apparent reaction times", as explained later in more detail.

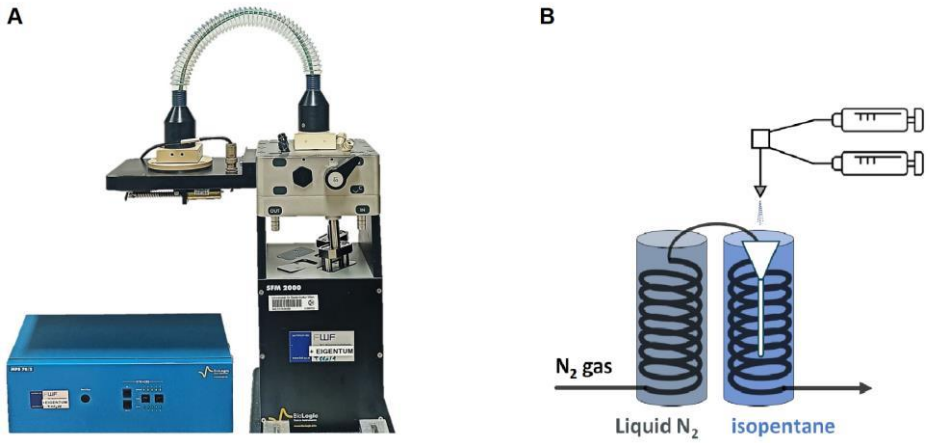

Figure 2.10 *RFQ instrumentation from BioLogic, including the SFM2000 and the MPS-70 units* ***(A)*** *and the cartoon representation of the in-house optimized cooling system based on a cold isopentane bath* ***(B)***.

2.3.4.4 The calibration reaction

Knowing the actual quenching time obtained during the sample preparation is essential to interpret the results of the EPR measurements and to correlate them with the enzyme kinetics. As described by Pievo *et al.* [107], the quenching time (t_Q) can be defined as the time which passes between the initiation of the reaction (*i.e.* the moment when the reagents get into contact) and the time of its quenching by fast freezing inside the cryogenic bath. This time can be considered as a sum of different components:

$$t_Q = t_M + t_T + t_F \tag{2.35}$$

where t_M is the time of mixing, t_T is the time of transport from the mixing chamber to the surface of the cryogenic bath and t_F is the freezing time. While t_M and t_T can be calculated by knowing the parameters of the experimental setup, t_F is a variable which cannot be easily estimated, since it depends on several physical factors including the efficiency of the heat transfer between the sample and the cryogenic bath and the size of the sample particles. For this reason, the estimation of the freezing time achievable with a particular freeze-quench setup is normally performed through a calibration of the system with a reaction of known kinetics. In literature, the standard reaction for this experiment is the binding of azide (N_3^-) to ferric myoglobin (Mb) which produces an easy-to-follow change in the CW-EPR signal, due to the conversion of the high-spin spin state of the aquomet Mb ($S = 5/2$) to the low-spin state ($S = 1/2$) of the azide-bound ferric form [95–97, 99, 107, 108] (**Figure 2.11** left panel). The principle of the calibration is that of freezing the sample at different time points in a controlled manner, such to correlate the observed freezing time (or "apparent reaction time") to the progression of the reaction (**Figure 2.12 A**). The apparent reaction time is nothing else than the sum of t_M and t_T and it can be calculated provided that all the parameters of the used setup are known, including the volume of the mixing chamber, the internal diameter of the tubing, the flow rates, the volume of the reagent solutions, the diameter of the exit nozzle and distance from the cryogenic bath. This time interval is the variable which can be controlled (*e.g.* by changing the flow rate) and that constitutes the X-coordinates in the calibration plot (**Figure 2.12 B**). On the Y-axis a parameter reflecting the progression of the reaction is plotted. In the case of the binding reaction discussed above, this term is an expression of the relative amounts of high-spin and low-spin myoglobin observed in the EPR spectrum. In this work the formalism used in [107] was followed, where the Y-coordinates are given by $\ln(Y_t)$, with Y_t is defined as:

$$Y_t = \frac{[HS]_0}{[HS]_t} = \frac{R_t}{R_t + \lambda} \tag{2.36}$$

where

$$R_t = \frac{(I_{HS})_t}{(I_{LS})_t} \tag{2.37}$$

and

$$\lambda = \frac{(I_{HS})_0}{(I_{LS})_\infty} \tag{2.38}$$

The terms I_{HS} and I_{LS} represent the intensities of the high-spin and low-spin signals, respectively. To calculate the parameter λ the signal from unreacted myoglobin ($(I_{HS})_0$, 100 % high-spin) and the one from the completed reaction ($(I_{LS})_\infty$, 100 % low-spin) need to be recorded carefully maintaining all the EPR measurements settings constant, including sample concentration, temperature, microwave power and modulation amplitude. Different methods can be used to calculate the relative EPR contributions of the HS and LS species. In this work they were calculated, for each time point and for the two extremes of the reaction, as the ratio between the peak-to-peak distance of the low-field feature of high-spin Mb and the peak-to-peak distance of the g_y feature of low-spin Mb-N_3^-, all taken as absolute positive values (**Figure 2.11**, right panel). The method was also validated by calculating the relative contributions through full spectral simulation. Once the fitting of the obtained data is done, the intercept on the time axis (**Figure 2.12 B**) gives the apparent negative time t_F which has to be added, in absolute value, to the apparent reaction time in order to calculate the actual quenching time.

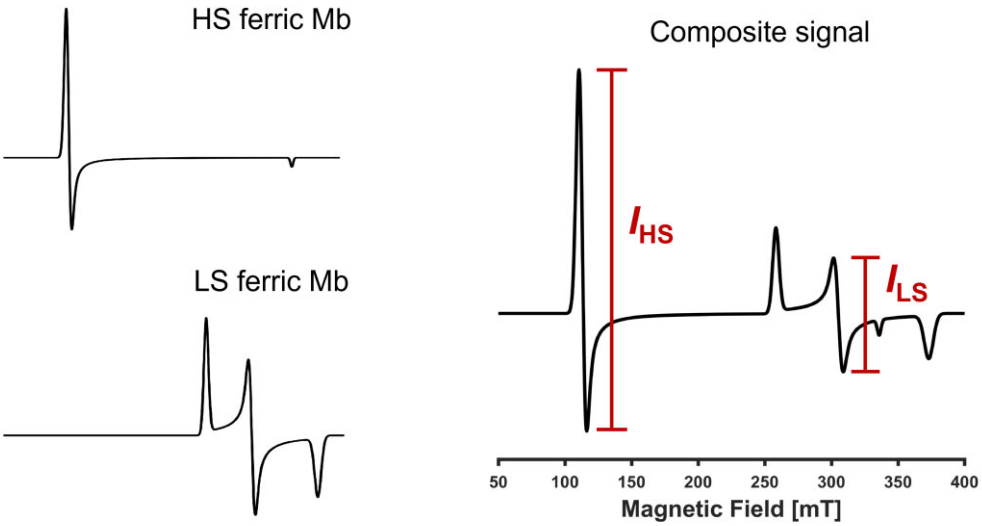

Figure 2.11 *Illustrative CW-EPR spectra of HS and LS ferric myoglobin (left) and simulated composite signal of a putative sample showing both HS and LS contributions (right). All the spectra are generated with EasySpin v. 6.0.0-dev.47* [188].

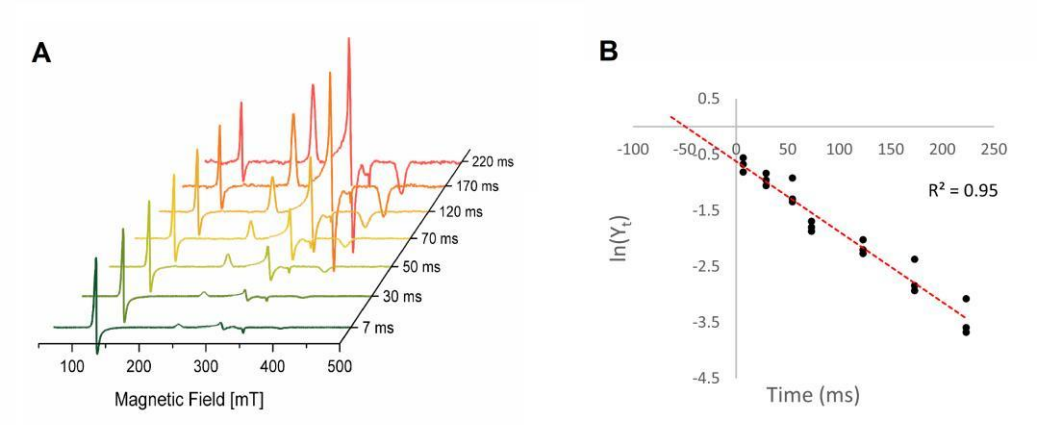

Figure 2.12 *Calibration of the rapid freeze-quench device from BioLogic.* ***(A)*** *The binding reaction of N_3^- to Mb was quenched at different apparent reaction times. The spectra are normalized to the intensity of the HS feature (B ~ 150 mt) to better visualize the increasing contribution from the LS species.* ***(B)*** *Calibration curve obtained from the experiment shown in (A), where the X-axis represents the apparent reaction time (ms), while the Y-axis values are calculated as described in equations 2.34 - 2.36. The intercept on the X-axis gives the freezing time as a negative value, which has to be added to the apparent reaction time to calculate the real quenching time.*

Chapter 3

EPR as a tool for the study of heme-containing biocatalysts

Abstract

Paramagnetic (open-shell) systems, including transition-metal ions, radical intermediates, and defect centers, are often involved in catalytic transformations. Despite the prevalence of such species in catalysis, there are relatively few studies devoted to their characterization, compared to their diamagnetic counterparts. Electron Paramagnetic Resonance (EPR) is an ideal technique perfectly suited to characterize such reaction centers, providing valuable insights into the molecular and supramolecular structure, the electronic structure, the dynamics and even the concentration of the paramagnetic systems under investigation. Furthermore, as EPR is such a versatile technique, samples can be measured as liquids, solids (frozen solutions and powders) and single crystals, making it ideal for studies in heterogeneous, homogeneous and enzyme catalysis. This chapter summarizes some examples of successful applications of EPR spectroscopy to heme-protein research. After a general introduction, the reader will find an overview of the principal features of an important reaction intermediate in heme enzymes turnovers, the so-called Compound I. Next, relevant studies involving the employment of EPR spectroscopy for the investigation of chlorite dismutases and other heme peroxidases will be discussed.

Partially redrafted after: Maruan Bracci, Paolo Cleto Bruzzese, Antonino Famulari, David Fioco, Andrea Guidetti, Yu-Kai Liao, Leonora Podvorica, Seyedeh Fardokht Rezayi, **Ilenia Serra**, Kavipriya Thangavel and Damien M. Murphy (2020), Paramagnetic species in catalysis research: a unified approach towards (the role of EPR in) heterogeneous, homogeneous and enzyme catalysis, in *Electron Paramagnetic Resonance: Volume 27*, 1-46.

Own contribution: draft writing and editing of section 3.1 “EPR of heme enzymes” (part 2 in the original paper) and 3.1.2 “Chlorite dismutases” (part 2.2 in the original paper). Section 3.1.1 “Compound I in heme systems” is summarized and rephrased from part 2.1 of the original paper, which was not written by myself. The remaining sections are not part of the above-mentioned paper, but constitute original work.

3.1 EPR of heme enzymes

As already mentioned in Chapter 1 (section 1.1.6), the increasing demand for a reduction in the environmental impact of industrial processes has resulted in the search for greener alternative processes. The field of biocatalysis has attracted increasing popularity, particularly with the advent of modern biotechnology. Biocatalysis is generally considered as a sustainable process, however, some challenges remain with respect to the widespread utilization of these biocatalysts, including their stability and reusability, the costs associated with downstream processing, and the time-to-market pressure which often favors more consolidated methods [109, 110]. Within this field, a well-known and diverse group of biocatalysts is based on heme enzymes. They belong to the larger class of heme proteins, which are widespread biomolecules in nature, holding a diverse range of functionalities. For example, the versatility of the heme group is often exploited in activities such as oxygen storage and transport, electron transfer, signal transduction and catalysis (Chapter 1, section 1.1.1) [111]. For the purpose of this section, the following discussion will focus on the latter aspects of their function.

It has already been outlined that the reactivity of heme enzymes is governed both by the chemistry at the heme iron center, and the interaction of the prosthetic group with the protein moiety (Chapter 1, section 1.1.1). Biological redox reactions involve electron transfer processes, for which efficiency is optimized when the free energy driving force (ΔG) is maximized and the reorganization energy (λ) is minimized, in accordance with Marcus's theory [112]. In heme systems, the electron delocalization over the porphyrin ring reduces the need for re-ordering in the local structure. As a result, the thermodynamics is defined by the redox potential of the couple donor-acceptor, which in the case of heme enzymes, is regulated by the protein matrix [113]. Among the representative heme-types found in biology (labelled *a*, *b*, *c*, d_1), the best studied is probably the heme *b* (iron protoporphyrin IX), common to the oxygenase and peroxidase families (**Figure 1.1**). These two broad classes of heme enzymes, oxidize substrates utilizing dioxygen and hydrogen peroxide respectively [114].

The iron center in heme systems can be found in various oxidation states, the most common of which are Fe^{2+}, Fe^{3+} and Fe^{4+}. The first two states are commonly found in two different spin configurations, either HS or LS, depending on the distribution of electrons in the *d*-orbitals, whose degeneracy is removed by the ligand field splitting (**Figure 3.1**, reproduced from [115]). The Fe^{4+} oxidation state is of notable importance for the catalytic mechanism of many heme enzymes, existing in transient states, which are formed during the turnover cycle upon binding of the

activator substrate. Indeed, the key intermediates in the reaction cycle are often described as Fe^{4+}-oxo species, known as Compound I and Compound II (Chapter 1, section 1.1.3). The former stores two oxidizing equivalents, one on the iron, and one in the form of a free radical. After one-electron reduction, the free radical is lost, resulting in the formation of Compound II [116].

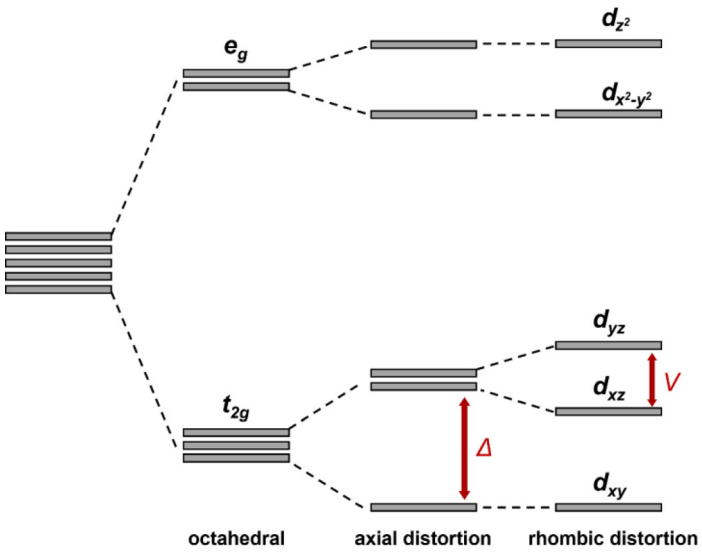

Figure 3.1 *Energy diagram for the 3d-orbitals of ferric heme iron. It shows the octahedral symmetry obtained as first approximation assuming equal axial ligands and additional axial and rhombic distortions responsible for a degeneracy lift of the* t_{2g} *orbitals. The figure is reproduced from* [115] *and it constitutes original work by myself.*

A summary of the variable oxidation and spin states occurring in heme systems is presented in **Table 3.1**. In heme proteins, the metal center commonly adopts a pseudo-octahedral coordination mode, with four equatorial nitrogen atoms from the porphyrin ring and a protein residue as proximal axial ligand in the fifth position, typically a histidine, cysteine, or tyrosine. The sixth axial position can either be occupied by another endogenous ligand, an external molecule (such as water), or even left free (uncoordinated) to promote substrate binding. Coordination by the porphyrin ring places the iron *d*-orbitals in an intermediate ligand field, close in energy to the 'low-spin to high-spin' transition, so that the spin state is sensitive to the nature of these axial ligands. A "strong" ligand will cause a splitting of the e_g and t_{2g} orbitals, larger than the pairing energy that is necessary to keep two electrons in the same orbital. Only the lower energy t_{2g} orbitals will be

occupied, leading to a LS configuration. Alternatively, a ''weak'' ligand will have an orbital energy separation small enough to prefer the occupancy of the e_g orbitals, thus contributing to a HS configuration [117].

	Fe^{2+}	Fe^{3+}	Fe^{4+}
HS	$S = 2$	$S = 5/2$	-
LS	$S = 0$	$S = 1/2$	$S = 1$

Table 3.1 *Electronic configurations of iron in heme systems.*

Since almost all of these iron states are paramagnetic, EPR spectroscopy is one of the most suitable techniques for the investigation of heme-based systems. Moreover, even if proteins are large, complex molecules, the EPR characterization method is still reliable as it focuses specifically on the paramagnetic active site, where the unpaired electrons reside. In metalloproteins possessing iron centers with multiple unpaired electrons ($S > ½$), the zero-field splitting (ZFS) term can be much larger than the X-band microwave quantum. In the case of high spin Fe^{3+}, the observed EPR spectrum is derived exclusively from transitions within the Kramer's doublets, and it can be treated as an effective $S = ½$ system [118] (**Figure 3.2**).

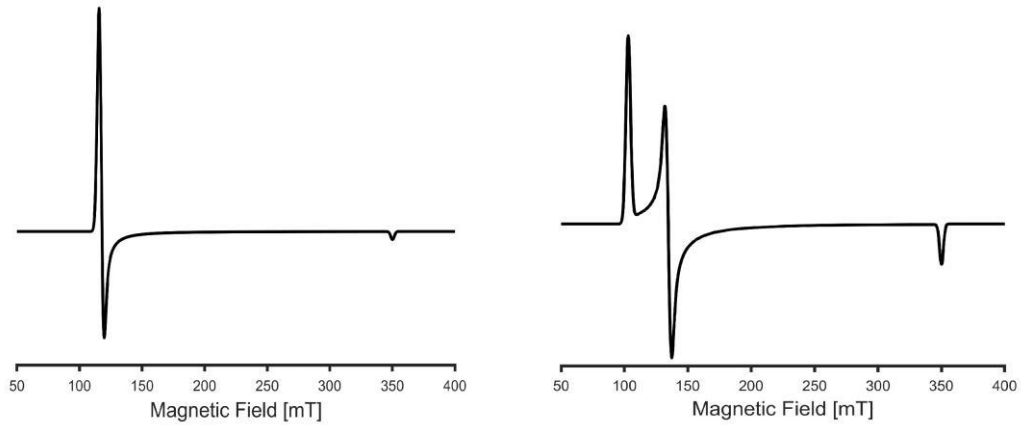

Figure 3.2 *Illustrative CW-EPR spectra of high-spin Fe^{3+} ($S = 5/2$) heme-based centers simulated using the EasySpin package* [188]*, with $g_{\perp}^{eff} \approx 6$, $g_{/\!/}^{eff} \approx 2$ for the axial case (left); $g_x^{eff} \approx 6.4$, $g_y^{eff} \approx 5.2$, $g_z^{eff} \approx 2$ for the rhombic case (right).*

However, for a more accurate description of the spin system, two independent parameters denoted as the tetragonal zero-field splitting (D) and rhombic zero-field splitting (E) terms, can be derived from the principal values of the $\boldsymbol{D}$ tensor, which describe the zero-field splitting interactions in the spin Hamiltonian (Chapter 2, section 2.3.2.5). The defined ratio $\eta = E/D$ (with $0 < \eta < ⅓$) is called the rhombicity term and is commonly used in the simulations of X-band CW-EPR spectra of heme proteins with high spin multiplicity since they depend, to a good approximation, on this single parameter [119].

Another example of high-spin iron is Fe^{2+} with $S = 2$, characterized by four unpaired electrons. Despite being an EPR-active species in principle, very few examples of high-spin ferrous heme have been reported in literature [120, 121]. The detection of this non-Kramer ion is impeded by the large ZFS which removes the $\Delta_{ms} = \pm 1$ levels above the accessible microwave energy *i.e.* the allowed transition. At X-band, only at very low applied magnetic fields can a broad structureless feature be detected. For these reasons it is generally assumed that the high-spin ferrous complexes are EPR silent at X-band [120]. Low-spin Fe^{3+} ($S = ½$) is commonly found in heme structures possessing strong axial ligands. In contrast to the high-spin states, this spin state can be represented by a simpler spin Hamiltonian, in which the zero-field splitting terms are absent, and thus a more readily interpreted EPR spectrum (**Figure 3.3**).

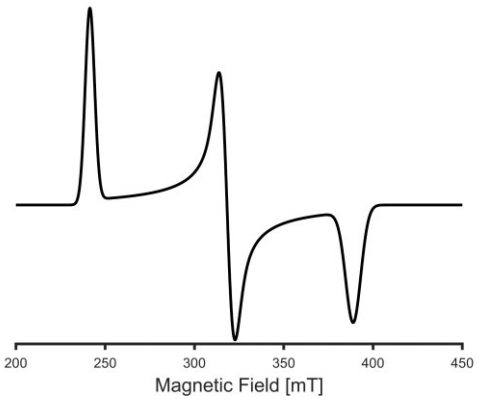

Figure 3.3 *Illustrative CW-EPR spectrum of a low-spin Fe^{3+} ($S = 1/2$) heme-based center simulated using the EasySpin package* [188] *with $g_z = 2.42$, $g_y = 2.25$, $g_x = 1.92$.*

The *g*-values for low-spin ferric heme proteins are very often interpreted with a crystal field model that correlates them to the relative energy splitting of the iron t_{2g} orbitals [122, 123], and therefore the corresponding spin distribution. How, and to what extent the electron system is affected by the axial substituents, can be related to the nature of the axial ligands and the active-site geometry [124–126]. A different case of low-spin iron occurs in its reduced state (Fe^{2+}, $S = 0$), although this species is not paramagnetic, having six paired electrons in the outer valence shell which fully occupy the t_{2g} orbitals due to the large separation from the ligand field. It is clear that whilst iron heme proteins possess diverse and variable electron configurations that may be challenging to study, they nevertheless offer highly desirable application in modern catalysis. In the following sections, more specific examples will be presented to demonstrate their applicability and reaction versatility as aerobic oxidation catalysts, and importantly how EPR can be exploited to understand their reaction cycles.

3.1.1 Compound I in heme systems

Although great uncertainty exists around the first reactive intermediate in heme-based systems, in several reported cases the catalytic activity starts with the species commonly referred to as Compound I (Chapter 1, section 1.1.3). For example, in peroxidases, Compound I is responsible for a diverse assortment of industrially relevant reactions including enantioselective epoxidation of olefins, oxidation of amines, alcohols and sulfides, as well as peroxidase-catalyzed polymerization of aromatic molecules (Chapter 1, section 1.1.6). For this reason, peroxidases have historically received great attention for their potential application in the field of biocatalysis [127]. During the catalytic cycle, these enzymes oxidize the iron above the ferric Fe(III) resting state to form Compound I [116] (see **Scheme 3.1** below). The formation of this intermediate occurs following the heterolytic cleavage of the substrate O–O bond, which leads to the storage of two oxidizing equivalents, one that resides on the Fe(IV) and the other one either localized on the porphyrin ring or onto a nearby amino acid, more commonly in the form of a cationic free radical [114].

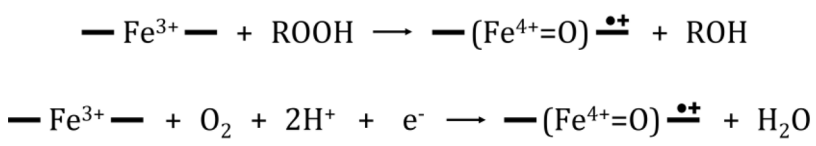

Scheme 3.1

In **Scheme 3.1**, R can be a hydrogen or an organic group, whereas the labels ——— represent the porphyrin ring. Numerous techniques have been used to unravel the exact nature of Compound I, however it remains a challenging task due to the transient nature of this intermediate. EPR plays a crucial role in the characterization of these species, thanks to the paramagnetic nature of Compound I, which can be readily detected with this technique.

To date, several CW-EPR spectra of Compound I with distinct features have been reported in the literature for different systems. They are usually described by a model consisting of two interacting spin systems, one from the heme iron (S = 1) and one from a free radical (S = ½). The spin distribution on the oxo-ferryl moiety is generally modelled by considering an almost purely axial zero-field splitting, which is sensitive to the ligand environment. The main interaction between the iron and the free radical, is the so-called *exchange interaction*, a weak spin–spin interaction that is caused by the partial overlap of the wave functions of the two paramagnetic centers. This interaction, which varies in strength and sign, is highly dependent on the electron distribution of both species. This ultimately determines the net spin state of Compound I [128–132]. It should also be noted that, although the ZFS is very sensitive to the molecular structure, the magnitudes reported for Fe(IV)=O in heme enzymes are usually much larger than the energy of the MW quantum (especially at X-band), thereby shifting the transitions outside the accessible magnetic field range [133]. Whilst the oxo-ferryl moiety is EPR silent, the electronic levels of Fe(IV) affect the relaxation properties of the interacting radical species. CW-EPR relaxation studies have therefore been used to obtain the ZFS parameters of Fe(IV)=O in some enzymes [129–134]. When the radical resides on the porphyrin ring, or on a residue close enough to the iron center, the EPR spectrum of Compound I appears broad and can be interpreted by considering the exchange interaction [135, 136]. On the other hand, if the radical resides on an amino acid (this intermediate is variously referred to as Compound ES, Compound I* or Compound-I_B [55, 137–139]), and is sufficiently remote from the iron center, no orbital overlap occurs. As a consequence, the exchange interaction is negligible and the shape of the EPR spectrum is dominated by the non-coupled organic radical contribution [137].

Interestingly, the nature of the amino acid in which the radical is stored can be determined from the CW-EPR spectrum assuming some of the characteristic hyperfine interactions can be resolved by suitable techniques. In most reported cases, the small hyperfine interactions between the electron spin and magnetic nuclei in Compound I, are completely unresolved in the CW-EPR spectra. In these cases, more advanced hyperfine spectroscopies are required to resolve these small interactions. For example, CW and pulsed ENDOR spectroscopies have been used to

fully characterize the location of the free radical and spin distribution on the active site in heme enzymes [140–142]. The ENDOR technique, combined with isotopic substitutions of Compound I in horseradish peroxidase, has provided detailed insights into hyperfine couplings between the free radical and ^{1}H, ^{14}N nuclei which originate from the porphyrin ring, indicating that the ferryl moiety is not protonated. Using ^{17}O labelling, it was found that the oxygen from the peroxide is transferred to the iron(IV)-oxo species where one of the oxidizing equivalents is stored [143, 144]. In addition to this information on spin-distribution, complementary information on local structural aspects can also be derived from the resolved hyperfine data. For example, using multi-frequency EPR and ENDOR, the ^{1}H hyperfine coupling observed in a Trp radical-type Compound I of a peroxidase, was used to calculate the dihedral angles of the aromatic radical and thus, with the aid of crystallographic structures, DFT and site-directed mutagenesis, identify the exact position of the radical in the protein [145, 146]. The power of EPR to characterize these heme-based systems is certainly enhanced by complementary theoretical calculations. In the future, further investigations involving hyperfine spectroscopies and computational studies will be required to better understand the role of the paramagnetic spin states in the reactivity of Compound I. This task remains challenging however, owing to the difficulties of isolating and stabilizing Compound I on short timescales. In these cases, a rapid freeze-quench approach might represent a solution (Chapter 2, section 2.3.4).

3.1.2 EPR investigations of chlorite dismutases

The heme *b*-containing enzymes chlorite dismutase (Cld) have been already introduced in Chapter 1 (section 1.1.5). Due to the paramagnetic nature of the Fe^{3+} present in their resting state, detailed insights into the active site configuration can be obtained by means of EPR spectroscopy, which has been extensively applied in the study of these enzymes. In particular, low-temperature CW-EPR spectroscopy at X-band revealed that chlorite dismutases from clade I typically exhibit rhombically distorted HS spectra at neutral pH [48, 49, 63, 147]. In contrast, the few representatives from clade II investigated so far, are characterized by purely axial HS signals [54, 147, 148] (**Figure 3.4**). Minor contributions from LS components were also detected by EPR at pH=7. In some cases, the low-spin signals observed at neutral pH were assigned to an imidazole adduct (strong ligand), derived from protein purification procedures involving a His-tag affinity step [59]. However, this could be ruled out for recombinant chlorite dismutases which were purified without the use of imidazole; in these systems LS components of uncertain origin are often observed [61, 147]. Chlorite dismutase activity has been shown to be critically

influenced by pH, having an optimum activity between 5.0 – 5.5, and a significant decrease in the reaction rate at higher pH values [54, 65]. EPR spectroscopy was also exploited in pH-dependence studies, revealing the formation of hydroxide-ligated heme iron at alkaline pH (**Figure 3.4**, grey traces) [49, 61, 148], which could contribute to slowing of the turnover rate.

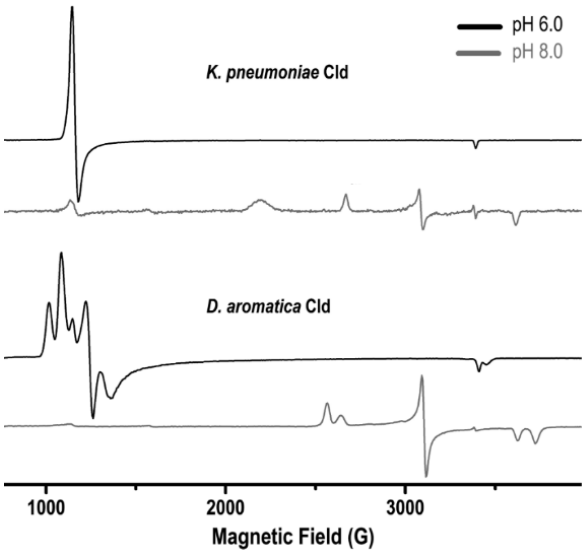

Figure 3.4 *X-band CW-EPR spectra of ferric Clds from Klebsiella pneumonia (dimeric clade II Cld) (top) and Dechloromonas aromatica (pentameric clade I Cld) (bottom), showing the different rhombicity in the HS signature of the two different Cld sub-families. At alkaline pH (grey traces), a transition from HS ferric to LS ferric states is observed in both Cld representatives. The figure is adapted from* [148].

The proposed catalytic mechanism has been outlined in Chapter 1 (section 1.1.5). It was already mentioned that the main uncertainty concerning this reaction is whether chlorite is cleaved via a heterolytic or homolytic mechanism, resulting in oxidation of the heme iron to a Compound I or Compound II species respectively. In any case, a transient radical must be formed, being either located on the porphyrin π-cation, or on the substrate intermediate. The identification and exact nature of this transient radical is not trivial to characterize, and for this reason EPR spectroscopy has played a pivotal role is these studies, since radicals of different origin exhibit distinct spectral features in frozen solution. The major hindrance to studies of these reaction intermediates is the time-scale limitation. Stopped-flow UV–vis spectroscopy showed that the dominant transient species is formed within

a few milliseconds from the addition of chlorite, and that it persists as long as chlorite is available, which is on the order of a few seconds using the experimental conditions applied until now [55, 65]. Due to technical aspects associated with sample preparation times for EPR analysis, little data is available on the reaction of chlorite dismutases with their substrate. In the work of Lee *et al.* [63], on chlorite dismutase from *Dechloromonas aromatica*, the protein sample containing chlorite was flash-frozen in liquid nitrogen within one second. The authors observed the complete loss of spectral features associated with the ferric enzyme, and the concomitant appearance of a broad and a sharp signal. These were assigned to an S=3/2 porphyrin π-cation radical (Compound I), and a tryptophanyl radical, respectively. However, the author's interpretation should be reconsidered in light of more recent studies, including the present work, which clearly show the formation of a chlorine dioxide radical in the millisecond time scale, when the Cld enzyme reacts with a high excess of chlorite [149, 150]. This aspect will be more extensively discussed in Chapter 8. In another study by Hofbauer and co-workers [65], the pentameric enzyme from *Candidatus nitrospira defluvii* was mixed with different amounts of chlorite, but in this case the reaction was allowed to go to completion before the sample was analyzed using EPR. With increasing concentrations of chlorite, the HS signal of the resting state progressively disappeared, with no concomitant formation of LS species. At very high excess of chlorite (>2500-fold), a protein radical was observed. These results were consistent with the hypothesis of an irreversible enzyme inactivation mechanism, also supported by UV–visible spectroscopy.

The application of rapid freeze-quench technology (Chapter 2, section 2.3.4) has recently entered the Clds research, providing mechanistic information in the sub-millisecond range. With the use of a home-made freeze hyperquenching device, Püschmann *et. al.* [151] observed Cld intermediates in < 100 μs. They proposed a completely new catalytic mechanism for the clade I *Azospira orizae* Cld (*Ao*Cld), involving the formation of transient spin-coupled cationic amino acid-based radicals, giving rise to a triplet state signal in the CW-EPR spectrum of the freeze-quenched *Ao*Cld in presence of a large excess of substrate. This interpretation is, however, still under debate and it will be treated more into details in Chapter 8. It is clear that EPR spectroscopy remains invaluable in studies of chlorite dismutases. Using less active variants, which can be obtained with relative ease by site-directed mutagenesis, working under different pH conditions and sample preparations using a freeze-quench apparatus, some of the existing technical limitations encountered in this field can be overcome.

3.1.3 Relevant examples of EPR applied to different heme peroxidases

The most investigated heme peroxidase is by far horseradish peroxidase (HRP), which has been already introduced in Chapter 1 (section 1.1.3). Examples of EPR spectroscopy applications for the study of the heme site environment of this enzyme date back to the 1970s [152–155]. In these studies, extensive spectroscopic analysis of the free enzyme and in complex with several ligands was conducted. Both different enzyme preparations and EPR measurement parameters were investigated to observe their effects on the resulting spectra. From these early works, it became immediately evident that the EPR spectrum of HRP was extremely sensitive to the experimental conditions, in some cases due to the coexistence of multiple isoenzymes, in others due to the propensity of HRP to react with a wide range of different molecules, including the buffers in which the samples were prepared. Surprisingly, the sole transfer of the same sample in a different EPR tube was sometimes enough to cause changes in the spectral features [155]. In general, the EPR spectrum of the ferric resting state of HRP at close-to-neutral pH consists of multiple features in the low-field region. They were assigned to an admixture of high S=5/2 and intermediate S=3/2 heme spin states, an effect referred to as quantum-mixed spin state [152, 155], which was also later described for other plant peroxidases, such as barley peroxidase [156]. Moreover, a great influence of pH on both the low-field and high-field regions of the HRP spectrum was observed. In addition to an overall change on the relative ratios of the HS features, an extra LS contribution defined 'alkaline form', was described at pH $\geq$ 7.0 for a sample of HRP extracted from horseradish roots, thus containing several isoenzymes [152]. Later spectroscopic studies on HRP aimed at the characterization of its most famous catalytic intermediates, Compound I. Tanaka and co-workers used a rapid freeze-quench approach to investigate the reaction of the recombinant HRP isoenzyme C with the substrate H_2O_2 [100]. They built a 'home-made' RFQ device (Chapter 2, section 2.3.4) and were able to quench the reaction with H_2O_2 at ~ 200 μs (**Figure 3.5**). By comparing the spectrum obtained by RFQ and the one from a conventional flash-freezing method, they were able to assign the signal to that of Compound I.

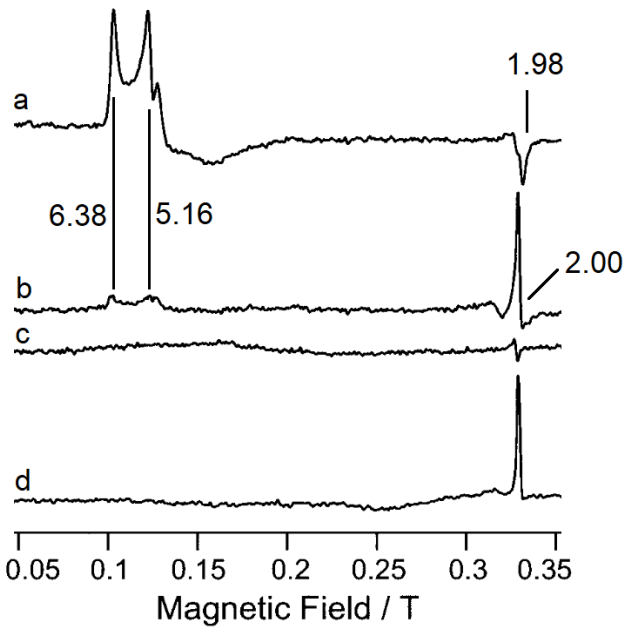

Figure 3.5 *X-band CW-EPR spectra of the reaction between ferric HRP and H_2O_2 freeze-quenched within 200 μs.* ***(a)*** *ferric resting state of HRP at pH 7.0 measured at 5 K. The sample was prepared by using the freeze-quench device.* ***(b)*** *reaction between ferric HRP and H_2O_2 (20-fold excess) quenched at 200 μs, measured at 5 K.* ***(c)*** *reaction between ferric HRP and H_2O_2 (20-fold excess) quenched at 200 μs, measured at 15 K.* ***(d)*** *reference EPR spectrum of compound I of HRP prepared by manually freezing the mixture of HRP and H_2O_2 measured at 5 K. The interval between the mixing and freezing was ~ 30 s. The g values of the principal features are indicated. The figure is adapted from* [100].

Another relevant subfamily of heme peroxidases, which is closely related to chlorite dismutases, is that of dye-decolorizing peroxidases (DyPs), described in Chapter 1 (section 1.1.4). Despite having a much shorter history compared to HRP, the potential industrial applications of DyPs fostered numerous mechanistic studies in the recent years. In this sense, EPR spectroscopy proved to be a powerful tool for the characterization of the ferric resting state of these enzymes [88, 157–159], but also for the investigation of catalytic intermediates [160, 161]. The EPR spectra of DyPs at neutral pH generally show a rhombically distorted HS signal, as in the case of the DyPs from *Rhodococcus jostii* [157], *Thermomonospora curvata* (*Tc*DyP) [162] and *Klebsiella pneumoniae* (*Kp*DyP) [88]. Conversely, it has been observed that at acidic pH (~3.0) they can adopt a more axial configuration (**Figure 3.6**) [158, 162]. In addition to the main HS species, minor LS contributions were also sometimes detected, but their origin remains uncertain [157, 162]. Site-directed mutagenesis

in combination with other techniques, including EPR spectroscopy, was used in a number of studies to identify catalytically important residues [37, 88, 158, 161, 163]. For instance, this approach was followed to elucidate the nature of an unusual organic radical species found in the EPR spectrum of the resting state of wild-type *Kp*DyP [37, 88]. Interestingly, this signal was absent in the spectra of *Kp*DyP variants lacking catalytically important aspartate and arginine residues at the distal heme site, suggesting that the radical could be linked to the peroxidase activity [88]. Next, multi-frequency EPR and a systematic site-directed mutagenesis strategy were used to individuate the residues responsible for the radical formation. In this way, it was eventually demonstrated that the signal comes from two distinct tyrosyl radicals, of which one forms a dyad with a nearby tryptophan, being stabilized by π – π stacking or charge resonance [37].

It is clear from the presented examples that the use of EPR spectroscopy in heme enzyme research is a successful approach to get insights into the electronic configuration of the environment at the heme site, thus revealing important information on its catalytic properties.

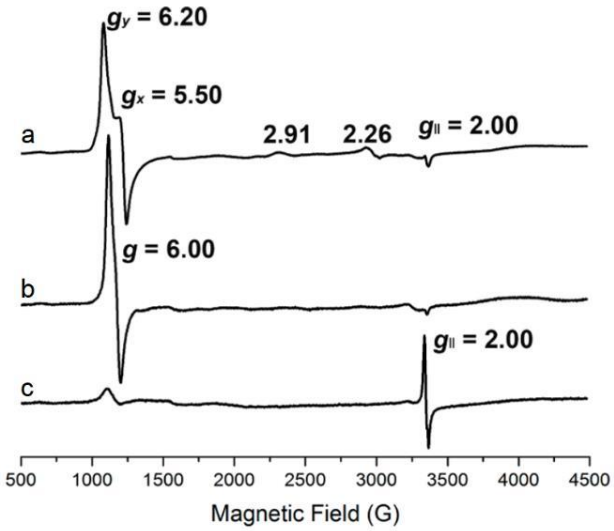

Figure 3.6 *X-band CW-EPR spectra of* ***(a)*** *TcDyP at pH 7.8,* ***(b)*** *TcDyP at pH 3.0, and* ***(c)*** *TcDyP in presence of a 10-fold molar excess of H_2O_2 at pH 3.0. All spectra were recorded at 5 K. The g values of the principal features are indicated, showing the change in rhombicity upon pH variation. The figure is adapted from* [162].

Chapter 4

Challenges in low-temperature EPR of metalloproteins

Abstract

Due to fast relaxation processes of transition metal ions, electron paramagnetic resonance (EPR) spectroscopy of metalloproteins needs to be performed at cryogenic temperatures. To avoid damaging the biological system upon freezing, a cryoprotectant is generally added to the sample as a glassing agent. Even though cryoprotectants are expected to be inert substances, evidences in literature show their non-innocent role in altering the shape of EPR spectra of proteins and biological objects in general. In this Chapter we present a systematic study on the impact of several experimental factors - such as buffer composition, choice of cryoprotectant, pH and temperature - on the EPR spectrum of myoglobin, taken as a reference system for being a well-characterized heme-containing protein. We focus on high-pH buffers to induce and investigate the alkaline transition of ferric myoglobin ($pK_a \sim 8.9$). A combined approach of continuous-wave EPR and UV–visible absorption spectroscopy shows that using particular pairs of buffers and cryoprotectants determines a considerable pH variation in the sample and that this effect is enhanced at cryogenic temperature. In addition, phase memory times were measured to evaluate the efficiency of different cryoprotectants and compared with spectral linewidths in continuous-wave EPR. Our findings suggest that among the selected cryoprotectants ethylene glycol is rather effective, even more than the widely used glycerol, without having unwanted effects.

Redrafted after: Ilenia Serra, Inés García-Rubio & Sabine Van Doorslaer (2021), Pitfalls in Sample Preparation of Metalloproteins for Low-Temperature EPR: The Example of Alkaline Myoglobin, *Appl Magn Reson* 53, 1105–1119

Own contribution: acquisition, analysis and interpretation of all the reported data; writing of paper manuscript.

4.1 Introduction

As already outlined in Chapter 2 and Chapter 3, metalloproteins possessing paramagnetic centres are widely investigated by electron paramagnetic resonance (EPR) spectroscopy to get insight into the spin and oxidation state of the paramagnet, as well as information on local symmetry and geometry. From a spectroscopic point of view, because of the rapid electron spin–lattice and spin–spin relaxation rates of paramagnetic transition metal-containing systems, the EPR experiment needs to be performed at cryogenic temperatures to detect a sufficiently intense and resolved signal [164]. Metalloproteins and biological samples in general are prepared and stored in aqueous media. The formation of ice crystals upon freezing represents an issue during the preparation of samples for low-temperature EPR measurements since, in addition to the risk of breaking the EPR tube, large ice crystals may damage the biological object [165] or cause a mechanical stress on the molecules causing a broader distribution of environments of the paramagnetic moiety which will result in an increased EPR linewidth (larger g-strain) and shortened phase memory times [164]. Moreover, the freezing process can induce the separation of the sample in a phase of pure ice crystals and another containing the concentrated solute [166], where proteins might suffer from a large variation in local concentration, ionic strength or pH. These inhomogeneities could in turn affect the EPR signal, giving rise to artefacts or poorly resolved features. To overcome these hindrances, a cryoprotectant is commonly added to the sample to prevent the formation of ice crystals promoting a homogenous glass upon freezing [167]. Glycerol is by far the most used glassing agent for EPR investigations of biological systems, but ethylene glycol, sucrose [168] and more recently trehalose [169] have been employed as well. Despite being generally considered as biologically inert, evidences of a non-innocent role of these substances can be found throughout the EPR literature of biological samples [170–176].

In Chapter 1, heme-containing proteins have been extensively described, as well as the features of their key prosthetic group, *i.e.*, the heme. Then, in Chapter 3, the relevance of EPR spectroscopy for the study of these metalloprotein has been discussed. This technique can provide valuable information on the architecture of the active site pocket, where the heme moiety is located [92, 111]. pH-dependent experiments are commonly carried out to elucidate protein behaviour, for instance with the attempt to reproduce a certain (or altered) physiological environment [177], or in applied research, to examine the performance of enzymes in sub-optimal conditions which might be necessary for industrial utilization [70]. Many heme proteins have been described to undergo an alkaline transition at high pH related to different deprotonation processes [178–182]. Here, we use the well-characterized myoglobin (Mb) as model heme protein to explore a number of

experimental setups using different alkaline buffers together with a chosen set of cryoprotectants to investigate the influence of such conditions on the EPR spectra. It is known that a HS to LS transition occurs in ferric Mb related to the deprotonation of the water molecule axially coordinated to the heme iron (pK_a values of ~ 8.9 were reported previously [178, 182, 183]). The EPR spectrum of alkaline ferric Mb is characteristic of LS (S = ½) heme iron, with earlier reported g values reflecting the proximal ligation of a histidine and distal ligation of a hydroxide group [178, 184, 185]. Because the impact of procedural factors on the observed EPR signal of heme proteins may lead to erroneous data interpretation, we want to draw the attention to the importance of tailoring the process of sample preparation to the investigated system. Our results demonstrate that the choice of buffer and cryoprotectant, as well as their combination, is not trivial in the design of low-temperature EPR experiments on proteins, not even for a well-known system, like myoglobin.

4.2 Experimental procedures

4.2.1 Materials

Myoglobin from horse skeletal muscle (95–100 % pure, essentially salt-free, lyophilized powder) was purchased from Sigma-Aldrich and used without further purification. Alkaline buffers (pH 9.8 to 10) boric acid–NaOH (herein referred to as borate buffer, Panreac), glycine–NaOH (glycine buffer, Sigma-Aldrich), Na_2CO_3–$NaHCO_3$ (carbonate–bicarbonate buffer, Panreac), 3-(cyclohexylamino)-1-propanesulphonic acid (CAPS, Sigma-Aldrich) and 2-(cyclohexylamino)-ethanesulphonic acid (CHES, Sigma-Aldrich) were prepared at a concentration of 0.1 M, filtered and de-gassed. For EPR measurements, the buffers were used at a final concentration of 0.05 M. The glassing agents glycerol, ethylene glycol and sucrose were purchased from Panreac, trehalose from Sigma-Aldrich.

4.2.2 Optical and EPR Spectroscopies

Myoglobin stock solutions were prepared by dissolving ~ 2 mg of lyophilized myoglobin in 100 µL of each buffer. For all solutions, protein concentration was determined spectrophotometrically with an Analytikjena Specord® 200 plus spectrometer, using 129.000 M^{-1} cm^{-1} as molar absorptivity of Mb at the Soret peak [186, 187], then samples for EPR measurements were prepared to a final concentration of 0.2 mM. For the samples containing glycerol or ethylene glycol, 20 µL of pure substance was added to 80 µL of protein solution to obtain a 20 % (v/v) concentration of the cryoprotectant. In the case of sucrose and trehalose,

myoglobin was dissolved in the buffer already containing the sugar at a concentration of 0.36 M. Representative concentrations of the cryoprotectants were chosen on the basis of the ones used in previous EPR studies [173, 176]. CW-EPR measurements were performed with a Bruker ELEXSYS E580 X-band spectrometer equipped either with an Oxford CF935 continuous-flow cryostat and a Bruker ER4118 SPT-N1 resonator (operating at a microwave (MW) frequency of ~ 9.7 GHz) or with an Oxford ESR 900 continuous-flow cryostat and a Bruker ER 4122 SHQ resonator (operating at a MW frequency of ~ 9.4 GHz). The spectra were taken at a temperature of 10 K with non-saturating MW powers, 1 mT of modulation amplitude and 100 kHz modulation frequency. Reported g values were obtained from simulations of EPR spectra performed with the Easyspin software (v. 6.0.0-dev.26) [188]. Pulse EPR experiments were performed at 10 K with an Oxford CF935 continuous-flow cryostat and a Bruker ER4118 SPT-N1 resonator operating at a MW frequency of ~ 9.7 GHz. A Hahn echo sequence $\pi/2–\tau–\pi–\tau–$echo with 2-step phase cycle and long pulses ($t_{\pi/2}$ ~ 50 to 96 ns) in order to minimize echo modulation was used to measure the phase memory times (T_m). A shot repetition time of 1020 µs was used and the interval between the pulses τ was varied from 148 to 3344 ns in steps of 4 ns. The T_m traces were fitted in MATLAB (MathWorks, R2020b) using an exponential decay function described by the following equation:

$$f(\tau) = Ae^{-B\tau} \qquad \text{(Eq. 4.1)}$$

where A is the amplitude and B is defined as $1/T_m$.

4.2.3 pH Measurements

The possible variation of pH upon addition of increasing amounts of glycerol to different buffers was monitored at room temperature (27 °C ± 0.5) with a Crison GLP 21 pH-meter. The initial pH was measured in 47.5 mL of each buffer at a concentration of 0.1 M. Aliquots of glycerol and fresh buffer were properly added to the initial volume to obtain 5, 10, 15, 20, and 30 % (v/v) glycerol/buffer solutions. For each concentration point, the solution was stirred with magnetic agitation for 5 min to avoid inhomogeneities in liquid density before measuring the pH. The pH stability of the buffers was also tested with a Thermo Scientific Orion Star A111 pH-meter at room temperature (23 °C ± 0.5) in the presence of 20 % (v/v) of ethylene glycol, 0.36 M of sucrose or 0.36 M of trehalose.

4.3 Results

4.3.1 EPR and UV–Visible Spectroscopy

To maintain biological samples at high pH, several well-known buffers can be used. In this study we chose borate, glycine, carbonate–bicarbonate, CAPS and CHES as exemplary buffers to have a varied set in terms of chemical composition. Being extensively used in EPR spectroscopy, glycerol was initially employed in a comparative EPR experiment, to check whether it had any influence on the high-pH spectrum of myoglobin. **Figure 4.1** shows the X-band CW-EPR spectra of myoglobin in several alkaline buffers (theoretical pH of 9.8–10) at 10 K, without and with 20 % (v/v) glycerol. In the absence of glycerol, the characteristic EPR signal attributable to the coordination of a hydroxide moiety to the ferric heme iron (LS state) is well resolved in all samples (principal g values are reported in **Table 4.1**), with the exception of the carbonate–bicarbonate buffer, where only the typical EPR signature of aquomet-myoglobin is detected (HS heme iron ($S = 5/2$)). In addition, in samples prepared in CAPS and CHES buffers, a minor contribution due to the HS state can be seen, though accounting for only less than 10 % of the total spectrum. Already in the samples without glycerol, the EPR spectra vary both in HS/LS ratio and in principal g values of the LS species (**Table 4.1**).

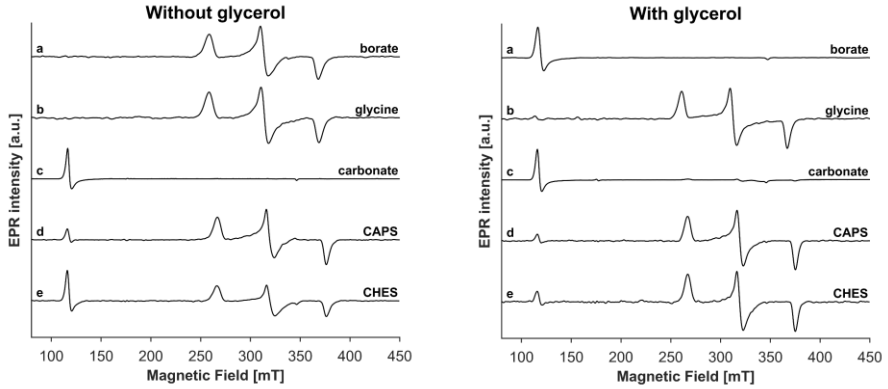

Figure 4.1 *X-band CW-EPR spectra of myoglobin in alkaline buffers (theoretical pH 9.8–10) without (left panel) and with (right panel) 20 % (v/v) of glycerol.* ***(a)*** *Borate,* ***(b)*** *glycine,* ***(c)*** *carbonate–bicarbonate,* ***(d)*** *CAPS and* ***(e)*** *CHES. Spectra were shifted along Y-axis for better visualization. Measurements were performed under non-saturating conditions with microwave powers ranging from* 2.4×10^{-3} *to* 1.9×10^{-2} *mW*

	Species	g_x^{eff}	g_y^{eff}	g_z^{eff}	g_z	g_y	g_x	*%*
Without glycerol								
Borate	LS				2.619	2.157	1.836	100
Glycine	LS				2.624	2.159	1.836	100
Carbonate-bicarbonate	HS	5.910	5.910	2.002				100
CAPS	HS	5.910	5.910	2.002				2
	LS				2.602	2.175	1.843	98
CHES	HS	5.912	5.912	2.000				7
	LS				2.600	2.172	1.841	93
With 20 % glycerol (v/v)								
Borate	HS	5.890	5.890	1.998				100
Glycine	LS				2.597	2.169	1.845	100
Carbonate-bicarbonate	HS	5.920	5.920	2.003				65
	LS				2.595	2.175	1.847	35
CAPS	HS	5.915	5.915	2.002				1
	LS				2.598	2.170	1.847	99
CHES	HS	5.910	5.910	1.998				2
	LS				2.595	2.170	1.846	98

Table 4.1 *Principal g values obtained by the simulations of X-band CW-EPR spectra of myoglobin in different alkaline buffers without and with 20% glycerol (v/v). % contributions were determined by adding each species with its corresponding weight in the final simulation (weights determined using EasySpin software* [188]*). Error margins: ± 0.005 for g values HS, ± 0.001 for g values LS, ± 1% for contributions.*

When glycerol is added to the sample, the expected narrowing of the signals of the LS form occurs due to the reduced mechanical stress on the biological molecule resulting from a better glass formation upon freezing, but also other changes are observed for some of the buffers indicating the non-innocent role of this cryoprotectant. The strongest and most unexpected effect is clearly observed in the spectrum of myoglobin in borate buffer. Here, the alkaline species completely reverts to the high-spin signal. Furthermore, a small but non-negligible change in the principal *g* values of the LS species - as well as a reduction in linewidth - is observed in the spectrum of myoglobin prepared in glycine buffer plus glycerol (**Figure 4.1b** and **Figure A.1** , **Table 4.1**). In the case of the carbonate–bicarbonate buffer, a small signal (~ 30 %) from the OH^--ligated LS species can be detected upon

the addition of the cryoprotectant (**Figure 4.1c** and **Figure A.2** , **Table 4.1**). Finally, when glycerol is present in the samples prepared in CAPS and CHES buffers, the contribution of the HS species is further diminished to 1–2 % and the linewidth of the EPR signature of the LS species is reduced (**Figure 4.1d & e, Table 4.1**).

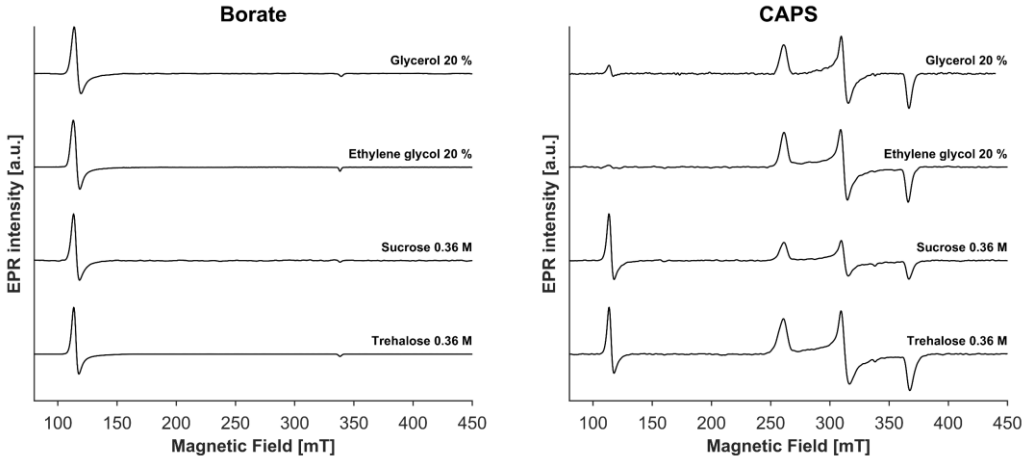

Figure 4.2 *X-band CW-EPR spectra of myoglobin in borate buffer (left panel) and CAPS buffer (right panel) in the presence of different cryoprotectants. Spectra were shifted along Y-axis for better visualization. Measurements were performed under non-saturating conditions with microwave powers in the range of 0.6–1.9 mW.*

Given the unexpected impact of glycerol in the measurements performed, the question is whether this effect is reproduced using alternative cryoprotectants. From **Figure 4.1** it follows that the borate and CAPS buffers yield, respectively, the highest and lowest change upon addition of glycerol. **Figure 4.2** highlights the comparison between the X-band CW-EPR spectra of frozen solutions of ferric myoglobin prepared in borate and CAPS buffers, in the presence of 20 % (v/v) glycerol, 20 % (v/v) ethylene glycol, 0.36 M sucrose or 0.36 M trehalose. Clearly, all chosen glassing agents prevent the formation of the LS OH^--ligated Mb adduct in the borate buffer (**Figure 4.2**, left). In contrast, the LS contribution remains dominant independent of the cryoprotectant used for the CAPS buffer, even though the HS to LS ratio is not constant in the different samples (**Figure 4.2**, right, principal *g* values are reported in **Table 4.2**).

		Species	g_x^{eff}	g_y^{eff}	g_z^{eff}	g_z	g_y	g_x	%
Borate	Ethylene Glycol 20 %	HS	5.911	5.911	1.999				100
	Sucrose 0.36 M	HS	5.910	5.910	2.000				100
	Trehalose 0.36 M	HS	5.910	5.910	2.000				100
CAPS	Ethylene Glycol 20 %	LS				2.588	2.167	1.846	100
	Sucrose 0.36 M	HS	5.910	5.910	2.001				11
		LS				2.590	2.167	1.844	89
	Trehalose 0.36 M	HS	5.910	5.910	2.000				5
		LS				2.597	2.166	1.840	95

Table 4.2 *Principal g values obtained by the simulations of X-band CW-EPR spectra of myoglobin in Borate and CAPS buffers in presence of alternative cryoprotectants % contributions were determined by adding each species with its corresponding weight in the final simulation (weights determined using EasySpin software* [188]*). Error margins: ± 0.005 for g values of HS, ± 0.001 for g values of LS, ± 1% for contributions.*

Finally, the cryoprotectants were tested for their effectiveness as glassing agents, by comparing the CW-EPR linewidth of the OH^--ligated myoglobin and the 2-pulse echo decay. In the case of glycine, CAPS and CHES buffers, the CW-EPR spectra of myoglobin in presence of the chosen cryoprotectants show clear differences in spectral linewidth. In particular, the narrowest lines are obtained with ethylene glycol, followed - in order - by glycerol, sucrose and trehalose (**Figure 4.3** and **Figure A.3**). For the samples prepared in carbonate–bicarbonate buffer, only glycerol and ethylene glycol allow the formation of the OH^--ligated LS species to some extent, while the addition of sucrose or trehalose does not cause any significant change from the sample prepared without cryoprotectant (**Figure A.4**). The CW-EPR results are furthermore corroborated by the differences observed in the exponential decay of a two-pulse electron spin echo (**Figure 4.4**), measured at the magnetic field position agreeing with $g = g_z$ for the sample of myoglobin in CAPS

buffer with the different cryoprotectants. The T_m values obtained from curve-fitting (**Figure A.5**) are presented in **Table A.1** . The highest T_m, which reflects the narrowest line in the CW-EPR, is given by the addition of ethylene glycol. On the opposite side, sucrose appears to be the least efficient glassing agent, different from what is observed in the CW-EPR spectrum, where the least resolved line is given by trehalose.

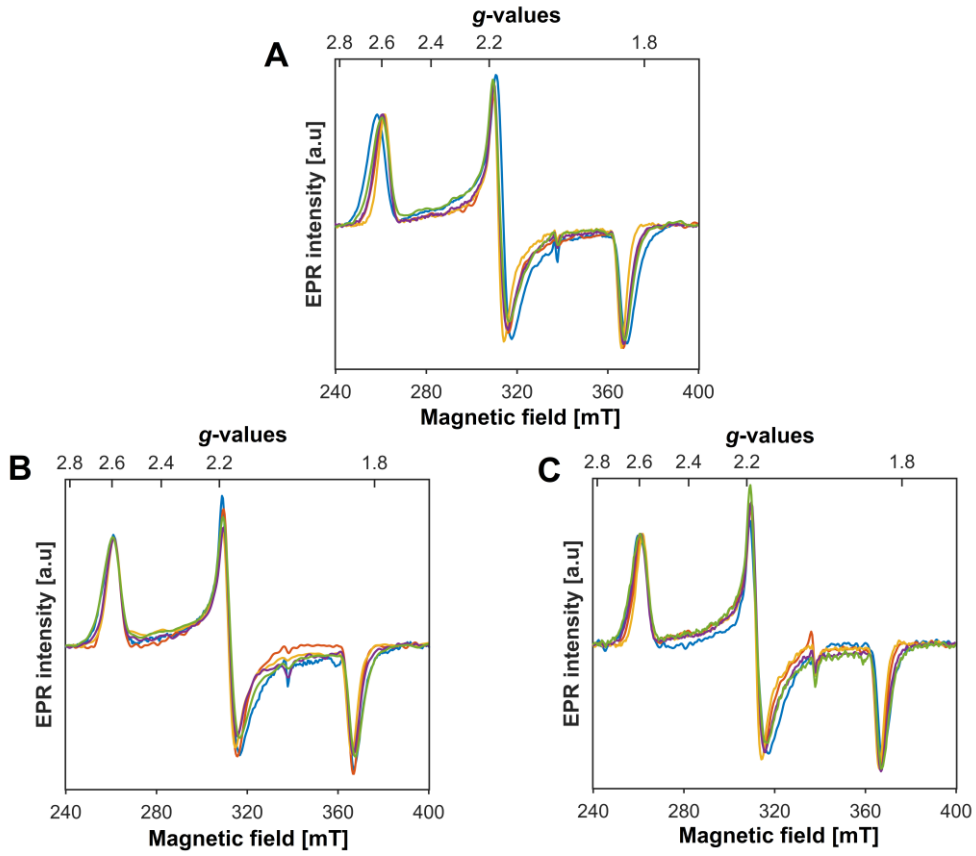

Figure 4.3 *X-band CW-EPR spectra of OH^--ligated LS of myoglobin samples prepared in **A)** glycine, **B)** CAPS and **C)** CHES buffer, respectively, in the presence of different glassing agents. Spectra were recorded under non-saturating conditions with a microwave power of ~ 0.3 mW. Plots are normalized at the centre of the g_z line. Cyan: no cryoprotectant added; red: 20 % glycerol; dark yellow: 20 % ethylene glycol; purple: 0.36 M sucrose; green: 0.36 M trehalose.*

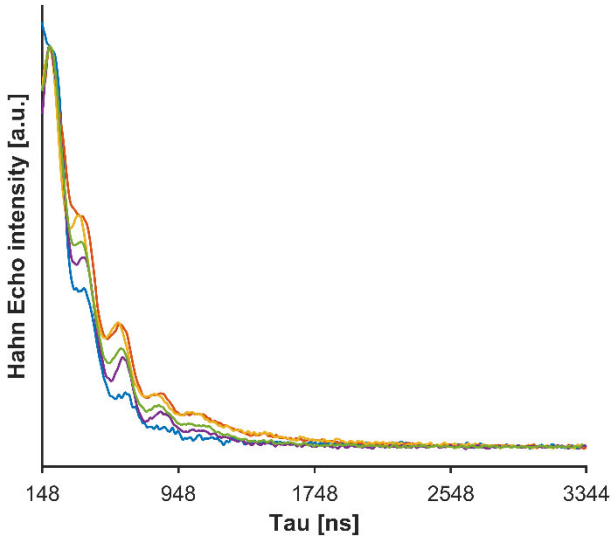

Figure 4.4 *X-band 2-pulse spin echo decay of myoglobin samples prepared in CAPS buffer with different cryoprotectants, measured at the g_z position. Cyan: no cryoprotectant added; red: 20 % glycerol; dark yellow: 20 % ethylene glycol; purple: 0.36 M sucrose; green: 0.36 M trehalose. Spectra were normalized at τ = 192 ns. $t_{\pi/2}$ and t_π were adjusted for each sample to minimize the echo modulation. No cryoprotectant: 50/100 ns; 20 % glycerol: 96/192 ns; 20 % ethylene glycol: 96/192 ns; 0.36 M sucrose: 80/160 ns; 0.36 M trehalose: 96/192 ns. The differences in pulse length do not affect the spin echo decay (see* ***Figure A.6*** *for details).*

In an attempt to better understand the effects observed in the EPR spectrum and relate them to concomitant effects on pH, freezing or interaction with the heme iron, samples of ferric myoglobin in the different alkaline buffers without or in presence of cryoprotectant were investigated at room temperature by means of UV–visible absorption spectroscopy. As a reference, an additional sample of myoglobin was prepared in a HEPES buffer at pH 7. The obtained optical absorption spectra are depicted in **Figure 4.5**. At neutral pH the typical bands of aquomet-myoglobin can be observed (Soret: 409 nm, Q-bands: 503 and 536 nm, CT band: 636 nm), in good agreement with data reported in earlier studies [185, 189, 190]. The spectra of ferric myoglobin at alkaline pH present a red-shifted Soret peak (413 nm) with a shoulder at 483 nm and distinct Q-bands at 543 and 583 nm (shoulder at 593 nm). These features are independent of the chosen buffer and are consistent with a six-coordinated LS ferric heme iron [185, 190] deriving from the distal ligation of an OH^- group to the heme iron. Thus, it is clear that all the buffers selected for this work

allow myoglobin to undergo an alkaline transition at room temperature. The addition of 20 % (v/v) of glycerol induces evident spectral changes only in the sample prepared in borate buffer (**Figure A.7**), where a mixture of contributions due to HS and LS species is detected. A similar result is obtained when ethylene glycol is added to the same buffer; however, there are no visible changes in presence of sucrose or trehalose. Consistent with the EPR results, the UV–visible spectra of myoglobin in the other buffers are not affected by the addition of any of these compounds.

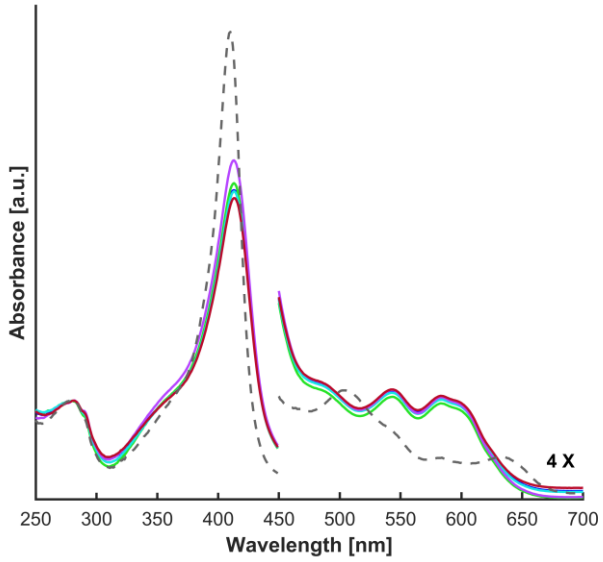

Figure 4.5 *UV–Vis absorption spectra of myoglobin in different buffers (theoretical pH 9.8–10) at room temperature. Blue: borate; green: glycine; cyan: carbonate–bicarbonate; purple: CAPS; red: CHES. The spectrum of myoglobin in 50 mM HEPES buffer pH 7 is reported in grey dashed line for comparison. For clarity, all the spectra are normalized to the absorption band at λ = 280 nm and inset is 4x-magnified.*

4.3.2 Buffering Capacity

EPR and UV–visible spectroscopy findings show that the pH of the selected buffers can be affected by either temperature or a direct interaction with the cryoprotectants. **Table 4.3** (top section) reports the pH of the different buffers, measured at room temperature, when glycerol is added to different final concentrations. It can be seen that the pH of the borate buffer is strongly affected by the addition of glycerol, with a drop of 1.5 units in the presence of only 5 % (v/v) of cryoprotectant and a further decrease until neutrality when glycerol is 30 % (v/v). Nonetheless, the other buffers are not significantly influenced by the presence of

this cryoprotectant. While carbonate appears to be the most stable, a decrease between 0.16 and 0.23 pH units in glycine, CAPS and CHES at the highest concentration of cryoprotectant could be attributed to the diminished buffering capacity due to dilution. Next, the pH of the buffers was measured in presence of ethylene glycol (20 % v/v), sucrose and trehalose (final concentration 0.36 M). The data in **Table 4.3** (bottom section) show that even in presence of these glassing agents the pH of the borate buffer is not stable, though the change is not as dramatic as with glycerol. On the other side, the pH of the other buffers is not significantly affected by the addition of either sucrose, trehalose or ethylene glycol at room temperature.

% Glycerol (v/v)	**pH**				
	Borate	**Glycine**	**Carbonate-Bicarbonate**	**CAPS**	**CHES**
0	9.99	9.92	9.96	9.88	10.13
5	8.69	9.92	9.96	9.85	10.11
10	8.11	9.86	9.96	9.79	10.08
15	7.75	9.83	9.96	9.74	10.05
20	7.48	9.80	9.96	9.70	10.02
30	7.04	9.75	9.96	9.65	9.97
Other glassing agents					
Buffer alone	10.00	10.40	10.36	9.80	10.53
20 % ethylene glycol (v/v)	8.91	10.38	10.60	9.80	10.46
0.36 M sucrose	9.38	10.34	10.24	9.82	10.46
0.36 M trehalose	9.50	10.37	10.24	9.80	10.51

Table 4.3 *pH changes of different alkaline buffers upon addition of glycerol and other cryoprotectants. Error margin of ± 0.01 pH units.*

4.4 Discussion

In this work, we observed the effects of particular combinations of buffer and cryoprotectant on the EPR spectra of myoglobin samples prepared at high pH. Our findings can be summarized as follows:

pH Effects. The first and plain observation is that a chemical reactivity with the cryoprotectant can substantially alter the pH of specific buffers, as it happens in the case of borate buffer. Boric acid is known to react with glycerol to form a boron–chelate complex, which increases the acidity of the solution [191, 192]. Our pH measurements are in good agreement with this evidence and demonstrate that this reaction can also occur, to a lesser extent, with different polyols such as ethylene glycol, sucrose and trehalose. When the pH is lowered from 10.0 to 8.91 in the presence of ethylene glycol (**Table 4.3**, bottom section), a mixture of high-spin and low-spin myoglobin is observed with UV–visible absorption spectroscopy. The minor decreases to 9.38 and 9.50, induced by sucrose and trehalose, still allow the protein to adopt a complete low-spin configuration (**Figure A.6**), as expected from the known pK_a value of the alkaline transition of myoglobin (~ 8.9) [178, 182, 183].

Temperature Effects. The EPR signals of the same samples were apparently inconsistent with UV–visible spectroscopy results, as we could not observe any LS OH^--ligated heme species no matter which cryoprotectant was added to the borate buffer (**Figure 4.2**, left panel). This indicates an additional influence of temperature on the pH stability of this buffer, which could also explain the complete absence of the EPR signal due to the LS species in the spectrum of myoglobin in carbonate–bicarbonate buffer (**Figure 4.1c**, left panel). The pH variation of common biological buffers upon freezing has been extensively described in the literature [193–195]. In particular, Orii and Morita, monitoring colour changes in pH-sensitives dyes, observed that even a minimum amount of glycerol (5 %) caused the pH of borate buffer to decrease from 8.5 to a value between 6.3 and 6.8 at room temperature, but this effect was dramatically enhanced by freezing, since they measured a pH drop to a value of 2–3. The same authors reported a similar evidence with a carbonate–bicarbonate buffer, whose pH was observed to decrease of more than 3 units upon freezing. Nonetheless, the addition of glycerol to this buffer had the opposite effect, as it was able to inhibit the pH drop to some extent [193]. The latter observation is consistent with the presence of a minor contribution from the OH^- LS species in the spectrum of myoglobin in the carbonate–bicarbonate buffer when 20 % (v/v) of glycerol or ethylene glycol is added to the sample (**Figure 4.1c**, right panel and **Figure A.2**). Finally, a temperature effect on CAPS and CHES buffers, though less severe in comparison with the above-mentioned buffers, should not be excluded. This speculation is supported by the presence of a residual HS signal in these

samples (**Figure 4.1d & e**, left panel) which suggests a modest pH decrease at the cryogenic temperature. It has been reported that the pH of CAPS can decrease about 1 unit upon freezing, opposite to other Good's buffers, which tend to increase their pH [193, 196]. Our findings suggest that the decrease in pH for CHES is even more pronounced than for CAPS; however, to our knowledge no information is reported about this particular buffer system.

Interactions with the Protein. On a different note, the chemical structure of the buffer molecule and its physical interactions either with the protein moiety or with the cryoprotectant might be responsible for some observations in the EPR spectra of the samples prepared in glycine and borate buffers. Being small molecules, glycine and borate can likely enter the heme pocket of myoglobin and both are expected to be mainly negatively charged at pH ~ 10 (pK_a of glycine α-amino group ~ 9.6 [197], pK_a of boric acid ~ 9.24 [198]). Therefore, it is possible that some of these charged molecules sitting close to the heme would influence the overall electronic distribution of the spin system, even without directly coordinating the iron [199], which would probably result in a consistent variation of the *g* values. In the EPR spectra of myoglobin in glycine buffer, a reduction in the *g* anisotropy occurs if any of the cryoprotectants is added, with the major shift observed in presence of ethylene glycol (**Figure 4.3**, **Figure A.1** and **Figure A.3**). Moreover, in the absence of cryoprotectant, the *g* values of alkaline myoglobin in the glycine buffer are similar to the ones of the sample prepared in the borate buffer, but differ from the ones of samples prepared in CAPS or CHES (**Table 4.1**), which is consistent with the latter being bigger molecules unable to approach the heme site. The small variations in the *g* values could be also attributed to a change in the dielectric constant of the solvent, a factor which could be likely affected by the addition of a cryoprotectant.

Effectiveness of the Cryoprotectant. Finally, we evaluated the efficiency of the chosen cryoprotectants as actual glassing agents. To do so, we first compared the linewidth of the OH^- low-spin features in the myoglobin samples prepared in presence of the different cryoprotectants (**Figure 4.3** and **Figure A.3**). A trend can be recognized for all the tested buffers, where ethylene glycol gives the most resolved signals, followed by glycerol and sucrose which have similar effects. When trehalose is employed, the strain is greater and close to the sample prepared in the absence of cryoprotectant, indicating the poor efficacy of this substance as a glassing agent, notwithstanding its structure being similar to sucrose. Phase memory times measurements are in line with CW-EPR results, pointing out ethylene glycol as the most effective cryoprotectant, in terms of glass formation, among the substances employed in this study.

4.5 Conclusions

In spectroscopic experiments, it is crucial to distinguish the results attributable to a certain experimental condition from those due to the intrinsic properties of the examined system. This work is intended to highlight the need of tailoring the procedural setup when performing EPR experiments on (heme) proteins, to identify possible artefacts. To this regard, by investigating the well-characterized myoglobin, we show a non-negligible relationship between multiple external factors such as pH, buffer composition, temperature and the addition of a cryoprotectant to the sample. Notably, our results corroborate many effects already observed and reported scattered in literature, but insufficiently tested in a systematic way in the context of EPR spectroscopy. In brief, we show that (i) borate buffer has a propensity to react with glycerol and polyols in general with a consequent lowering of the pH, so it should be avoided if such cryoprotectants are needed; (ii) some high-pH buffers, such as carbonate–bicarbonate buffer, undergo dramatic pH change upon freezing, preventing the observation of expected alkaline transitions; (iii) small buffer molecules can affect the heme environment as it happens in the case of glycine and borate; (iv) in the chosen set of cryoprotectants, ethylene glycol forms the best glass for low-temperature EPR experiments.

Chapter 5

Heme coordination patterns in chlorite dismutases

Abstract

Chlorite dismutases are heme *b*-containing oxidoreductases that can decompose chlorite to chloride and molecular oxygen. They are divided in two clades that differ in oligomerization, subunit architecture, and the hydrogen-bonding network of the distal catalytic arginine, which is proposed to switch between two conformations during turnover. To understand the impact of the conformational dynamics of this basic amino acid on heme coordination, structure, and catalysis, Cld from *Cyanothece* sp. PCC7425 (*C*Cld) was used as a model enzyme. As typical for a clade II Cld, its distal arginine 127 (R127) is hydrogen-bonded to glutamine 74 (Q74). The latter has been exchanged with either glutamate (Q74E) to arrest R127 in a salt bridge or valine (Q74V) that mirrors the setting in clade I Clds. In this Chapter EPR spectroscopy is used to investigate the heme coordination in the wild-type form of *C*Cld and the variants mentioned above; the EPR spectra of a representative from clade I are also presented for comparison. The results are integrated with a discussion on the findings obtained from other techniques performed by our collaborators at the BOKU university of Vienna. All together, the data suggest that the conformational dynamics of R127 has a significant role in heme coordination during the alkaline transition of *C*Cld and in the thermal stability of the heme cavity, whereas its impact on the catalytic efficiency of chlorite degradation is relatively small.

Redrafted after: Daniel Schmidt*, **Ilenia Serra***, Georg Mlynek, Vera Pfanzagl, Stefan Hofbauer, Paul G. Furtmüller, Kristina Djinović-Carugo, Sabine Van Doorslaer, and Christian Obinger (2021) Arresting the Catalytic Arginine in Chlorite Dismutases: Impact on Heme Coordination, Thermal Stability, and Catalysis, *Biochemistry* 60 (8), 621-634 (*D.S. and I.S. contributed equally to this work)

Own contribution: acquisition, analysis and interpretation of EPR data; writing of paper manuscript

5.1 Introduction

Chlorite dismutases (Clds, EC 1.13.11.49) are heme *b*-containing oxidoreductases found exclusively in prokaryotic organisms [72, 200]. They belong to the structural superfamily of porphyrin-binding dimeric α + β barrel proteins that typically show a high degree of functional diversity. Clds convert chlorite (ClO_2^-) to chloride (Cl^-) and dioxygen, therefore being of interest for biotechnological and bioremediation applications [72, 200]. The formation of an oxygen–oxygen bond during turnover constitutes an unusual biochemical reaction that otherwise is performed by only the water-splitting manganese complex of photosystem II in oxygenic organisms and an enzyme from an anaerobic methane-oxidizing bacterium [62]. The main structural and biochemical features of Clds have been extensively discussed in Chapter 1 and they will not be treated in detail in this section.

Briefly, chlorite dismutases are divided into two lineages denoted as clade I ("long Clds") and clade II ("short Clds"). In the ferric resting state, the heme iron of Clds is ligated by a proximal histidine (H114 in *C*Cld) and a distal water [55]. The only charged amino acid in the hydrophobic distal heme cavity is a fully conserved arginine (R127 in *C*Cld), which is proposed to be flexible and to switch between two conformations during catalysis, *i.e.*, pointing toward either the heme iron ("in") or the substrate entry channel ("out") [53, 55, 56, 59, 65, 67]. Importantly, the hydrogen-bonding network of this catalytic arginine is different in clade I and clade II Clds. In clade II Clds, R127 is H-bonded to Q74 located on a flexible α-helical loop (**Figure 1.5 D**), which in general connects the N-terminal and C-terminal ferredoxin-like domains in porphyrin-binding α + β barrel proteins [67]. By contrast, in clade I Clds the corresponding residue turns away from the arginine due to a different conformation of this loop. The conserved arginine has been the center of numerous structural and functional studies for its putative involvement in substrate recognition and/or in preventing irreversible enzyme inactivation [57, 58, 65]. It has been postulated that this basic residue supports the (either heterolytic or homolytic) cleavage of chlorite and the recombination reaction between the postulated transient intermediates (hypochlorite and Compound I or chlorine monoxide and Compound II) [55, 65, 72, 200] and dictates the pronounced pH dependence of chlorite degradation [58, 181]. In the crystal structure of *C*Cld, in the resting state the heme iron participates in a distal H-bonding network that includes the metal ion, two water molecules, R127 in the "out" conformation, and Q74 [55]. At alkaline pH, deprotonation of the water molecule at the distal side causes a rearrangement of the overall H-bonding network in the heme proximity. It was hypothesized that this alkaline transition might contribute to the pronounced pH dependence of chlorite degradation activity, which significantly decreases at alkaline pH [54, 56–58, 60, 72, 181, 200].

CW-EPR spectroscopy results provided insights into the heme coordination of wild-type *C*Cld and the variants Q74V and Q74E, where the flexibility of R127 was either enhanced by breaking the hydrogen-bond to the glutamine Q74 or restricted by imposing a salt bridge with a glutamate residue. An alkaline transition due to the coordination of an OH^- group to the heme iron was detected by performing EPR measurement at different pH values. The alkaline transition correlated with a decrease in the enzymatic activity. The flexibility of R127 was found to have an impact in the alkaline transition of *C*Cld, suggesting a possible role in substrate binding. Besides heme coordination, the mutations were shown to have a strong impact on the thermal stability of the heme cavity but only a weak effect on the chlorite degradation activity. Finally, a representative of clade I chlorite dismutase from *Candidatus "Nitrospira defluvii"* (*Nd*Cld) was also investigated by CW-EPR spectroscopy at neutral pH. The effects of the addition of 20 % (v/v) glycerol to the sample were briefly discussed.

5.2 Experimental procedures

This section will include exclusively the details of the EPR spectroscopy experiments. For further information on the other techniques used in this work, the reader is referred to [201].

5.2.1 EPR spectroscopy

CW-EPR spectroscopy measurements were performed to assess the spin state of ferric wild-type forms of *Nd*Cld and *C*Cld as well as the Q74V and Q74E variants and to investigate pH-induced changes in the local environment of the heme iron. To maintain the consistency with other spectroscopic and biochemical assays, the EPR samples of *Nd*Cld and *C*Cld were prepared in the same (or most similar) buffers used for the other experiments described in this work. Samples of wild-type *Nd*Cld were prepared at a concentration of 400 µM in 50 mM HEPES buffer (pH 7.0), in 50 mM MES buffer (pH 5.5), and in 50 mM borate buffer (pH 10.0). Solutions of wild-type *C*Cld, Q74V, and Q74E were prepared in a 50 mM sodium phosphate-citrate buffer mixture (pH 5.0), 50 mM sodium phosphate (sodium phosphate monobasic-dibasic mixture) (pH 7.0), 50 mM sodium-phosphate-borate buffer mixture (pH 9.0), and 50 mM borate buffer (pH 10.0) at a concentration of ~400 µM. To check the effect of a potential pH change upon freezing on EPR signatures, the EPR spectra of wild-type *Nd*Cld and *C*Cld at pH 7 were also recorded in a "temperature-independent" buffer (45% HEPES and 55% sodium phosphate [195]), and no significant changes were observed (data not shown). The influence of the cryoprotectant glycerol on

the EPR spectra of wild-type *Nd*Cld and *C*Cld was tested at neutral pH. In the quartz EPR tubes (diameter of 4 mm) containing the samples, the excess of paramagnetic O_2 was removed in several freeze–pump–thaw cycles prior to the starting of the EPR experiment and all tubes were vacuum-pumped during the measurements. X-Band CW-EPR experiments were performed on a Bruker ESP300E spectrometer equipped with a liquid helium cryostat (Oxford Inc.) and operating at a microwave frequency of ~ 9.44 GHz. Spectra were recorded at 10 K, under non-saturating conditions at microwave powers in the range of 2–5 mW, a modulation frequency of 100 kHz, and a modulation amplitude of 1 mT. Simulations of experimental spectra were performed with EasySpin software implemented in MATLAB [188].

5.3 Results

5.3.1 Altering R127 flexibility by site-directed mutagenesis

In this study we aimed at investigating the impact of the flexibility of the conserved arginine 127 on several enzyme properties. The variants Q74V and Q74E were obtained by site-directed mutagenesis. The Q74V variant was produced to mimic the more open and flexible configuration of clade I Clds by substituting the H-bonding glutamine 74 with a valine. On the other hand, in the Q74E mutant, the arginine is more constrained than in the wild-type *C*Cld, since it forms a salt bridge with a glutamate. The structure of the *C*Cld variants Q74V and Q74E were resolved by X-ray crystallography. For the experimental details and in-depth description of the structures, the reader is referred to [201]. Here, the main structural differences are shortly presented to aid the reader in the understanding of the spectroscopic results discussed later.

The X-ray crystal structure of ferric wild-type *C*Cld was already determined under various conditions, *i.e.*, at pH 6.5 and 8.5, and with soaked-in distal ligands (F^- and SCN^-) at pH 6.5 [55]. In all available *C*Cld structures, the (putatively) flexible arginine (R127) is present in the "out" conformation, *i.e.*, pointing toward the substrate entry channel. This conformation is stabilized by a hydrogen bond to glutamine 74 (Q74), which is in the proximity of R127 (2.85 Å) [55]. Similar to the wild-type *C*Cld, variants Q74V and Q74E are dimers in which each subunit binds one heme *b*. The structure consists of a ferredoxin-like fold that is defined by five α-helices along with a β-barrel composed of three-stranded and five-stranded antiparallel β-sheets. Histidine 114 serves as the fifth heme ligand on the proximal side, with the $N_\varepsilon 2$ atom being 2.15 Å from the heme iron in both structures (**Figure**

5.1). On the distal side, a H_2O molecule is situated above the heme iron at a distance of 2.6 Å. The conformation of the distal arginine was significantly affected by exchange of Q74. While in Q74E (pH 6.5) R127 adopts a nearly identical ("out") conformation as in wild-type *C*Cld [55] (**Figure 5.1 A, B**), in Q74V (pH 8.5) it is pointing toward the heme iron (**Figure 5.1 C**).

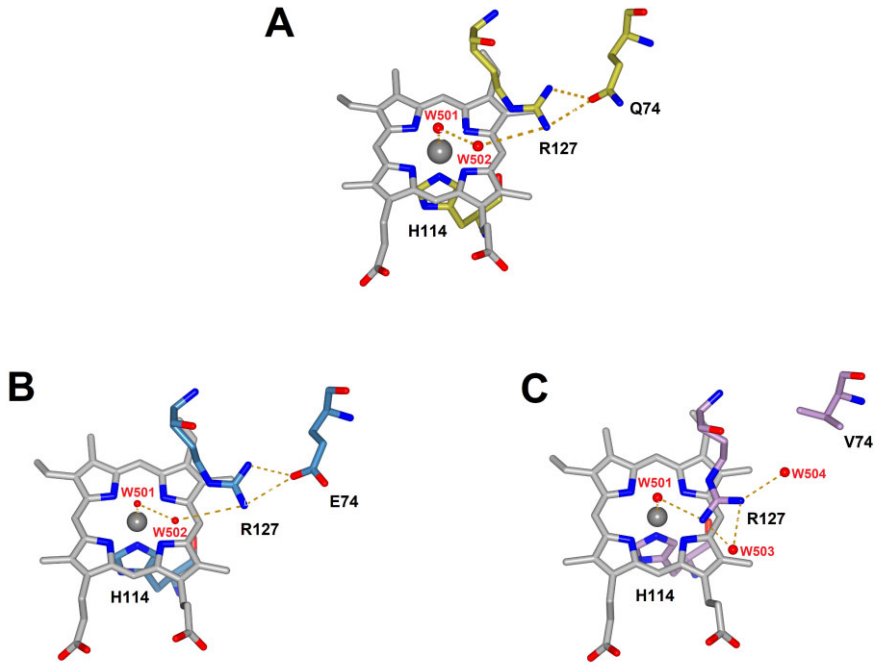

Figure 5.1 *Active site architecture of CCld* ***(A)*** *wild-type,* ***(B)*** *Q74E and* ***(C)*** *Q74V variants. Q74E depicts an almost identical conformation compared to the wild-type structure, while Q74V shows a conformational change to the "in" conformation. Bonds are depicted as yellow dashed lines. Highly conserved H114 serves as the fifth heme ligand on the proximal side. Figures were made with CCP4mg v 2.10.10. PDB accession codes: 5MAU (wild-type), 7ASB (Q74E) and 7ATI (Q74V).*

5.3.2 pH dependence of *C*Cld heme coordination

Optical and electronic circular dichroism (ECD) spectroscopies were used to investigate the electronic configuration of the ferric wild-type *C*Cld and variants Q74V and Q74E. For the details of the results, which are only summarized here, the reader is referred to [201]. The far-UV ECD spectra (200–260 nm) of wild-type *C*Cld and the two variants are very similar, suggesting that the overall secondary structure has not been altered by the inserted mutations. While the far-UV ECD

shows no significant differences in the pH range 5.0-9.0, the ECD spectra in the visible region are strongly dependent on pH. At pH 5, the Soret bands exhibit a positive ellipticity with similar maxima in all the three proteins. By increasing the pH, the Soret maxima of the wild-type and Q74V variant undergo a pronounced red-shift, while in the Q74E variant this change occurs to a lesser extent (see Figure S1A and S1B in the original paper [201]). At pH 5.0, the UV-visible absorption spectrum of wild-type *C*Cld is that of a ferric high-spin species, with a Soret band at 406 nm, Q-bands at 502, 535, and 575 nm, and a CT band at 635 nm. Under more alkaline conditions, a distinct shift to a low-spin form is observed. The Soret band is shifted to 414 nm, and Q-bands at 540 and 575 nm and a weak CT band at 610 nm appear (**Figure 5.2 A**). These spectral properties are found in all *C*Cld variants investigated in this study and are consistent with previously reported data for the wild-type enzyme [54, 55]. Interestingly, while the spectral changes of the observed alkaline transition (*i.e.*, deprotonation of distal water) are similar, the calculated pK_a values differ significantly from that of wild-type *C*Cld (pK_a = 8.11 ± 0.36) with a pK_a of 7.41 ± 0.24 for Q74V and a pK_a of 9.33 ± 0.29 for Q74E (**Figure 5.2 B**).

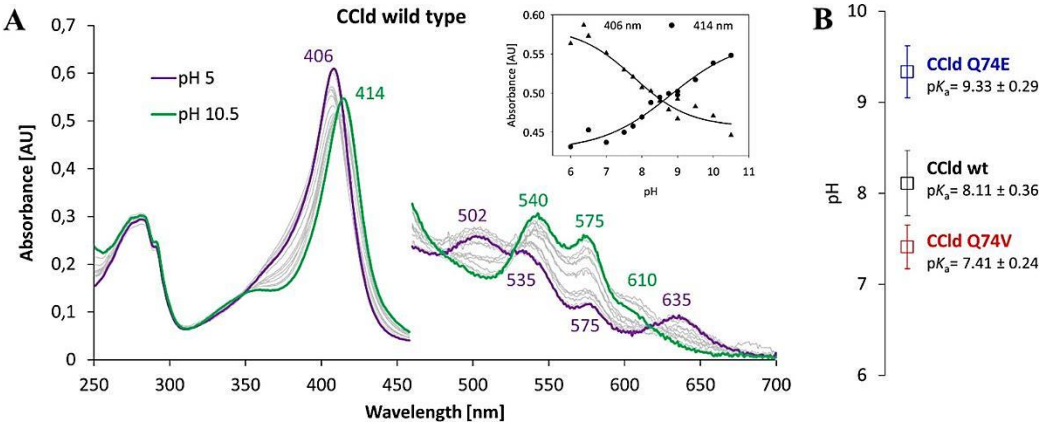

Figure 5.2 *pH-dependent UV–vis spectral changes of wild-type CCld and variants Q74V and Q74E.* ***(A)*** *UV–vis spectra of wild-type CCld in the pH range of 5.0–10.5. The enzyme concentration was 5 µM. Very similar spectra were obtained for both variants [200]. For better visualization of the CT bands and Q-bands, the spectra in the wavelength range between 460 and 700 nm are magnified 6-fold. The inset shows an increase and a decrease in absorbance at 406 and 414 nm, respectively, with a change in pH. The sigmoidal fit is shown as a black line.* ***(B)*** *Differences in pK_a values of the alkaline transition between wild-type CCld and variants.*

A comprehensive EPR analysis with particular attention to pH-induced changes, provided novel information about the amino-acid environment at the heme site in clade II Clds. In high-spin (S = 5/2) ferric heme proteins, a very large zero-field splitting (ZFS) is responsible for the typical CW-EPR spectral shape observed at X-band. Because the ZFS is much larger than the photon energy of the microwaves used, only transitions in the first Kramers doublet (m_s = ±1/2) can be detected. For this reason, EPR spectra of these proteins can be simulated either as effective S = 1/2 systems, using a $\boldsymbol{g}^{\mathrm{eff}}$ tensor, where g_x^{eff} and g_y^{eff} are symmetrically split at ~ 6 and g_z^{eff} is close to 2, or as real S = 5/2 systems, where the $\boldsymbol{g}$ tensor is almost isotropic with principal values close to 2, and the observed features depend essentially on the E/D ratio between the rhombic (E) and tetragonal (D) zero-field splitting parameters (Chapter 2, section 2.3.2.5.) In this study, both simulation methods were used to obtain a complete picture of the systems under investigation. If a strong base is present at the sixth distal coordination position, the iron spin converts to the low-spin state (S = 1/2). In this case, the principal g values can be taken as a fingerprint and can be compared with those of other LS hexacoordinated heme systems in an attempt to identify the nature of the distal ligand. The EPR spectra of wild-type *C*Cld at different pH values are shown in **Figure 5.3 A**. In a manner consistent with previously published results [54], the spectrum of *C*Cld at pH 7.0 is composed of two components due to high-spin heme centers (HS1 and HS2) and a smaller low-spin contribution of uncertain origin (LS1) (EPR parameters used for the simulation are reported in). The most dominant spectral contribution (HS1) is characterized by a near-axial effective $\boldsymbol{g}$ tensor ($g_x^{\mathrm{eff}} \approx g_y^{\mathrm{eff}}$) and concomitant very small E/D value. No significant variations are observed when *C*Cld is brought to acidic pH (**Figure 5.3 A**, top), while a trend becomes evident when the pH is increased to 10 (**Figure 5.3 A**, bottom). An alkaline transition is partially observed at pH 9.0, when the appearance of new low-spin features is accompanied by a change in the high-spin component, from axial to rhombic $\boldsymbol{g}^{\mathrm{eff}}$ tensor. At pH 10.0, two main low-spin species, denoted as LS1-alkaline and LS2-alkaline, are nicely resolved and the leftover high-spin (~ 25 %) is found to be completely rhombic (HS3). The principal g values of the low-spin components are typical of an OH^- coordination of the heme iron at the sixth position on the distal site [48, 49, 61, 148].

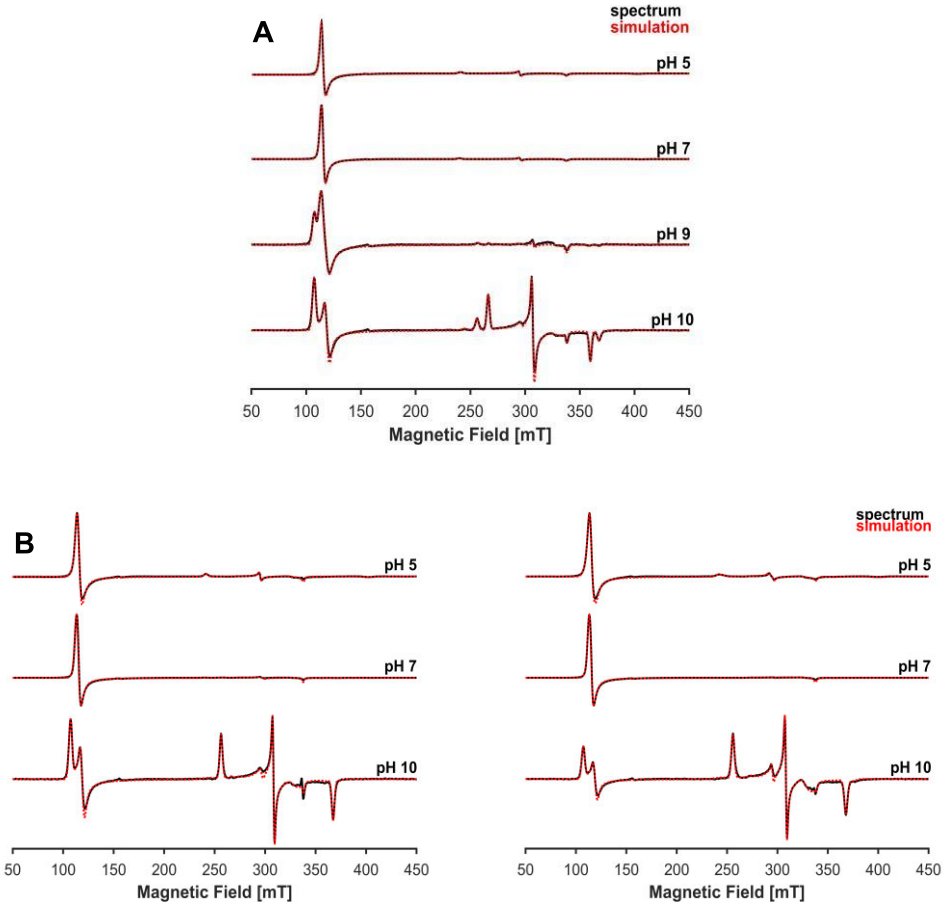

Figure 5.3 *pH dependence of the X-band CW-EPR spectrum of wild-type CCld and variants Q74V and Q74E. Samples were prepared in 50 mM phosphate-citrate buffer (pH 5.0), 50 mM phosphate buffer (pH 7.0), 50 mM phosphate-borate buffer (pH 9.0), and 50 mM borate buffer (pH 10.0). A microwave power of 2 mW was applied to record the spectra. Solid black for the experimental spectrum, dashed red for the simulation.* ***(A)*** *Wild-type CCld and* ***(B)*** *Q74E (left) and Q74V (right).*

	Species	g_x^{eff}	g_y^{eff}	g_z^{eff}	g_x	g_y	g_z	*E/D*	*%*
pH 5	HS1	5.92	5.84	2.00	1.96	1.96	2.00	0.002	53
	HS2	6.09	5.68	1.99	1.96	1.96	2.00	0.009	19
	LS1				1.67	2.28	2.80	-	28
pH 7	HS1	5.90	5.86	2.00	1.96	1.96	2.00	< 0.001	63
	HS2	6.09	5.68	2.00	1.96	1.96	2.00	0.009	17
	LS1				1.66	2.28	2.81	-	20
pH 9	HS1	5.90	5.86	2.00	1.96	1.96	2.00	< 0.001	13
	HS2	6.03	5.69	2.00	1.95	1.95	2.00	0.007	22
	HS3	6.28	5.65	1.99	1.99	1.99	2.00	0.013	47
	LS1-alkaline				1.88	2.26	2.53	-	7
	LS2-alkaline				1.83	2.19	2.63	-	11
pH 10	HS3	6.29	5.66	1.99	1.99	1.99	2.00	0.013	25
	LS1-alkaline				1.87	2.20	2.53	-	46
	LS2-alkaline				1.83	2.19	2.63	-	23
	LS3-alkaline				1.80	2.27	2.75	-	6

Table 5.1 *EPR simulation parameters of wild-type CCld at different pH values. Errors in g values of ±0.01, errors in E/D ratios of ±0.001, and errors in contributions of ±1%.*

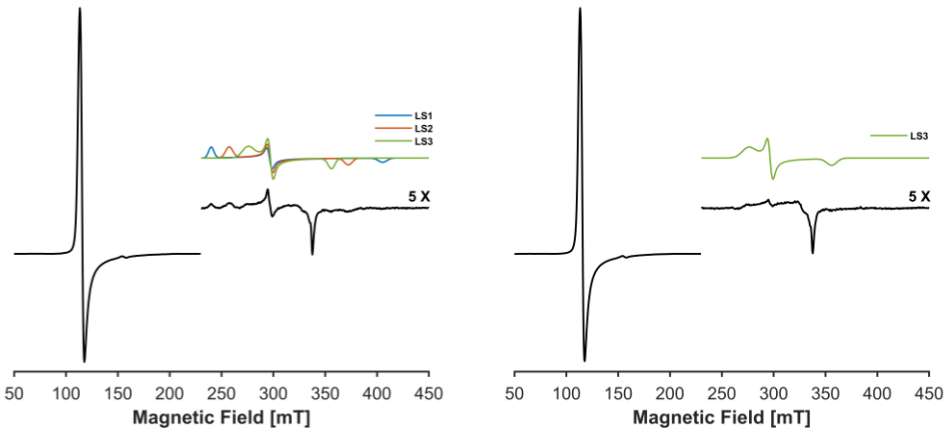

Figure 5.4 *X-band CW-EPR spectra of Q74E (left) and Q74V (right) variants of CCld, at neutral pH. Samples were prepared in 50 mM phosphate buffer, pH 7.0; a microwave power of 2 mW was applied to record the spectra. For clarity, insets of the high-field region are 5x-magnified and single low-spin species obtained from simulations are shown according to color legend.*

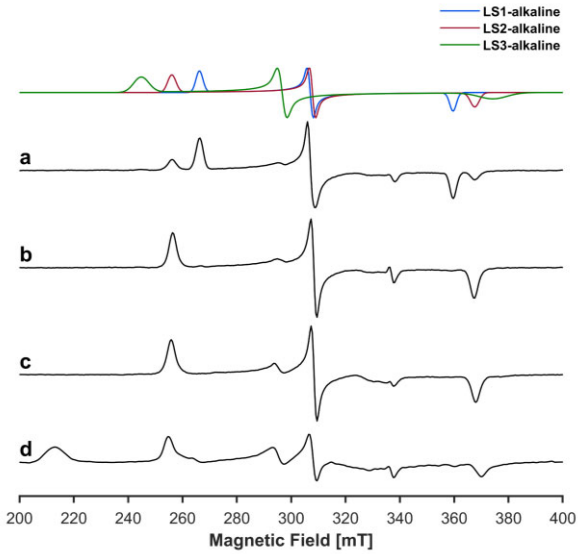

Figure 5.5 *X-band CW-EPR spectra (low-spin region only) of* ***(a)*** *wild-type CCld,* ***(b)*** *Q74E,* ***(c)*** *Q74V and* ***(d)*** *NdCld in 50 mM borate buffer, pH 10. Solid black: experimental spectrum; single species obtained from simulations of wild-type CCld are shown according to color legend. The broad feature at ~ 210 mT in the spectrum of NdCld (trace d) arises from the contribution of the low-spin species already observed at neutral pH (LS1' and LS2',* ***Table*** **5.3***).*

At pH 7.0, the EPR spectra of variants Q74E and Q74V largely resemble that of the wild-type protein (**Figure 5.3** and **Figure 5.4**) and can be simulated with similar parameters (**Table 5.1**). In addition, Q74E shows the presence of small contributions from three different low-spin components, while in the spectrum of Q74V, a single weak low-spin signal is barely observed (**Figure 5.4**). Remarkably, when the two proteins are measured at pH 5.0 (**Figure 5.3B**, top), a contribution of the same low-spin species found in the wild-type protein (LS1) is detected. In all three proteins, the spectral contribution of this species accounts for ~ 30 % of the total EPR spectrum. At pH 10.0, the dominant low-spin component in the variants has the same *g* values as LS2-alkaline, while this was less abundant than LS1-alkaline in the wild-type case (**Figure 5.3 B** and **Figure 5.5**). Furthermore, similar to wild-type *C*Cld, an axial-to-rhombic conversion occurs for the high-spin state of both Q74E and Q74V when the pH is increased (**Figure 5.3 B**). Overall, these data indicate that the site-directed mutation of the glutamine does not substantially perturb the spin state of the heme iron in the resting state of *C*Cld. In addition, the EPR findings corroborate the pH-dependent trend observed by UV–vis absorption spectroscopy and resonance Raman spectroscopy of wild-type *C*Cld [55].

	Species	g_x^{eff}	g_y^{eff}	g_z^{eff}	g_x	g_y	g_z	*E/D*	*%*
Q74E									
pH 5	HS1	5.92	5.83	2.00	1.96	1.96	2.00	0.002	48
	HS2	6.14	5.69	2.00	1.97	1.97	2.00	0.010	22
	LS1				1.67	2.28	2.79	-	30
pH 7	HS1	5.91	5.89	2.00	1.96	1.96	2.00	0.002	68
	HS2	6.16	5.68	2.00	1.97	1.97	2.00	0.010	13
	LS1				1.66	2.28	2.81	-	7
	LS2				1.81	2.27	2.62	-	8
	LS3				1.89	2.27	2.45	-	4
pH 10	HS3	6.29	5.66	1.99	1.99	1.99	2.00	0.013	24
	LS1-alkaline				1.88	2.20	2.53	-	1
	LS2-alkaline				1.83	2.19	2.63	-	65
	LS3-alkaline				1.82	2.27	2.75	-	10
Q74V									
pH 5	HS1	5.93	5.84	2.00	1.96	1.96	2.00	0.002	40
	HS2	6.15	5.68	1.99	1.97	1.97	2.00	0.010	23
	LS1				1.68	2.30	2.79	-	29
	LS2				1.89	2.28	2.72	-	8
pH 7	HS1	5.91	5.89	2.00	1.97	1.97	2.00	< 0.001	81
	HS2	6.16	5.68	2.00	1.97	1.97	2.00	0.010	16
	LS3				1.89	2.27	2.45	-	3
pH 10	HS3	6.29	5.66	1.99	1.99	1.99	2.00	0.013	14
	LS2-alkaline				1.83	2.19	2.64	-	75
	LS3-alkaline				1.80	2.28	2.75	-	11

Table 5.2 *EPR simulation parameters of Q74E and Q74V variants of CCld at different pH values. Errors: g values ±0.01, E/D ratio ±0.001, contribution ±1 %.*

5.3.3 Insights from a representative of clade I Clds

In the case of *Nd*Cld, at neutral pH the contributions due to high-spin hemes account for only ~ 23 % of the spectrum, which is instead dominated by a highly anisotropic low-spin signal (**Table 5.3**, simulations shown in **Figure 5.6**). It is interesting to note that in the alkaline spectrum of *Nd*Cld (**Figure 5.6**) the major low-spin species (excluding that already present at neutral pH) is characterized by *g* values close to those of LS2-alkaline (**Table 5.3**). This similarity with the Q74 *C*Cld variants is coherent with the absence of the conserved glutamine in *Nd*Cld, which would suggest that the positioning of the arginine has a role in determining the binding mode of hydroxide.

	Species	g_x^{eff}	g_y^{eff}	g_z^{eff}	g_x	g_y	g_z	***E/D***	***%***
	HS1'	5.87	5.87	1.98	1.96	1.96	1.98	< 0.001	< 1
	HS2'	6.17	5.52	1.99	1.95	1.95	2.00	0.014	21
pH 5.5	HS3'	6.47	5.28	1.98	1.96	1.96	2.00	0.026	2
	LS1'				1.24[a]	2.11	3.15	-	71
	LS2'				1.43[a]	2.25	2.98	-	5
	HS1'	5.89	5.89	1.98	1.97	1.97	1.98	0.002	1
	HS2'	6.17	5.52	1.99	1.95	1.95	2.00	0.014	20
pH 7	HS3'	6.47	5.29	1.99	1.96	1.96	2.00	0.025	2
	LS1'				1.24[a]	2.11	3.16	-	71
	LS2'				1.36[a]	2.26	3.01	-	6
	HS4'	6.18	5.75	2.00	1.99	1.99	2.00	0.009	7
	HS5'	6.35	5.54	1.99	1.98	1.98	2.00	0.017	2
	LS1'				1.27[a]	2.10	3.16	-	59
	LS2'				1.22[a]	2.28	3.05	-	6
pH 10	LS1'-alkaline				1.87	2.28	2.55	-	1
	LS2'-alkaline				1.82	2.19	2.65	-	21
	LS3'-alkaline				1.80	2.28	2.60	-	4

Table 5.3 *EPR simulation parameters of wild-type NdCld at different pH values. Errors: g values ±0.01, E/D ratio ±0.001, contribution ±1%.* [a)] *These values are calculated assuming* $g_x^2 + g_y^2 + g_z^2 \approx 16$.

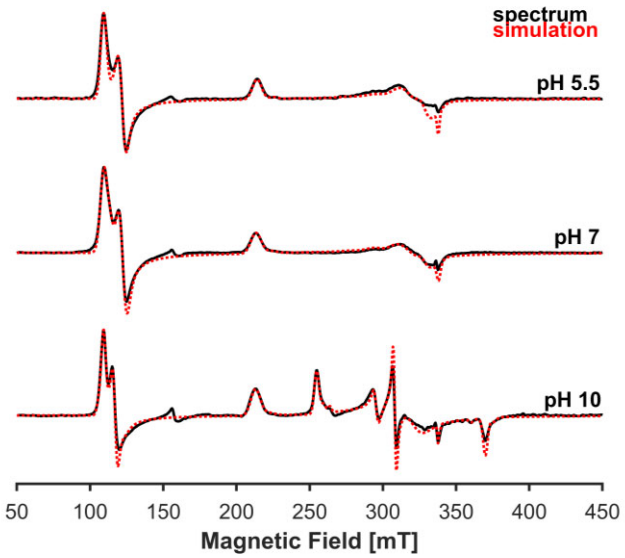

Figure 5.6 *X-band CW-EPR spectra of wild-type NdCld at acidic (top), neutral (middle) and alkaline pH (bottom). Samples were prepared in 50 mM MES buffer, pH 5.5, 50 mM HEPES buffer, pH 7, and 50 mM borate buffer pH 10; a microwave power of 5 mW was applied to record the spectra. Solid black: experimental spectrum, dashed red: simulation.*

5.3.4 The non-innocent role of glycerol in chlorite dismutase sample preparation

The restricted flexibility of the arginine in wild-type *C*Cld, compared to that of *Nd*Cld, might also be responsible for the different behavior of the two proteins in the presence of glycerol, at least at neutral pH. As depicted in **Figure 5.7**, the addition of 20 % (v/v) glycerol causes dramatic changes in the low-field part of the spectrum of *Nd*Cld (contributions of high-spin species), which now reveals a species with increased rhombicity and a well-resolved axial component. On the contrary, the spectrum of *C*Cld is scarcely affected by this compound, suggesting that the active site of this enzyme is less prone to accommodating the glycerol molecule. In Chapter 4, we discussed the effects of using particular combinations of buffers and cryoprotectants when performing EPR spectroscopy of the model heme protein myoglobin at low temperature. Here, we provide an example of the importance of testing different experimental conditions when investigating an unknown sample. In addition to the glycerol influence described for *Nd*Cld and *C*Cld at neutral pH, the disappearance of the alkaline low-spin species was also observed for wild-type *C*Cld when the samples were prepared in borate buffer (pH ~ 10) with the addition of 20

% (v/v) of glycerol (**Figure 5.8**). The spectrum in presence of glycerol is almost identical to the one of *C*Cld measured previously at pH 5.0 and 7.0, which is consistent with a pH shift in the sample when glycerol is added, due to the interaction of boric acid with this cryoprotectant (Chapter 4). Interestingly, in addition to the unknown LS species already described for *C*Cld at neutral pH (principal *g* values ~ [2.8 2.3 1.6],), an extra highly anisotropic LS with $g_z \sim 2.9$ is observed, which is reminiscent of LS2' described for *Nd*Cld (**Figure 5.8 b, inset**). A pH shift as the cause of the unexpected behavior of *C*Cld was further confirmed by the fact that the effects caused by glycerol can be reverted by washing out the cryoprotectant with a simple buffer exchange procedure. **Figure 5.8 c** shows the EPR spectrum of the sample in **Figure 5.8 b** after the glycerol is removed. The alkaline form of the protein is recovered, however only one LS form is detected, which corresponds to the LS2-alkaline previously observed in both wild-type *C*Cld and variants (**Table 5.1** and **Table 5.2**).

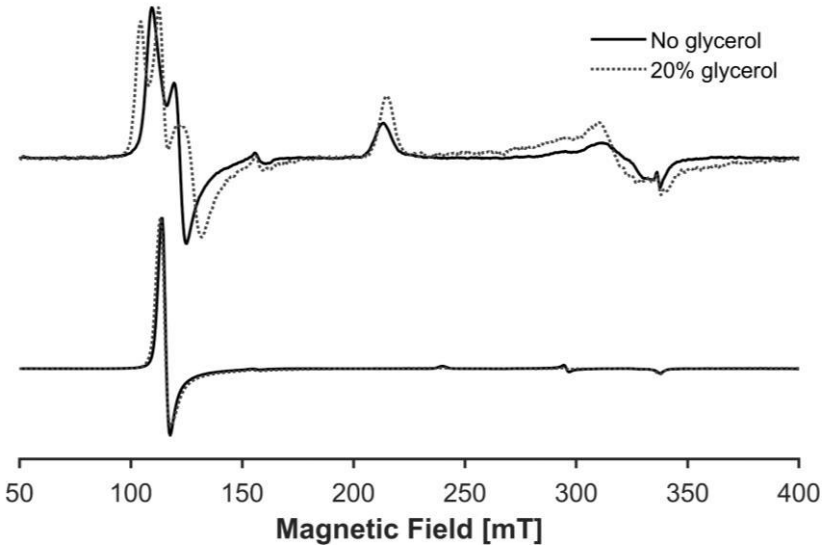

Figure 5.7 *Effects of glycerol on the EPR spectra of wild-type NdCld and CCld at neutral pH. Samples were prepared in 50 mM HEPES buffer (pH 7.0) (NdCld, top) and 50 mM phosphate buffer (pH 7.0) (CCld, bottom). A microwave power of 5 mW was applied to record the spectra of NdCld, while a microwave power of 2 mW was used for CCld spectra. Solid black for the sample without glycerol, dashed grey for the sample with 20 % glycerol.*

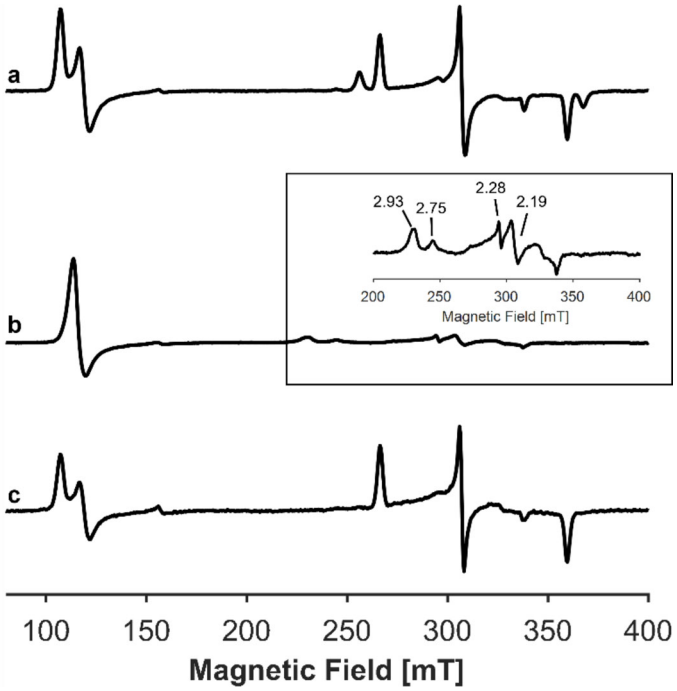

Figure 5.8 *CW EPR measurements of wid-type CCld in* ***(a)*** *borate buffer alone,* ***(b)*** *in borate buffer with 20 % (v/v) glycerol and* ***(c)*** *after removing the glycerol by washing the sample in* ***(b)*** *with fresh borate buffer. The inset shows an enlargement of the area between 200 and 400 mT for better visualization. In all cases, a microwave power of 2 mW was used.*

5.3.5 Impact of the R127 flexibility on thermal stability and chlorite degradation activity

To investigate the influence of the introduced mutations and pH on protein stability, differential scanning calorimetry (DSC) and temperature-dependent ECD spectroscopy were performed by our collaborators at BOKU. **Figure 5.9** compares the thermograms of wild-type *C*Cld and variants at pH 5.0. Two distinct endotherms were observed, suggesting a non-two-state transition (T_m1 and T_m2) as described previously [202]. In the pH range 5.0–9.0, the second transition (T_m2) is at ~ 58 °C for all three proteins, while significant differences were observed in T_m1 values, ranging from 38.3 °C (Q74V) to 50.9 °C (Q74E) (**Figure 5.9**). Both wild-type *C*Cld and variants show the highest thermal stability at pH 6.0 which decreases progressively at more alkaline pH (**Figure 5.9**). The pH dependence of thermal stability was also investigated by ECD in the far-UV and visible region at pH 5.0, 7.0,

and 9.0 to assign the observed transitions to distinct unfolding events. Similar to DSC, two transitions were observed with similar T_m values (See Table S4 in the original paper [201]). ECD in the visible region clearly correlates with the first unfolding event and heme release due to disappearance of Soret ellipticity (411–423 nm), whereas the second endotherm reflects melting of the secondary structures due to the loss of ellipticity at 210 nm.

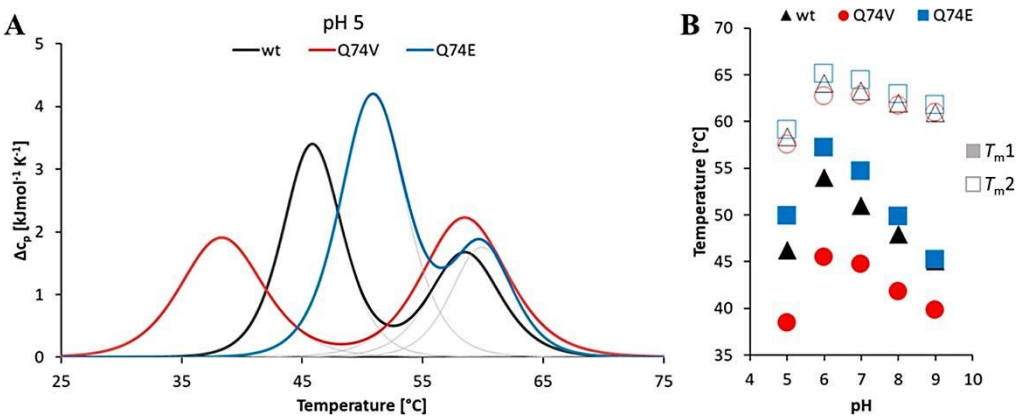

Figure 5.9 *Thermal stability of wild-type CCld and variants measured at different pH values by DSC. The enzyme concentration was 20 µM.* ***(A)*** *Normalized thermograms of wild-type CCld (black), Q74V (red), and Q74E (blue) at pH 5.0. Colored lines represent experimental data, and gray lines show a fit of the endotherm to a non-two-state transition model.* ***(B)*** *Calculated T_m1 (filled symbols) and T_m2 (empty symbols) plotted vs pH values. Measurements were performed in 50 mM citrate phosphate buffer (pH 5.0–6.0) and 50 mM phosphate buffer (pH 7.0–9.0).*

Interestingly, the catalytic efficiency (k_{cat}/K_M) of chlorite degradation of all the three proteins was similar, with a pH optimum around 5.0; the results of the polarographic measurements are reported in **Table 5.4**. In the pH regime from 5.0 to 9.0, Q74V exhibits the lowest K_M values, which also decrease with an increase in pH. The same pH dependence of K_M is observed for the wild-type *C*Cld and Q74E. Similarly, in all three proteins the k_{cat} values are highest at acidic pH values and decrease with an increase in pH. At the pH optimum, the k_{cat} values decrease in the following order: Q74E > wild-type *C*Cld > Q74V. It must be mentioned that above 100 µM chlorite (5000-fold excess) irreversible inactivation is observed with all three proteins. At pH > 7.0, both Q74V and Q74E are more prone to inactivation compared to wild-type *C*Cld (Figure S7 in the original paper [201]).

*C*Cld	K_M (μM)	k_{cat} (s^{-1})	k_{cat} / K_M (M^{-1} s^{-1})
pH 5.0			
wild-type	127.1 ± 28.0	475.8 ± 34.7	(3.7 ± 1.2) × 10^6
Q74V	47.8 ± 4.7	280.2 ± 2.8	(5.9 ± 0.7) × 10^6
Q74E	327.0 ± 6.6	977.4 ± 34.4	(3.0 ± 0.2) × 10^6
pH 7.0			
wild-type	43.2 ± 5.2	60.0 ± 0.7	(1.4 ± 0.2) × 10^6
Q74V	18.8 ± 3.5	50.8 ± 0.4	(2.7 ± 0.5) × 10^6
Q74E	53.8 ± 13.1	37.2 ± 1.1	(6.9 ± 2.0) × 10^5
pH 9.0			
wild-type	59.2 ± 20.1	33.4 ± 1.5	(5.6 ± 2.5) × 10^5
Q74V	19.3 ± 6.0	43.0 ± 0.7	(2.2 ± 0.8) × 10^6
Q74E	21.0 ± 11.2	18.91 ± 0.5	(0.9 ± 0.7) × 10^6

Table 5.4 *Kinetic parameters of wild-type CCld and variants Q74V and Q74E at pH 5.0, 7.0, and 9.0. Chlorite degradation was monitored polarographically.*

5.4 Discussion

As outlined in Chapter 1 and in section 5.1 of this Chapter, functional Clds possess a conserved distal arginine in an otherwise hydrophobic active site pocket, which in all crystal structures of clade II Clds published thus far (including the model enzyme *C*Cld) is in the "out" conformation and forms a hydrogen bond to Q74. Glutamine 74 is located on the α-helical loop that connects the N- and C-terminal domains of a protomer [53, 55]. In clade I Clds, a hydrogen-bonding partner is missing due to different conformations of this loop region [56, 57, 60]. *C*Cld variant Q74V was designed to mimic this setting in clade I Clds, whereas the design of *C*Cld variant Q74E aimed to study the impact of arresting R127 in a salt bridge with E74. In the crystal structure of Q74V determined at pH 8.5, R127 adopts the "in" conformation and directly interacts with the deprotonated distal W501 (**Figure 5.1 B**), which is different to the orientation of R127 in X-ray and neutron structures of wild-type *C*Cld determined at pH 6.5, 8.5, and pH 9.0 as well as those of complex structures with fluoride and thiocyanate [55]. In all of these wild-type *C*Cld data sets [55], the R127 side chain is positioned away from the heme moiety. This "out" conformation is stabilized by hydrogen bonding between R127 and Q74 [55]. Because the pK_a for the alkaline transition in Q74V has been determined to be 7.41 compared to 8.11 for wild-type *C*Cld (**Figure 5.2 B**), it is reasonable to assume that its (more flexible) guanidinium group promoted the deprotonation of W501. Both the decrease in the pK_a of the alkaline transition and the X-ray structure suggest a higher flexibility in solution of R127 in Q74V compared to the wild-type protein. The opposite trend is visible for variant Q74E. At pH 6.5, its active site architecture strongly resembles that of wild-type *C*Cld with the exception that R127 is arrested in a salt bridge with E74 (**Figure 5.1**). As a consequence, its guanidinium group is not able to stabilize the conjugated base of W501 and the pK_a of the alkaline transition is significantly increased to a pK_a of 9.33 (**Figure 5.2 B**). These findings clearly demonstrate that (i) the distal arginine in wild-type Clds is flexible, (ii) its dynamics is influenced by its remote H-bonding partner, and (iii) in Q74V (mirroring clade I enzymes) this flexibility is more pronounced than in wild-type *C*Cld.

Most interestingly, these differences in the conformational dynamics of R127 had a strong impact on the thermal stability of the heme cavity. In principle, the thermal stability of pentameric clade I Clds (*i.e., Nd*Cld) is significantly higher than that of dimeric clade II Clds like *C*Cld. Thermal unfolding of clade I enzymes follows a simple two-state transition, suggesting a cooperative process, in which separation of subunits, monomer melting, and release of the heme cofactor occur simultaneously [202]. By contrast, dimeric Clds, including *C*Cld, follow a non-two-state unfolding pathway with two consecutive unfolding events. The differences in N-terminal domain architecture and protomer interactions [53, 55, 56, 59, 60] have been proposed to be responsible for these observations [61]. As typical clade II Clds,

wild-type *C*Cld and variants Q74V and Q74E show two endotherms in DSC with the second unfolding event (*i.e.,* melting of the overall secondary structures) occurring at similar T_m2 values (~ 58 °C) in the three proteins. By contrast, the first unfolding event strongly depends on the H-bonding network and conformational dynamics of R127. At pH 5.0, the T_m1 values increase in the following order: Q74V (38.3 °C) < wild-type *C*Cld (45.8 °C) < Q74E (50.9 °C) (**Figure 5.9**). As suggested by thermal ECD data in the visible region, at these temperatures the active site unfolds and heme is released. In the case of Q74E, the salt bridge of R127 with E74, which is located at the α-helical loop (see above), stabilizes the heme cavity. Disruption of the salt bridge at 50.9 °C (pH 5.0) seems to initiate unfolding of the loop and opening of the heme cavity in Q74E.

At acidic and neutral pH, the EPR spectra of the wild-type *C*Cld and variants do not show significant differences (**Figure 5.3**). At pH 7.0, the high-spin ferric heme signal of Q74V still accounts for 97% of the spectrum, whereas the spectrum of Q74E already shows some minor low-spin signals (**Figure 5.4**). This may seem partially inconsistent with the pKa values obtained from UV–vis spectroscopy (**Figure 5.2**); however, in EPR, the effects of freezing and formation of artifacts at cryogenic temperatures have to be taken into account [171, 203] (Chapter 4). In any case, the spectroscopic findings clearly demonstrate that at the pH optimum of chlorite degradation activity (*i.e.,* pH 5) (i) the heme coordination in the three proteins is similar, *i.e.*, the geometry of the paramagnetic center is not substantially perturbed, and consequently (ii) the impact of the conformational dynamics of R127 is small.

In the alkaline pH regime, the geometries of the heme pockets of wild-type *C*Cld and the variants Q74V and Q74E change. This includes changes in the rhombicity of the EPR signals of the high-spin components and formation of new low-spin species whose EPR features are consistent with the ones of hydroxo-ligated forms described for other chlorite dismutases [48, 49, 61, 148]. The attribution of these signals to OH^- adducts is additionally supported by resonance Raman spectroscopy studies, which highlighted the presence of a Fe–OH bond in the alkaline forms of several chlorite dismutases from both clade I and clade II [55, 58, 148, 181]. In wild-type *C*Cld (**Figure 5.3 A**), the high-spin components with an axial $\boldsymbol{g}^{eff}$ tensor, which dominate the spectrum at acidic and neutral pH (HS1 and HS2), progressively convert to a single and well-resolved rhombic species (HS3) at pH 10.0 (**Figure 5.3 A**). This reflects a different symmetry and altered geometry of the active site pocket most probably by repositioning of R127 and its H-bonding network. This is further corroborated by the analysis of the low-spin species identified at pH 10.0 in both *C*Cld and *Nd*Cld (**Table 5.1**, **Table 5.2** and **Table 5.3**; **Figure 5.5** and **Figure 5.6**). LS1-alkaline (g_x = 1.87, g_y = 2.20, g_z = 2.53) and LS2-alkaline (g_x = 1.83, g_y = 2.19, g_z = 2.63) are the principal contributions in the high-pH spectrum of wild-type *C*Cld, while a third species (LS3-alkaline: g_x = 1.80, g_y = 2.27, g_z = 2.75) contributes to the

spectrum to a lesser extent. These components have *g* values similar to those of OH^- adducts of other heme proteins, such as cytochrome *c* peroxidase, [204] human hemoglobin [178], horse heart myoglobin [178], and *Caenorhabditis elegans* globin-33 [205]. Nicoletti *et al.* showed that at high pH hemoglobin from *Thermobifida fusca* forms two hydroxo complexes with different sets of *g* values [206], which they explained with the OH^- group being hydrogen-bonded to different extents to nearby residues. In the case of hemoglobin, the component with broader features was assigned to a strong His/OH^- coordination. The differences in the H-bonding network most probably result in a different electron density distribution between the axial ligand(s) and the porphyrin, which primarily determines the magnitude of the tetragonal parameter according to crystal field theory [123, 207]. Indeed, as nicely exemplified by Svistunenko *et al*. [178], the more unpaired electron density is on the heme iron, the more anisotropic is the $\boldsymbol{g}$ tensor of the low-spin signal. Therefore, it is possible that the LS contributions in the spectrum of wild-type *C*Cld derive from the dynamics of R127, which allows the hydroxide group to attend different H-bonding networks. In contrast to wild-type *C*Cld, the EPR spectrum at pH 10 in both Q74E and Q74V is dominated by an LS2-alkaline contribution with larger $\boldsymbol{g}$ anisotropy than the LS1-alkaline component, which suggests a higher spin density on the heme (**Figure 5.5**). This points to a different H-bonding dynamics of the hydroxide group due to the altered flexibility of R127. Interestingly, the main hydroxide adduct in *Nd*Cld is characterized by *g* values similar to those of LS2-alkaline (**Figure 5.6**), suggesting that the heme pocket of the pentameric Cld is very similar to that of *C*Cld Q74V, which was designed as a model for clade I Clds.

The EPR spectra of both *Nd*Cld and *C*Cld show features of low-spin states even at pH ≤7; however, their interpretation is not trivial. In the case of *Nd*Cld, two broad low-spin contributions (**Table 5.3**, LS1′ and LS2′) have *g* values consistent with other low-spin species previously observed in several EPR studies of chlorite dismutases at neutral pH. While in certain cases their origin could not be determined [148], in the work of De Schutter *et al.* [61] it was demonstrated that some of these species may represent “ready” states still accessible to the binding of external molecules. Moreover, in a comparative study of native and recombinant chlorite dismutase from *Ideonella dechloratans*, it was shown that a low-spin signal consistent with a bis-histidine coordination was present in only the recombinant form [208]. In another work, the occurrence of the typical features of an imidazole adduct was explained as artefacts from the protein purification procedure [59]. In the case of *Nd*Cld, no imidazole was used during purification; therefore, this explanation can be ruled out. Furthermore, the predominance of the LS1′ signal in *Nd*Cld samples prepared at different pH values and in different buffers makes it unlikely to be due to the binding of an external molecule present in the medium and suggests a strong coordination from a ligand that cannot be easily displaced. For these reasons, the

nature of the LS species remains elusive. In the case of *C*Cld, the *g* values of LS1 (g_x = 1.66, g_y = 2.28, g_z = 2.81) found at neutral and acidic pH are unique and (to the best of our knowledge) have never been reported before in Clds. This species is characterized by features that are consistent with neither imidazole–heme complexes [59, 148, 209] nor the OH^- adducts formed at high pH, as shown above. However, these values present some similarities with the hydroxide complexes found in other heme protein samples at non-alkaline pH [171, 178].

Both UV–vis and EPR data have demonstrated that modulation of the H-bonding network of R127 in wild-type *C*Cld and the two variants do not substantially perturb the spin state of the heme iron in the ferric resting state in solution in the acidic and neutral pH region. This fits with the observation that at a pH optimum (*i.e.,* pH 5.0) the catalytic efficiency of wild-type *C*Cld and of the two variants is in the range of 3.0×10^6 to 5.9×10^6 M^{-1} s^{-1}, very similar to those of previously studied chlorite dismutases from clade II and most of clade I Clds (**Table 5.4**) [53–57, 148, 210]. Because even arresting R127 in a salt bridge (**Figure 5.1**) had almost no effect on the catalytic efficiency, this suggests that the impact of the conformational dynamics of R127 on catalysis is relatively small. At the pH optimum and neutral pH, the K_M values decrease in the following order: Q74E > wild-type *C*Cld > Q74V. This mirrors the hierarchy of the thermal stability of the heme cavity (**Figure 5.9**). By contrast, the catalytic efficiency follows the opposite order at pH 5.0.

The reaction cycle of dimeric *C*Cld is initiated by binding of the anionic substrate chlorite (pK_a = 1.72) to the ferric heme center. At first sight, at the pH optimum the flexibility of the arginine seems to facilitate this reaction to some extent, because the K_M of Q74E was significantly higher compared to that of wild-type *C*Cld. The differences in K_M values are less pronounced at higher pH values. It has been shown that R173 in *Nd*Cld has a negligible role in chlorite binding, but most likely plays a role in the correct orientation of this charged molecule [57, 211]. By contrast, in clade I Cld from *Dechloromonas aromatica* exchange of R183 with alanine increased the K_M from 0.2 to 14.6 mM [58]. Differences between clade I and clade II Clds may be related to the differences between the α-helical loop that connects the N- and C-terminal domains of Cld protomers. Due to its location at the entrance to the heme cavity, it governs the accessibility to the heme cavity. In *C*Cld variant Q74V and clade I Clds, the interaction between the distal arginine and the loop is small, whereas in wild-type *C*Cld, a hydrogen bond between R127 and Q74 is formed. By contrast, Q74E increases the rigidity of the loop (as reflected by the DSC data) and thus decreases its dynamics, which seems to be important for chlorite accession and binding.

This study also rules out that the alkaline transition is responsible for the pH dependence of chlorite degradation activity. Despite the fact that the pK_a of the alkaline transition is significantly different in the three proteins due to differences in the flexibility of R127, the pH dependence of the catalytic efficiency was similar in wild-type *C*Cld and the two variants. In any case, the impact of the conformational dynamics of R127 in *C*Cld on the cleavage reaction seems to be small because at the pH optimum Q74E exhibits the highest turnover number. Apparently, R127 in the arrested "out" conformation is still able to support the homolytic or heterolytic cleavage of chlorite [55–57, 59, 60, 72, 148, 200]. Independently of the mechanism of chlorite cleavage, the resulting transient intermediates (either Compound I and hypochlorite or Compound II and chlorine monoxide) must be kept in the reaction sphere for the following rebound step, where the guanidinium group seems to play an important role. Computational studies suggest that in the rebound step the transient intermediates must rotate. This rotation requires rearrangements of H-bonds with the arginine to support O–O bond formation. Finally, the H-bond between the arginine and the two oxygen atoms needs to rearrange again to the terminal chlorine atom [66]. The data presented here clearly suggest that R127, arrested in a salt bridge with E74 and thus in the "out" conformation, can still participate in these proposed reaction steps.

In summary, in this Chapter it is demonstrated that the conformational dynamics of the catalytic arginine can be modulated by its remote H-bonding network. This is underlined by the presented high-resolution crystal structures and the impact of the flexibility of R127 on the alkaline transition. Formation of the LS hydroxide complex is shown by UV–vis and EPR spectroscopies, and the calculated pK_a values strongly depended on the flexibility of R127. By contrast, the effect on the catalytic efficiency in the pH range 5.0-9.0 was small, suggesting that R127 in the "out" conformation can support chlorite cleavage and keep the transient intermediates in place. Most interestingly, the strongest impact of the exchange R127 was on the thermal stability and the K_M values at the pH optimum. This seems to be related to the fact that R127 is H-bonded to the Cld-typical (flexible) α-helical loop in *C*Cld that might act as a gatekeeper for the active site. Arresting this loop in the salt bridge (Q74E) significantly increases the thermal stability of the heme cavity but at the same time decreases the loop dynamics that is necessary for chlorite to enter the active site and bind to the heme iron

Chapter 6

Impact of R127 dynamics on nitrite and chlorite binding by chlorite dismutase

Abstract

This Chapter analyses the impact of the distal, flexible, and catalytic arginine of chlorite dismutases on the binding of anionic angulate ligands like nitrite and the substrate chlorite. Dimeric Cld from *Cyanothece sp.* PCC7425 was used as a model enzyme. Q74V and Q74E variants, already introduced in Chapter 5, were investigated as well. In addition, two mutants were generated in which the catalytic arginine was substituted by either alanine (R127A) or lysine (R127K). Here, we discuss the electronic and spectral signatures of the high-spin ferric proteins and the corresponding low-spin nitrite complexes. Electron paramagnetic resonance spectroscopy, together with crystal-field analysis of low-spin species parameters, provided evidence for two binding *modi* of nitrite, which was also corroborated by molecular dynamics (MD) simulations. Furthermore, we demonstrate the impact of R127 dynamics on the thermal stability of the nitrite adducts and we present the X-ray crystal structures of the nitrite complexes of wild-type *C*Cld and the variants Q74V, Q74E and R127A. The findings are discussed with respect to the role(s) of R127 in ligand and chlorite binding and substrate degradation.

Redrafted after: Ilenia Serra*, Daniel Schmidt*, Vera Pfanzagl, Georg Mlynek, Stefan Hofbauer, Kristina Djinović-Carugo, Paul G. Furtmüller, Inés García-Rubio, Sabine Van Doorslaer and Christian Obinger, (2022) Impact of the dynamics of the catalytic arginine on nitrite and chlorite binding by dimeric chlorite dismutase, *J. Inorg. Biochem.* 227, 111689 (*I.S. and D.S. contributed equally to this work)

Own contribution: recombinant expression and purification of *C*Cld variant R127K; acquisition, analysis, and interpretation of EPR data; writing of paper manuscript

6.1 Introduction

As already explained in previous chapters, chlorite dismutases attracted attention because of their ability to convert chlorite (ClO_2^-) to chloride (Cl^-) and dioxygen (O_2), therefore being potentially applied in the bioremediation of harmful anthropogenic chlorite present in groundwater, drinking water, and soil [72, 200]. The reaction mechanism of Clds is still debated, as is the role of the flexible catalytic arginine, which is the only charged amino acid in an otherwise hydrophobic distal heme cavity [72, 200]. As already outlined in Chapter 1, Clds convert chlorite in three steps (Chapter 1, Reactions 1.1 – 1.3) in which the catalytic arginine might be involved. The reaction is initiated by the binding of negatively charged chlorite [pK_a (chlorous acid) = 1.96; bond angle 111°; electronegativity (Cl) = 3.16] to the ferric state of Cld thereby forming the substrate adduct. Similar to chlorite, nitrite is also an angulate oxoanion of the same formal charge at neutral pH and very similar bond angle [pK_a (nitrous acid) = 3.15; bond angle 115°, electronegativity (N) = 3.04] that forms a low-spin (LS) complex with the ferric Cld, mimicking the substrate adduct. The *C*Cld-chlorite adduct cannot be trapped since chlorite is a strong oxidant that immediately oxidizes the ferric enzyme to an oxoiron(IV) intermediate, either Compound I [$Por^{\bullet+}Fe(IV)=O$] or Compound II [$PorFe(IV)=O$]. As a consequence, chlorite is either reduced to hypochlorite (ClO^-) (**Scheme 1.2, Reaction 2A**) or chlorine monoxide ($ClO^\bullet$) (**Scheme 1.2**, **Reaction 2B**). The actual molecular mechanism is still under discussion [53–60, 65, 147, 148, 181, 201, 211]. Finally, the transient chlorite reduction products must rearrange before rebinding to and reacting with the respective oxoiron(IV) intermediate to release dioxygen and chloride (**Scheme 1.2, Reactions 3A, 3B and 4**).

Here, in order to get more insights into the role of the flexible catalytic arginine and its role(s) in substrate binding and degradation, we investigated its involvement in the formation of the substrate adduct, mirrored by the formation of the LS nitrite complex. In this Chapter, the binding of nitrite to the wild-type *C*Cld and variants Q74V, Q74E, R127A and R127K is extensively investigated by means of electron paramagnetic resonance spectroscopy. The results are analyzed using the crystal-field theory formalism introduced by Taylor [123] and are discussed in the context of the different heme architectures of the selected proteins. The X-ray crystal structures of the nitrite complexes of wild-type *C*Cld and the variants Q74V, Q74E and R127A are presented as well. Additionally, MD simulations of the active site of wild-type *C*Cld and variants, performed by our collaborators at BOKU, are given. The combined data show that (i) the flexibility of the catalytic arginine has a strong impact on the binding of these oxoanions and that (ii) NO_2^- and ClO_2^- exhibit different binding *modi* to the ferric resting state of Cld.

6.2 Experimental procedures

6.2.1 Site-directed mutagenesis, expression and purification

The *C*Cld variant R127K and R127A were obtained by site-directed mutagenesis using the QuikChange Lightning Kit (Agilent, Santa Clara, CA, USA). The modified wild-type plasmid described previously [201] was used as template. For control, the final plasmid was sequenced from the primer pET-up (Microsynth, Balgach, Switzerland). Recombinant protein expression was performed in *E. coli* BL21 Gold (DE3) cells (Agilent) in LB-medium supplemented with ampicillin as described in [201]. For protein purification the cell pellets were thawed and resuspended in lysis buffer (50 mM phosphate buffer, pH 7.4, 500 mM NaCl, 0.5 % Triton X-100 and 5 % glycerol) and supplemented with ~ 100 µM hemin. After ultrasonication (two 3 min-cycles, pulsed mode, 1 s sonication, 1 s rest, 90 %) on ice, the cell lysate was centrifuged (4 °C, 17000 g, 35 min). Following a filtration step (0.45 µm, Durapore Membrane, Merck, Darmstadt, Germany) the resulting crude extract was loaded onto a His-trap affinity column (5 mL; GE Healthcare, Chicago, IL, USA) pre-equilibrated with binding buffer (50 mM phosphate buffer, pH 7.4, 500 mM NaCl). After the protein-loaded column was washed with binding buffer, on-column cleavage of the His-tag was performed. Therefore, the column was equilibrated with cleavage buffer (50 mM Tris-HCl with 150 mM NaCl and 1 mM EDTA) and cleaving with a His-tagged HRV 3C PreScission Protease was performed overnight at 4 °C. Elution was carried out with storage buffer (50 mM phosphate buffer, pH 7.0) accompanied by a concentration and desalting step using an Amicon Ultra-15 centrifugal filter unit (10 kDa molecular weight cut-off; Merck, Darmstadt, Germany). As a final polishing step, the concentrated protein was applied to a pre-equilibrated (50 mM phosphate buffer, pH 7.0) HiLoad 16/60 Superdex 200 prep grade column (GE Healthcare). The collected fractions were pooled, concentrated to a concentration of ~ 20 mg mL^{-1} using centrifugal filter unit and stored at −80 °C in 50–100 µL aliquots.

6.2.2 Electron paramagnetic resonance spectroscopy and crystal field analysis

The effects of the addition of a large excess of $NaNO_2$ to wild-type ferric *C*Cld and variants were assessed by EPR spectroscopy. In addition, measurements of ferric *Nd*Cld and myoglobin in presence of nitrite were performed as well. EPR samples of chlorite dismutases were prepared taking care of consistency with the other experiments presented in this work. More specifically, for measurements at neutral pH *C*Cld samples were either prepared in 50 mM sodium-phosphate buffer (sodium phosphate monobasic-dibasic mixture), pH 7.0 (R127A, R127K) or in a 50 mM

"temperature-independent" (TIP) buffer, pH 7.0, composed of 45% HEPES and 55% sodium phosphate [195] (NO_2^- complex of wild-type *C*Cld). *Nd*Cld samples were prepared in 50 mM HEPES buffer, pH 7.0 (storage buffer following protein purification [57]). Myoglobin from equine skeletal muscle (HsMb) (95–100 % pure, essentially salt-free, lyophilized powder) was purchased from Sigma-Aldrich and used without further purification. HsMb samples were prepared in 50 mM Tris-HCl buffer, pH 7.0. For measurements at basic pH, samples of NO_2^- complexes of Q74E and Q74V were prepared either in 50 mM phosphate/borate buffer, pH 8.5, or in 50 mM Tris-HCl, pH 8.5 (both buffers were filtered and degassed before use). Where not otherwise specified, protein concentration was 400 µM and $NaNO_2$ was added in a 500-fold excess (final concentration of 200 mM). Samples of nitrite adducts for EPR experiments were freshly prepared before each measurement to avoid possible effects due to the high concentration of nitrite and interference of NO, which can be formed at acidic pH (see section 6.3.2) [212]. In particular, the following procedure was used: first, the appropriate volumes of protein stock solution and buffer were mixed together in a standard 1.5 mL-Eppendorf tube to obtain the correct dilution; next, an aliquot of a concentrated $NaNO_2$ solution was added to the mixture to get the desired protein-to-NO_2^- ratio. The sample was then quickly transferred in an EPR tube (Ø = 4 mm) and immediately frozen in liquid N_2.

X-band CW-EPR measurements of *C*Cld and *Nd*Cld samples at pH 7.0 (with and without $NaNO_2$) were performed on a Bruker ESP300E spectrometer operating at microwave frequencies of ~ 9.44 GHz. Temperature was set to 10 K with the use of a liquid-helium cryostat (Oxford Inc.) and excess of paramagnetic O_2 was removed by applying several freeze-pump-thaw cycles to the quartz EPR tubes containing the samples, before starting the EPR experiment. Measurements of NO_2^- complexes of Q74E and Q74V at pH 8.5 and HsMb were carried out with a Bruker ELEXSYS E580 X-band spectrometer equipped with an Oxford ESR 900 continuous-flow helium cryostat and a Bruker ER 4122 SHQ resonator (operating at a microwave frequency of ~ 9.4 GHz). Spectra were recorded at 10 K under non-saturating conditions. In particular, the microwave power was adjusted in each experiment according to protein concentration or resonator sensitivity in order to obtain non-saturated spectra. A modulation frequency of 100 kHz and a modulation amplitude of 1 mT were also used. Simulations of EPR parameters were performed with the EasySpin tool (v. 6.0.0-dev.26) [188].

The EPR spectra of the low-spin NO_2^- complexes of chlorite dismutases and reference heme proteins were further analyzed with a crystal-field model, which allows to correlate the g values obtained from the simulations to the energy differences of the iron t_{2g} orbitals [122, 126, 213]. The rhombic (V/λ) and the

tetragonal (Δ/λ) crystal field parameters were calculated according to Taylor's formalism [123] using the following relations (Eq.6.1 – Eq. 6.3), where V is defined as the energy splitting between the d_{xz} and d_{yz} orbitals, Δ as the splitting between the d_{xy} and the average of the energy levels of the d_{xz} and d_{yz} orbitals and λ as the spin-orbit coupling factor (**Figure 3.1**):

$$A = \frac{g_x}{g_y + g_z} + \frac{g_y}{g_z - g_x} = V/\lambda \qquad \text{(Eq. 6.1)}$$

$$B = \frac{g_x}{g_y + g_z} + \frac{g_z}{g_y - g_x} \qquad \text{(Eq. 6.2)}$$

$$\Delta/\lambda = B - A/2 \qquad \text{(Eq. 6.3)}$$

A "Blumberg-Peisach" diagram [124] (**Figure 6.14**) was constructed by plotting the rhombicity (V/Δ), which reflects the relative rhombic-to-axial character of the system, versus the tetragonal field parameter (Δ/λ) for each low-spin species.

6.2.3 Other techniques

In addition to EPR, the binding of the angulate oxoanions nitrite and chlorite to wild-type *C*Cld and selected variants was investigated by means of several techniques to obtain a better understanding of the role(s) of the flexible catalytic arginine. The detailed experimental procedures of X-ray crystallography, UV-Vis and ECD spectroscopies, kinetic measurements, DSC and MD simulations, which were performed by our collaborators at BOKU, can be found in [115].

6.3 Results

6.3.1 X-ray crystal structures of ferric HS proteins and the corresponding LS nitrite complexes

The X-ray crystal structures of wild-type *C*Cld and the variants Q74V and Q74E have been already presented in Chapter 1 and Chapter 5. Here, in order to analyze the impact of R127 on binding of the anionic angulate ligand nitrite, which mirrors the substrate chlorite, I briefly introduce the crystal structures of the variants R127A and R127K and the ones of the nitrite adducts of wild-type *C*Cld, Q74E, Q74V and R127A, respectively, obtained by our collaborators at BOKU. For a detailed description of the structures, the reader is referred to [115]. In short, the crystal structures of both R127A and R127K show the typical ferredoxin-like fold that is defined by five α-helices along with a β-barrel composed of three-stranded and five-stranded antiparallel β-sheets [55, 201]. The introduced mutations did not lead to significant changes in the overall fold of the *C*Cld variants. Similar to wild-type *C*Cld, histidine 114 serves as the fifth ligand on the proximal side and in the resting state, an H_2O molecule is typically situated above the heme iron. This water molecule is visible in 50 % of the subunits of the variant R127A, whereas the other subunits showed the presence of the cryoprotectant 2-methyl-2,4-pentanediol (MPD) being bound to the heme iron [115]. Exchange of R127 by alanine increases the bottleneck radius from 2.2 to 2.8 Å, thereby allowing MPD to enter the active site. In the crystal structure of R127K the lysine acts as sixth heme ligand, thereby eliminating the distal water molecule (**Figure 6.1**).

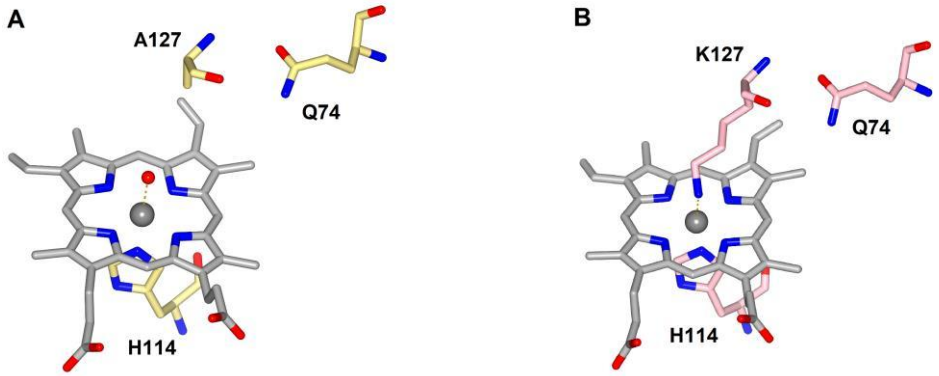

Figure 6.1 *Active sites of the CCld variants R127A* ***(A)*** *and R127K* ***(B)****. R127A is represented in the configuration having a water molecule sitting above the heme cofactor. Differently, in the variant R127K the lysine residue coordinates the heme iron (dark grey sphere). Figures have been generated with the software CCP4mg from the deposited PDB structures with accession codes 7OWI and 7OUA for the variants R127A and R127, respectively.*

Upon addition of nitrite to wild-type *C*Cld, Q74V and Q74E, R127 shows the "in" conformation and interacts with the anionic ligand (**Figure 6.2 A-C**). In wild-type *C*Cld the direct H-bond between R127 and Q74 is lost; nevertheless, the two residues are hydrogen-bonded *via* a water molecule (**Figure 6.2 A**). In the absence of the catalytic arginine (R127A) a nitrite molecule is still visible in the active site and a water molecule replaces the basic amino acid. Interestingly, in all nitrite-soaked crystals, NO_2^- is coordinated to the heme iron *via* an oxygen atom with O-Fe distances ranging from 2.1 to 2.4 Å. The anionic ligand interacts with the arginine's $N_\eta 2$ and/or with N_ε. In R127A a water molecule in a similar position is coordinating one of the oxygens of the bound ligand in a distance of ~ 3 Å (**Figure 6.2 D**).

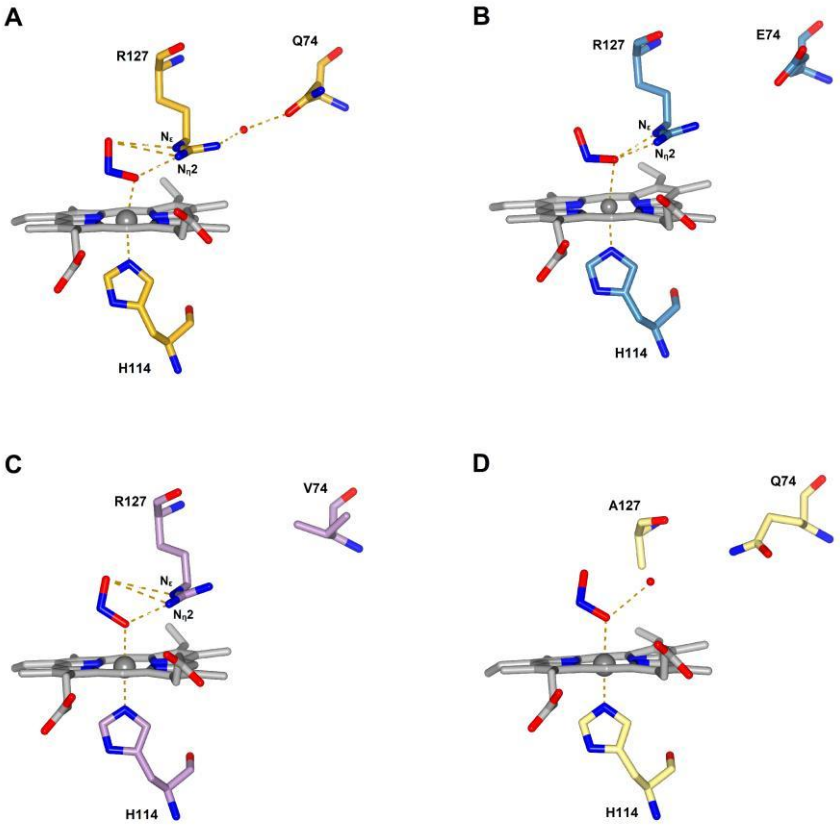

Figure 6.2 *Crystal structures of the heme cavity of nitrite adducts of wild-type CCld (**A**, dark gold), Q74E (**B**, steel blue), Q74V (**C**, lilac) and R127A (**D**, pale yellow). The amino acid residue at position 127, arginine (in A, B and C) or alanine (in D), and the heme b cofactor (grey) are shown in stick representation. The soaked ligand, nitrite (NO_2^-), is shown in stick representation (blue and red). Water molecules are depicted as red spheres. Figures have been generated with the software CCP4mg from the deposited PDB structures with accession codes 7OU5 (wild-type), 7OU9 (Q74E), 7OU7 (Q74V) and 7OUY (R127A).*

6.3.2 Nitrite affinity in wild-type *C*Cld and variants

The proper folding of R127A and R127K in the pH range 5.0-9.0 was validated by comparing the far-UV ECD spectral features of these variants with the ones of wild-type, Q74E and Q74V *C*Cld (Chapter 5, [201]). Then, UV-vis spectroscopy was used to investigate the affinity for the ligand nitrite all the proteins object of this work. For an in-depth discussion of the obtained results, the reader is referred to [115].

At pH 5.0 and 7.0 in the visible region, wild-type *C*Cld and the variants Q74V and Q74E show absorption spectra characteristic of the ferric HS states, which have been already discussed in Chapter 5 and [201]. Upon addition of nitrite, spectra in line with LS complex formation of these three proteins were obtained. All these spectra are characterized by a red-shifted Soret band at 414 nm, new Q-bands, and a CT-band (**Figure 6.3**). While the UV–vis spectral transitions during conversion of HS to LS states of wild-type *C*Cld and the variants Q74V and Q74E are similar, the calculated K_D-values of the nitrite complexes vary significantly (**Table 6.1**) with Q74V showing the highest affinity both at pH 5.0 and 7.0, followed by wild-type *C*Cld and Q74E. At pH 9.0 the affinity of nitrite is low for all three proteins. The spectra of R127A and R127K present some differences from the proteins discussed above. While the ferric R127A show a similar spectroscopic profile to the wild-type and variants Q74E, Q74V [115], in R127K the lysine residue acts as distal heme ligand (**Figure 6.1**) giving rise to a spectrum of a LS heme species already at acidic and neutral pH, which differs from the alkaline forms of *C*Cld observed so far [115, 201]. In addition to that, different spectral changes are observed upon titration with nitrite. In the case of R127A, the resulting Soret maximum of the nitrite-bound LS spectrum was significantly red-shifted compared to that of wild-type *C*Cld, Q74V or Q74E (shift to 420 nm, **Figure 6.4**). A similar shift was also seen for R127K at pH 5.0, which however was already in a LS configuration in absence of nitrite due to the coordination of the lysine to the heme iron (**Figure 6.4**). Finally, elimination of the distal arginine dramatically reduces the affinity for nitrite (**Table 6.1**) and for R127K no reliable K_D-values could be calculated. It has to be mentioned that at very high nitrite concentrations formation of nitrogen monoxide and formation of the respective NO-heme complex could occur at acidic and neutral pH which impedes both correct spectral assignment of the respective nitrite complexes of the two R127 variants and reliable calculation of the dissociation constants. In fact, spectroscopic evidence of NO-heme complex formation upon addition of nitrite at acidic pH was recently observed in the ferric protoglobin from *Methanosarcina acetivorans* (*Ma*Pgb) [214], which will be more extensively discussed in Chapter 7.

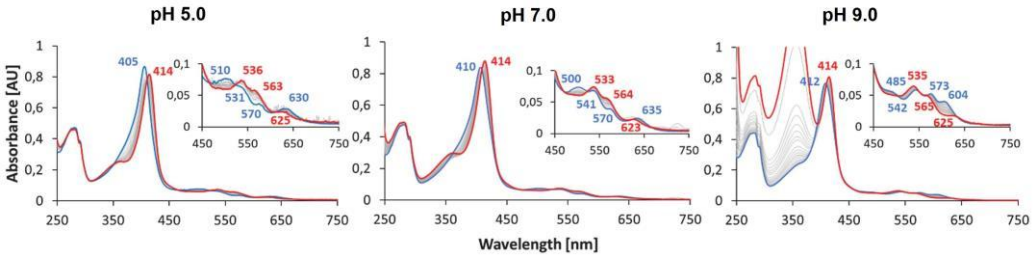

Figure 6.3 *Formation of nitrite complexes of wild-type CCld at pH 5.0, 7.0 and 9.0. Spectral transitions during HS to LS transition of wild-type CCld at pH 5.0, 7.0 and 9.0. The insets display a zoom-in of the wavelength range 450-750 nm for better visualization of the Q-bands and CT-bands. Blue spectra represent ferric HS spectra or partially hydroxo-LS spectra, whereas red spectra represent the LS nitrite complexes at the end of titration. A 100- to 3000-fold excess of nitrite was used to obtain the final spectra, for pH 5 and pH 9 respectively. Note that the background absorbance in the UV-region at pH 9.0 derives from the high nitrite concentration that is necessary for formation of a stable nitrite-complex.*

K_D [mM]	pH 5.0	pH 7.0	pH 9.0
WT	0.060 ± 0.004	0.336 ± 0.084	3.255 ± 0.191
Q74V	0.031 ± 0.002	0.153 ± 0.041	2.657 ± 0.177
Q74E	0.199 ± 0.009	1.246 ± 0.254	2.030 ± 0.204
R127A	6.345 ± 0.994	272.772 ± 28.534	> 4000

Table 6.1 *Derived dissociation constants for the nitrite complex of WT CCld and the variants Q74V, Q74E and R127A at pH 5.0, 7.0 and 9.0.*

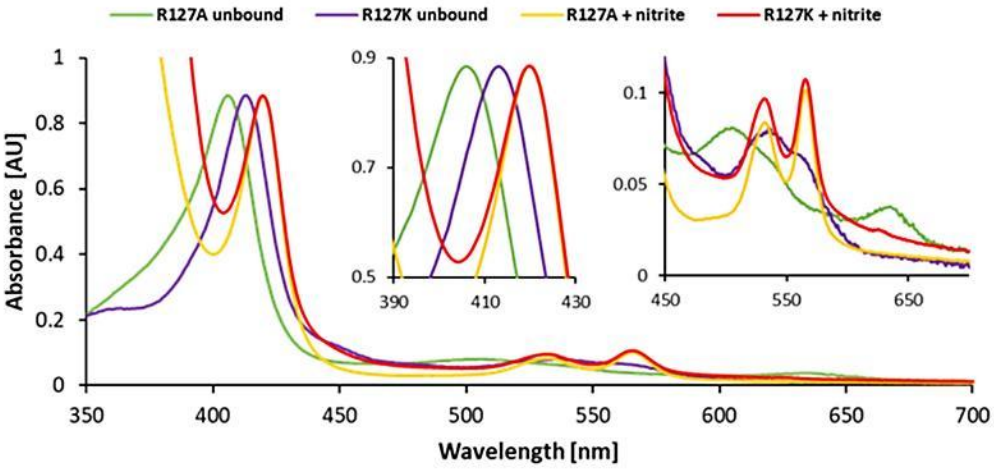

Figure 6.4 *UV-vis spectra of R127A and R127K at pH 5.0 (50mM citrate-phosphate buffer) without (green and purple) and with nitrite (yellow and red).*

6.3.3 EPR spectroscopy reveals multiple low-spin species upon nitrite binding in all CCld variants

EPR analysis of wild-type *C*Cld and variants in the presence of nitrite reveals the formation of LS ferric species with distinct EPR features, corroborating the UV–visible spectroscopy findings. The X-band CW-EPR spectrum of wild-type *C*Cld at pH 7 has been already shown elsewhere [54, 201], however, it is reported in **Figure 6.5** and in **Figure 6.7** to highlight the changes induced by the addition of nitrite at neutral pH.

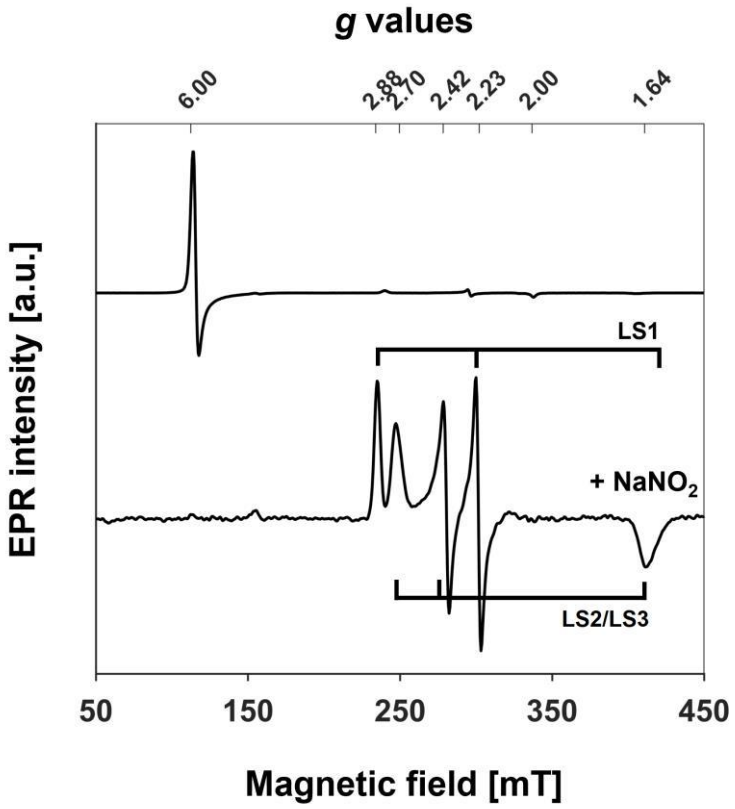

Figure 6.5 *X-band CW-EPR spectra of wild-type CCld (top) and NO_2^--CCld complex (bottom), at neutral pH. Samples were prepared either in 50 mM sodium-phosphate buffer (unbound CCld)* [201] *or in 50 mM TIP buffer (NO_2^--CCld complex), pH 7.0. Measurements were performed with microwave powers of either 2 mW (unbound CCld) or 5 mW (NO_2^--CCld complex). Spectra are shown normalized to their maximum intensity.*

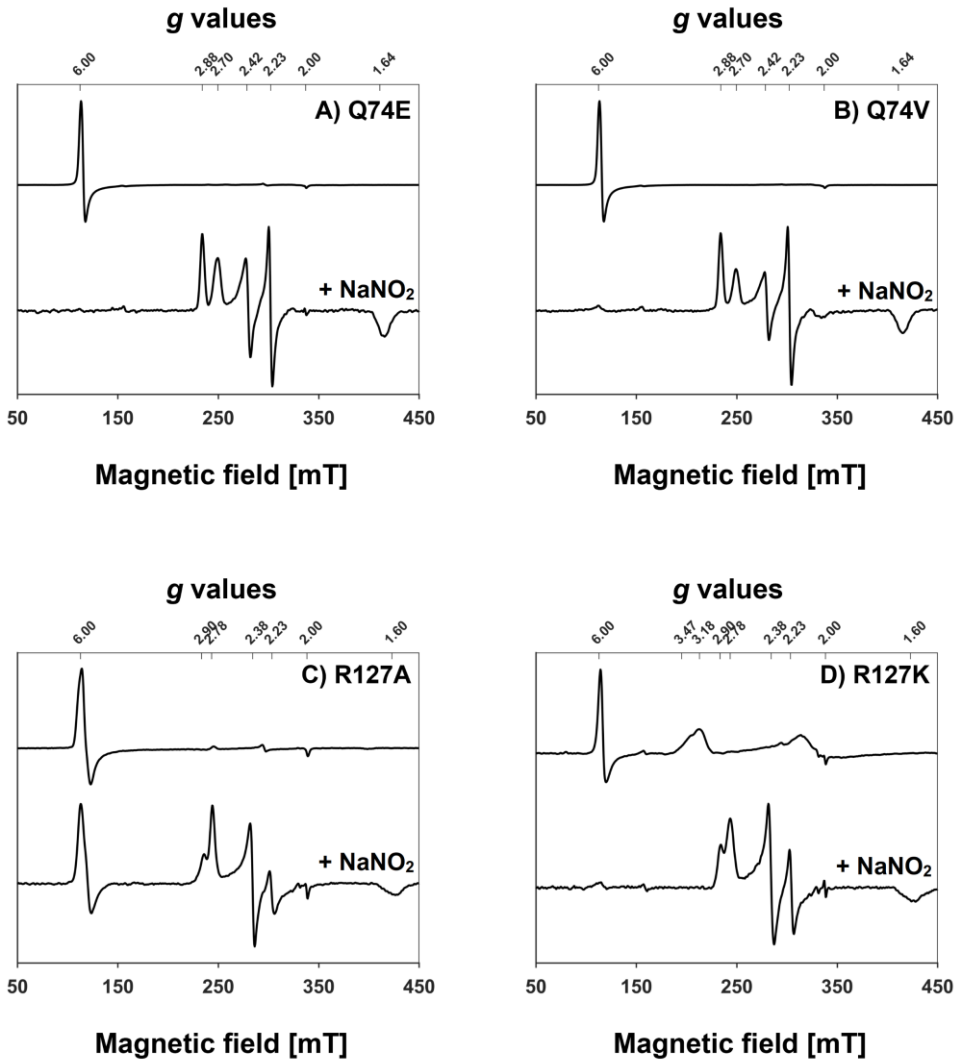

Figure 6.6 *X-band CW-EPR spectra of ferric HS CCld variants (upper spectra) and the corresponding LS nitrite adducts (bottom spectra) at pH 7.0.* ***(A)*** *Q74E;* ***(B)*** *Q74V;* ***(C)*** *R127A;* ***(D)*** *R127K; Samples were prepared in 50 mM sodium-phosphate buffer, pH 7. Measurements were performed with microwave powers of either 2 mW (Q74 CCld variants and NO_2^--Q74 variants complexes) or 1 mW (resting state of R127 variants and NO_2^--R127 variants complexes). Spectra are normalized to their maximum intensity.*

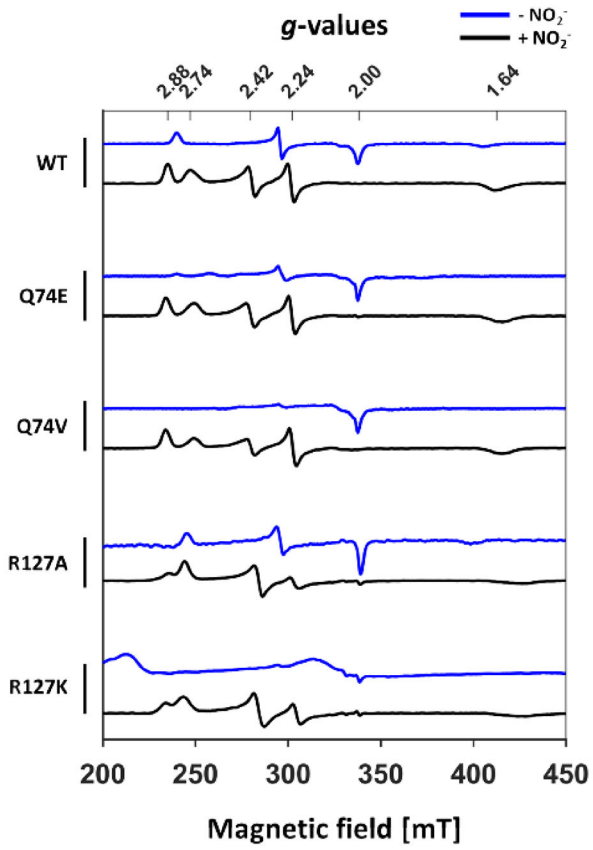

Figure 6.7 *X-band CW-EPR spectra of CCld variants (blue) and the corresponding nitrite adducts (black) at pH 7.0. Magnification of the LS region. Spectra in absence of nitrite are either ~ 33x-magnified (WT, Q74E and Q74V), ~ 16x-magnified (R127A) or ~ 3x-magnified (R127K) with respect to their corresponding nitrite complexes. The g values of the LS contributions in the spectra in the absence of nitrite are reported in Chapter 5 (WT, Q74E and Q74V) and in* ***Table*** **6.3** *(R127A and R127K).*

Protein	Species	g_z	g_y	g_x	%
WT	LS1	2.87	2.24	1.64	58
	LS2	2.73	2.40	1.62	29
	LS3	2.69	2.42	1.62	13
Q74E	LS1	2.88	2.23	1.63	59
	LS2	2.74	2.41	1.62	19
	LS3	2.70	2.42	1.62	22
Q74V	LS1	2.88	2.23	1.63	68
	LS2	2.72	2.41	1.62	21
	LS3	2.70	2.43	1.62	11
R127A	HS	1.99	5.61	6.00	9
	LS1*	2.88	2.23	1.58	35
	LS4	2.78	2.38	1.60	56
R127K	LS1*	2.90	2.22	1.57	49
	LS4	2.78	2.38	1.60	51

Table 6.2 *EPR parameters of NO_2^- complexes of WT CCld and variants at pH 7.0 obtained by simulation of the spectra. Simulation of HS species were performed both with the g values of an effective S = ½ system and the g values of a real S = 5/2 system (data not shown); the latter were used to determine % contributions (errors: g values ±0.01, contribution ±1%).*

	Species	g_z^{eff}	g_y^{eff}	g_x^{eff}	g_z	g_y	g_x	E/D	%
***C*Cld R127A**	HS1	2.00	5.86	5.86	2.00	1.95	1.95	0.0011	32
	HS2	2.00	5.59	6.14	2.00	1.95	1.95	0.0115	49
	LS-a				2.76	2.29	1.70	-	19
***C*Cld R127K**	HS1	2.00	5.86	5.86				0.0013	3
	LS-b				3.18	2.09	1.24*	-	53
	LS-c				3.34	2.01	0.91*	-	25
	LS-d				3.47	2.01	0.34*	-	19

Table 6.3 *EPR parameters of the variants R127A and R127K of CCld at pH 7. Simulation of HS species were performed both with the g values of an effective S = ½ system and the g-values of a real S = 5/2 system (with E/D parameter representing the rhombicity); the latter were used to determine % contributions (errors: g values ± 0.01 for R127A, ± 0.1 for R127K, contribution ± 1 %, E/D = ± 0.0005). * Values were calculated assuming the sum of the squares of the g principal values is ~ 16.*

The HS signal of ferric *C*Cld completely converts into new multiple LS contributions, characterized by different *g* anisotropy (simulation parameters reported in **Table 6.2**, simulation in **Figure 6.8**). Among these, LS1 represents the major contribution and it is well distinguishable from LS2 and LS3, which possess rather similar *g* values and are mostly overlapped. When nitrite is added to the Q74E and Q74V variants at the same pH value (**Figure 6.6 A-B** and **Figure 6.7**), the spectrum profile is comparable to the one of wild-type *C*Cld, as the same LS contributions can be detected in similar relative ratios (**Table 6.2** and **Figure 6.8**).

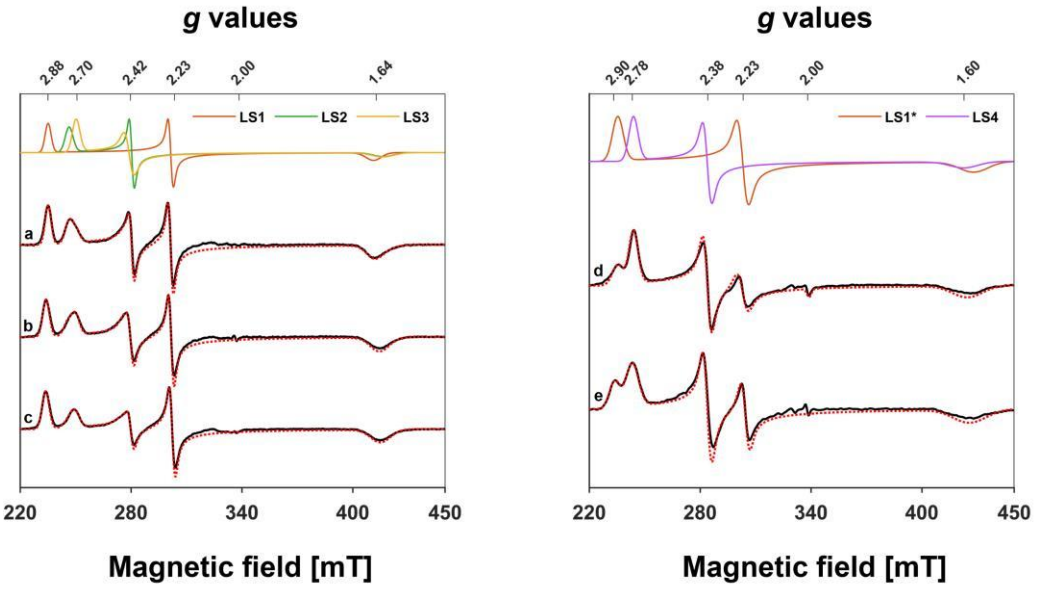

Figure 6.8 *X-band CW-EPR spectra and simulations of NO_2^- complexes of* ***(a)*** *wild-type CCld,* ***(b)*** *Q74E,* ***(c)*** *Q74V,* ***(d)*** *R127A and* ***(e)*** *R127K at neutral pH (low-spin region only). Samples were prepared either in 50 mM TIP buffer (WT CCld) or in 50 mM sodium-phosphate buffer (CCld variants), pH 7. Solid black: experimental spectrum; dashed red: simulation; single species obtained from simulations are shown according to color legend. Measurements were performed with microwave powers of either 2 mW (NO_2^--Q74 variants complexes) or 1 mW (NO_2^--R127 variants complexes). Spectra are shown normalized to their maximum intensity.*

Figure 6.6 C and D depict the EPR spectra of the variants ferric R127A and R127K with and without nitrite at pH 7.0. The exchange of the catalytic arginine to alanine in R127A does not cause dramatic changes in the spectrum, which remains essentially dominated by a HS Fe(III) signal (**Figure 6.9**, left panel), although with increased rhombic character (**Table 6.3**). On the other hand, the EPR spectrum of R127K is clearly different and dominated by new highly anisotropic LS features

characterized by very broad and poorly resolved lines, which impede precise estimation of the *g* values and even the detection of the HS features (**Figure 6.9**, right panel, **Table 6.3**). These spectral features, in accordance with the previously shown UV–vis spectral signatures, indicate that the lysine in the R127K mutant is able to coordinate the heme iron, as demonstrated by the X-ray crystal structure presented above (**Figure 6.1**, B). The EPR spectra of the NO_2^- complexes of R127A and R127K are again dominated by LS species. A signal with similar principal *g* values to LS1 (therefore referred as LS1*) and a new LS species (LS4) contribute almost equally to the spectrum (**Figure 6.6**, C and D). Notably, in the case of R127A some contribution from the HS signal (9 %) remains after the addition of nitrite (**Table 6.2**).

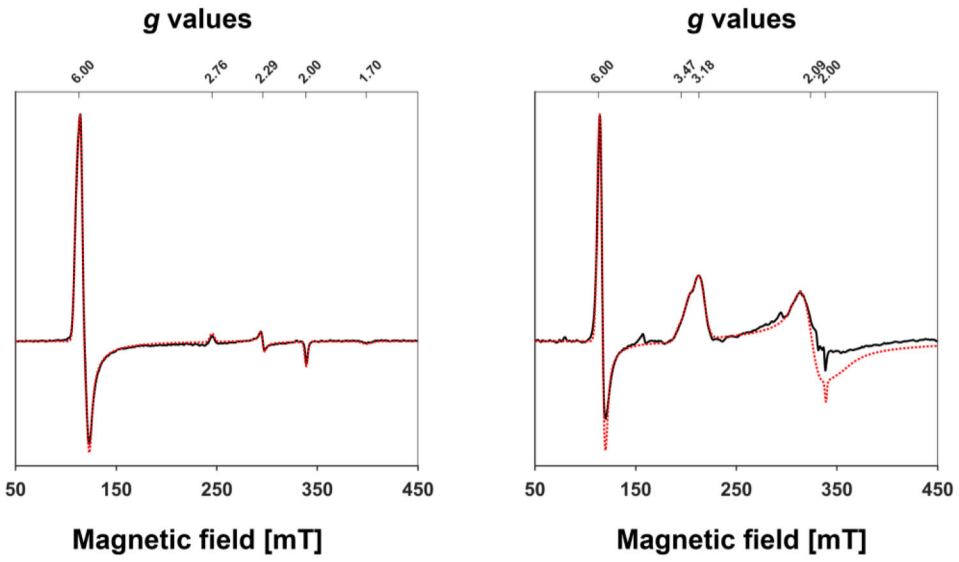

Figure 6.9 *X-band CW-EPR spectra and simulations of R127A (left panel) and R127K (right panel) at pH 7. Samples were prepared in 50 mM sodium-phosphate buffer. Solid black: experimental spectrum; dashed red: simulation. Measurements were performed with microwave powers of 1 mW. Spectra are shown normalized to their maximum intensity.*

In addition, the EPR spectra of wild-type *C*Cld and the variants Q74V and Q74E with nitrite were also measured at pH 8.5, using either a mixture of phosphate and borate buffers or a Tris-HCl buffer (**Figure 6.10**). The samples were prepared in two different buffers in order to be able to compare the EPR results with other biochemical experiments, where phosphate-based buffers are used, and with the crystal structures, since Tris-HCl buffer is the system used in the crystallization conditions. Moreover, as extensively discussed in Chapter 4, it is a good practice to test different buffers and experimental conditions when preparing samples for low-temperature EPR spectroscopy, since they might have an unexpected impact in the resulting spectral features.

In the EPR spectra of nitrite-ligated wild-type *C*Cld all three LS species are retained at high pH, although small differences in relative ratios can be observed, with even a very minor contribution from a OH^--ligated LS species noticeable in the sample prepared in Tris-HCl (**Figure 6.10 A** and **Table 6.4**). Conversely, significant changes occur when the NO_2^- complexes of the Q74E and Q74V variants are prepared at alkaline pH. While the LS2 species is no longer detected (as it can be seen by the disappearance of asymmetry in the peaks corresponding to the overlapping LS2/LS3), the EPR contribution from the other species is also altered in favor of LS1, as indicated by the diminished intensity of the g_z and g_y features of LS3 (see red arrows in **Figure 6.10**) and by the ratios calculated from simulations (**Table 6.4**).

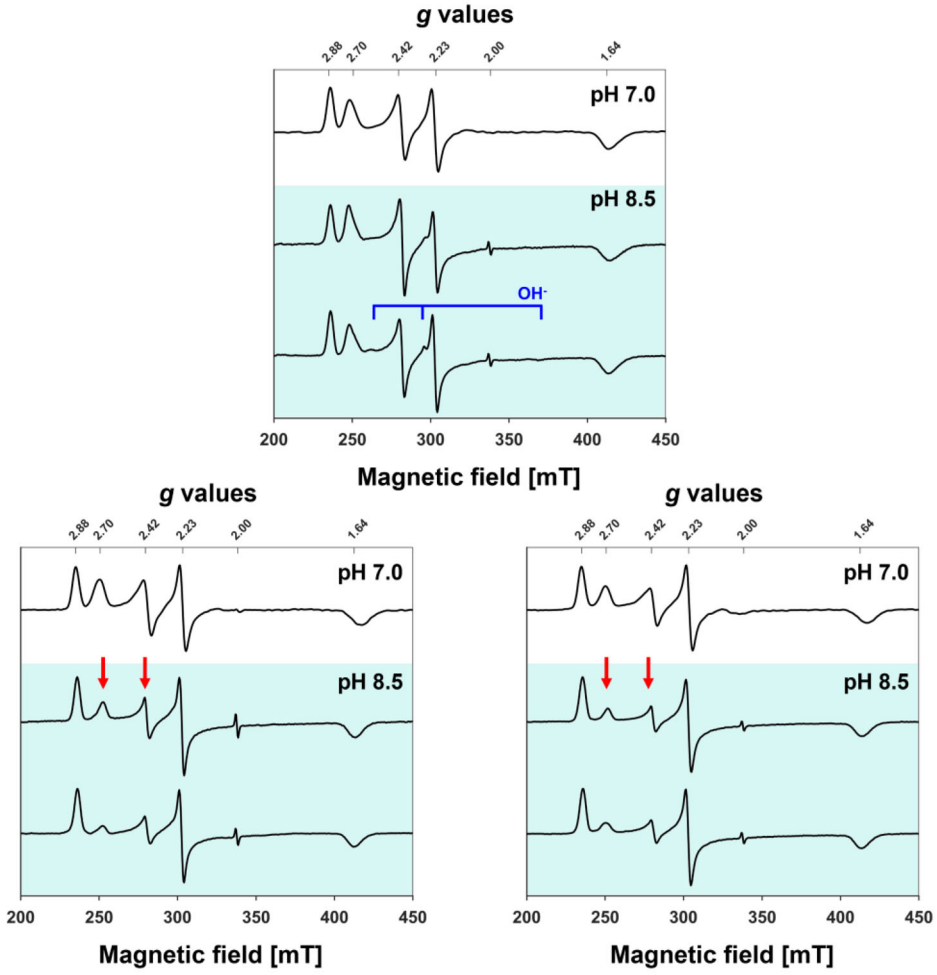

Figure 6.10 *X-band CW-EPR spectra of NO_2^--CCld complexes at different pH values and buffers (LS region only). Top: 50 mM sodium-phosphate buffer, pH 7; middle: 50 mM phosphate/borate buffer, pH 8.5; bottom: 50 mM Tris-HCl pH 8.5. The OH^- LS species is highlighted in blue; red arrows indicate the features with most significant changes. Measurements were performed with microwave powers of either 2 mW (NO_2^- complexes pH 7) or 0.6 mW (NO_2^- complexes pH 8.5). Spectra are shown normalized to their maximum intensity.*

	Species	%
WT		
Phosphate/borate	LS1	49
	LS2	33
	LS3	17
Tris-HCl	LS1	60
	LS2	25
	LS3	13
	OH^-	2
Q74E		
Phosphate/borate	LS1	75
	LS3	25
Tris-HCl	LS1	80
	LS3	20
Q74V		
Phosphate/borate	LS1	85
	LS3	15
Tris-HCl	LS1	86
	LS3	14

Table 6.4 *Relative contributions to the EPR spectra of the NO_2^- complexes of WT CCld and the variants Q74E and Q74V at pH 8.5 in different buffers. Principal g values are given in Table 6.2 for LS1, LS2 and LS3. The OH^- species has $g_z = 2.59$, $g_y = 2.28$ and $g_x = 1.83$ (errors: g values ± 0.01, contribution ±1 %).*

A well-defined predominance of a LS species with *g* values close to those of LS1 (referred as LS1**) is also observable in the EPR spectrum of the NO_2^- adduct of the clade I pentameric chlorite dismutase from "*Candidatus Nitrospira Defluvii*" (*Nd*Cld) [56] at pH 7 that is shown in **Figure 6.11**. Here the addition of nitrite induces the complete disappearance of the rhombic HS signal of ferric *Nd*Cld, but it is not sufficient to remove the highly anisotropic LS contribution (LS0, **Table 6.5**) which dominates the spectrum of *Nd*Cld in absence of the ligand (Chapter 5 and [147]).

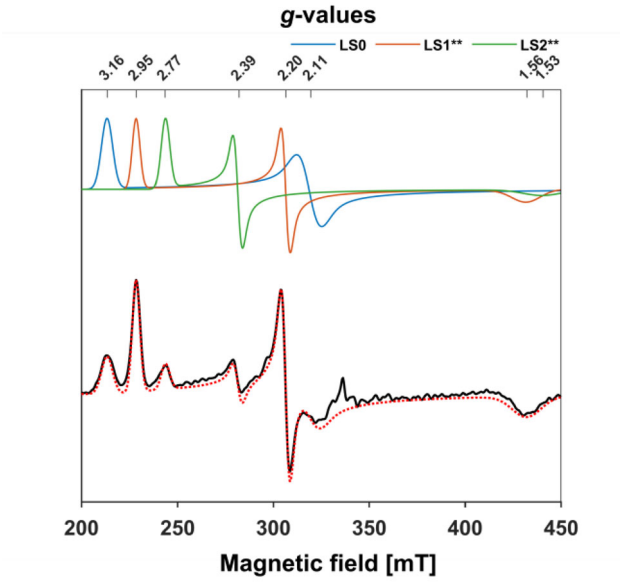

Figure 6.11 *X-band CW-EPR spectrum and simulation of the NO_2^- complex of wild-type NdCld (LS region only). The sample was prepared in 50 mM HEPES buffer, pH 7. Protein concentration was 0.2 mM and $NaNO_2$ was added in a 1000-fold excess. Solid black: experimental spectrum; dashed red: simulation; single species obtained from simulation are shown according to color legend. Measurements were performed with microwave powers of 5 mW. The spectrum is normalized shown to its maximum intensity.*

	Species	g_z	g_y	g_x	%
	LS0	3.16	2.11	1.25*	38
***Nd*Cld**	LS1**	2.95	2.20	1.56	53
	LS2**	2.77	2.39	1.53	9

Table 6.5 *EPR simulation parameters of NO_2^- complexes of WT NdCld at neutral pH (errors: g values ± 0.01, contribution ± 1 %). * Values were calculated assuming the sum of the squares of the g principal values is ~ 16*

6.3.4 MD simulation of nitrite and chlorite binding modes

The dynamics of R127 in ferric HS wild-type *C*Cld, Q74V and Q74E as well as in the respective nitrite complexes was probed by MD simulations. The reader is referred to [115] for the details of the simulations. In brief, in wild-type ferric *C*Cld, without NO_2^-, at least one H-bond is present between R127 and Q74 at all times, being in good agreement with the crystal structure in which R127 is in the "out" conformation. Interestingly, neither Q74E nor Q74V show a comparable homogeneous distribution. In the Q74E variant, the salt bridge seen in the crystal structure between R127 and E74 is only present in 10 or 20 % of the simulation time, while in Q74V the distance between R127 and the heme iron is slightly higher compared to wild-type *C*Cld, most probably because more space is available as valine is smaller [115]. Simulation of the nitrite adducts shows that in wild-type *C*Cld R127 is in the "in" conformation (**Figure 6.12**, top left). Interestingly, the H-bond between $N_\eta 1$ of R127 and Q74 is persistent, whereas the oxoanion is H-bonded to N_ε and $N_\eta 2$. In the ligand-bound Q74V variant, the arginine is in the "in" conformation throughout the whole simulation time and interacts with nitrite *via* N_ε and $N_\eta 2$ (**Figure 6.12**, top right). Interestingly, the nitrite complex of Q74E shows two distinct distances of R127, namely an "in" conformation and an "out" conformation, where this residue is still in a salt bridge with E74 for at least 30 % of the simulation time. As a consequence, two distinct ligation states of nitrite are observed with NO_2^- either ligated directly above the heme iron (as in wild-type *C*Cld and Q74V) or in a "dragged off" conformation. Importantly, MD simulations of the nitrite complexes suggest that besides dominating *O*-ligation, also ligand binding *via* a nitrogen atom could occur. In Q74E *N*-ligation is seen more frequently than in Q74V [115]. Finally, the dynamics of chlorite binding to wild-type *C*Cld and the variants Q74V and Q74E was investigated. MD simulations suggest that if chlorite is bound in the active site, it is positioned in a more upright manner compared to nitrite which adopts a conformation more plane parallel with the heme (**Figure 6.12**). With nitrite, both *O*- and *N*-coordination of the heme iron are observed whereas with chlorite exclusively *O*-ligation is found.

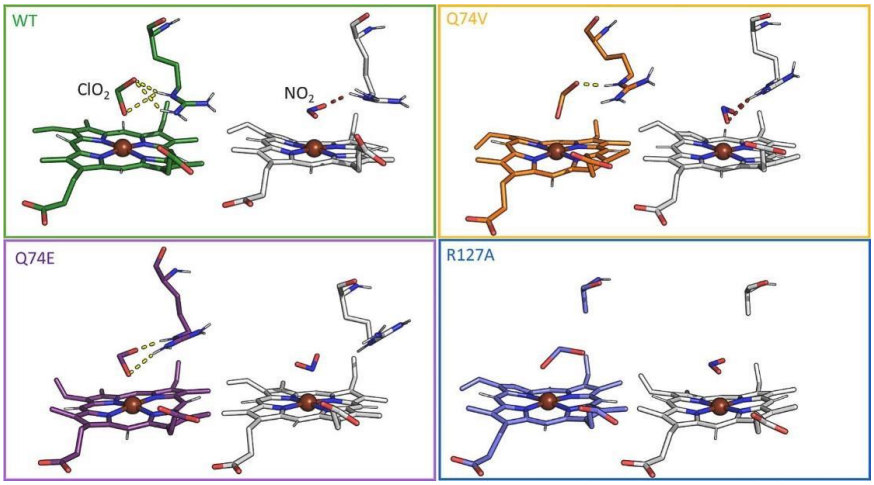

Figure 6.12 *Comparison of exemplary structures showing chlorite (left) or nitrite (right) bound to WT CCld (green) or the variants Q74E (magenta), Q74V (yellow) and R127A (blue) variant. The heme cofactor, the amino acid residues and the ligands are shown as stick representation. Hydrogen bonds between chlorite/nitrite and R127 are shown when present (yellow = chlorite, firebrick = nitrite).*

6.3.5 Chlorite degradation activity of *C*Cld wild-type and variants

It has been shown in Chapter 5 that the flexibility of the catalytic R127 has an impact in the K_M values for chlorite, especially at the pH optimum. The hierarchy of K_M values, being Q74V < wild-type *C*Cld < Q74E, reflects the hierarchy of the K_D values of the nitrite adducts. Exchange of R127 significantly reduces the catalytic efficiency of chlorite degradation. At pH 7.0 for both variants (R127A and R127 K) the k_{cat}/K_M values are decreased by almost 3 orders of magnitude reflected by K_M values in the low mM range and decreased turnover numbers (**Table 6.6**).

***C*Cld**	K_M (µM)	k_{cat} (s^{-1})	k_{cat}/K_M (M^{-1} s^{-1})
Wild-type	43.2 ± 5.2	60.0 ± 0.7	1.4 ± 0.2 × 10^6
Q74V	18.8 ± 3.5	50.8 ± 0.4	2.7 ± 0.5 × 10^6
Q74E	53.8 ± 13.1	37.2 ± 1.1	6.9 ± 2.0 × 10^5
R127A	2031.0 ± 616.1	3.2 ± 0.1	1.7 ± 0.6 × 10^3
R127K	2129.5 ± 111.2	10.1 ± 0.4	4.8 ± 0.5 × 10^3

Table 6.6 *Kinetic Parameters of wild-type CCld and the variants Q74V, Q74E, R127A and R127K at pH 7.0.*

6.3.6 Thermal stability of the nitrite adducts

Next, the impact of nitrite binding on the thermal stability of the five heme proteins was probed by DSC. As mentioned in Chapter 5, unfolding of *C*Cld follows a non-two state transition reflected by two distinct endotherms (T_m1, T_m2). The first unfolding event represents the unfolding of the heme cavity and the release of the prosthetic group, whereas the second transition corresponds to the melting of the overall tertiary fold and the secondary structural elements. In the pH range 5.0 to 9.0, the second transition (T_m2) is similar for ferric wild-type *C*Cld, Q74V, Q74E and R127A whereas R127K exhibits a higher overall stability (**Figure 6.13**). By contrast, significant differences are observed in the T_m1 values of the ferric HS proteins. At pH 5.0 and pH 7.0 the order of stability of the heme cavity follows the order Q74E > wild-type CCld > R127K/R127A > Q74V (**Figure 6.13**). The impact of nitrite binding on the T_m2 values of the respective LS adducts is relatively small. On the other hand, at pH 5.0 the T_m1 values of wild-type *C*Cld, Q74V and R127A are increased by 4.5–6.6 °C, whereas the impact on Q74E and R127K is relatively small (**Figure 6.13**). At pH 7.0, nitrite binding to the heme cavity stabilized the active site architecture of wild-type *C*Cld, Q74V and Q74E, whereas no effect is seen with R127A and R127K. At pH 9.0 the impact of nitrite was modest with all proteins.

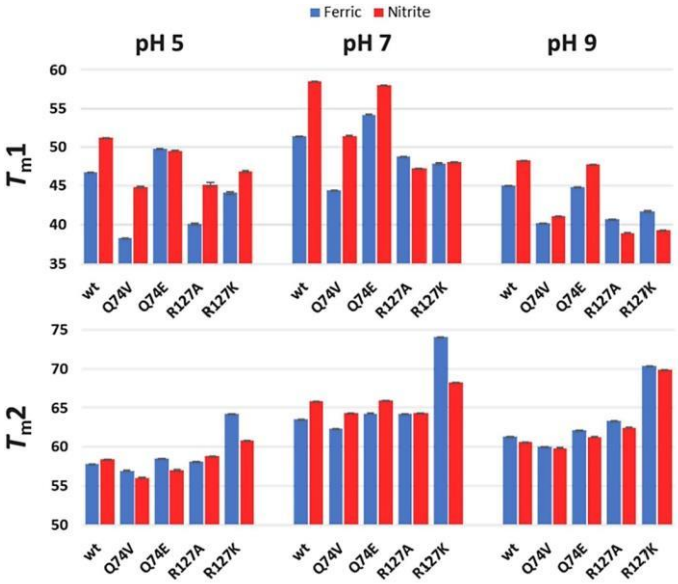

Figure 6.13 *Thermal stability of unbound HS wild-type CCld and the Q74V, Q74E, R127A and R127K and of the corresponding LS nitrite complexes. The comparison of calculated T_m1 and T_m2 values of in the absence (blue) and presence of nitrite (red) at pH 5.0, 7.0 and 9.0 is depicted.*

6.4 Discussion

Catalysis mediated by heme enzymes may involve (among others) the basic amino acid arginine. Often, this arginine can adopt different conformations in the heme cavity within a reaction cycle and thus can influence the reactivity of distinct enzyme intermediates in different ways. This also applies in particular to the enzyme chlorite dismutase, which has only one catalytic amino acid in the distal hydrophobic heme cavity, namely a fully conserved arginine. In Chapter 5 we have demonstrated that (i) this residue in wild-type Clds is flexible, (ii) its dynamics is influenced by its remote H-bonding partner, and (iii) in Q74V this flexibility is more pronounced than in wild-type *C*Cld, whereas in Q74E, R127 is arrested in a salt-bridge with Q74E. Moreover, the differences in the conformational dynamics of R127 has also a strong impact on the HS to LS alkaline transition of the three proteins and on the thermal stability of their corresponding heme cavities.

In general, ligation of nitrite at the distal heme position further increases the thermal stability of the resulting LS complex heme cavity architecture (section 6.3.6). The importance of R127 in the stabilization of the nitrite complexes is underlined by the fact that addition of nitrite to R127A has little impact on the thermal stability (**Figure 6.13**). Interestingly, in the absence of the catalytic arginine, both chlorite and nitrite are still able to bind to the heme iron, as demonstrated by activity assays and spectroscopic findings. In these variants, nitrite mediates the HS to LS transition, but the affinity for this ligand is significantly lower than in wild-type *C*Cld and Q74 variants and it mirrors the increased K_M for the substrate chlorite (**Table 6.1** and **Table 6.6**). This clearly underlines the importance of R127 in stabilizing both the substrate adduct and the nitrite complex. The higher the flexibility of R127, the higher is its stabilizing effect on the respective complexes. At pH optimum and neutral pH, Q74V shows the highest affinity for both chlorite and nitrite, followed by wild-type *C*Cld and Q74E. The K_D values for nitrite significantly increase with increasing pH suggesting that the interaction between R127 and the nitrite is impaired at alkaline pH (**Table 6.1**). This is supported by the fact that addition of nitrite to wild-type *C*Cld as well as to Q74V and Q74E at pH 9.0 has no impact on the thermal stability compared to pH optimum or neutral pH.

In contrast to the published fluoride and thiocyanate complexes of *C*Cld, where R127 is in the “out” conformation [55], the crystal structures of the nitrite complexes of wild-type *C*Cld, Q74V and Q74E show R127 in the “in” conformation (**Figure 6.2**, A-C) suggesting that the anionic distal ligand offers energetically more favorable interactions for the guanidinium group compared to the H-bond between R127 with Q74 in the ferric HS wild-type *C*Cld or even the salt-bridge between R127 and E74 in the variant Q74E. This is supported by the UV–vis data that suggest

similar solution structures of the nitrite adducts of wild-type *C*Cld, Q74V and Q74E (section 6.3.2). The pronounced differences seen in the respective absorption spectra of the three proteins in their HS ferric resting state are in large part diminished upon addition of the anionic ligand between pH 5.0 and pH 7.0.

The crystal structures of the nitrite complexes of wild-type *C*Cld suggest that nitrite is coordinated to the heme iron *via* an oxygen atom with O-Fe distances ranging from 2.1 to 2.4 Å. The two oxygen atoms of the ligand are hydrogen bonded to $N_{\eta}2$ and/or N_{ε} of the arginine. On the other hand, differences are observed in the MD simulations of the nitrite complexes, offering an explanation for the increased K_D and K_M values observed in Q74E. In the nitrite and chlorite complex of this variant, R127 can adopt two conformations and, as a consequence, two binding *modi* for nitrite are observed. This seems to have a more pronounced effect on k_{off} than on k_{on} and could explain the increased K_D value of the nitrite complex of this variant. Importantly, MD simulations show that *N*-ligation of nitrite is also possible; this agrees with the EPR data, which also clearly show the presence of multiple LS species in the spectra of the NO_2^- ligated proteins. All the NO_2^- adducts investigated in this work show at least two well-resolved contributions from LS ferric heme species in their X-band CW-EPR spectra (**Figure 6.5** and **Figure 6.6**). The appearance of multiple LS signals in the EPR spectra of heme proteins upon addition of nitrite has been extensively described [215–219]. These observations have been attributed either to nitrite linkage isomerism [216], different ligand orientations in distinct subunits [219], heme ruffling (*e.g.*, distortions outside the porphyrin plane) or variations in the extended H-bonding network both at the proximal and the distal side of the heme iron [217, 218].

We propose that the different LS contributions in the EPR spectra of NO_2^--Clds complexes might represent the binding of the ligand via either *O*-linkage or *N*-linkage. To support this hypothesis, an analysis of the crystal-field parameters using Taylor's formalism for ferric low-spin heme complexes was performed [122, 123, 126, 213]. The parameters, calculated for each LS contribution according to equations 6.1 – 6.3 (see section 6.2.2), are reported in **Table 6.7** and were used to construct the "Blumberg-Peisach" diagram depicted in **Figure 6.14** [124], which has been used in the past to classify different iron ligation patterns. In this case, the LS species clearly fall into two distinct clusters. LS1 and the closely related LS1* and LS1** form a compact group with predominant tetragonal character characterized by $\Delta/\lambda \sim 4$ and $V/\Delta \sim 0.5$, while LS2, LS3 and LS4 constitute a more heterogeneous set with $2.35 \leq \Delta/\lambda \leq 2.70$ and $0.86 \leq V/\Delta \leq 1.09$.

Protein	Species	Crystal field parameters			Ref.
		V/λ	**Δ/λ**	**V/Δ**	
	LS1	2.14	4.05	0.53	
*C*Cld wild-type	LS2	2.47	2.56	0.96	
	LS3	2.57	2.41	1.06	
	LS1	2.10	4.03	0.52	
*C*Cld Q74E	LS2	2.46	2.55	0.96	
	LS3	2.56	2.40	1.07	
	LS1	2.09	4.05	0.52	
*C*Cld Q74V	LS2	2.49	2.51	0.99	This work
	LS3	2.56	2.35	1.09	
*C*Cld R127A	LS1*	2.03	3.70	0.55	
	LS4	2.34	2.68	0.87	
*C*Cld R127K	LS1*	1.98	3.76	0.53	
	LS4	2.32	2.70	0.86	
*Nd*Cld wild-type	LS1**	1.89	3.98	0.47	
	LS2**	2.23	2.38	0.94	
HsMb		1.74	4.06	0.46	
MetHb		1.77	2.91	0.61	[218, 220]
		1.80	3.59	0.50	
NP4		2.26	2.17	1.04	[217]

Table 6.7 *Crystal field parameters of NO_2^- complexes determined from the principal g values for different chlorite dismutases and reference heme proteins; HsMb = horse heart myoglobin, MetHb = human hemoglobin, NP4 = nitrophorin 4.*

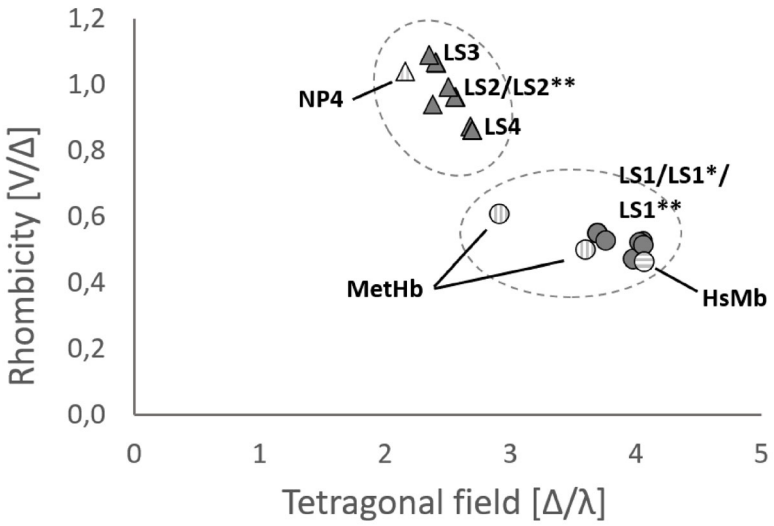

Figure 6.14 *"Blumberg-Peisach" diagram constructed with crystal-field parameters values from* ***Table 6.7****. LS species obtained from simulations of NO_2^--ligated complexes of wild-type CCld and variants are represented in filled circles and triangles. Reference nitrite-bound heme proteins are depicted in striped circles and triangles.*

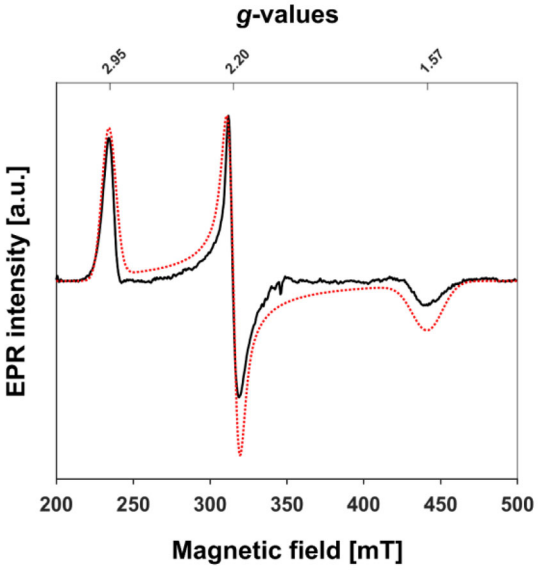

Figure 6.15 *X-band CW-EPR spectrum and simulation of NO_2^--HsMb complex (LS region only). Sample was prepared in 50 mM Tris-HCl buffer, pH 7. Mb 0.3 mM, $NaNO_2$ 150 mM. Solid black: experimental spectrum; dashed red: simulation. Measurement was performed with a microwave power of 0.6 mW. The spectrum is shown normalized to its maximum intensity.*

The only LS species formed when nitrite is added to the model heme protein myoglobin at pH 7 (**Figure 6.15**) has *g* values and crystal-field parameters similar to LS1, falling therefore in the same cluster. In fact, the EPR parameters found for the NO_2^--Mb complex are consistent with the ones reported in previous studies on globins [216, 219, 221]. Interestingly, it has been shown that both myoglobin and hemoglobin coordinate the nitrite anion with a *O*-nitrito mode [16, 220]. In globins this mode of binding is promoted by the presence of a H-bond donor residue at the distal side of the heme iron, a role that in Clds could be likely played by the catalytic arginine. In particular, as shown by Yi *et al.*, in the H64V/V67R double mutant of myoglobin a rearrangement of the mutated arginine sidechain toward the nitrite anion is observed [220], which is reminiscent of the conformational switch described for the catalytic arginine in chlorite dismutases turnover [53–60, 65, 148, 181, 201, 211]. The attribution of the LS1 cluster to the *O*-linkage binding mode is also consistent with previous findings on clade I chlorite dismutases. A spectroscopic investigation of the hexameric chlorite dismutase from *A. orizae* (*Ao*Cld) in presence of nitrite showed the formation of a LS species (*g* values = [2.93 2.18 1.55]) with very similar features to the LS1** of *Nd*Cld (**Figure 6.11** and **Table 6.5**) [48] . Later, the crystal structure of the nitrite complex of the pentameric (clade I) chlorite dismutase from *Dechloromonas aromatica* (*Da*Cld) was published, revealing a coordination of nitrite to the heme iron through *O*-linkage [59]. Additional LS components, namely LS2 (LS2** for *Nd*Cld), LS3 and LS4, have remarkably similar *g* values to the ones of nitrite adducts of some heme *b*-containing proteins from the class of nitrophorins. Indeed, a LS species with *g* values = ~ [2.7 2.4 1.5] was identified as the major contribution in the CW-EPR spectra of these proteins, however, other signals from LS with higher *g* anisotropy were observed as well [217, 218]. Among the known isoforms of nitrophorins, NP4 has been crystallized in presence of nitrite, showing a *N*-nitro coordination mode. It is therefore tempting to attribute the signals from LS2, LS3 and LS4 in chlorite dismutases to the coordination of nitrite via the nitrogen atom.

Particularly interesting is that even in the absence of the catalytic arginine (R127A and R127K) the features of a nitrite adduct are clearly distinguishable in the EPR spectra (**Figure 6.6 C-D**). The residual HS signal in the spectrum of the NO_2^- complex of R127A (**Figure 6.6 C**) reflects the very low affinity of nitrite for this mutant. In the case of R127K, the highly anisotropic LS features present in the unbound protein (**Figure 6.6 D** and **Figure 6.9**, right panel) are assigned to the coordination of the heme iron by the lysine residue replacing the catalytic arginine, in accordance with UV–vis findings (**Figure 6.4**) and crystal structure (**Figure 6.1**). The *g* values of these contributions (**Table 6.3**) are consistent with the ones reported for lysine coordination in other heme systems [180, 222–224]. It has to be noted that due to the high pK_a of Lys (~ 10.5), its binding to the heme iron should

be unfavored at neutral pH. On the other hand, the ferric heme iron is a strong Lewis-acidic species that significantly decreases the pK_a values of protic ligands. Nonetheless, it has been reported that lysine can act as a distal ligand in particular heme systems, giving rise to a mixture of penta- and hexacoordinate heme iron, both in its reduced and oxidized states [225]. The factors responsible for Lys-Fe stabilization have been shown to be related to specific interactions established either between the side-chains of (polar) residues found in the heme proximity or between the heme propionate groups and the protein moiety [226]. In the case of Cld, such polar and anionic interactions need to be excluded, given the hydrophobic character of the heme pocket. Similarly, a change in local pH, which could explain the deprotonation of lysine, appears unlikely, since the UV–vis and EPR spectra of alkaline Clds show clear differences from the Lys-coordinated form [201]. Therefore, the determinants of lysine coordination in chlorite dismutases remain to be elucidated. Nonetheless, the *g* values of LS-b (**Table 6.3**), which is the main LS contribution in the R127K variant, are remarkably similar to those of the highly anisotropic LS species found in *Nd*Cld both at acidic/neutral and basic pH values (LS0, see **Table 6.5** and **Figure 6.11**) [201]. This would suggest a similar nature of the distal ligand and a possible coordination by the catalytic arginine in *Nd*Cld, provided that particular factors could allow a suitable protonation state of this residue at low pH. However, this hypothesis is purely speculative to date.

Interestingly, while LS0 in *Nd*Cld persists in the nitrite-adduct of the same enzyme to some extent (**Table 6.5** and **Figure 6.11**), from the EPR spectra of the NO_2^- complex of R127K it is evident that nitrite is able to displace the lysine, at least when present in high excess, since the LS features of the unbound enzyme are replaced by LS1* and LS4 (**Figure 6.6 D** and **Figure 6.7**). Finally, in R127A and R127K the *N*-linkage binding mode could be favored by the absence of a H-bond donor residue, in line with what was stated above. This is also supported by the increased contribution of LS4 in the EPR spectra (**Figure 6.6 C-D**, **Figure 6.7** and **Table 6.2**). Although all the crystal structures of the available NO_2^--*C*Cld complexes (**Figure 6.1** and **Figure 6.2**) show a nitrite molecule bound to the heme iron through *O*-linkage, it is possible that only one mode of coordination is stable enough to be resolved under the crystallization conditions. On the other side, the EPR of frozen samples might be considered as a more representative "snapshot" of a natural state in which less favored binding *modi* can occur as well, without excluding that cryogenic conditions may also favor states that are less populated at higher temperatures.

6.5 Conclusions

In summary, it has been demonstrated that the flexibility of the catalytic arginine of clade II chlorite dismutases has a strong impact on the thermodynamics of binding of the angulate oxoanions nitrite and chlorite. At pH optimum (*i.e.*, pH 5.5) and neutral pH the K_D value for nitrite and the K_M value for chlorite are lowest when R127 is highly flexible and highest when R127 exhibits a salt bridge with E74. Upon ligand binding this salt bridge is broken and, similar to wild-type *C*Cld and Q74V, R127 forms two H-bonds with nitrite that is mainly *O*-ligated to the heme iron. Nevertheless, multiple binding *modi* of nitrite are suggested by both MD-simulations and EPR spectroscopy. By contrast, MD simulations demonstrate that chlorite is always *O*-ligated and interacts with R127 in a slightly different manner compared to nitrite. In the absence of the catalytic arginine both oxoanions are still able to bind, but the resulting low-spin ferric heme complexes are extremely unstable as reflected by significantly increased K_D and K_M values. A pronounced increase in K_M has also been observed in the R183A variant of *Da*Cld [58], whereas the effect was smaller with clade I Cld from *Nd*Cld [57]. Importantly, the K_D value of nitrite significantly increases with increasing pH and differences within variants with modulated H-bonding network of the catalytic arginine (Q74V, Q74E) disappear at pH values higher than 8.5. The spectroscopic data clearly suggest structural rearrangements in the heme cavity at alkaline pH that could be responsible for the decrease in affinity of the oxoanions. In any case, this suggests that the thermodynamics of substrate binding, *i.e.*, substrate adduct formation, might contribute to shaping the overall pH-dependence of chlorite degradation.

Immediately after substrate binding via *O*-ligation to Fe(III) and concomitant establishment of H-bonds between the two oxygen atoms of chlorite with R127 in the “in” conformation, the redox reaction takes place and chlorite is converted to chloride and dioxygen. As already explained in Chapter 5, in the course of the reaction, the catalytic R127 most probably stays in the “in” conformation and keeps the transient intermediates in the reaction sphere in order to avoid oxidative damage of the protein matrix and the prosthetic group [65, 66]. However, this implies dynamic rearrangements of the original hydrogen bonds, which are established in Compound I or Compound II. After the cleavage of chlorite, migration and rotation of the intermediates, the rebound step and molecular oxygen formation take place with both oxygen atoms being H-bonded with R127 as suggested by a density-functional theory (DFT) study [66]. Finally, to facilitate the departure of the chloride anion, the hydrogen bonds between R127 and the two oxygen atoms are required to rearrange again to the terminal negatively charged chloride [66]. The present data suggest that at pH < 7 the impact of the flexibility of R127 on the formation of the intermediate states and release of the products is

small. However, at alkaline pH - due to structural rearrangement of the distal H-bonding network - the function of R127 as dynamic H-bonding partner seems to be impaired and the catalytic efficiency significantly decreases. Transient oxidizing intermediates are released from the reaction sphere and as a consequence the level of irreversible inhibition increases with increasing pH as observed in all Clds studied so far [65, 148].

Chapter 7

HYSCORE spectroscopy of nitrite-bound myoglobin and chlorite dismutase

Abstract

The physiological roles of nitrite and its interaction with heme proteins have received a great deal of attention from the late 1980s. Alongside with its several biological functions in mammals, nitrite is known to play a fundamental role in the environmental nitrogen cycle and to be able to interact with different bacterial enzymes. In Chapter 6, I presented a CW-EPR investigation and crystal-field analysis of the binding modes of nitrite to the heme-containing enzyme chlorite dismutase. Nitrite was taken as a substrate analogue of chlorite for its similarity with this angulate oxoanion. EPR spectroscopy, supported by molecular dynamics simulations, provided preliminary evidence for two possible coordination modes of nitrite, either *via O*-nitrito or *N*-nitro ligation, for the wild-type and mutant forms of the chlorite dismutase from *Cyanothece* sp. PCC7425 (*C*Cld). In this Chapter, HYSCORE spectroscopy is used to investigate the hyperfine interaction of the heme unpaired electron with the surrounding nuclei in wild-type *C*Cld. Because of the complexity of the *C*Cld-nitrite EPR profile, which includes at least two different low-spin contributions, ferric myoglobin was taken as a model system. The EPR of the nitrite-bound myoglobin is characterized by a single low-spin species, ascribed to the coordination *via* the *O*-nitrito binding mode, through comparison with crystallographic data. Thus, the nitrite-bound myoglobin is here investigated to obtain a "fingerprint" HYSCORE spectra for the *O*-nitrito coordination mode. In addition, experiments with ^{15}N-labelled nitrite have been performed in the attempt to discriminate the signals ascribed to the N nuclei of nitrite from the many endogenous N nuclei of the heme and protein moieties. These findings are discussed in the context of the interaction of nitrite with heme-containing systems in general, in addition to their relevance in the biochemistry of chlorite dismutases.

Own contribution: experiments execution and data analysis. This chapter contains original, unpublished work.

7.1 Introduction

Some knowledge on the physiological effects of inorganic nitrogen oxides has been there for centuries. Historical records suggest that nitrate and nitrite salts may have been used in Chinese traditional medicine to treat cardiovascular diseases as early as 800 AD [227]. Towards the end of the 19th century, it was observed that addition of nitrite to cured meat helped to preserve its red color. The use of nitrite as food preservative became a common practice, especially later in the 1970s when it was demonstrated its beneficial effect in controlling contaminations from *Clostridium botulinum*. However, the widespread use of nitrite raised some controversies when it was associated to a higher incidence of cancer due to the formation of N-nitrosamines [228, 229].

From a medical point of view, by the first half of the 20th century it was already proposed that nitrite-derived nitric oxide (NO) and nitrite itself could interact with hemoglobin and that their metabolism might be linked to blood flow regulation [230]. Later in the 1980s, the breakthrough scientific discovery of the role of NO as a signaling molecule in the cardiovascular system, which granted its authors the Nobel Prize in Physiology or Medicine in 1998 [231], boosted the research on the (patho)physiological relevance of other nitrogen oxides anions, including nitrite (NO_2^-). In the early 2000s a previously unknown nitrite reductase activity of deoxyhemoglobin was described for the first time [232]. This finding, among others, redefined the role of NO_2^- as an active player in several biological functions, with potential implications in oxygen sensing, signaling pathways and as an oxygen-independent reservoir of NO. In addition to hemoglobin, the reductase activity was later demonstrated for other proteins in mammalian cells, including myoglobin [233] and xanthine oxidase [234]. The relevance of nitrite in the medical field was further highlighted by studies on its interaction with myeloperoxidase (MPO) and eosinophil peroxidase (EPO), the most abundant heme peroxidases in the leukocytes. These enzymes were shown to be able to catalyze the NO_2^--mediated formation of nitrotyrosine, a marker of oxidative damage induced by the formation of reactive nitrogen species (RNS) in inflammatory processes [235, 236].

In addition to its importance in the physiology of mammals, nitrite plays a fundamental role in the environmental nitrogen cycle, being the substrate of bacterial nitrite reductases (NiR), heme enzymes which reduce it to ammonia in a six-electron transfer process [237, 238]. Moreover, a unique disproportionation of nitrite to NO and NO_3^- was described for heme-containing enzymes found in the saliva of the blood feeding insect *Rhodnius prolixus* [217, 239, 240]. These enzymes, which were given the name of nitrophorins (NPs), have been extensively

characterized from a structural point of view, in order to understand the determinants of their peculiar reactivity [217, 218, 241]. In fact, the coordination chemistry of NO_2^- in different heme systems has been subject of numerous works which aimed at elucidating the mode of binding of this anion to the heme iron and thus gaining mechanistic insights. While in most case studies nitrite binds to the ferric heme iron through the so-called *N*-nitro mode [218], the crystal structures of the nitrite-bound *met*-myoglobin and *met*-hemoglobin show a less common *O*-nitrito ligation [16, 220]. A site-directed mutagenesis approach coupled to structural and spectroscopic analysis revealed that in myoglobin the distal E7His is responsible for the *O*-ligation mode [17] and suggested a possible analogue role of the conserved distal histidine in human hemoglobin. Recently, the interaction of nitrite with the ferric protoglobin from *Methanosarcina acetivorans* (*Ma*Pgb) was explored with different spectroscopic techniques [214]. This protein was chosen as a model for the characterization of the heme-nitrite interaction because of some unique characteristics, including a highly-distorted heme group and an unusual valine residue replacing the E7His normally conserved in globins (Chapter 1). Interestingly, evidence of the formation of a Fe(III)-NO complex, instead of a nitrite-bound species, was found. Since this study was conducted at pH 5, the authors proposed that *Ma*Pgb would quickly trap the NO formed by the spontaneous disproportionation of nitrite in acidic conditions [242]. Although the binding of NO could also suggest a nitrite dismutase activity, no clear evidence was obtained to support this hypothesis; on the other hand, the intrinsic resilience to nitration of *Ma*Pgb, pointed at a possible RNS scavenging role of this protein, as also suggested in a former study [243]. In another recent work from Van Brempt *et al.* [244], the binding of nitrite to the heme group of largest known globin (GLB-33) of the model system *Caenorhabditis elegans* (*C. elegans*) was studied by means of resonance Raman, optical and EPR spectroscopies. GLB-33 consists of a globin domain (GD) and a 7 α-helices transmembrane domain. Although the role of GLB-33 *in vivo* has still to be elucidated, it was observed that, *in vitro*, the GD of GLB-33 possesses a significant nitrite reductase activity [245]. Through CW-EPR experiments, Van Brempt *et al.* observed that upon addition of nitrite, at least two signals ascribed to LS NO_2^--bound species were present and that the amount of these different contributions was highly pH-dependent. With the aid of crystal field analysis, they attempted the attribution of the two signals to two different binding modes of nitrite, as similarly proposed in this thesis for the chlorite dismutase enzyme (Chapter 6). A more detailed discussion on these findings and how they compare with the results presented in this Chapter, will be given in section 7.4.

Following the increased interest on the interaction of nitrite with heme proteins, this Chapter focuses on the in-depth spectroscopic analysis of nitrite binding to the wild-type *C*Cld and ferric Mb. In Chapter 6, nitrite was used as a substrate analogue

of chlorite to investigate the initial steps of the chlorite dismutase catalytic cycle. The CW-EPR spectra of wild-type and variants *C*Cld in complex with nitrite, both at neutral and alkaline pH, were presented. The appearance of multiple LS species upon addition of nitrite was attributed to the possible co-existence of the *N*-nitro and *O*-nitrito binding modes, as suggested by the analysis of the crystal-field parameters and supported by MD simulations [115]. In this work, we used HYSCORE spectroscopy (Chapter 2) such to reveal the hyperfine interactions between the unpaired electron of the paramagnetic heme iron and the surrounding nuclei and thus to elucidate the binding modes of nitrite to *C*Cld. In an attempt to distinguish the nitrite-specific signals from the ones of the numerous nitrogen nuclei in the heme iron proximity (*i.e.* from the pyrrole and the proximal histidine), both ^{14}N and ^{15}N-labelled NO_2^- were used. Moreover, the binding of nitrite to Mb was investigated with the same approach to obtain a spectroscopic "fingerprint" of the *O*-nitrito binding mode, which is known to exclusively occur in this system [16]. Even though the ability of *C*Cld to bind nitrite *via* both *N*- and *O*-ligation does not necessarily reflect the actual binding of chlorite, the characterization of this interaction might shed a light on how different heme systems can modulate the binding of this biologically important anion.

7.2 Experimental procedures

7.2.1 Materials

Standard and ^{15}N-labelled sodium nitrite ($NaNO_2$) were purchased from Sigma Aldrich. Tris-HCl pH 7.0 was prepared at a concentration of 100 mM. A "temperature independent (TIP)" buffer was prepared by mixing 45% HEPES pH 7.0 and 55% sodium phosphate buffer pH 7.0 in order to minimize the variation in pH due to the freezing [195]. Both buffers were filtered and degassed prior use. Myoglobin (Mb) from horse skeletal muscle (95–100% pure, essentially salt-free, lyophilized powder) was also purchased from Sigma-Aldrich and used without further purification. Wild-type chlorite dismutase from *Cyanothece* sp. PCC7425 (*C*Cld) was recombinantly produced in *E. coli* BL21 Gold (DE3) cells (Agilent) and purified as previously described [201]. The solutions of $NaNO_2$ were freshly made before each experiment. Myoglobin samples were prepared as follows: sodium nitrite (either standard or ^{15}N-labelled) was dissolved in 100 mM Tris-HCl pH 7 to a final concentration of 1 M. Then, 50 µL of this solution were mixed with 50 µL of glycerol in order to obtain a solution containing 50 mM Tris-HCl, 500 mM $NaNO_2$ and 50% (v/v) glycerol. Next, ~ 2 mg of lyophilized Mb were dissolved in the buffered nitrite solution to reach a final protein concentration of ~ 1 mM. Samples of wild-type *C*Cld

were prepared by mixing 50 µL of glycerol and 50 µL of a solution containing 100 mM TIP buffer pH 7.0, 1 M $NaNO_2$ and 2 mM *C*Cld in order to obtain the same final concentrations and nitrite-to-protein ratio as in the Mb samples.

7.2.2 EPR spectroscopy

Both CW and pulsed EPR measurements were performed on a Bruker ELEXSYS E580 X-band spectrometer equipped with an Oxford CF935 continuous-flow cryostat and a Bruker ER4118 SPT-N1 resonator (operating at a MW frequency of ~ 9.7 GHz). CW-EPR spectra were recorded at 10 K under non-saturating conditions, with a modulation amplitude of 1 mT and a modulation frequency of 100 kHz. For field-swept ESE-detected EPR measurements, a Hahn echo sequence $\pi/2$–τ–π–τ–echo with 2-step phase cycling was used. $\pi/2$ (π) pulse length of 16 (32) ns, a shot repetition time of 1 ms and τ of 264-268 ns (for myoglobin samples) or 240 ns (for *C*Cld samples) were chosen. The HYSCORE experiments were performed using the sequence $\pi/2$–τ– $\pi/2$-t_1-π–t_2- $\pi/2$-τ–echo with $\pi/2$ (π) pulse length of 16 (32) ns and t_1 and t_2 varied from 112 to 4284 ns in steps of 28 ns, with a shot repetition time of 1 ms. Simulations of CW- and pulsed EPR spectra were performed with the EasySpin software implemented in MATLAB (v. 6.0.0-dev.41) [188].

7.3 Results

7.3.1 Spectral signature of the *O*-nitrito binding mode in ferric myoglobin

As discussed in Chapter 6, the binding of nitrite to the ferric (wild-type) myoglobin occurs through the uncommon *O*-nitrito mode. As a continuation of the work presented there, in this Chapter this system is used to obtain a spectral fingerprint of the *O*-binding mode in HYSCORE spectra. With the intent of discerning the signals from the multiple nitrogen atoms in the heme iron proximity from the coupling with the ligand nuclei, ^{15}N-labelled nitrite was used in addition to standard nitrite. As shown in **Figure 7.1 A**, the CW-EPR, performed either with standard or ^{15}N-labelled nitrite, do not show significant differences, indicating that the binding mode in the two cases is the same. The spectra can be successfully simulated with the g values reported in Chapter 6 (section 6.4). Note that the different echo intensities in the corresponding ESE-detected EPR spectra (**Figure 7.1 B**) can be attributed to distortions induced by nuclear modulation effects [246].

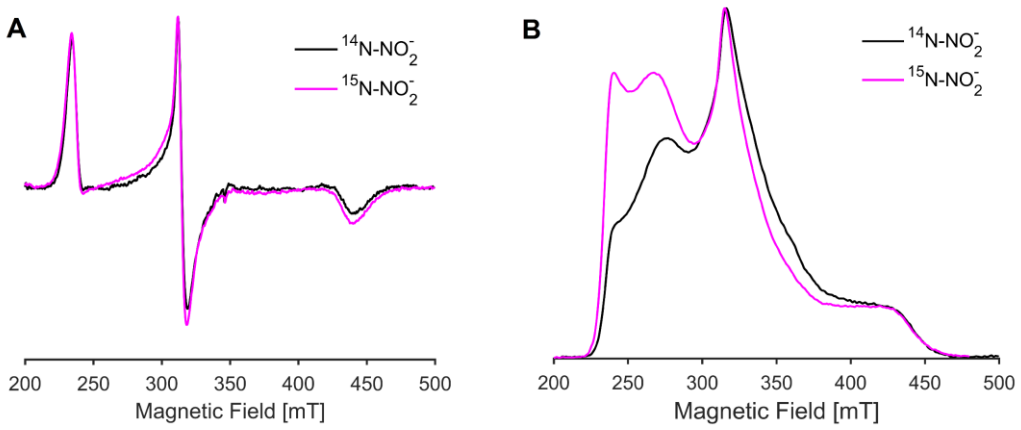

Figure 7.1 (A) *X-band CW-EPR and* ***(B)*** *ESE-detected EPR spectra of 1mM ferric horse heart myoglobin in presence of 500 mM of either standard (black) or ^{15}N-labelled (magenta) nitrite, at pH 7.0.*

The ^{14}N-HYSCORE spectra of the nitrite-bound myoglobin, taken at the observer positions corresponding to the principal g values, are depicted in **Figure 7.2 A-C**. At the position corresponding to $g = g_z$ (orientation selection along the normal of the heme plane), the spectral features appear better resolved (**Figure 7.2 A**) and allow a relatively easy peak assignation. The characteristic spectral shape typical of a heme system, with strong double-quantum (DQ) peaks in the (-, +) quadrant ascribed to the four pyrrole nitrogens, can be easily recognized [247, 248]. This assignment is further corroborated by the presence of peaks in the high-frequency region of the (-, +) quadrant that agree with combinations of the DQ frequencies of individual ^{14}N nuclei. These peaks are clearly resolved at both $g = g_z$ and $g = g_x$ positions, the latter depicted in **Figure 7.2 D**. An additional DQ peak is clearly distinguishable at all magnetic field positions, which is assigned to the strongly coupled ^{14}N from the proximal histidine (F8His, Chapter 1). The single-quantum (SQ) peaks assigned to the coupling with the histidine nitrogen are also easily identified at the $g = g_z$ position (**Figure 7.2 A**). In the (+,+) quadrant, extra signals in the low frequency region can be attributed to the weakly-coupled ^{14}N from nitrite, as explained later. In line with the expected *O*-nitrito binding mode, these spectra do not provide evidence of a strongly-coupled ^{14}N nucleus from nitrite.

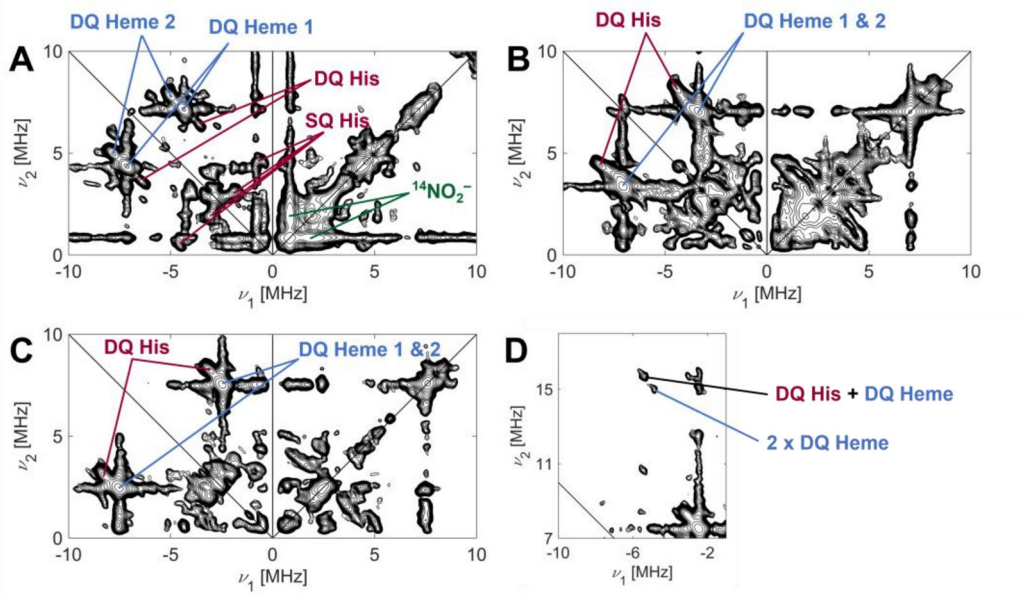

Figure 7.2 *X-band ^{14}N-HYSCORE spectra of 1 mM ferric horse heart myoglobin in presence of 500 mM of $^{14}NO_2^-$, pH 7.0, taken at the magnetic-field observer positions corresponding to* ***(A)*** *g_z (234.7 mT),* ***(B)*** *g_y (315.8 mT) and* ***(C)*** *g_x (440 mT). The spectra represent the sum of three τ values (96, 176 and 208 ns), normalized to the noise level. Panel* ***(D)*** *depicts the high-frequency region of the spectrum in* ***(C)****, highlighting the cross peaks which result from the combination of the DQ cross peaks assigned to the heme and histidine nitrogen nuclei, as indicated in the figure.*

In **Figure 7.3**, the HYSCORE spectra of nitrite-bound myoglobin in the presence of either $^{14}NO_2^-$ (black) or $^{15}NO_2^-$ (magenta) are overlaid to highlight the spectral differences induced by the isotope-labelled ligand. At all the magnetic field positions, the DQ and SQ cross peaks in the (-, +) quadrant can be almost superimposed, suggesting that the coordination to the ^{15}N-labelled nitrite does not significantly alter the heme electronic structure. On the other hand, a major difference is observed at the $g = g_z$ position, where two well-resolved cross peaks in the (+,+) quadrant appear. These are split around the Larmor frequency of ^{15}N, revealing the weak coupling to the isotope-labelled nitrite. The assignment of these peaks to the ^{15}N of nitrite is further corroborated by spectral simulations (*vide infra*). Additional spectral changes can be observed also in the (+,+) quadrants at the other observer positions.

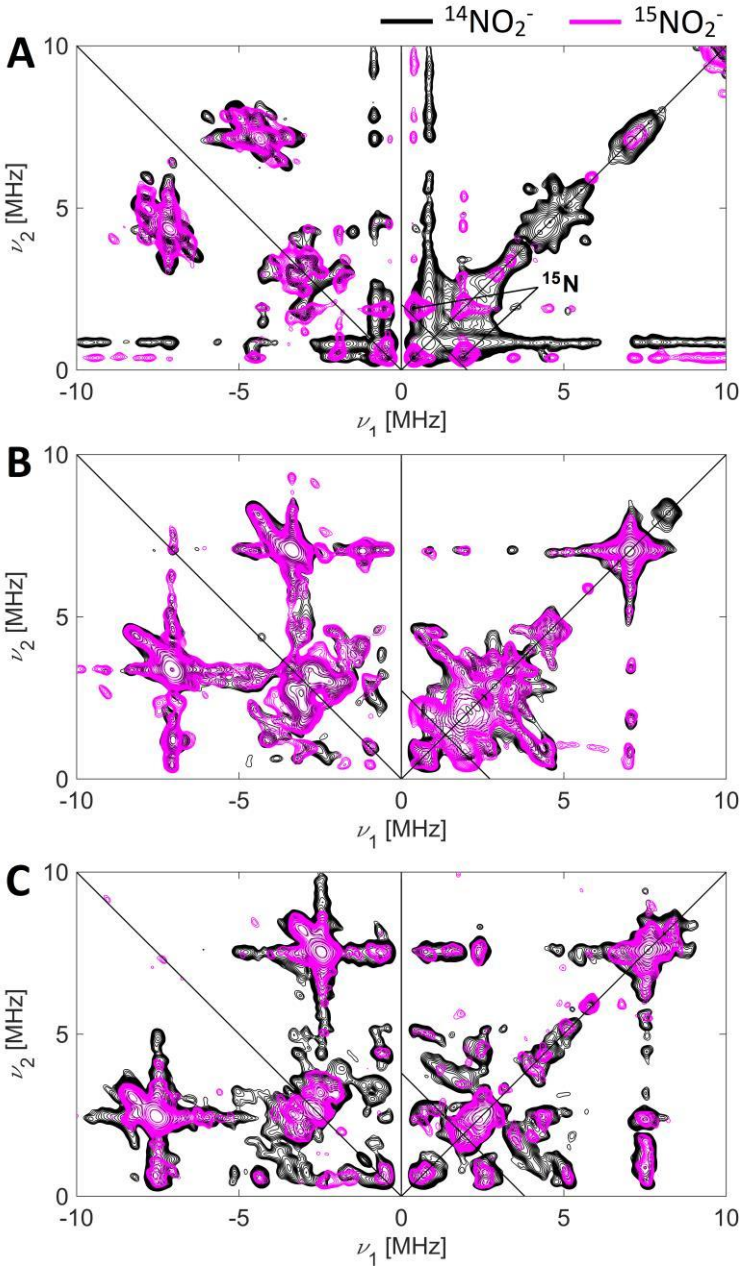

Figure 7.3 *X-band HYSCORE spectra of 1 mM ferric horse heart myoglobin in presence of 500 mM of either $^{14}NO_2^-$ (black) or $^{15}NO_2^-$ (magenta), taken at the observer position corresponding to $g = g_z$* ***(A)****, $g = g_y$* ***(B)*** *and $g = g_x$* ***(C)****, respectively. The spectra are the sum of τ = 96, 176 and 208 ns, normalized to the noise level. The antidiagonal drawn in the (+,+) quadrant crosses the main diagonal at the Larmor frequency of ^{15}N at the selected magnetic field positions (234.7, 315.8 and 440 mT, respectively).*

To accurately reproduce the spectral features of the presented nitrite-myoglobin system, computer simulations would require the use of a 7-spin system (S = ½, four porphyrin nitrogens, one N from the proximal histidine and one N from the nitrite). However, the computational time needed to simulate such a complex system can become very long. Here, by considering the symmetric structure of the heme, the simulation has been reduced to a 4-spin system, where the four heme nitrogens, being two-by-two magnetically inequivalent, are treated as two single nuclei. A third N nucleus is included in the simulation to account for the coupling with the proximal F8His. An independent simulation was performed to consider exclusively the contribution from the N nucleus of nitrite, and it will be discussed separately. The simulations of the HYSCORE spectra of nitrite-bound myoglobin ($^{14}NO_2^-$) are shown in **Figure 7.4** (red spectra), overlaid to the experimental data (black). To obtain the starting values for the hyperfine and nuclear quadrupole coupling constants, the analysis of the DQ frequencies have been performed, using Eq. 2.34 (Chapter 2). These values were adjusted manually and simulations were performed using the EasySpin package. The final simulation parameters are compared with values reported in literature for other myoglobin-ligand complexes (**Table 7.1**) [249, 250]. The simulations of the HYSCORE spectra of nitrite-bound myoglobin in presence of ^{15}N-labelled nitrite, are shown in Appendix B (**Figure B.1**). Note that the same sets of values describing the porphyrin nitrogens and proximal His, already obtained for the case of $^{14}NO_2^-$, were used to simulate these spectra.

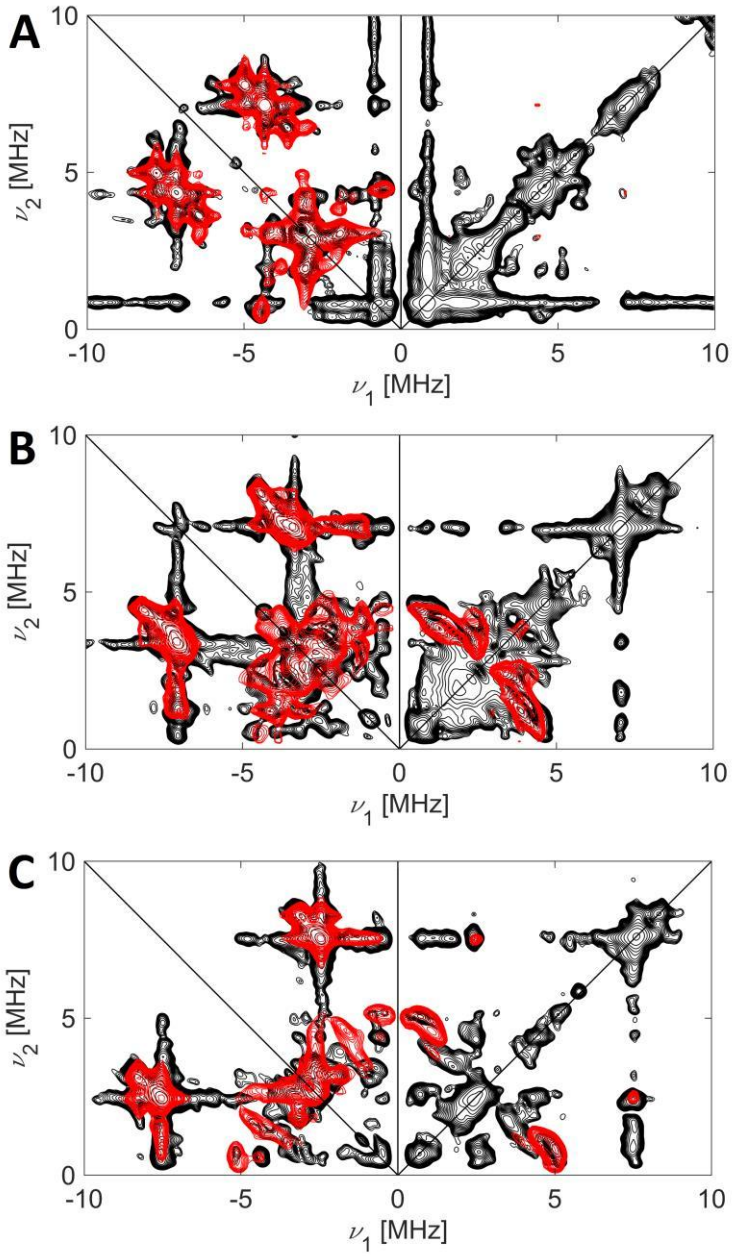

Figure 7.4 *Experimental (black) and simulated (red) X-band HYSCORE spectra of 1 mM ferric horse heart myoglobin in presence of 500 mM of $^{14}NO_2^-$, recorded at the observer positions corresponding to $g = g_z$* ***(A)****, $g = g_y$* ***(B)*** *and $g = g_x$* ***(C)****, respectively. The spectra are the sum of τ = 96, 176 and 208 ns, normalized to the noise level. The simulation includes the contributions of the heme and proximal histidine ^{14}N nucleus. The contribution of the weakly-coupled N nucleus from nitrite was omitted and it is shown separately in Figure 7.5.*

	A_{zz}	A_{yy}	A_{xx}	Q_{zz}	Q_{yy}	Q_{xx}	α,β,γ (deg)	Ref.
hhMb-NO_2^-								
Heme 1	-5.64	-4.70	-4.70	-0.45	-0.40	0.85	70, 0, 0	This work
Heme 2	-6.37	-5.00	-5.00	-0.45	-0.40	0.85	-20, 0, 0	
His	-4.95	-6.15	-5.50	-0.90	0.10	0.80	0, 0, 0	
^{14}N-NO_2^-	1.35	0.57	0.11	-0.95	0.05	0.90	90, 20, 90	
^{15}N-NO_2^-	1.90	0.80	0.15	-	-	-	90, 20, 90	
hhMb-Im[a]								
Heme 1	5.60[b]	n.d.	n.d.	0.50[b]	n.d.	n.d.	n.d.	[249]
Heme 2	6.20[b]	n.d.	n.d.	0.50[b]	n.d.	n.d.	n.d.	
His/Im	5.00[b]	n.d.	n.d.	0.85[b]	n.d.	n.d.	n.d.	
swMb-Im[a]								
Heme 1	5.80[b]	n.d.	n.d.	0.46[b]	n.d.	n.d.	n.d.	[250]
Heme 2	6.40[b]	n.d.	n.d.	0.53[b]	n.d.	n.d.	n.d.	
His/Im	5.70[b]	n.d.	n.d.	n.d.	n.d.	n.d.	n.d.	
hhMb-N_3^-[a]								
Heme 1	-5.64	n.d.	n.d.	n.d.	n.d.	-0.55	n.d.	[251, 252]
Heme 2	-6.14	n.d.	n.d.	n.d.	n.d.	-0.62	n.d.	
His	-3.00	-4.60	-4.60	-0.80	0.36	0.44	0, 10, 0	

Table 7.1 *Principal hyperfine (A) and quadrupole (Q) values (in MHz) of the nitrite-bound myoglobin in comparison with literature data for other myoglobin complexes. α, β, and γ are the Euler angles (in degrees) applied to the **A** and **Q** tensors frames for each nucleus. Errors on A values: ±0.05 MHz; errors on Q values: ±0.05 MHz; errors on Euler angles: ± 5 deg. hhMb = horse heart myoglobin, swMb = sperm whale myoglobin, Im = imidazole, N_3 = azide, n.d. = not determined. [a] The errors on these values are reported on original papers; [b] Originally reported as absolute values;*

As it can be seen from **Table 7.1**, the A_{zz} and Q_{zz} values which describe the coupling with the heme nitrogens are in line, at least in absolute value, with the ones previously reported for myoglobin in complex with other ligands, such as imidazole or azide. The features ascribed to the ^{14}N nucleus from the coordinating proximal histidine can be simulated with similar $|A_{zz}|$ as the myoglobin-imidazole complexes [249, 250], but differ from the values reported for a myoglobin-azide complex [251, 252]. This can be explained because the coordination of the proximal histidine is affected by the nature of the sixth ligand; however, the values reported for the myoglobin-azide complex need to be taken with caution since they were determined by 3-pulse ESEEM data only, which are normally less accurate than HYSCORE (Chapter 2).

The contribution from a weakly-coupled nitrogen atom from nitrite was simulated independently (values in **Table 7.1**) and the obtained simulated spectra are shown in **Figure 7.5**. First, the ^{15}N-labelled nitrite signal was analyzed taking advantage of the simpler I = ½ system which does not include the quadrupole contribution, making that the signals are centered around the ^{15}N Larmor frequency $\nu_{L(^{15}N)}$. The ^{15}N $\boldsymbol{A}$ tensor principal values can then be transferred in the corresponding ^{14}N hyperfine values by multiplying them by the ratio $\nu_{L(^{14}N)}/\nu_{L(^{15}N)}$. The determination of the $\boldsymbol{Q}$ tensor principal values was less trivial. The hyperfine coupling values are consistent with a near-cancellation regime ($A/2 \sim \nu_L$), where the quadrupole principal values are defined as follows: $Q_{zz} = 2K\eta$; $Q_{yy} = K(3-\eta)$; $Q_{xx} = K(3+\eta)$ [253], and K is defined by Eq. 2.21 (Chapter 2). The nuclear quadrupole values which allow to obtain a satisfactory simulation correspond to a $|e^2Qq/h|$ (= $4K$) value of 1.9 MHz for nitrite and display an almost completely axial character of the $\boldsymbol{Q}$ tensor. The value is unexpectedly low in comparison to the value obtained from NQR spectroscopy on $NaNO_2$ ($|e^2Qq/h|$ values in range of 5.5 – 5.79 MHz are reported [254, 255]).

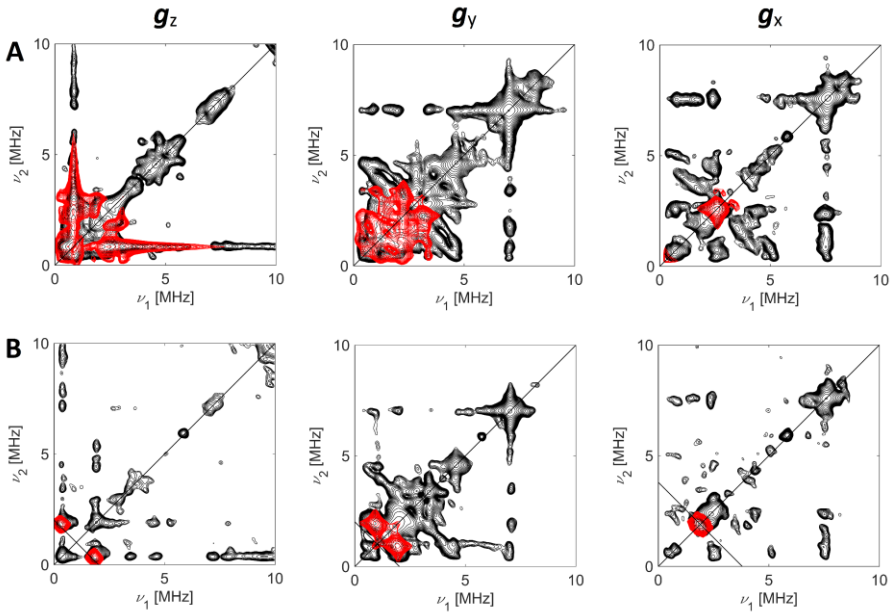

Figure 7.5 *Experimental (black) and simulated (red) X-band HYSCORE spectra ((+,+) quadrant only) of 1 mM ferric horse heart myoglobin in presence of 500 mM of $^{14}NO_2^-$* ***(A)****, or $^{15}NO_2^-$* ***(B)****, recorded at the observer positions corresponding to $g = g_z$, $g = g_y$, and $g = g_x$, as indicated above the panels. The spectra are the sum of τ = 96, 176 and 208 ns, normalized to the noise level. The simulation includes exclusively one weakly-coupled N nucleus from nitrite.*

Moreover, the *z*-axis of the ***Q*** tensor appears to be tilted of about ~ 20° with respect to the ***g*** tensor *z*-axis, which is expected to be collinear with the Fe-O bond. This is consistent with the angulate structure of the nitrite molecule (O-N-O bond angle ~ 115°, Chapter 6) and a O-Fe-N angle of ~ 26° estimated from the PDB structure of the nitrite-bound myoglobin (accession code: 2FRF).

The ^{1}H-HYSCORE spectrum of the myoglobin complex with standard nitrite, recorded at a position corresponding to $g = g_z$ (**Figure 7.6**) reveals two sets of weakly-coupled protons as observed in many 6-coordinated heme systems [247, 248, 256]. The two more extended ridges (indicated with **(1)** in **Figure 7.6**) stem from the two histidine protons situated close to the heme, while a second narrower ridge (indicated with **(2)**) originates from the coupling with more remote protons.

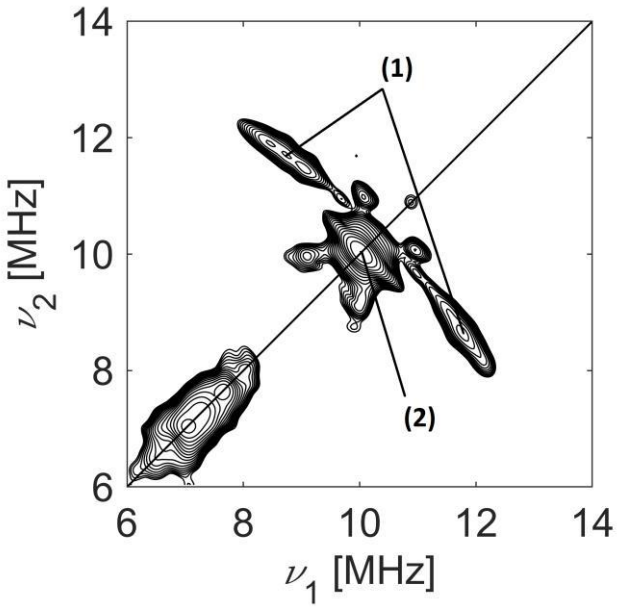

Figure 7.6 *X-band ^{1}H-HYSCORE spectra of 1 mM ferric horse heart myoglobin in presence of 500 mM of $^{14}NO_2^-$, recorded at the observer position corresponding to g = g_z. The spectra are the sum of τ = 96, 176 and 208 ns, normalized to the noise level.*

7.3.2 The complex HYSCORE profile of NO_2^--bound *C*Cld: looking for evidence of *N*-nitro binding mode

Similar as with myoglobin, preliminary X-band CW-EPR measurements of wild-type *C*Cld bound to either ^{14}N or ^{15}N-labelled nitrite were performed, revealing no significant differences in the two cases, as shown in **Figure 7.7**. In both spectra, three LS contributions can be identified and simulated with the *g* values reported in **Table 6.2** (Chapter 6).

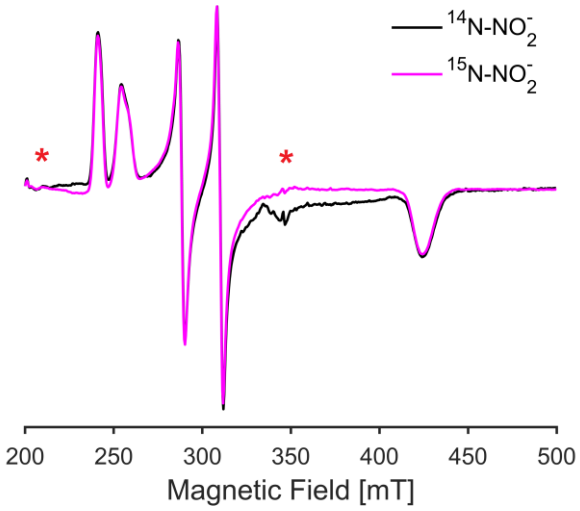

Figure 7.7 *X-band CW-EPR spectra of 1mM wild-type CCld in presence of 500 mM of either $^{14}NO_2^-$ (black) or $^{15}NO_2^-$ (magenta), at pH 7.0. The red asterisks indicate small differences in background due to imperfect baseline correction.*

The analysis of the ^{14}N- and ^{15}N-HYSCORE spectra of nitrite-bound *C*Cld is even more challenging than the myoglobin case, due to the presence of multiple co-existing low-spin species whose signal admixes at all observer positions, except for the lowest magnetic field position, which corresponds to the $g = g_z$ of the most anisotropic LS1 species (Chapter 6). The HYSCORE spectra recorded at this position are the only ones which can be attributed exclusively to LS1. From the analysis of the *g* values and crystal-field parameters presented in Chapter 6, this species is expected to be the one mirroring the *O*-nitrito binding mode described for myoglobin, therefore allowing a direct comparison of the two protein systems. As depicted in **Figure 7.8**, at the $g = g_z$ position (herein referred to as "$g_z(1)$"), the DQ cross peaks typical of the heme nitrogens are visible, as well as the SQ transitions

univocally attributed to the Fe-binding nitrogen of the proximal histidine (His114). On the other hand, the DQ peak due to the coordination of His114 is not clearly resolved at this magnetic field position, differently from the case of myoglobin (**Figure 7.2**, A). In the (+, +) quadrant, the strong signal from the weakly-coupled nitrite is analogous to the one observed at the $g = g_z$ position in the nitrite-bound myoglobin.

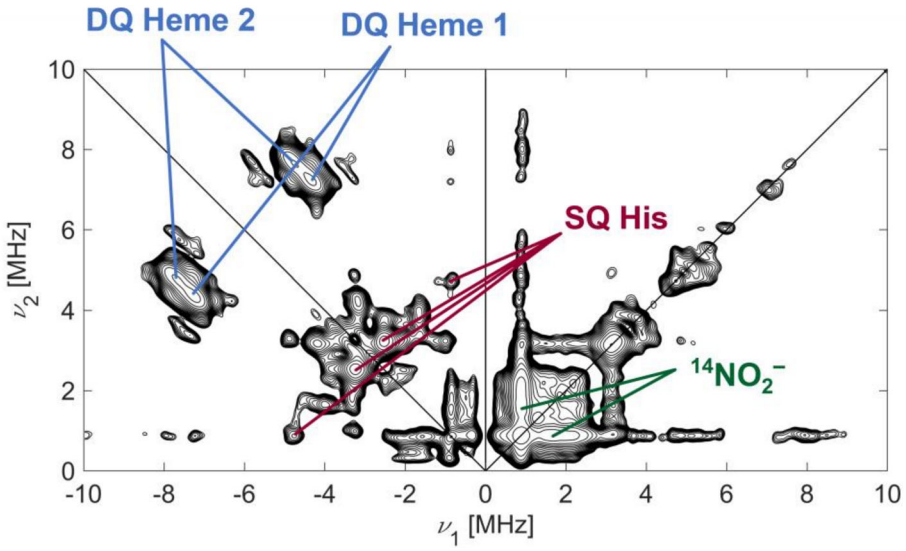

Figure 7.8 *X-band ^{14}N-HYSCORE spectrum of 1 mM WT CCld in presence of 500 mM of $^{14}NO_2^-$, pH 7.0, taken at the observer position corresponding to g_z(1) (243 mT). The spectrum represents the sum of two τ values (176 and 208 ns), normalized to the noise level.*

The HYSCORE spectra of the *C*Cld-$^{15}NO_2^-$ obtained at the observer positions corresponding to $g = g_z(1)$ and $g = g_z(2)$ are shown in **Figure 7.9** A and B, respectively, overlaid to the spectra of the sample prepared with $^{14}NO_2^-$. The discussion will be first focused on the $g = g_z(1)$ position since it is the only one exclusively arising from LS1. Similarly as for myoglobin, the features in the (-,+) quadrant are almost completely superimposable. Note that the presence of extra peaks in the case of $^{14}NO_2^-$ is due to the different noise level in the two spectra; by lowering the cutoff of the contour levels, all the peaks are clearly visible in the two cases (not shown). In the (+,+) quadrant, two well-resolved cross peaks centered around the Larmor frequency of ^{15}N appear when the isotope-labelled nitrite is used, which is consistent with the changes observed in the myoglobin sample. This confirms the *O*-nitrito coordination mode of nitrite hypothesized in Chapter 6 for

the LS1 species. At position $g = g_z(2)$ (**Figure 7.9 B**) all LS complexes overlap. When using ^{15}N-labelled nitrite, we again see a strong change in the (+,+) quadrant with the appearance of peaks centered around the ^{15}N Larmor frequency, stemming from the contribution of LS1. Besides this, no signal can be identified that would suggest the presence of the strongly coupled ^{15}N nucleus from the ligand, expected to occur for *N*-nitro ligation.

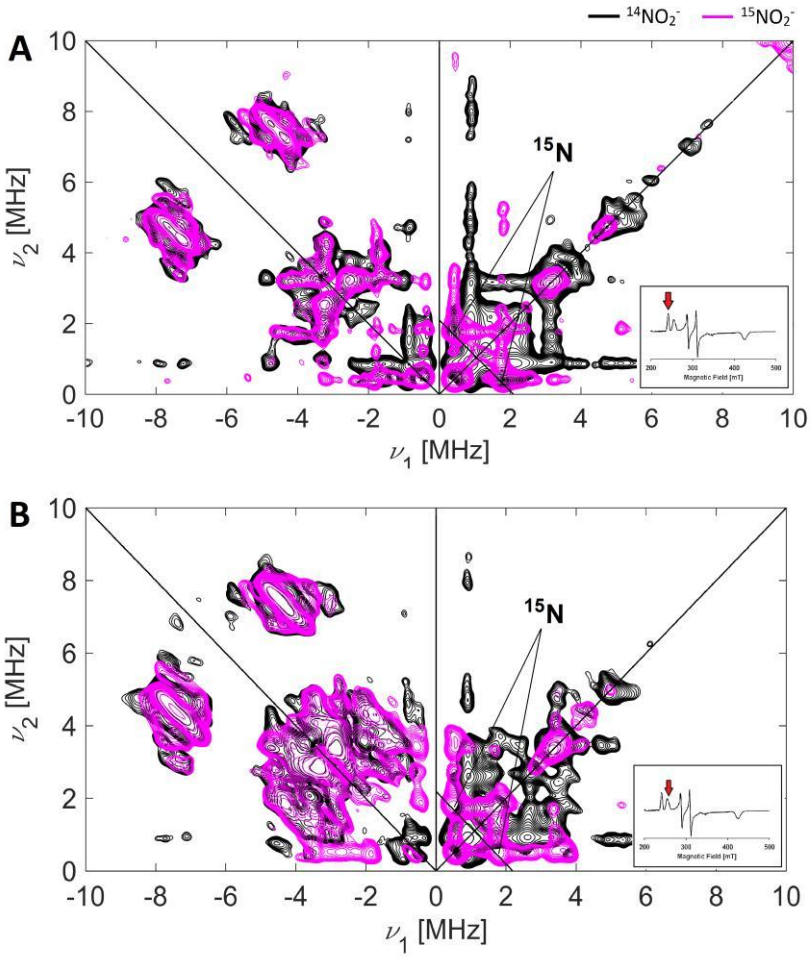

Figure 7.9 *X-band HYSCORE spectra of 1 mM WT CCld in presence of 500 mM of either $^{14}NO_2^-$ (black) or $^{15}NO_2^-$ (magenta), taken at the observer position corresponding to $g = g_z(1)$* ***(A)*** *and $g = g_z(2)$* ***(B)****, respectively. The spectra are the sum of τ = 176 and 208 ns, normalized to the noise level. The antidiagonal drawn in the (+,+) quadrant crosses the main diagonal at the Larmor frequency of ^{15}N at the selected magnetic field positions (243 and 254 mT, respectively). The inset depicts the X-band CW-EPR spectrum of the nitrite-bound CCld, already shown in Figure 7.7, with a red arrow highlighting the observer position.*

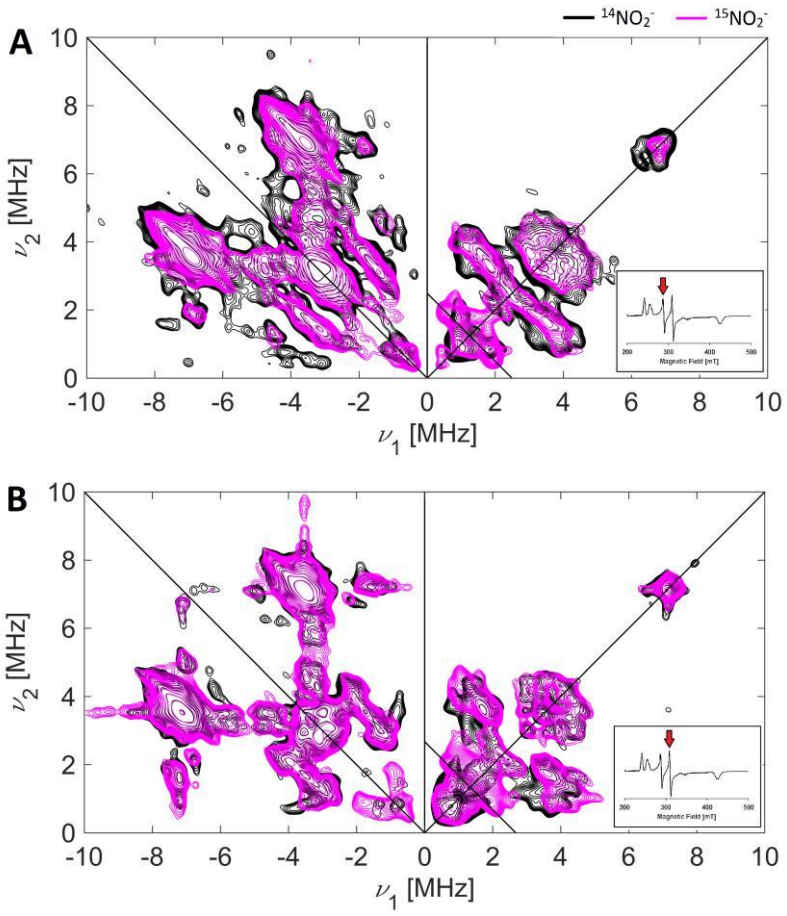

Figure 7.10 *X-band HYSCORE spectra of 1 mM WT CCld in presence of 500 mM of either $^{14}NO_2^-$ (black) or $^{15}NO_2^-$ (magenta), taken at the observer position corresponding to g = g_y(1)* ***(A)*** *and g = g_y(2)* ***(B)****, respectively. The spectra are the sum of τ = 176 and 208 ns, normalized to the noise level. The antidiagonal drawn in the (+,+) quadrant crosses the main diagonal at the Larmor frequency of ^{15}N at the selected magnetic field positions (288 and 310 mT, respectively). The inset depicts the X-band CW-EPR spectrum of the nitrite-bound CCld, already shown in Figure 7.7, with a red arrow highlighting the observer position.*

Similarly to the g_z(1) and g_z(2) observer positions, also at the magnetic field positions corresponding to g_y(1), g_y(2) and g_x no significant differences in the (-,+) quadrant can be observed when $^{14}NO_2^-$ or $^{15}NO_2^-$ are used (**Figure 7.10** and **Figure 7.11**). The superimposed signals must originate from the protein/heme nuclei,

since the N nucleus from nitrite would be characterized by different ***A*** (and ***Q***, for $^{14}NO_2^-$) principal values in case ^{14}N or ^{15}N were used. Interestingly, in the high frequency region of the (-,+) quadrant at the $g_y(1)$ and $g_y(2)$ positions, a pair of cross peaks cannot be superimposed, even using a low contour cutoff level (**Figure 7.12**). While several peaks consistent with the combinations of DQ frequencies are visible and perfectly superimposable in the $^{14}NO_2^-$ and $^{15}NO_2^-$ spectra, two peaks centered around ~ 9.4 MHz are present exclusively in the $^{14}NO_2^-$ spectra (**Figure 7.12**, blue arrows). These peaks do not correspond to combinations of other frequencies and they are spaced ~ 3.7-3.9 times the Larmor frequency of ^{14}N at the relative magnetic field positions. This led to the hypothesis that they might represent DQ cross peaks of an additional strongly-coupled N nucleus, potentially from a molecule of nitrite coordinating through the N-nitro mode.

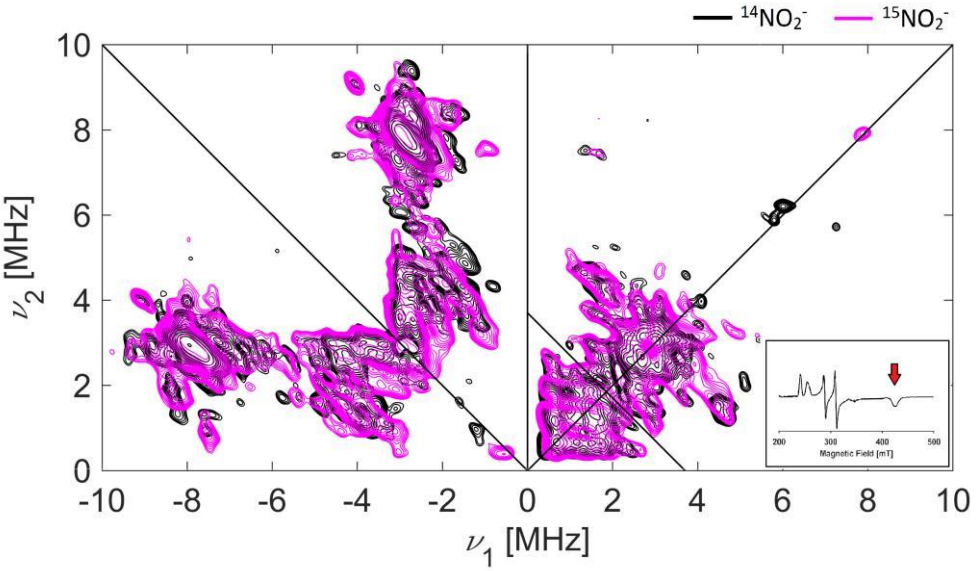

Figure 7.11 *X-band HYSCORE spectra of 1 mM WT CCld in presence of 500 mM of either $^{14}NO_2^-$ (black) or $^{15}NO_2^-$ (magenta), taken at the observer position corresponding to $g = g_x$. The spectra are the sum of τ = 176 and 208 ns, normalized to the noise level. The antidiagonal drawn in the (+,+) quadrant crosses the main diagonal at the Larmor frequency of ^{15}N at the selected magnetic field positions (425 mT). The inset depicts the X-band CW-EPR spectrum of the nitrite-bound CCld, already shown in Figure 7.7, with a red arrow highlighting the observer position.*

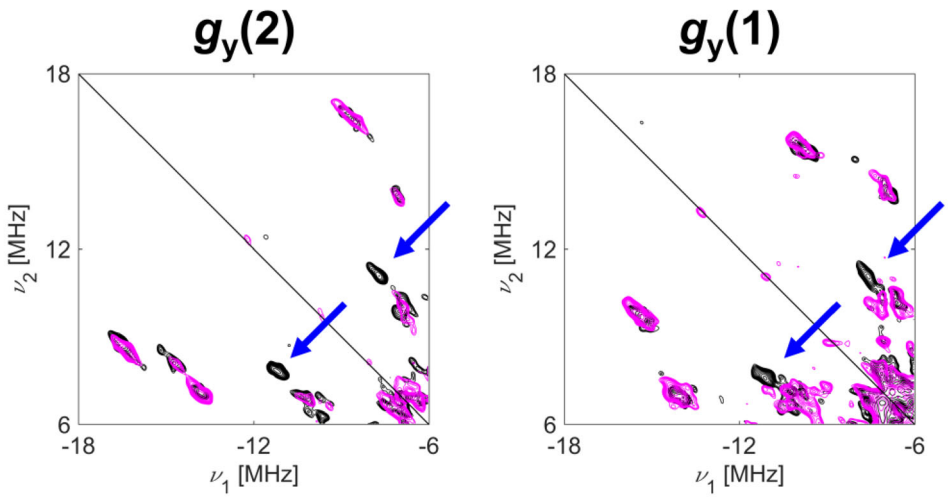

Figure 7.12 *X-band HYSCORE spectra (high-frequency region) of 1 mM WT CCld in presence of 500 mM of either $^{14}NO_2^-$ (black) or $^{15}NO_2^-$ (magenta), taken at the observer position corresponding to g = g_y(2) (288.4 mT) and g = g_y(1) (310 mT). The spectra are the sum of τ = 176 and 208 ns, normalized to the noise level. The blue arrows indicate the additional peaks exclusively observable in the $^{14}NO_2^-$ spectrum.*

The simulations of the nitrite-bound *C*Cld HYSCORE spectra were performed with a similar approach used for myoglobin. Initially, the observer positions corresponding to $g_z(1)$, $g_y(1)$ and g_x were considered, being the ones mostly resembling the LS form of the Mb-nitrite complex. The simulation values already optimized for myoglobin were taken as an input and adjusted to match the spectral features in the *C*Cld spectra. It has to be noted that, while at the $g_z(1)$ position a 4-spin system (S = ½, 2 x Heme N, 1 x His N) was sufficient to describe the "single species" spectrum and resulted in a rather satisfactory simulation (**Figure 7.13 A**), this was not the case for the intermediate positions, where the signals stemming from either the LS1 or the LS2/LS3 contributions admix (**Figure 7.13 B** and **C**). The corresponding spectra obtained with $^{15}NO_2^-$ have been simulated with the same parameters (Appendix B, **Figure B.2**). An additional weakly-coupled N from nitrite was simulated separately, using the same approach already described for the myoglobin case (**Figure 7.14**). All the simulation values are reported in **Table 7.2**, in comparison with the values previously found for a clade I chlorite dismutase forming a LS complex with either imidazole or azide [61]. The ***A*** and ***Q*** principal values assigned to the heme N nuclei in *C*Cld are rather similar to the ones obtained in the case of myoglobin. The hyperfine coupling of the proximal histidine, however,

differs to a larger extent and the tensor frame appears to be rotated by approximately 30° about the ***g*** tensor *z*-axis. These differences can be explained with the different orientation of the histidine plane with respect to the N-Fe-N direction of the heme plane in the two protein systems (**Figure 7.15**).

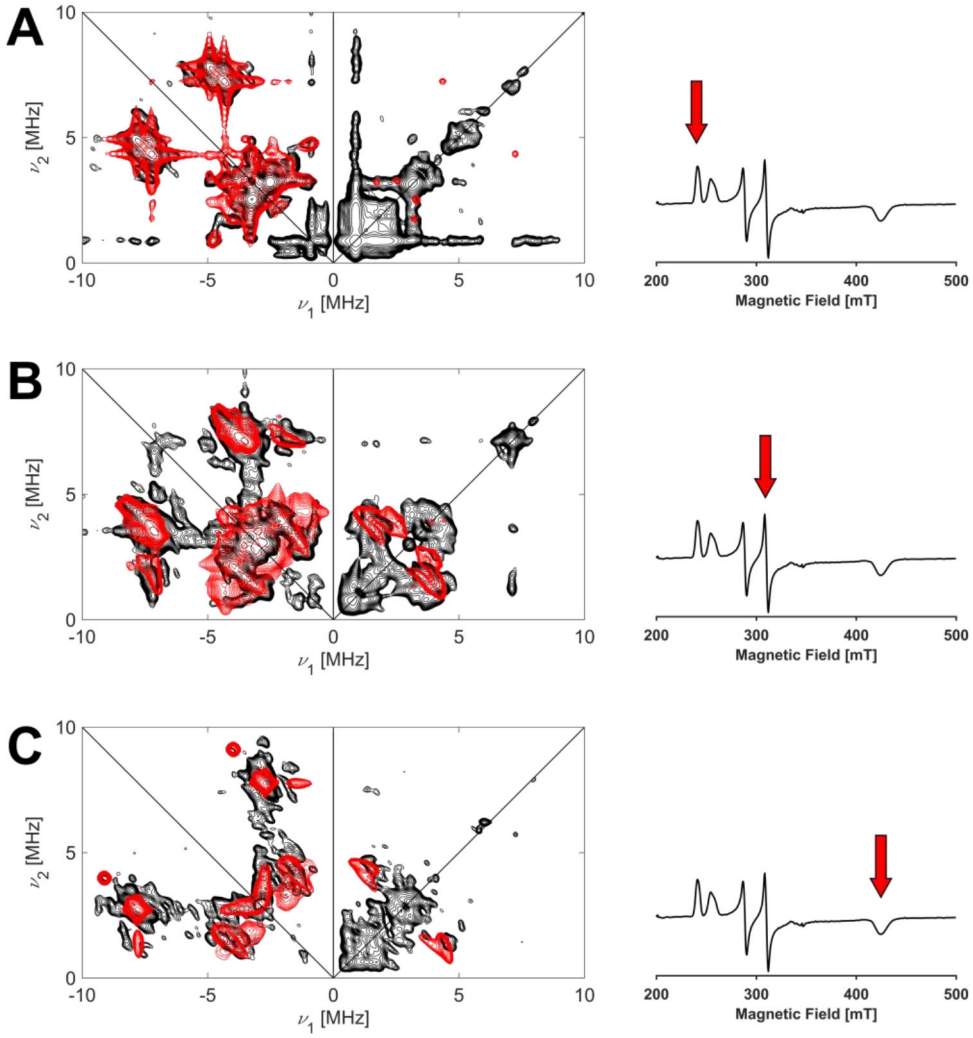

Figure 7.13 *Left panel: Experimental (black) and simulated (red) X-band HYSCORE spectra of 1 mM WT CCld in presence of 500 mM of* $^{14}NO_2^-$*, recorded at the observer positions corresponding to* $g = g_z(1)$ ***(A)***, $g = g_y(1)$ ***(B)*** *and* $g = g_x$ ***(C)***, *respectively. The spectra are the sum of* $\tau = 176$ *and 208 ns, normalized to the noise level. The simulation includes the contributions of the heme and proximal histidine nitrogen nuclei. Right panel: X-band CW-EPR spectrum of the nitrite-bound CCld, with the red arrows indicating the observer position for each corresponding HYSCORE spectrum.*

	A_{zz}	A_{yy}	A_{xx}	Q_{zz}	Q_{yy}	Q_{xx}	α,β,γ (deg)	Ref.
***C*Cld-NO_2^- (LS1)**								
Heme 1	-5.70	-5.10	-4.90	-0.30	-0.45	0.75	60, 0, 0	This work
Heme 2	-6.33	-5.95	-4.90	-0.30	-0.45	0.75	-30, 0, 0	
His	-5.65	-6.30	-6.45	-0.87	0.55	0.32	30, 0, 0	
^{14}N-NO_2^-	1.07	1.14	-0.14	-0.95	0.05	0.90	90, 20, 90	
^{15}N-NO_2^-	1.50	1.60	-0.20	-	-	-	90, 20, 90	
***Ma*Cld-Im** [a]								
Heme 1	-5.70	-4.70	-4.70	-0.33	0.85	-0.52	10, 0, 0	[61]
Heme 2	-6.40	-5.40	-5.30	-0.33	0.85	-0.52	110, 0, 0	
His/Im	-5.10	-5.20	-6.00	-0.90	0.38	0.32	40, 0, 0	
***Ma*Cld-N_3^-** [a]								
Heme 1	-5.80	-5.00	-5.40	-0.33	0.85	-0.52	45, 0, 0	[61]
Heme 2	-6.30	-5.00	-5.40	-0.33	0.85	-0.52	-45, 0, 0	
His/Im	-4.80	-5.70	-5.30	-0.80	0.12	0.68	90, 0, 0	

Table 7.2 *Principal hyperfine (A) and quadrupole (Q) values (in MHz) of the nitrite-bound myoglobin in comparison with literature data on another chlorite dismutase representative. α, β, and γ are the Euler angles (in degrees) applied to the **A** and **Q** tensors frames for each nucleus. Errors on A values: ±0.05 MHz; errors on Q values: ±0.05 MHz; errors on Euler angles: ± 5 deg. MaCld = Magnetospirillum sp. chlorite dismutase, Im = imidazole, N_3^- = azide.* [a] *The errors on these values are reported on the original paper.*

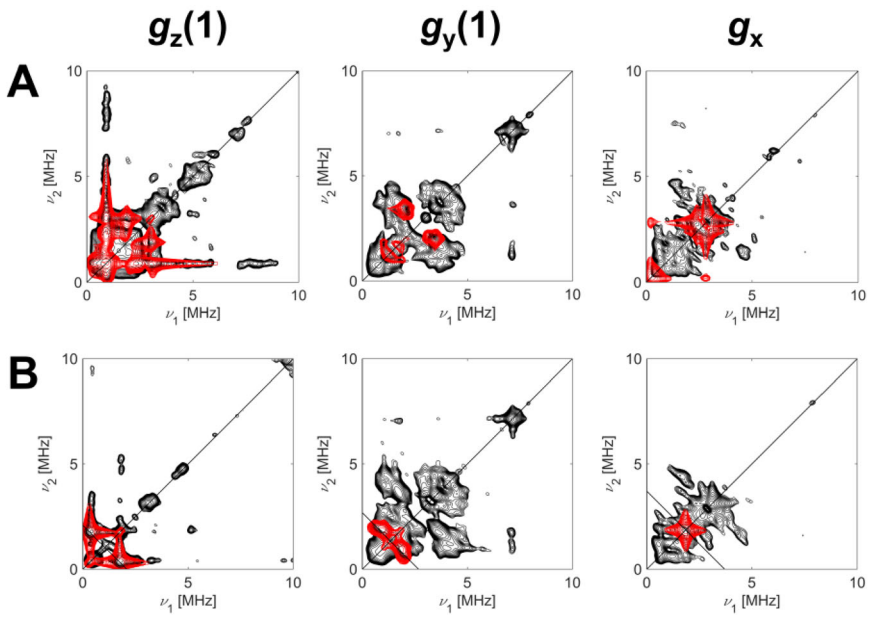

Figure 7.14 *Experimental (black) and simulated (red) X-band HYSCORE spectra ((+,+) quadrant only) of 1 mM WT CCld in presence of 500 mM of* $^{14}NO_2^-$ ***(A)****, or* $^{15}NO_2^-$ ***(B)****, recorded at the observer positions corresponding to* $g = g_z(1)$, $g = g_y(1)$, *and* $g = g_x$, *as indicated above the panels. The spectra are the sum of* τ *= 176 and 208 ns, normalized to the noise level. The simulation includes exclusively one weakly-coupled N nucleus from nitrite.*

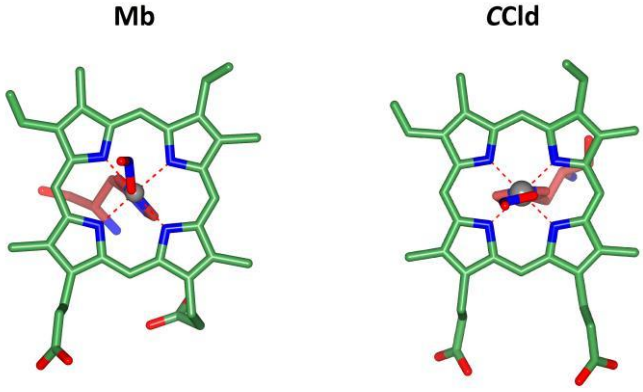

Figure 7.15 *Active site (top view) of wild-type Mb (left) and CCld (right) bound to the nitrite molecule through the O-nitro mode. In the case of myoglobin, the imidazole plane of the proximal histidine (foggy dark red) is parallel to one of the N-Fe-N bond line of the heme plane. Differently, in CCld, the proximal histidine is rotated about ~ 40-45° with respect to the N-Fe-N direction.*

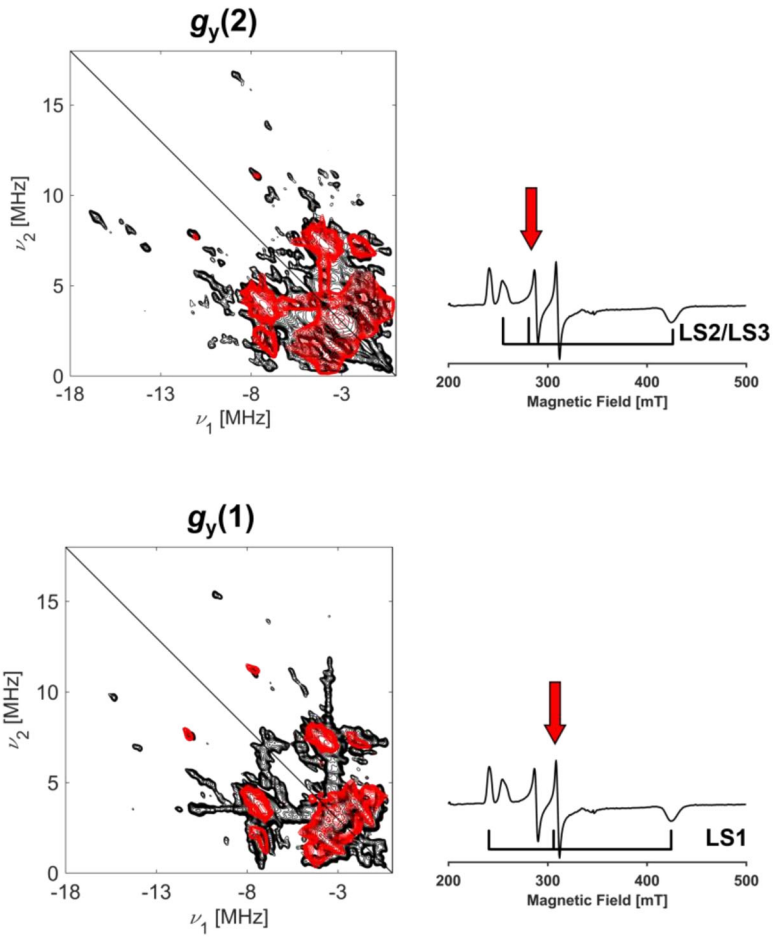

Figure 7.16 *Left panel: Experimental (black) and simulated (red) X-band HYSCORE spectra ((-,+) quadrant only) of 1 mM WT CCld in presence of 500 mM of* $^{14}NO_2^-$ *recorded at the observer positions corresponding to* $g = g_y(2)$ *(top) and* $g = g_y(2)$ *(bottom) as indicated above the plots. The spectra are the sum of* $\tau = 176$ *and 208 ns, normalized to the noise level. Right panel: X-band CW-EPR spectrum of the nitrite-bound CCld, with the red arrows indicating the observer position for each corresponding HYSCORE spectrum. This simulation includes the heme nuclei and one strongly-coupled N nucleus from nitrite.*

As mentioned earlier, at the observer positions corresponding to $g = g_y(1)$ and $g = g_y(2)$, two cross peaks are visible in the high-frequency region, which cannot be easily assigned to endogenous N nuclei from the protein. **Figure 7.16** shows a tentative simulation of the spectra taken at these magnetic field positions, which

include the heme N nuclei and one additional strongly-coupled N nucleus. The latter might originate from the binding of a nitrite molecule *via* the *N*-nitro mode. The $\boldsymbol{A}$ and $\boldsymbol{Q}$ principal values used for the simulation need to be taken with caution, since the peaks (treated as DQ) are visible only at these magnetic field positions. In any case, a simulated spectrum without unrealistic extra peaks at all the magnetic field positions could be obtained with the parameters A_{zz} = 16 MHz, A_{yy} = 9 MHz and A_{zz} = 7.7 MHz; Q_{zz} = 2 MHz, A_{yy} = -1.5 MHz and A_{zz} = -0.5 MHz.

7.4 Discussion and conclusions

In an enzymatic reaction, the binding of the substrate constitutes the first step of the catalytic cycle. Its investigation may provide important information on the interactions which are established between the substrate and the catalytic groups in the active site and thus reveal details on the enzymatic mechanism itself. In Chapter 6, an approach based on the use of a substrate analogue was employed to study the substrate binding in chlorite dismutases, whose investigation is typically challenging due to the rapid reactivity of these enzymes, as it will be more extensively discussed in Chapter 8. As already explained in Chapter 6, nitrite was chosen as substrate analogue for its similarities with chlorite and for its ability to form a stable complex with the chlorite dismutase enzyme, therefore allowing an easy investigation by EPR spectroscopy, among other techniques. CW-EPR of the nitrite-bound *C*Cld, in its WT or variant forms, revealed the contributions of three LS complexes, of which one (denoted as LS1, see section 6.3.3) is characterized by g values consistent with what reported in literature for other heme proteins binding nitrite through an *O*-nitrito coordination mode, such as myoglobin and hemoglobin [17, 220]. The other two LS complexes (denoted as LS2 and LS3, section 6.3.3) have features which almost completely superimpose and their g values resemble the ones described for certain representatives of the NP family, known to bind nitrite through the *N*-nitro mode [217, 218, 241]. Corroborated by MD simulations and analysis of the crystal field parameters, the CW-EPR findings suggested that in *C*Cld the different LS complexes might indeed arise from the coexistence of the *O*-nitrito and *N*-nitro binding modes. A similar hypothesis was recently taken by Van Brempt and co-workers regarding the binding of nitrite to the GLB-33 of *C. elegans* [244]. Differently from other heme proteins, the CW-EPR spectrum of ferric GLB-33 is dominated by LS complexes consistent with the ligation of an OH^- group over a wide range of pH. When an excess of NO_2^- was added to the protein, new LS complexes were formed, with their relative ratio being highly pH-dependent. In the same work,

the species denoted as LS3 and LS4 were tentatively assigned to the binding of nitrite *via* the *O*-nitrito and *N*-nitro binding modes, respectively. This interpretation was supported by the consistency of their *g* values and crystal field parameters with other heme-nitrite complexes reported in literature, including chlorite dismutases (Chapter 6). In addition to CW-EPR, Van Brempt *et al.* performed pulsed EPR experiments with ^{15}N-labelled nitrite in the attempt to further corroborate their assignment. While 3-pulse ESEEM and HYSCORE measurements did not provide clear differences between $^{14}NO_2^-$ and $^{15}NO_2^-$, the 2-pulse ESEEEM recorded at the observer position corresponding to $g = g_z$ of LS3, *i.e.* the only one unequivocally assigned to the nitrite-bound GLB-33, revealed a ^{14}N hyperfine coupling below 7 MHz. This is consistent with the assignment to the *O*-nitrito binding mode, since in a DFT study the hyperfine coupling for a directly-coordinated N was estimated to be ~ 20 MHz along g_z by quantum chemical calculations [257]. Similar to these results, the findings presented in this Chapter only provide conclusive information about the LS complexes assigned to the *O*-nitrito binding mode, in both myoglobin, where it is the sole occurring mode, and *C*Cld, where the analysis of the intermediate observer positions is hampered by the admix of different LS contributions. In the case of nitrite-bound myoglobin, the use of isotope-labelled nitrite allowed to unambiguously assign the strong signal in the (+,+) quadrant to a weakly-coupled N from nitrite (**Figure 7.5** and **Table 7.1**). In the (-,+) quadrant the $^{14}NO_2^-$ and $^{15}NO_2^-$ spectra are almost completely superimposable and no signal attributable to a strongly-coupled N nucleus is present in addition to the heme and proximal histidine nitrogen nuclei (**Figure 7.3**). This confirms the crystallographic data showing nitrite binding to myoglobin *via* the *O*-nitrito mode [220].

The analysis of the nitrite-bound *C*Cld was less trivial and initially limited to the observer positions corresponding to the ***g*** principal values of LS1, *i.e.* the LS species with features comparable with the myoglobin-nitrite complex (Chapter 6). Among these, only the feature at the position corresponding to $g = g_z$ arises from the "pure" LS1 species and its HYSCORE spectrum (**Figure 7.8**) closely resembles the corresponding one in the nitrite-bound myoglobin. The signal of the weakly-coupled N from nitrite is clearly resolved in the (+,+) quadrant and as expected, no evidence for a strongly-coupled N nucleus from nitrite was found in the (-,+) quadrant. The comparison between the $^{14}NO_2^-$ and $^{15}NO_2^-$ spectra revealed almost completely superimposable features at all magnetic field positions corresponding to the principal *g* values of both LS1 and LS2/LS3 species (**Figure 7.9**, **Figure 7.10** and **Figure 7.11**). The only remarkable difference is appreciable at $g = g_y(1)$ and $g = g_y(2)$ (**Figure 7.12**), where two additional cross peaks in the (-,+) quadrant are detected in the spectra recorded with $^{14}NO_2^-$, but not with $^{15}NO_2^-$. As already mentioned, these peaks do not stem from the combination of other frequencies and are spaced approximately 4 times the ^{14}N Larmor frequency at the selected

magnetic field. This led to the hypothesis that they might originate from an additional strongly-coupled N nucleus from a nitrite molecule bound through the *N*-nitro mode. The estimation of the anisotropic $\boldsymbol{A}$ and $\boldsymbol{Q}$ principal values is, however, very challenging due to the absence of clearly distinguishable peaks at other magnetic field positions. This is not unexpected since hyperfine coupling values of ~ 20 MHz, as estimated in [257], would move the peaks out of the range of the acquired spectra. A tentative simulation of this strongly-coupled N nucleus was performed considering the peaks as DQ frequencies; the resulting simulated spectra, depicted in **Figure 7.16**, show a good match with the DQ peaks and do not give rise to unwanted features. However, the values need to be taken with caution as they are likely subjected to a considerable error.

Whether the binding of nitrite to chlorite dismutases through different modes has a biological importance can be debated. In first place, despite the similarity with chlorite, nitrite remains a substrate analogue whose binding to Clds does not necessarily mirror the interaction with the actual substrate. In fact, as also exemplified by MD simulation (Chapter 6, section 6.3.4), the binding of chlorite is expected to occur exclusively through one of the oxygen atoms. This would be in line with the proposed catalytic intermediates, which must involve at least one oxoiron(IV) species (Chapter 1, section 1.1.5). As far as nitrite is concerned, the crystal structures of the nitrite-bound WT and variant forms of *C*Cld show the *O*-nitrito as the sole binding mode, which nicely mirrors what is expected for chlorite (Chapter 6, section 6.3.1). However, it has to be noticed that the crystallization conditions might favor one configuration over the other(s). The simultaneous presence of LS complexes assigned to either *O*-nitrito and *N*-nitro binding modes observed in the CW and pulsed EPR of *C*Cld indicates that this enzyme can accommodate the nitrite molecule in different orientations; on the other hand, this cannot be directly translated into mechanistic information on the enzyme functionality for the reasons mentioned above.

From a structural point of view, the preference for the *O*-nitrito mode in Clds seems to be promoted by the H-bonding distal arginine, which might exert a similar role as the distal E7His in myoglobin [17]. However, the presence of an H-bonding partner is not an essential condition for the occurrence of this binding mode. This is demonstrated by the case of nitrophorins, where the binding through the *N*-nitro mode is observed not only in the WT form of NP4 [217], which completely lacks any H-bonding residues in the active-site, but also in the NP4(L130R) variant, where an arginine was introduced in the heme proximity [241]. Similarly, in all the nitrite-NiR enzyme complexes characterized so far, the *N*-nitro is the sole binding mode observed, even though the ligand is further hydrogen-bonded to nearby amino acids [238, 258–260]. Complementary to crystallographic studies, this in-depth HYSCORE analysis of nitrite complexes of myoglobin and *C*Cld provides a unique set of high-

resolution spectroscopic data and simulations which may be taken as a reference for the investigation of other heme-nitrite systems. A full non-ambiguous spectroscopic characterization of nitrite binding to myoglobin through the *O*-nitrito mode is given. In addition to that, the first (tentative) evidence for a *N*-nitro coordinated nitrite molecule is shown for the chlorite dismutase enzyme. This could hopefully aid in the elucidation of the binding mode(s) of nitrite in other heme proteins, which appears to be strongly enzyme-specific.

Chapter 8

Reactivity of Clds and heme peroxidases studied by RFQ-EPR

Abstract

In Chapter 4 and 5, the electronic, structural, and biochemical features of the wild-type chlorite dismutase from *Cyanothece sp.* PCC7425 (*C*Cld) and selected variants were discussed, while in Chapter 6 and 7 the interaction of these enzymes with the substrate analogue nitrite (NO_2^-) was extensively investigated. Nevertheless, many questions about their molecular reaction mechanism have remained unanswered, including the electronic nature of the relevant oxoiron(IV) intermediate(s) and their interaction with the catalytically active arginine. In this Chapter, I present a combined RFQ–EPR approach for the investigation of the short-lived intermediate(s) formed during the reaction of wild-type *C*Cld with either chlorite (ClO_2^-) or hypochlorite (ClO^-). The results are contextualized with stopped-flow UV-visible findings and the pitfalls related to the different experimental conditions used in the two techniques. Next, we attempted to identify the nature of the Compound I*/II species observed in the later stage of *C*Cld catalytic cycle by turning to high-frequency (W-band) EPR. Finally, in order to get a more comprehensive understanding of the interaction with ClO_2^- and ClO^- with heme peroxidases, RFQ-EPR experiments were performed on the model horseradish peroxidase (HRP) and a representative of the dye-decolorizing peroxidases from *Escherichia coli* (*Ec*DyP).

Partially redrafted after: Daniel Schmidt, Nikolaus Falb, **Ilenia Serra**, Marzia Bellei, Vera Pfanzagl, Stefan Hofbauer, Sabine Van Doorslaer, Gianantonio Battistuzzi, Paul G. Furtmüller, and Christian Obinger, (2023) Compound I Formation and Reactivity in Dimeric Chlorite Dismutase: Impact of pH and the Dynamics of the Catalytic Arginine, *Biochemistry*, 62(3), 835-850.

Own contribution: acquisition, analysis and interpretation of EPR data; writing of paper manuscript. Sections 8.3.5, 8.3.6 and 8.3.7 constitute original, unpublished work.

8.1 Introduction

Chlorite is an angulate anionic and harmful oxidant known to react with heme proteins in different ways. For example, it was shown to induce the formation of methemoglobin [261] or to act as a hydroxylating agent in cytochrome P450 [262]. Horseradish peroxidase (HRP) mediates the heterolytic cleavage of chlorite which oxidizes the ferric enzyme to Compound I, thereby releasing hypochlorous acid that acts as a chlorinating agent [263]. Furthermore, chlorite has been shown to act as a one-electron reductant of both Compound I and Compound II of heme peroxidases, thus forming chlorine dioxide [263]. In contrast to HRP, chlorite cannot mediate the oxidation of the human peroxidases lactoperoxidase (LPO) or myeloperoxidase (MPO) to Compound I. These peroxidases are rapidly and irreversibly inactivated by heme bleaching and iron release, and the LPO/chlorite and MPO/chlorite systems do not mediate chlorination of target molecules [264].

In the case of Clds, chlorite oxidizes the ferric state to an oxoiron(IV) intermediate that efficiently reacts with the transient chlorite reduction product to release dioxygen (O_2) and chloride (Cl^-) (Chapter 1). This reactivity has not been observed in any other biological heme system to date and the exact mechanism is still under debate. Why can HRP [263] but not other peroxidases [264] mediate the heterolytic cleavage of chlorite to hypochlorite? Are Clds able to catalyze a similar reaction? Which discrepancies and peculiarities between peroxidases and chlorite dismutases are responsible for these significant different reactivities? Finally, why is chlorite consumption in Clds always coupled to O_2 generation?

In this Chapter, these questions are mainly addressed with the use of EPR spectroscopy, taking advantage of the paramagnetic nature of the catalytic intermediates formed during the reaction of these enzymes with either chlorite or hypochlorite. A comparative RFQ-EPR study of *C*Cld, HRP and *Ec*DyP was conducted, in order to identify the spectroscopic fingerprints of their short-lived intermediates. The results are discussed with respect to the similarities in the active sites of the selected enzymes and the known key catalytic residues.

8.2 Experimental procedures

This section will include exclusively the experimental details of the RFQ samples preparation and EPR spectroscopy measurements. For further information on the other techniques used in this work, the reader is referred to [150].

8.2.1 RFQ sample preparation of *C*Cld with ClO_2^- and ClO^-

Samples for EPR spectroscopy were prepared using an RFQ device from BioLogic (Grenoble, France), consisting of an SFM-2000 stopped-flow unit and an MPS-70 controller unit, combined with a freeze-quench sample collector adapted for EPR tubes (Chapter 2, section 2.3.4.3). The ejected volumes and flow rate were controlled by the BioLogic BIOKINE software, v. 4.72. This RFQ setup was calibrated by quenching the binding reaction of azide (N_3^-) to ferric myoglobin (Mb) at selected time points as described by Pievo *et al.* [107] (Chapter 2, section 2.3.4.4). The calibration showed that the shortest achievable freezing time was ~50 ms (**Figure 2.12 B**). Therefore, for all *C*Cld samples, the reaction was quenched at ~60 ms, including the aging and the flying time of the reacting mixture that can be calculated from the chosen settings of the freezing experiment. In all cases, protein samples were prepared in 100 mM sodium phosphate–citrate buffer (pH 5), which was filtered and degassed prior to use. For the reaction with hypochlorite, the samples were prepared in triplicate by mixing 50 µL of a solution containing *C*Cld at a concentration of 0.5 mM with 50 µL of a 5 mM sodium hypochlorite (NaClO) solution prepared in 1 mM NaOH. In this way, the substrate-to-protein ratio was maintained at a 10-fold molar excess, with the concentrations of *C*Cld and NaClO in the final sample being 0.25 and 2.5 mM, respectively. The ratio was chosen accordingly to the results of stopped-flow measurements (Figure 4 on original paper), which showed the formation of Compound I within 75 ms, a time range theoretically accessible by the RFQ setup used in this work. The samples containing chlorite were prepared in duplicate by mixing 50 µL of a solution containing *C*Cld at a concentration of 0.2 mM with 50 µL of a 60 mM sodium chlorite ($NaClO_2$) solution prepared in Milli-Q water. In this case, the substrate-to-protein ratio was set at a 300-fold molar excess, with the concentrations of *C*Cld and $NaClO_2$ in the final sample being 0.1 and 30 mM, respectively. In this case, the amount of substrate was chosen to keep consistency with other stopped-flow measurements performed in this work. In fact, in the stopped-flow experiments, this high substrate-to-protein ratio was selected because it allowed the full degradation of chlorite over a large pH range. Finally, additional samples were prepared with a conventional "manual freezing" method. More specifically, to freeze the sample in the shortest time possible, the solution containing *C*Cld was first poured at the bottom of a quartz EPR tube, and then an appropriate volume of NaClO solution was added to the sample,

quickly mixed, and immediately flash frozen in liquid N_2 within 10 s. The same procedure was followed to prepare the sample in the presence of serotonin, which was added in a 50-fold molar excess before initiating the reaction cycle with NaClO.

8.2.2 RFQ sample preparation of HRP and *Ec*DyP with ClO_2^- and ClO^-

Peroxidase from horseradish (Type VI, essentially salt-free, lyophilized powder) was purchased from Sigma Aldrich and used without further purification. *Ec*DyP was recombinantly produced and purified by our collaborators from BOKU, as described in [37]. Samples for EPR spectroscopy were prepared either using a RFQ device from BioLogic, as described in the previous section, or with a standard flash freezing procedure in liquid N_2 (time scale of 1 – 4 minutes). All samples were prepared in 50 mM phosphate-citrate buffer pH 5.0. In the case of HRP, the protein concentration was in the range of 0.2-0.5 mM, according to the individual experiments. $NaClO_2$ and H_2O_2 were used in a 3-fold molar excess with respect to the protein concentration, while NaClO was added in a 10-fold molar excess.

8.2.3 Sample preparation for W-band experiments

*C*Cld samples were prepared in phosphate-citrate buffer 0.1 M, pH 5.0 and CAPS buffer 0.1 M, pH 10.0. Both buffers were filtered and degassed before use. CAPS was chosen as alkaline buffer because of its stability at cryogenic temperatures and in presence of glycerol, since cryoprotectants are beneficial when performing low-temperature EPR and especially pulse techniques (Chapter 4). Then ~ 1 µL of a 0.14 mM *C*Cld solution at pH 5.0 was inserted in the capillary and quickly centrifuged (1-2 s). Subsequently, ~ 1 µL of a 2 mM NaClO solution was added and pushed to the bottom of capillary by a quick centrifugation (1-2 s) to mix with the already present protein solution. Finally, the sample was flash frozen in liquid N_2. The final concentrations of *C*Cld and NaClO were 70 µM and 1 mM, respectively (with a final 14-fold molar excess of NaClO).

8.2.4 EPR measurements

X-band CW-EPR spectra were recorded with an ELEXSYS E580 spectrometer (Bruker BioSpin GmbH) operating at a microwave frequency of ~9.4 GHz and equipped with a standard TE102 cavity and a liquid He cryostat (Oxford Inc.). Measurements were performed in the range of 5-10 K, under non-saturating conditions, with a modulation frequency of 100 kHz and a modulation amplitude within 0.2 and 1 mT according to the different experiments. W-band EPR measurements were performed in the laboratory of Dr. Alexander Schnegg at the

Max Planck Institute for Chemical Energy Conversion (Mülheim an der Ruhr, Germany). Spectra were recorded using a modified Bruker Elexsys E680 spectrometer equipped with a lab built 94 GHz (W-band) microwave extension and a cryogen free Cryogenic 6 T magnet.

W-band CW-EPR measurements were performed at 40 and 80 K, under non-saturating conditions, with a modulation frequency of 100 kHz and a modulation amplitude of 0.5 mT. ESE-detected EPR was performed at 80 K with a short repetition time of 1000 μs , a τ value of 140 ns and a π/2 pulse length of 20 ns. The magnetic field was calibrated as follows: a W-band CW-EPR spectrum of a certified Mn(II)-ZnS standard sample was recorded. A simulation of the Mn(II)-ZnS sample was performed using as an input the spin system parameters g_{iso} = 2.0024 ± 0.0003 and A_{iso} = 190.68 MHz, previously accurately determined in the laboratory of Dr. Schnegg. The shifts (ΔB) between each line of the recorded and of the simulated spectra were calculated and plotted against the positions of the lines in the recorded spectrum (**Figure 8.1**, left panel). The shift variation was fitted with a linear model using the MATLAB Basic Fitting tool, to obtain the following equation:

$$\Delta B = 0.04 * B - 1.32E02 \qquad \text{(Eq. 8.1)}$$

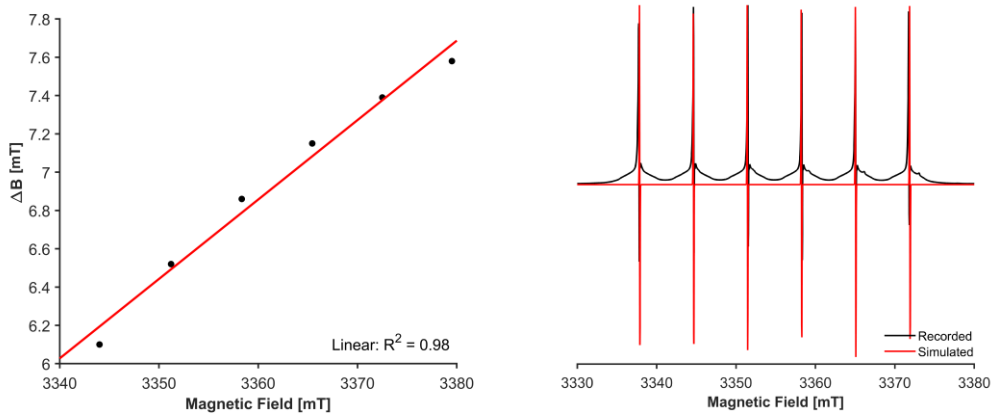

Figure 8.1 *Left panel: Magnetic field calibration curve showing the linear dependence of the shift on the magnetic field. Right panel: validation of the magnetic field calibration by overlaying the recorded Mn(II)-ZnS spectrum (black) and the corresponding simulation (red) after correcting the magnetic field axis with Eq. 8.*

Then, a new magnetic field vector was calculated by subtracting Eq. 8.1 from the original magnetic field vector and the goodness of the calibration was validated by the overlay of the recorded Mn(II)-ZnS spectrum, now plotted with the corrected

magnetic field axis, with the corresponding simulation (**Figure 8.1**, right panel). The same equation was used to correct the magnetic field axis of the unknown sample. In all cases, EPR simulations were performed with the EasySpin toolkit (v. 6.0.0-dev.41) implemented in MATLAB [188].

8.3 Results

8.3.1 Compound I formation in the reaction with ClO_2^- and ClO^- and its pH-dependent degradation to Compound I*/II

The results presented in this section are a part of a more extended stopped-flow investigation on wild-type *C*Cld and variants Q74E and Q74V, already introduced in Chapter 5. Here the discussion will be limited to the wild-type form of the enzyme to contextualize the EPR findings presented later. For more details, the reader is referred to [150].

Ferric wild-type *C*Cld was mixed with a 330-fold excess of chlorite, which guaranteed full degradation of the substrate. Typically, a significantly prolonged phase of chlorite decomposition was observed with increasing pH. At pH 7.0, immediately after mixing of the ferric protein with chlorite, the Soret band absorbance at 408 nm is lost, suggesting Compound I formation (absorbance maximum ~ 410 nm) (**Figure 8.2** middle panel). Within ~7 ms, the maximum of hypochromicity is reached, immediately followed by a rapid shift of the Soret maximum to 418 nm (7–118 ms) that dominates until chlorite is fully degraded after ~5800 ms. The spectral features (418, 528, and 551 nm) of this redox intermediate are reminiscent of an oxoiron(IV) species. Finally, this redox intermediate is slowly and directly converted to the resting state (isosbestic point at 413 nm).

At pH 5.0, chlorite degradation is significantly faster (**Figure 8.2**, top panel). When the resting state *C*Cld is mixed with chlorite, similar hypochromicities are observed in the initial fast phase and the kinetics are comparable to that at pH 7.0. Interestingly, the oxoiron(IV) species fails to fully form. The resulting species that dominates during chlorite degradation exhibits Soret maxima around 406 nm, whereas Compound I*/II-typical Q-band maxima at 528 and 551 nm do not occur. Finally, this redox intermediate slowly and directly converts back to the resting state. On the other hand, at pH 9.0 chlorite is still fully degraded, but the reaction is very slow. The ferric state appears to convert directly to the oxoiron(IV) species (418 nm), which is very slowly converted to the ferric resting state after chlorite degradation (**Figure 8.2**, bottom panel).

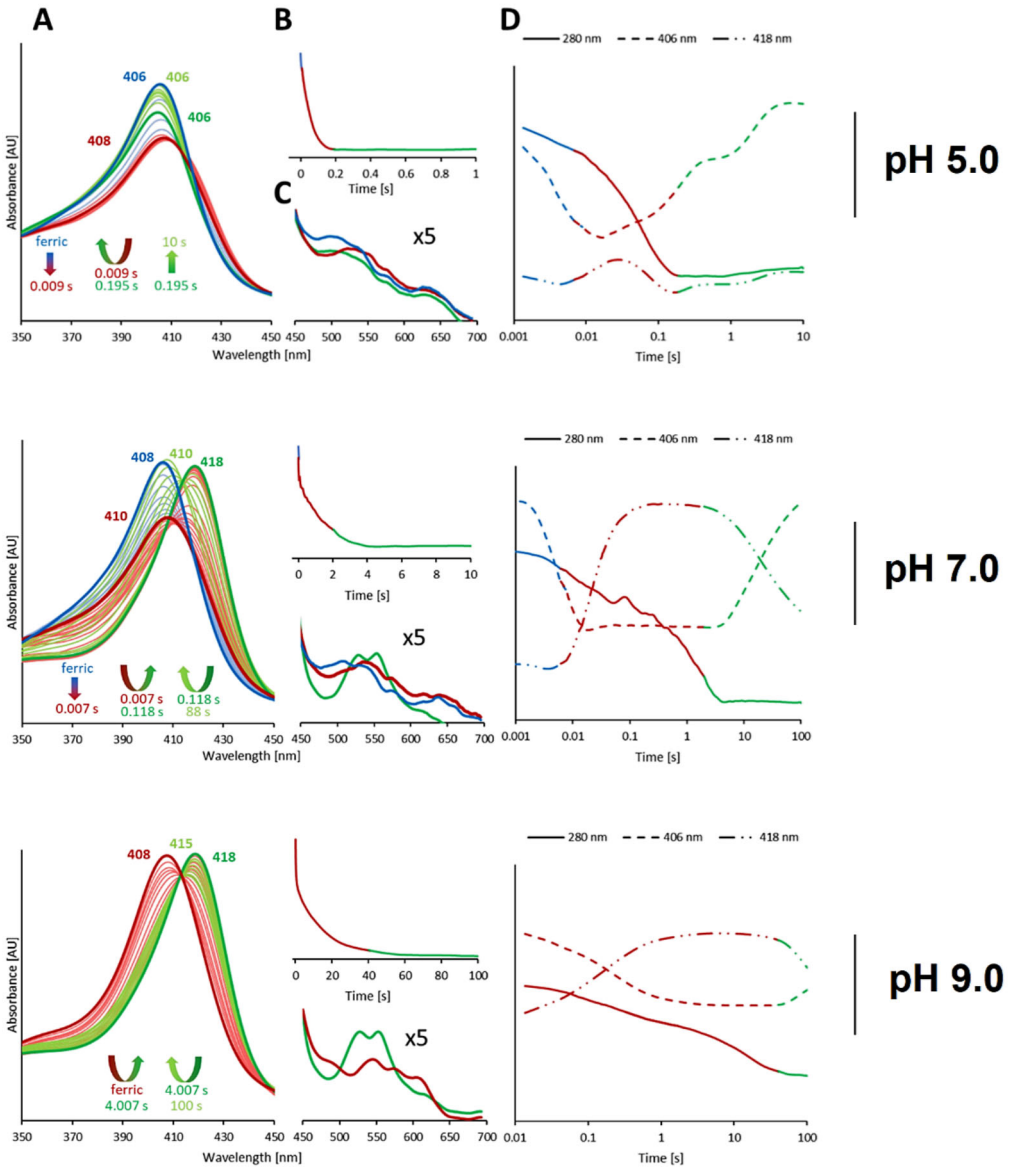

Figure 8.2 *Reaction of 1.5 µM CCld with 500 µM ClO_2^- at pH 5.0 (top), 7.0 (middle) and 9.0 (bottom). Reactions were followed by conventional stopped-flow spectroscopy.* ***(A, C)*** *Interconversion of redox intermediates during the reaction.* ***(B)*** *Chlorite degradation monitored by loss of absorbance at 280 nm.* ***(D)*** *Time traces reflecting chlorite degradation (280 nm, solid line), formation of Compound I and resting state (406 nm, dashed line), as well as formation and conversion of Compound II/Compound I* (418 nm, dash-dotted line). The x-axis is shown in logarithmic scale to have a better overview on the whole reaction.*

To probe the pH dependency of Compound I stability, the reactions of ferric *C*Cld with hypochlorite were followed at different pH values (**Figure 8.3**). Hypochlorous acid (HOCl) is known to convert heme proteins including peroxidases, catalases, and Clds to Compound I [55, 263–266]. At pH 5.0 (**Figure 8.3 A**), fast redox reaction of *C*Cld with HOCl (k_{app} = 6.3 × 10^5 M^{-1} s^{-1}) is accompanied by a ~ 50 % hypochromicity in the Soret region and the formation of a band at ~ 650 nm. Compound I is relatively stable despite the fact that an excess of HOCl is present in the reaction mixture. This fact suggests that the rebinding step between hypochlorite and Compound I, which would support the heterolytic pathway in chlorite degradation (**Scheme 1.2, Reaction 2A**), does not occur. Finally, the spectral transitions suggest the (slow) conversion of Compound I to an oxoiron(IV) species with bands at 418, 528, and 550 nm, which might represent Compound I*. At pH 7.0 (**Figure 8.3 B**), a similar interconversion of *C*Cld redox intermediates occur; however, the formation of Compound I* is more pronounced compared to pH 5. Because the rate of Compound I formation is similar to that at pH 5.0, this clearly suggests a higher instability of Compound I and an increased rate of conversion of Compound I to Compound I*. This is even more pronounced for the reaction at pH 9.0 (**Figure 8.3 C**), where Compound I formation is already difficult to trap despite the fact that the rate of its formation is similar to that at pH 5.0 or 7.0.

The pH-dependence of Compound I conversion to Compound I* was additionally confirmed by pH-jump experiments. The ferric wild-type *C*Cld was mixed with a 10-fold excess of ClO^- at pH 5 and after a delay time of 75 ms, the resulting Compound I was mixed with the buffer at selected pH values. The results demonstrated that the stability of Compound I significantly decreases with increasing pH, with k_{obs} values of decay ranging from 1.5 s^{-1} (pH 5.0) to 701 s^{-1} (pH 9.0) (results shown in [150]).

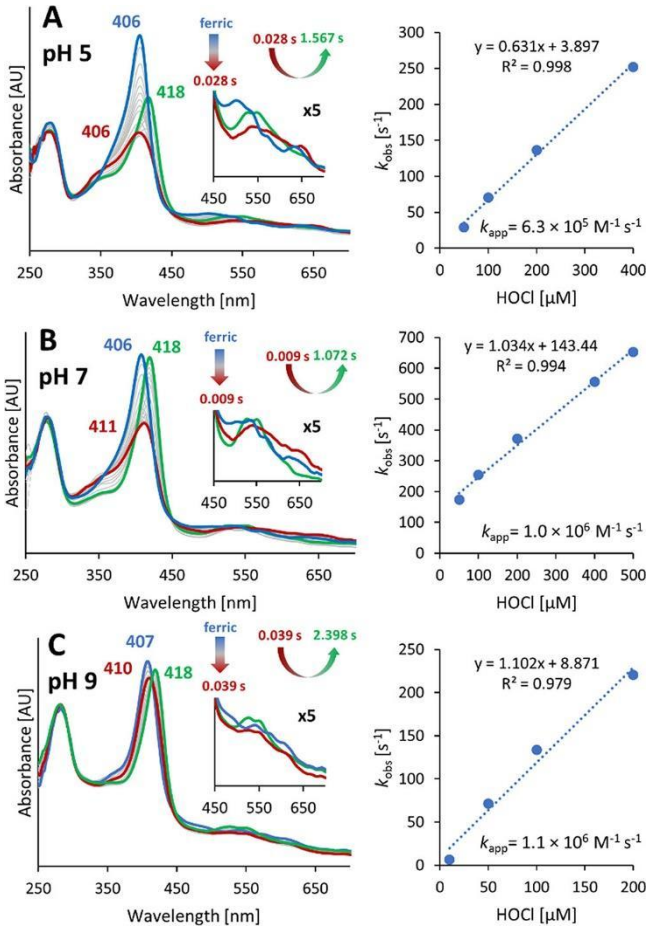

Figure 8.3 *Reaction of 1.5 µM ferric CCld with 200 µM ClO^- at pH* ***(A)*** *5.0,* ***(B)*** *7.0, and* ***(C)*** *9.0. Reactions were followed by conventional stopped-flow spectroscopy. Blue: initial spectrum of ferric protein, red: compound I, green: compound I*, grey: intermediate spectra. Right panels: plots of k_{obs} versus hypochlorite concentration. The rate constant k_{app} of Compound I formation was obtained from the slope of the linear regression.*

8.3.2 RFQ-EPR Spectroscopy of *C*Cld with ClO_2^- at pH 5.0

Compound I has been characterized in many heme systems [267], and it can be described as an oxoiron(IV) delocalized porphyrin π-radical, being therefore a suitable target to be investigated by EPR spectroscopy. In addition to that, whereas the oxoiron(IV) species Compound II would be EPR silent, the remote amino acid radical responsible for the quenching of the porphyrin radical in the so-called Compound I* species can be in principle detected and identified by means of this

technique. Hence, we decided to use a combined RFQ-EPR spectroscopy method to trap the fast-evolving intermediates formed during the catalytic reaction of *C*Cld in the presence of ClO_2^-. **Figure 8.4** shows the X-band CW-EPR spectrum of wild-type *C*Cld at pH 5.0, whose reaction in the presence of a 300-fold excess of chlorite was freeze-quenched within ~ 60 ms. The full spectrum, represented in **Figure 8.4 A**, is dominated by a strong signal in the high-field region, with well-resolved hyperfine splittings. A weak signal at around 115 mT (g ~ 5.9) indicates the presence of a residual high-spin signal from unreacted *C*Cld [201]. The magnification of the dominating signal (solid black) and its corresponding simulation (dashed red) are depicted in **Figure 8.4 B**. The spectral shape closely resembles that of a chlorine dioxide radical ($ClO_2^{\bullet}$), as reported in several studies where gaseous $ClO_2^{\bullet}$ was trapped in inert matrices [268] or adsorbed in zeolite materials [269]. Additionally, in a recent study on the pentameric Cld from *Dechloromonas aromatica* [149], evidence of the EPR spectral signature of chlorine dioxide were reported for the reaction with chlorite at both pH 5.2 and 9.0. The species characterized in this work presents axial g and A tensors with principal values of g = [2.002 2.011 2.017] and A = [212 −36 −21] (in MHz), respectively. These parameters are in good agreement with the ones of the same radical species reported so far [268, 269] and are supported by density functional theory (DFT) calculations (**Table 8.1**). It is noteworthy that no evidence of the typical features of a Compound I signal, or those of an amino-acid radical, were observed in the spectrum. As will be discussed later, the strong signal from $ClO_2^{\bullet}$, which likely represents a byproduct, might hamper the observation of weaker underlying signals.

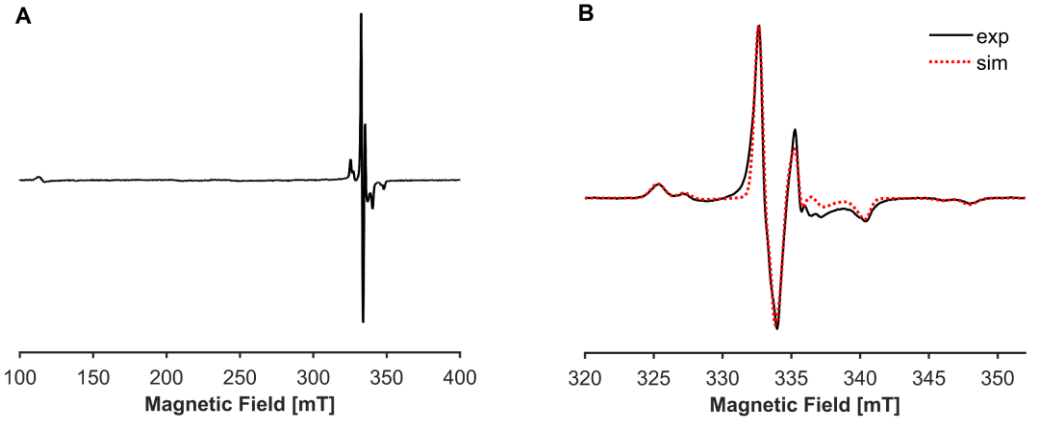

Figure 8.4 *X-band CW-EPR spectrum of 0.1 mM CCld in presence of a 300-fold molar excess of chlorite (30 mM) at pH 5.0. The sample was prepared by RFQ (quenching time of ~ 60 ms) and the spectrum was recorded at 10 K, with a MW power of 1 mW and a modulation amplitude of 1 mT.* ***(A)*** *Full spectrum showing a minor feature at 115 mT representing a residual resting state signal;* ***(B)*** *Zoom into the high field region of spectrum in* ***(A)*** *(solid black) and corresponding simulation (dashed red).*

	g_x	g_y	g_z	$^{Cl}A_x$ (MHz)	$^{Cl}A_y$ (MHz)	$^{Cl}A_z$ (MHz)
DFT	2.0019	2.0133	2.0174	200	-40	-31
Exp.	2.002	2.011	2.017	212	-36	-21

Table 8.1 *Comparison between the DFT-computed g and ^{35}Cl hyperfine values for $ClO_2^{\bullet}$ (details of computation in* [150]*) and the parameters used to simulate the EPR spectrum in* ***Figure 8.4****. The experimental error is 1 on the last digit.*

8.3.3 RFQ-EPR Spectroscopy of *C*Cld with ClO^- at pH 5.0

When the reaction of 0.25 mM wild-type *C*Cld with a 10-fold excess of ClO^- (2.5 mM) at pH 5.0 is freeze-quenched within ~ 60 ms, a sharp featureless signal appears in the EPR spectrum around $g \sim 2.0$ (**Figure 8.6A**). Although Compound I would theoretically show a component at a similar field position [63, 88, 129, 131, 270] other factors suggest that the detected species may represent an amino acid radical instead. On the one hand, the EPR spectra of Compound I described in previous studies of chlorite dismutases [63, 149] or other heme enzymes [88, 129, 131, 270] present some differences in terms of line shape and broadening. Second, this signal is easily saturated at very low temperatures (2.5–5 K), and it can be observed up to 80 K (**Figure 8.5**), which in fact excludes the possibility that it represents a Compound I species [271]. Hence, this narrow line can be assigned to an unknown amino acid radical, which would indicate the formation of Compound I*, the decay product of Compound I, in the absence of electron donors. The failure to observe an EPR signal of Compound I, despite the fact that the time range corresponds to its maximum formation according to stopped-flow experiments performed with the same substrate-to-protein ratio (**Figure 8.3**), is undoubtedly due to the larger concentrations needed for the EPR experiment because the formation rate depends on the protein and substrate concentration. It has to be noted that when the sample is prepared with a "conventional" flash-freezing in liquid N_2 (quenching time of ~10 s), the same EPR signal is still visible, confirming the slow decay of the oxoiron(IV) species already observed in the UV–vis measurements. **Figure 8.6 B** depicts a magnification of the high-field region in which the RFQ and the flash-frozen samples are compared. The two spectra only show a minor variation in line-shape, which may be due to small differences in the unresolved anisotropy of the EPR tensors or to the presence of a composite signal where the ratio of the individual components varies over time.

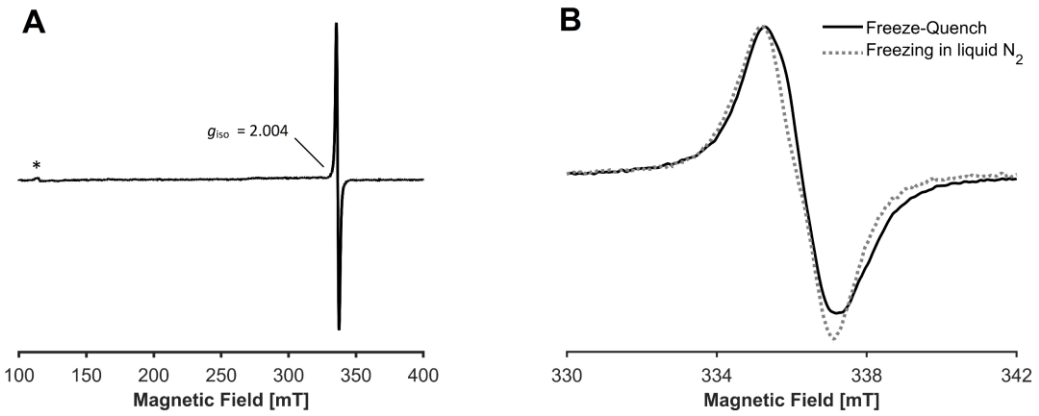

Figure 8.6 *X-band CW-EPR spectrum of 0.25 mM CCld in presence of a 10-fold molar excess of hypochlorite (2.5 mM) at pH 5.0.* ***(A)*** *Full spectrum of the sample prepared by RFQ (quenching time of ~ 60 ms), recorded at 10 K, with a MW power of 0.2 mW and a modulation amplitude of 1 mT. The asterisk indicates the presence of a residual high-spin signal corresponding to unreacted CCld.* ***(B)*** *Comparison of the samples obtained by RFQ (solid black) and N_2 flash-freezing (dashed grey), high-field region only. The spectra were recorded at 10 K, with a MW power of 0.2 mW and 0.1 mW for the RFQ and the N_2 flash-frozen samples, respectively, and a modulation amplitude of 0.2 mT in both cases. The intensities are normalized to the maximum positive peak to highlight differences in line shape.*

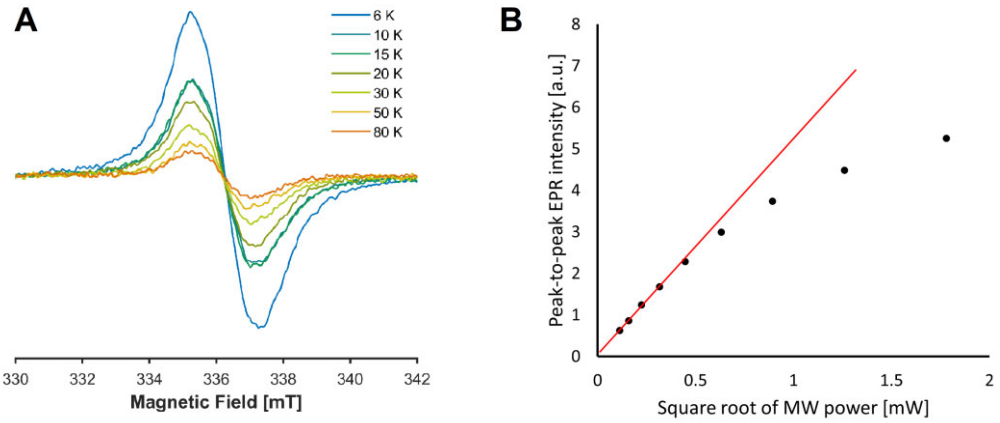

Figure 8.5 (A) *Temperature dependence of the amino acid radical-type EPR signal observed in the reaction of 0.25 mM CCld with a 10-fold molar excess of hypochlorite (2.5 mM) at pH 5.0 and* ***(B)*** *MW power saturation curve of the sample measured at 3 K. The red line shows how the dependence of the EPR intensity on the MW power deviates from linearity already at low MW power values.*

8.3.4 EPR Spectroscopy of *C*Cld with ClO^- at pH 5.0 in the absence or presence of serotonin

Serotonin is an efficient one-electron donor for Compound I and Compound II of heme peroxidases [272]. Stopped-flow experiments performed in this work showed that serotonin reduces *C*Cld Compound I in a biphasic reaction, within the sequence Compound I → oxoiron(IV) → Fe(III), where both steps exhibit a clear concentration dependency [150]. Next, serotonin was also found to be able to react with Compound I*, the decay product of Compound I in the absence of an external electron donor. The concentration-dependent monophasic conversion to the ferric resting state suggests that serotonin could recover *C*Cld from the unproductive Compound I degradation to Compound I* [150].

This was further corroborated by EPR spectroscopy findings. **Figure 8.7** shows the EPR spectra of 0.2 mM *C*Cld in the presence of a 50-fold molar excess of serotonin (**Figure 8.7 a**) as well as *C*Cld reacting with a 10-fold molar excess of hypochlorite (2 mM) in the presence (**Figure 8.7 b**) or absence (**Figure 8.7 c**) of serotonin at pH 5.0. The addition of serotonin alone has no effect on the spectrum of resting state *C*Cld, whose features have been previously reported (Chapter 5) [201]. Interestingly, when serotonin is added to the protein sample prior to the addition of hypochlorite, the intensity of the protein radical signal described earlier (**Figure 8.6** and **Figure 8.7 c**) is substantially reduced (**Figure 8.7 b**), confirming that serotonin is indeed able to act as a one-electron reductant of Compound I and Compound II as well as Compound I*.

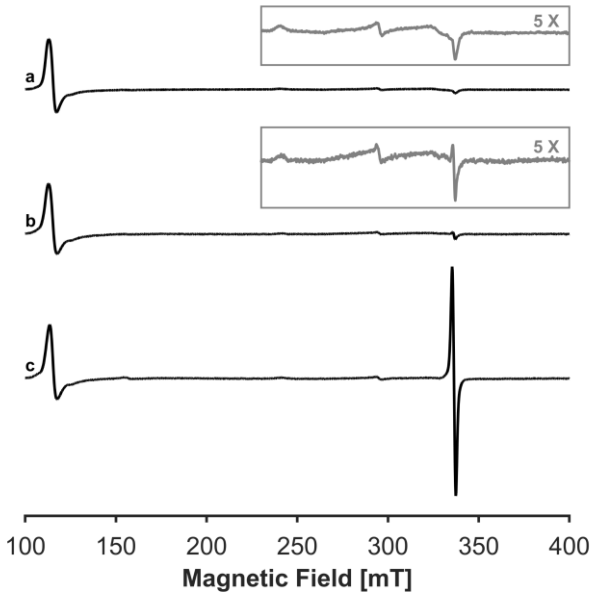

Figure 8.7 *X-band CW-EPR spectra of 0.2 mM wild-type CCld in the presence of serotonin alone* ***(a)*** *and reacting with 2 mM hypochlorite at pH 5.0 in the presence* ***(b)*** *or absence* ***(c)*** *of 10 mM serotonin. The samples were prepared with a "conventional" liquid N_2 flash-freezing method (quenching time < 10 s). The spectra were recorded at 10 K, with an MW power of 1 mW and a modulation amplitude of 1 mT. Intensities are normalized at 115 mT (g^{eff} ~ 6 of high-spin component), and a 5X magnification of the high-field region is depicted in the insets for spectra* ***(a)*** *and* ***(b)****.*

8.3.5 The reaction of *C*Cld with ClO^- investigated by high-frequency EPR

The EPR experiments conducted at X-band suggest that the signal at $g \sim 2$ observed during the reaction of *C*Cld with ClO^- could represent an amino-acid radical (Compound I*) formed as a decay product of Compound I in absence of electron donors. Next, the spin trap 2-methyl-2-nitrosopropane (MNP), known to specifically attack and modify tyrosyl radicals to yield 3-nitrotyrosine, was used in a mass spectrometry analysis in presence or absence of hypochlorite to individuate possible candidates to host the radical of Compound I*. After the addition of 10 – 100 μM of hypochlorite, four different tyrosine residues showed some modification to a certain extent (for the details of the experiment the reader is referred to [150]).

Following the above-mentioned findings, W-band (~ 94 GHz) CW-EPR measurements were performed in the attempt to identify the amino acid(s) responsible for the radical formation. **Figure 8.8** depicts the CW-EPR spectrum and the corresponding simulation of a sample of *C*Cld reacting with a 14-fold molar excess of ClO^- at pH 5.0. A broad signal, possibly consistent with a tyrosyl radical, is observed between 3345 and 3360 mT, while an additional sharp line of uncertain origin, is centered at ~ 3358 mT. The broad signal was simulated using a rhombic g tensor with principal g values g_x = 2.0067, g_y = 2.0045 and g_z = 2.0021, and introducing two equivalent proton nuclei with small hyperfine coupling (A_{iso} = 25 MHz). The g values are consistent with the ones reported for tyrosyl radicals in other protein systems [273] and remarkably similar to the ones of tyrosyl radicals transiently generated during the reaction of selected peroxidases with hydrogen peroxide [136, 274, 275].

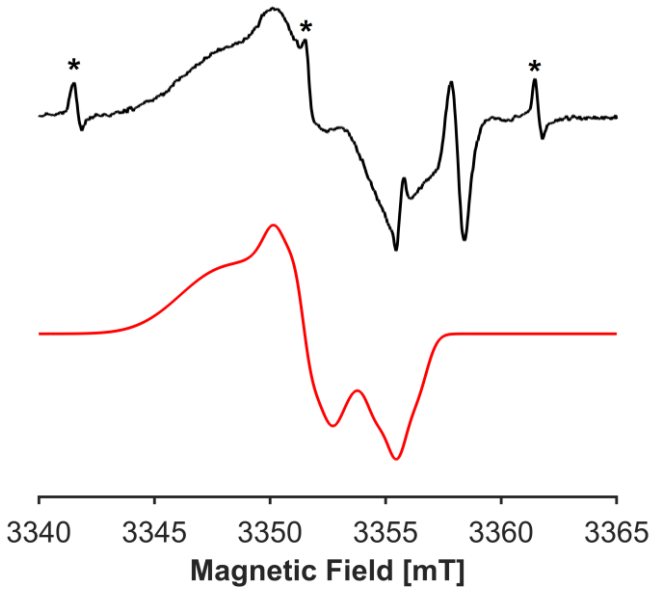

Figure 8.8 *W-band CW-EPR spectrum (top, black) and its corresponding simulation (bottom, red) of the reaction of 70 µM CCld with 1 mM of ClO^- at pH 5.0. The spectrum was recorded at 80 K, with a MW power of 1.7x10^{-3} mW and a modulation amplitude of 0.5 mT. The simulation was performed with an anisotropic gaussian linewidth described by the parameters [110 30 28] MHz. The asterisks indicate a Mn(II) background. The simulation does not take into account a Mn(II) impurity, nor the sharp signal centered at ~ 3358 mT.*

8.3.6 RFQ-EPR of HRP reacting with ClO_2^- and ClO^-

As briefly discussed in section 8.1, the model heme peroxidase HRP is known to react with ClO_2^- forming chlorine dioxide, as observed by UV-vis spectroscopy [263]. This was confirmed by EPR spectroscopy results. **Figure 8.9** shows the CW-EPR spectrum of HRP reacting with a 3-fold molar excess of chlorite, trapped by rapid freeze-quench. The spectral features, as well as the EPR parameters obtained by simulation, are remarkably similar to the ones of the $ClO_2^{\bullet}$ radical found in the spectrum of *C*Cld reacting with a high excess of chlorite (**Figure 8.4** and **Table 8.1**). While the HS signature of the resting state completely disappears in presence of ClO_2^- (**Figure 8.9**, inset), the obtained species can be simulated with *g* and *A* tensors with principal values of *g* = [2.002 2.011 2.017] and *A* = [212 −35 −22] (in MHz), respectively. Note that a control experiment was performed by recording the spectrum of a buffered solution of 0.6 mM $NaClO_2$ (the one used in the HRP sample) with the same experimental parameters. Nor the $ClO_2^{\bullet}$ radical signal, nor other signals, were detected in the control sample.

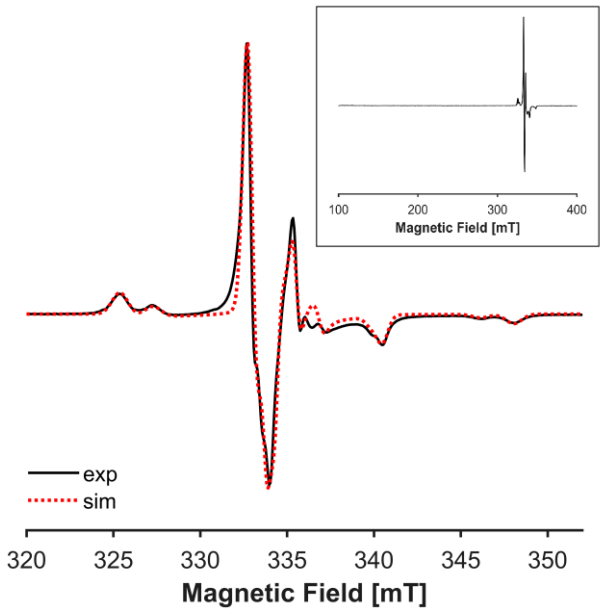

Figure 8.9 *CW X-band EPR spectrum of 0.2 mM HRP in presence of a 3-fold molar excess of chlorite (0.6 mM) at pH 5.0. The sample was prepared by RFQ (quenching time of ~ 60 ms) and the spectrum was recorded at 10 K, with a MW power of 0.1 mW and a modulation amplitude of 0.3 mT. The inset shows the complete absence of HS resting state HRP.*

Given the difficulties in trapping Compound I from the reaction of wild-type *C*Cld with hypochlorite, we wanted to test whether this species could be observed in the reaction of HRP with a 10-fold molar excess of NaClO. Several experiments were performed, including both RFQ and flash freezing in liquid N_2. We found that different quenching times have a significant impact on the resulting spectra (**Figure 8.10**). When the sample is prepared *via* RFQ or flash frozen in liquid N_2 in the shortest time possible (< 1 min) (**Figure 8.10**, black and blue traces), a broad signal centered at ~ 337 mT is detected, which might originate from a superimposition of two co-existing species. Differently, by incubating the reaction for 4 minutes before freezing (**Figure 8.10**, magenta trace), the linewidth is reduced and the signal almost superimposes with the left feature of the signal obtained in the previous conditions. As a positive control, the EPR spectrum of Compound I, obtained by reacting HRP with its natural substrate H_2O_2, was recorded (**Figure 8.10**, green trace).

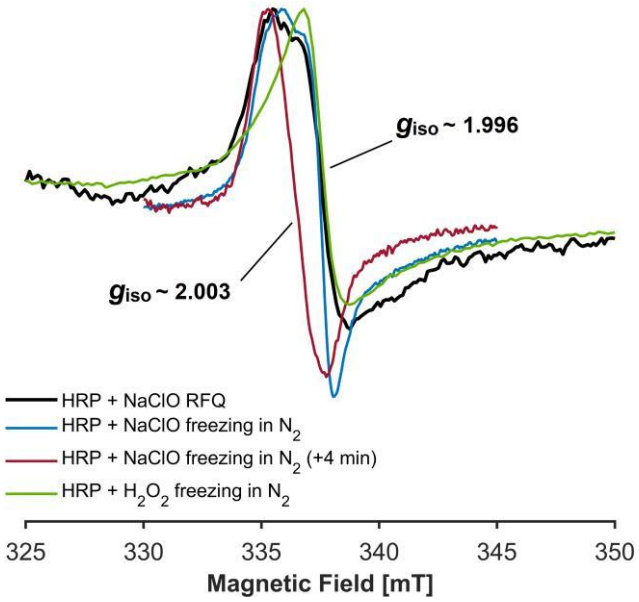

Figure 8.10 *X-band CW-EPR spectra (high-field region only) of HRP reacting with either NaClO or H_2O_2, where the reactions were quenched with different freezing methods.* ***Black****: 0.3 mM HRP reacting with 3 mM NaClO stopped with RFQ;* ***blue****: 0.5 mM HRP reacting with 5 mM NaClO flash frozen in liquid N_2 in the fastest time possible;* ***magenta****: 0.5 mM HRP reacting with 5 mM NaClO flash frozen in liquid N_2 after 4 minutes of incubation at room temperature;* ***green****: reference spectrum of Compound I obtained by reacting 0.2 mM HRP with 0.6 mM H_2O_2 and subsequent freezing in liquid N_2. All samples were prepared in 50 mM phosphate-citrate buffer, pH 5.0 and measured at 3 K, except for the H_2O_2 -containing sample (green trace), which was measured at 5.5 K*

Interestingly, this time the signal almost coincides with the right feature of the previous spectra. This suggests that in fast freezing conditions, Compound I might co-exist with a later-forming species, possibly Compound I*. The difference in the approximate g_{iso} values (indicated in **Figure 8.10**) additionally supports the assignation of the different features. Indeed, while a $g_{iso} \sim 2.003$ is comparable with other amino-acid radical signals reported in literature [274, 275], a $g_{iso} \sim 1.996$ is more in line with what reported on EPR of Compound I species [267].

Next, 0.5 mM HRP was mixed with 5 mM NaClO and 20 % (v/v) of ethylene glycol and flash frozen in liquid N_2 after an incubation of 2 minutes at room temperature. In addition to the strong signal centered at $g \sim 2$ already observed in the previous experiments, the resulting CW-EPR spectrum contained some residual HS protein (Chapter 3) and a further LS contribution with g values of $g_z = 2.55$, $g_y = 2.14$ and $g_x = 1.86$ which closely resembles an OH^--ligated heme-iron species (Chapter 5 and [48, 49, 61, 148, 178, 204–206]) (**Figure 8.11 A**). Closer inspection of the signal at $g \sim 2$ reveals the presence of a sub-structure which was simulated as a sum of two different contributions. (**Figure 8.11 B**). For both species, a g tensor with principal g values = [2.0068 2.0035 2.0023] was used. In one case, two proton nuclei with A_{iso} of 48 MHz and 17 MHz, respectively, were added, while for the second species only a proton coupling of 18 MHz was used for the simulation. These values are similar to those found in the reaction of *C*Cld with hypochlorite (section 8.3.5) and to those reported in literature for tyrosyl radicals [136, 273–275]. In any case, due to the broad linewidth, this simulation might be the result of an over-fitting, therefore these values need to be taken with caution. ^{1}H-ENDOR might be of help in the determination of the proton coupling and it can be considered for further investigation of this sample.

When a replicate of this sample was frozen in liquid N_2 without any incubation time (freezing time < 1 minute), the features of the sub-structure observed before are not resolved (**Figure 8.11 C**, grey trace). As shown in **Figure 8.11 D**, a signal centered at $g \sim 1.996$ and consistent with a Compound I intermediate, becomes more pronounced at higher MW power values. As already mentioned in section 8.3.3, the signal of an amino-acid based radical would be highly saturated at such low measurement temperatures (3-4 K) and high MW powers; on the other hand, the signal of a Compound I species is expected to follow an opposite trend.

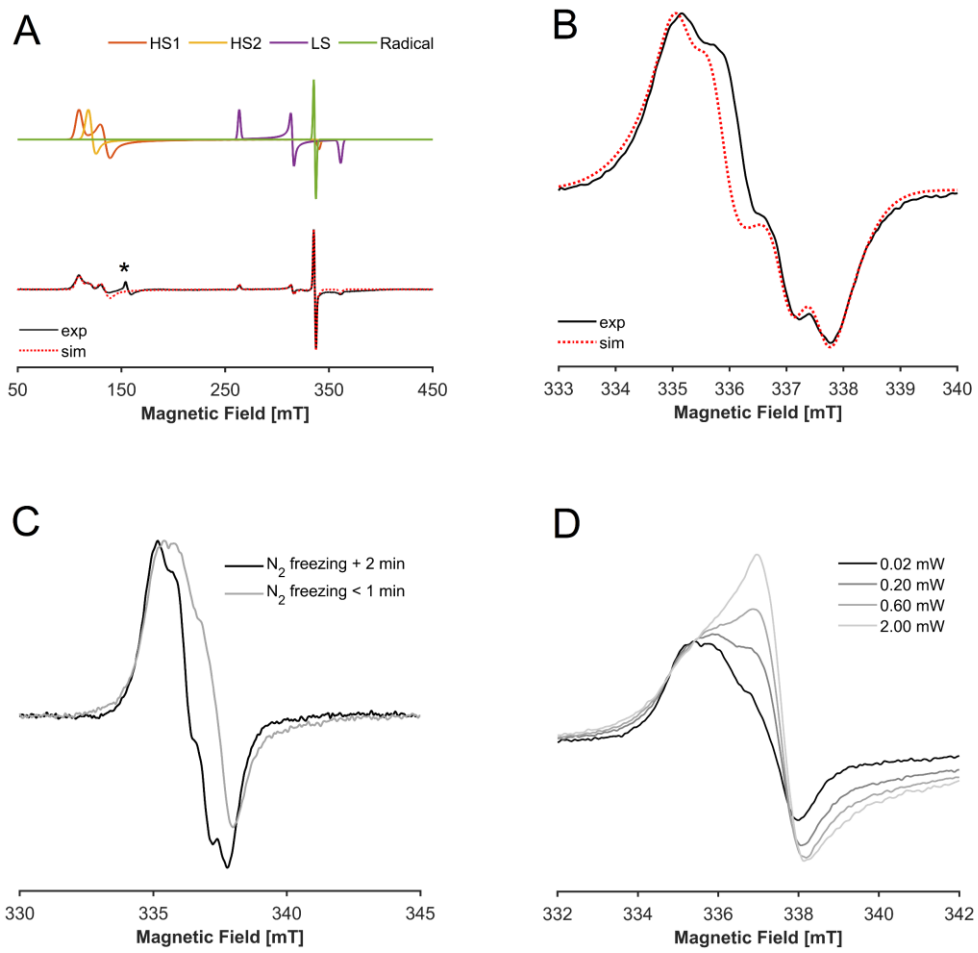

Figure 8.11 *0.5 mM HRP reacting with a 10-fold molar excess of NaClO (5 mM) quenched with different freezing methods.* ***(A)*** *Full CW-EPR spectrum (solid black) recorded at 10 K and corresponding simulation (dotted red) of a sample flash frozen in liquid N_2 after 2 minutes of incubation at room temperature. The asterisk indicates the presence of free iron (g ~ 4.3) possibly due to protein denaturation caused by the excess of hypochlorite. The individual contributions used for the simulation are shown on top with the colors defined in the figure legend.* ***(B)*** *Zoom-in of the high-field region of spectrum in (A) (solid black), recorded at 4 K, and its corresponding simulation (dotted red), showing the sub-structure attributed to the presence of different amino acid-based radicals (simulation parameters in the main text).* ***(C)*** *Comparison between samples frozen at different time points (high-field region only), where the black trace is the same sample shown in (A) and (B), while the grey trace represents a sample frozen in liquid N_2 in the shortest time possible.* ***(D)*** *MW power dependence of the spectrum (grey trace) shown in (C), performed at 3 K, highlighting the presence of a signal center at g ~ 1.996 consistent with the Compound I intermediate. All samples were prepared in 50 mM phosphate-citrate buffer, pH 5.0.*

8.3.7 The reaction of *Ec*DyP with H_2O_2, ClO_2^- and ClO^-

Dye-decolorizing peroxidases are closely related to chlorite dismutases, with a comparable overall structure and a strikingly similar heme site architecture, despite possessing different enzymatic activities (Chapter 1, section 1.1.4). To get insights into the reactivity of the dye-decolorizing peroxidase from *E. coli* (*Ec*DyP) with different (potential) substrates, several CW-EPR experiments in presence of H_2O_2, ClO_2^- and ClO^- were conducted. The reactions were stopped either *via* RFQ or through flash freezing in liquid N_2. The EPR spectrum of resting state *Ec*DyP (**Figure 8.12**, left panel, trace a) is comparable with the one of another member of this family, the dye-decolorizing peroxidase from *K. pneumoniae* (*Kp*DyP). It shows multiple HS contributions with different rhombicity and a stable "resting state" radical ($g \sim 2$), already investigated in detail for *Kp*DyP [37, 88]. When *Ec*DyP is mixed with either H_2O_2, ClO_2^- or ClO^- and the reaction is quenched by flash freezing in liquid N_2 (< 1 minute), no significant changes in the $g \sim 2$ feature can be appreciated, at least in the chosen experimental conditions (**Figure 8.12**, left panel, trace b, c and d). Importantly, different from the case of HRP and *C*Cld, the addition of chlorite does not result in the formation of chlorine dioxide (**Figure 8.12**, left panel, trace d). The addition of different compounds, however, has an impact on the HS signature of *Ec*DyP (**Figure 8.12**, right panel). Changes in overall amount, rhombicity and relative contribution of different HS species are clearly observed. Interestingly, in presence of the natural substrate H_2O_2, almost no residual HS is detected, despite no evident differences can be observed in the high-field region of the spectrum (**Figure 8.12**, left panel, trace b and right panel, green trace). Indeed, in this case, the signal centered around $g \sim 2$ must arise, at least in part, from the Compound I intermediated which is expected to form during the peroxidase cycle (Chapter 1, section 1.1.3).

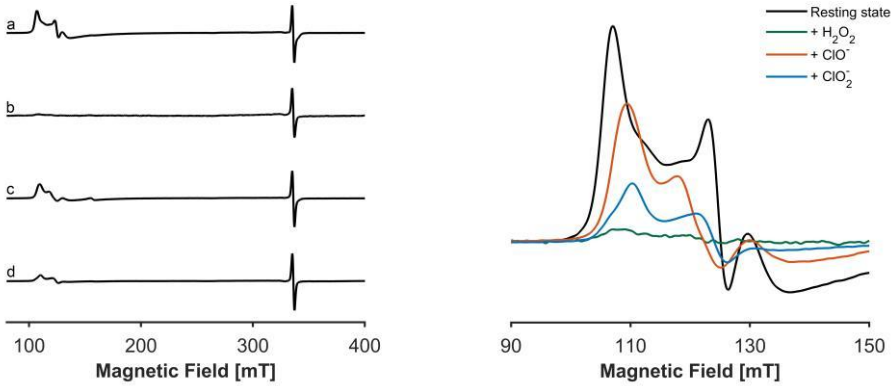

Figure 8.12 *CW-EPR spectra of EcDyP in its resting state or in the presence of different compounds. Left panel: full spectra of* ***(a)*** *resting state EcDyP,* ***(b)*** *with a 3-fold molar excess of H_2O_2,* ***(c)*** *with a 10-fold molar excess of NaClO and* ***(d)*** *with a 3-fold molar excess of $NaClO_2$. Right panel: zoom-in the low-field region of the spectra, highlighting the changes in the HS features in the presence of different compounds. Colors explained in the figure legend. All samples were prepared in 50 mM phosphate-citrate buffer, pH 5.0 and flash frozen in liquid N_2 (freezing time < 1 minute).*

8.4 Discussion and conclusions

It has been demonstrated with pentameric (clade I) Cld from *Dechloromonas aromatica* (*Da*Cld) that chlorite is the sole source of dioxygen as determined by oxygen-18 labeling studies and that Cld uses chlorite neither for oxygen atom transfer to aliphatic or aromatic molecules nor in halogenation reactions [63]. This distinguishes Clds from peroxidases and other heme enzymes. By contrast, when peroxyacetic acid was used as an alternative oxidant of *Da*Cld, oxidation and oxygen atom transfer reactions occurred and Compound I could be trapped by rapid-mixing UV–visible spectroscopy [64]. Peroxyacetic acid (PAA) is an extremely strong oxidant with $E^{\circ\prime}$[(CH_3COOOH, H^+/CH_3COO^-, H_2O) = 1636 mV at pH 6.0] [276], known to mediate the two-electron oxidation of heme proteins. Whereas reactions with hydrogen peroxide resulted in slow heme destruction [64], at acidic pH, heterolytic cleavage of the O–O bond of PAA yielded clean *Da*Cld Compound I [64]. At alkaline pH, rapid formation of Compound I* was observed. The authors concluded that PAA mediates Compound I formation at all pH values and that radical migration is strongly promoted at alkaline pH regimes. Additionally, the authors proposed that (by analogy with PAA) the heterolytic Cl–O bond cleavage of chlorite to yield an oxoiron(IV) porphyrin cation radical is the most likely initial step in Cld catalysis, accompanied, therefore, by O–O bond formation from Compound I and hypochlorite [64]. Recently, Geeraerts *et al.* demonstrated the formation and accumulation of

Compound I in the reaction between *Da*Cld and bromite [149]. Bromite was used as the surrogate substrate because the reaction between *Da*Cld and chlorite did not allow clear assignments of the relevant catalytic intermediates. Importantly, bromite decomposition was coupled with the evolution of O_2 [149].

Formation and Reactivity of Compound I of *C*Cld. Here, we have investigated the dimeric (clade II) Cld from *Cyanothece* sp. PCC7425 (*C*Cld). We demonstrate that, similar to PAA, the surrogate oxidant hypochlorite is also able to mediate the two-electron oxidation of ferric Cld to Compound I. Hypochlorous acid is a strong two-electron oxidant [$E°'$ (HOCl, H^+/Cl^-, H_2O) = 1280 mV at pH 7.0] [265]. At pH 5.0, *C*Cld mediates the heterolytic cleavage of the O–Cl bond of hypochlorite, yielding Compound I. The spectral signatures, *i.e.*, 50% hypochromicity in the Soret region and formation of a band at ~650 nm, clearly suggest the presence of an oxoiron(IV) porphyryl radical species (**Figure 8.3**). Similar to Compound I of heme peroxidases, *C*Cld Compound I is able to react with two- and one-electron donors like iodide and serotonin and also with chlorite. With iodide, the reduction of *C*Cld Compound I was monophasic and directly converted this intermediate to ferric *C*Cld. By contrast, reduction by one-electron donors like serotonin and chlorite was biphasic, suggesting the reaction sequence Compound I → Compound II → ferric *C*Cld [150]. One-electron oxidation of chlorite by the redox intermediates Compound I and Compound II of heme peroxidases produces chlorine dioxide, $ClO_2^{\bullet}$ [264]. The standard reduction potential, $E°'$, of the couple (ClO_2/ClO_2^-) has a value of 934 mV and is independent of pH above pH 2.0 [55, 277]. The fact that *C*Cld Compound I and Compound II are also able to rapidly produce chlorine dioxide at rates of ~10^5 M^{-1} s^{-1} indicates that (i) the respective $E°'$ values of the redox couples Compound I/Compound II and Compound II/ferric *C*Cld must be >1000 mV and (ii) these reactions could contribute at least as side reactions in Cld turnover under certain reaction regimes, *e.g.*, excess of chlorite. This is underlined by the fact that during chlorite degradation, an increase in absorbance at 360 nm has been observed [55], a wavelength at which chlorine dioxide exhibits its characteristic absorption maximum [129]. In addition, in this study we demonstrated by EPR spectroscopy the formation of chlorine dioxide in the Cld/chlorite system with *C*Cld (section 8.3.2, **Figure 8.4**), which was recently observed also with the pentameric *Da*Cld [149].

pH-Dependent Conversion of Compound I to Compound I*. Similar to clade I *Da*Cld Compound I formed by PAA, the stability of *C*Cld Compound I formed by hypochlorite significantly decreased with increasing pH [150]. Compound I converted to an oxoiron(IV) species, with concomitant formation of amino acid radicals (Compound I*). This in turn resulted in oxidative damage of the protein matrix, which has been demonstrated by spin-trapping experiments using MNP

combined with mass spectrometric analysis [150] as well as by EPR (section 8.3.3, **Figure 8.6**). Importantly, Compound I* formation occurs both in the system *C*Cld/hypochlorite and in the system *C*Cld/chlorite, and all tyrosines are modified in the presence of excess oxidants, even though Y121 shows the highest modification by MNP [150]. Compared to the other tyrosines (Y5, Y170, Y61), Y121 exhibits both a relatively short distance to the heme iron (12.9 Å) and noncovalent interactions with E157 and R161. Given the featureless character of the high-field EPR signal obtained upon mixing *C*Cld with hypochlorite (**Figure 8.6**), W-band EPR measurements were performed in the attempt to identify the nature of the hypothesized amino acid radical. Preliminary data suggest that indeed one or more tyrosine residues could be the target of the migrating radical (section 8.3.5, **Figure 8.8**), thus corroborating the findings from the MNP assay. Even though further experiments on Tyr mutants of *C*Cld will be required to confirm these results, a tentative assignment of the radical signal observed at W-band is supported by the consistency of the g values with the ones reported in literature for tyrosyl radicals in other enzymatic systems. On a different note, the formation of Compound I* can be correlated with the fact that the Cld activity significantly decreases with increasing pH values. Interestingly, serotonin acts as a one-electron donor not only for *C*Cld Compound I and Compound II but also for Compound I*, thereby providing the possibility to get the enzyme out of this dead end and back to catalytically active intermediate(s). This is demonstrated by EPR spectroscopy, where the addition of a 50-fold molar excess of serotonin before starting the reaction with hypochlorite had a clear impact in the resulting spectrum. The signal attributed to the amino acid radical associated to Compound I* formation is greatly reduced in the presence of serotonin (**Figure 8.7**). The fact that serotonin partly prevents inhibition of *C*Cld is an important finding for the use of chlorite dismutase in a wide variety of applications [72]. Future studies will have to determine which cost-effective substitute for serotonin can be used as a single-electron donor in practice to improve the performance of this heme enzyme.

Compound I Is the Catalytically Active Redox Intermediate during Chlorite Degradation. The question remains about the catalytically relevant redox intermediate in chlorite degradation. The provided stopped-flow data demonstrate that upon mixing of *C*Cld with chlorite, Compound I is the dominating redox intermediate at optimum pH (section 8.3.1, **Figure 8.2**). An oxoiron(IV) species with Soret maximum at 418 nm fails to fully form at pH 5.0. With increasing pH, the oxoiron(IV) species dominates the spectral signatures during chlorite degradation. In principle, both Compound II and Compound I* can contribute to these spectral features. The present study suggests that Compound I converts to Compound I* as an important side reaction of dimeric chlorite dismutases, which is more pronounced at high pH values. The fact that (unlike in stopped-flow spectroscopy)

it was not possible to identify the EPR signature of *C*Cld Compound I in the presence of chlorite is due to the working conditions of EPR spectroscopy, which require a much higher concentration of the reagents. This scaling up could promote off-pathway reactions such as the production of chlorine dioxide, whose strong spectral features can easily cover any weaker underlying signals (**Figure 8.4**). This would also explain why, with a similar substrate-to-protein ratio and same time range, the characteristic chlorine dioxide band at 360 nm is not visible in the stopped-flow experiments performed in this work. Our results are consistent with the recent work of Geeraerts *et al.* [149], who described the formation of chlorine dioxide during the reaction of the pentameric Cld from *Da*Cld with a high excess of chlorite. To our knowledge, this is the only reported EPR signal assigned to a $ClO_2^{\bullet}$ radical in chlorite dismutase studies. However, it is important to note that similar spectra reported in previous works were given a completely different interpretation. In particular, in the seminal study of Lee *et al.* [63] on *Da*Cld, the EPR spectrum of the enzyme in the presence of chlorite was dominated by an intense signal whose features are remarkably similar to the ones we here unambiguously assign to chlorine dioxide. Hence, in the absence of simulation data and a zoomed image of this spectral area, the authors' assignment to a tryptophyl radical is not convincing to us. More recently, the group of Püschmann *et al.* [151] proposed a brand-new mechanism for chlorite dismutases on the basis of hyperquenched EPR spectroscopy results. The authors reported an EPR spectrum recorded < 100 μs after the start of the reaction with chlorite and described the obtained signal as a triplet state resulting from two coupled amino-acid cation radicals. However, the spectrum shows a significant resemblance with that of chlorine dioxide, and the attempt of the authors to exclude this hypothesis by highlighting the absence of "satellite" signals is, in our opinion, undermined by poor signal-to-noise ratio. If Compound I is the relevant catalytic redox intermediate in Cld catalysis, the two-electron oxidation of ferric Cld to Compound I must include heterolytic cleavage of chlorite to hypochlorite (**Scheme 1.2, Reaction 2A**) that must stay in the reaction sphere and rearrange, rebind, and react with Compound I to produce O_2 and Cl^- (**Scheme 1.2, Reactions 3A and 4**). The absence of any reaction between Compound I and HOCl as demonstrated in the stopped-flow experiments [150] might, however, contradict an efficient rebound mechanism between Compound I and hypochlorite. An analogous experiment was performed with *Da*Cld and PAA followed by addition of hypochlorite. Similarly to the present study, no reaction of Compound I with hypochlorous acid was observed, and no O_2 formation could be detected [149]. However, in contrast to the natural substrate chlorite that reacts with the ferric enzyme to form the geminate pair Compound I/OCl^-, exogenous hypochlorite may not arrange correctly with the oxoiron(IV) species or might have limited access to the active center.

Reactivity of ClO_2^- and ClO^- with other heme peroxidases. As outlined in the introduction of this chapter, chlorite and hypochlorite can react with a variety of heme peroxidases, including the model horseradish peroxidase. It was previously demonstrated with stopped-flow experiments that HRP forms $ClO_2^{\bullet}$ upon mixing with chlorite [263]. Here, we show by CW-EPR spectroscopy the signature of the $ClO_2^{\bullet}$ radical in the reaction of HRP with a 3-fold molar excess of chlorite (**Figure 8.9**). The spectral features are essentially identical to the ones of the species observed in the reaction of *C*Cld with ClO_2^-, and the spectrum can be simulated with almost identical EPR parameters. This not only confirms the assignment of the detected species in the *C*Cld/ClO_2^- system, but also that chlorite can act as one-electron donor in both enzymes, even though their overall reactivity is different. Similar to *C*Cld, hypochlorite is also able to oxidize the heme iron of HRP (**Figure 8.10** and **Figure 8.11**). In this case, the time at which the reaction is quenched is critical for the observation of sequential intermediate states. RFQ and fast N_2 flash-freezing allows the trapping of a Compound I-like signal, which is enhanced at high MW powers and very low temperature (**Figure 8.11 D**). However, at longer quenching times, the only detected signal is consistent with the presence of one or more amino-acid radicals (**Figure 8.11 B**), which suggests the conversion of Compound I to Compound I*, similar to the *C*Cld/ClO^- system. Overall, these findings indicate that both *C*Cld and HRP interact in a similar way with the two oxoanion compounds, again highlighting the question of which are the determinants for the unique chlorite degradation activity of the Cld enzyme. Even more surprising are the results obtained with the dye-decolorizing peroxidase *Ec*DyP reacting with ClO_2^- and ClO^-. Despite its peroxidase activity and its high structural similarity with the Cld enzyme, when *Ec*DyP is mixed with chlorite, no evidence for the $ClO_2^{\bullet}$ radical formation was observed in the CW-EPR spectrum (**Figure 8.12**). Analogously to another member of the DyP family, *Kp*DyP [88], *Ec*DyP possesses a "resting-state radical" (**Figure 8.12**, left panel, trace a). In *Kp*DyP, this species was attributed to a combination of two tyrosyl radicals, one of which stabilized by a Tyr-Trp dyad [37]. On the other hand, the origin of the observed radical in *Ec*DyP remains to be determined. The addition of either the substrate H_2O_2, ClO^- or ClO_2^- does not cause appreciable changes in the high-field signal attributed to the above-mentioned radical, at least when CW-EPR is performed at X-band. Nevertheless, the interaction with the different compounds can be noticed by inspecting in detail the low-field region of the spectra (**Figure 8.12**, right panel), where changes are observed in the HS heme iron signal, both in terms of rhombicity and relative contribution of different HS species. It is clear that a similar active site architecture and even the presence of the same conserved amino acids (Chapter 1, 1.1.3.4) are not sufficient conditions to determine the reactivity of these enzymes, which most likely fine tune their catalytic activities with multiple, even more subtle, biochemical features.

Chapter 9

Immobilization of heme-containing biocatalysts: initial data and perspectives

Abstract

In this Chapter, the principles and scope of enzyme immobilization for industrial usage will be introduced and more details on immobilization by ion-exchange and incorporation in mesoporous materials will be provided. Furthermore, particular attention will be given to the pitfalls which can be encountered when developing immobilization protocols for a scale-up process. This extended introduction is meant to provide the reader with a suitable background to understand the rationale of two preliminary experiments of heme enzyme immobilization presented afterwards. An initial test of incorporation of the chlorite dismutase from *Cyanothece* sp. PCC7425 (*C*Cld) in silica and titania materials will be described. Additionally, the optimization of specific parameters for the adsorption of the peroxidase from horseradish (HRP) onto an ion-exchange resin, will be presented. The latter work was conducted in the context of a short industrial internship in the biotech company ADM Biopolis in Valencia, Spain.

Own contribution: experiments execution and data analysis. This chapter contains original, unpublished work.

9.1 Introduction

9.1.1 Scope of enzyme immobilization

In Chapter 1 the concept of *biocatalysis* was introduced and some examples of the industrial application of heme peroxidases were presented. In view of developing more cost-effective processes, the idea of using immobilized enzymes in industrial biotransformation emerged in the 1960s aiming at higher long-term stability, easy recovery/re-use of the biocatalyst and facile separation from the product(s). A pioneer in this field was Tanabe Seiyaku, who first commercialized the stereoselective hydrolysis of racemic acyl-amino acids to produce L-amino acids. Seiyaku developed several racemic resolution methods between 1954 and 1969, using the aminoacylase from *Aspergillus oryzae* immobilized on DEAE-Sephadex, an ion-exchange resin (*vide infra*). By applying this system in continuous-flow bioreactors, Seiyaku was able to reduce the production cost of L-amino acids of ~ 40 %, compared to the use of the native enzyme [278].

In the last decades, plenty of methods for enzyme immobilization have been described and reviewed, most of them finding successful employment from laboratory to industrial scale. Traditionally, they are classified either depending on the type of physico-chemical interaction between the enzyme and the support (van der Waals, ionic, covalent binding…), or on the relative arrangement of the two (surface binding, cross-linking, encapsulation…). For simplicity, I will use here the formalism given in [279], where the traditional enzyme immobilization approaches are divided in three main categories: i) support binding, ii) entrapment and iii) cross-linking. The difference between the first two is not always clear, however they can be distinguished by the fact that in the support-binding approach, the carrier (*i.e.* the support) is prefabricated, independently on the location of the enzyme after the binding; on the other hand, in the case of entrapment, a polymeric network (such as an organic polymer or a silica sol-gel) is synthetized *in the presence* of the enzyme, which remains trapped *inside* the carrier afterwards. In addition to the carrier-based methods introduced above, a carrier-free cross-linking approach received a great deal of attention for the possibility of achieving higher concentration and stability of the biocatalyst, through easy protocols and without the need of adding an expensive support. The most widely used cross-linking methods are the so-called cross-linked enzyme crystals (CLECs) and cross-linked enzyme aggregates (CLEAs), the latter relying on the well-known protein precipitation effects occurring under determined conditions (*e.g.* addition of salts). An in-depth description of these systems is, however, out of the scope of this Chapter and the reader is referred to [279] for further information.

The support-binding approach is actually an extended and varied collection of different methods which rely on different interactions, including van der Waals, ionic and covalent binding, as well as their combination. While the physical, weak, interactions might have a milder effect on the enzyme structure (and thus activity), they are often not sufficient to prevent the leaching of the biocatalyst from its support in an industrial environment. Covalent binding represents a solution to this problem, with the drawbacks of i) possible irreversible modifications of the enzyme structure and therefore hampering of its catalytic activity and ii) impossibility to re-use both the support and the catalyst if/when the latter gets inactivated. Nevertheless, these adverse effects can be mitigated by using a combination of different methods, as demonstrated by the many successful applications of immobilized enzymes in different industrial biotransformations [279]. Since the results presented in this Chapter refer to enzyme immobilization onto ion-exchange resins and in mesoporous materials (silica and titania), in the following sections I will discuss these approaches more into details.

9.1.2 Enzyme immobilization by ion-exchange

The immobilization onto ion-exchange resins is based on ionic/electrostatic interactions, in a similar way as the well-known ion-exchange chromatography used in many protein purification protocols. Basically, the charged groups on the surface of the enzyme interact with the opposite charges of the resin, allowing the binding (**Figure 9.1**). To understand this principle, it is important to know the concept of *isoelectric point*, the pH value at which the net charge of the protein is equal to zero. When the pH of the medium in which the enzyme is dissolved is higher than the isoelectric point, more surface amino acids will be deprotonated, thus resulting into a net negative charge. In this case, the enzyme will interact with positively charged resins. Conversely, when the pH is lower than the isoelectric point, the net charge will be positive due to the higher amount of protonated amino acids. In this case, the enzyme will have affinity for negatively charged carriers. This simple principle allows the development of easy and cost-effective protocols, which often consist in the sole mixing of the carrier and the biocatalyst, under tight pH and ionic strength control. Because of the weak nature of the ionic interaction and its susceptibility to small changes in the medium characteristics, enzyme leaching might constitute a problem. In this sense, a solution could be the use of a cross-linking agent, such as glutaraldehyde, to form stronger covalent bonds [280].

Ion-exchange resins are generally commercially available, mechanically, and chemically stable and non-toxic, characteristics that make them appealing carrier materials for enzyme immobilization applications, especially in the food industry. Indeed, among the most successful examples of this approach, are the

immobilization of glucose isomerase in DEAE-cellulose for fructose and glucose isomerization [281] and the immobilization of β-galactosidase in the Duolite® A568 resin for the production of lactose-free products [282]. In this Chapter, preliminary findings on the adsorption of horseradish peroxidase on the Duolite® A568 resin will be presented and discussed.

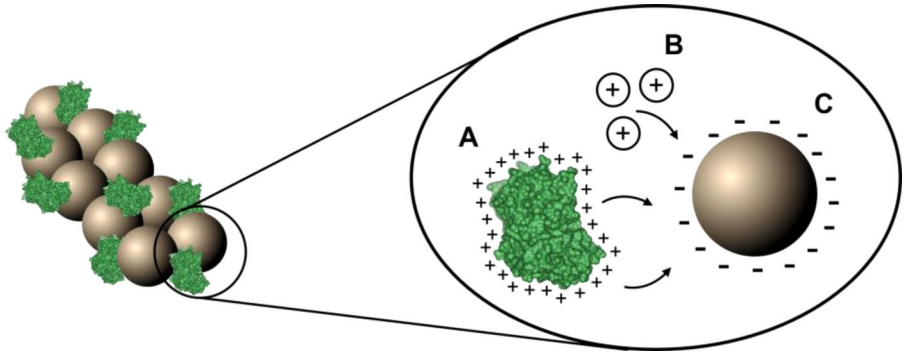

Figure 9.1 *Principle of enzyme immobilization by ion-exchange interactions. The inset shows A) a positively-charged protein; B) positive ions present in the medium competing for the sites on the resin; C) a negatively-charged resin particle. Note that the protein and the resin particle are not represented in realistic scale. Moreover, the charge distribution on the protein surface is represented as homogeneously positive, for the sake of simplicity.*

9.1.3 Enzyme immobilization by incorporation in porous materials

Among the most common inorganic carriers for enzyme immobilization are certainly (meso)porous silica and, to a minor extent, metal oxides such as titania or alumina. In addition to the several benefits of enzyme immobilization discussed above, porous materials have other advantages. First, the curvature of the pore allows a better accommodation of the globular protein structures, compared to flat surfaces. Secondly, enzyme leaching is reduced thanks to a restricted diffusion due to the pore network. Spatial separation might also play a role in preventing enzyme deactivation, distortion, autolysis, or aggregation. However, the same factors that in certain cases constitute an advantage, may be a drawback in different systems. Spatial restrictions, for instance, might reduce the efficiency of the biocatalyst by partially shielding the active site or by hampering the diffusion of the substrate. Owing to the presence of different functional groups on the surface of the enzymes (polar or non-polar amino acids, charged residues, etc.) adsorption normally occurs

through a series of non-site-specific interactions, which include electrostatic forces, hydrophobic interactions, hydrogen bonds and van der Waals forces. As in the case of immobilization by ion-exchange, adsorption in porous materials can be in principle performed by just mixing the enzyme and the support under the control of a certain number of parameters, such as pH, ionic strength, temperature, etc. (**Figure 9.2**). One of the advantages of this approach is its intrinsic reversibility, which allows the recovering of both the carrier and the biocatalyst [283].

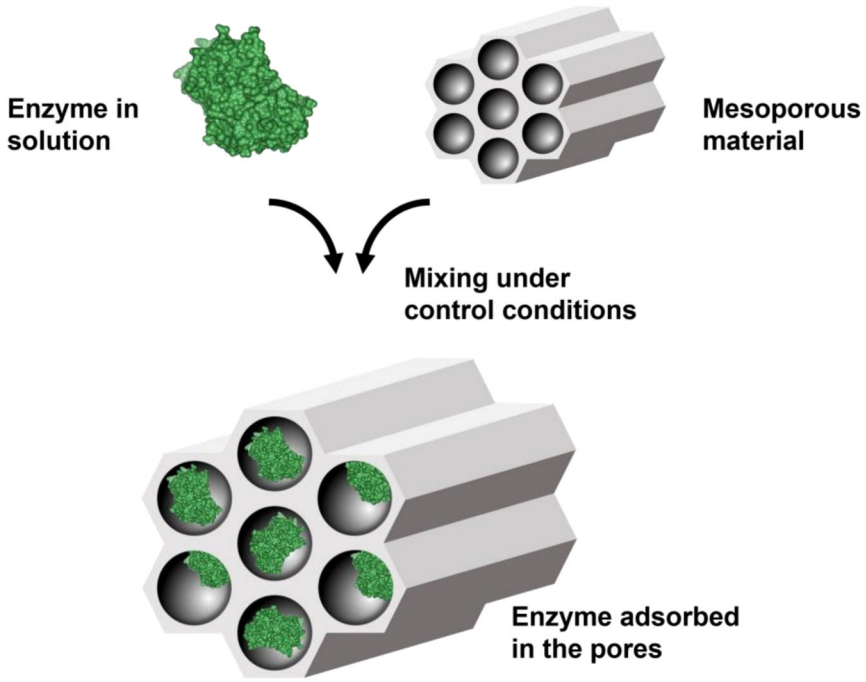

Figure 9.2 *Cartoon representation of a simple process of enzyme incorporation in a mesoporous material.*

Beside the environmental conditions in which the adsorption is performed, the properties of the material itself are crucial for a successful incorporation. First, the size and the morphology of the material particles have an influence on the protein loading. Short pore channels and small size particles favor the diffusion of the protein, which can access the surface from many pore entrances. Likewise, an irregular and rough particle surface increases the available space for protein adsorption, compared to smooth surfaces. Secondly, but not less important, are the dimension and the geometry of the pores. Balkus and Diaz in 1996 reported the first

application of mesoporous silica for protein immobilization. They showed that while cytochrome *c*, papain and trypsin could enter the 4.0 nm-wide pores of the mesoporous silica MCM-41, horseradish peroxidase was instead adsorbing on the outer surface due to its width of ~ 4.6 nm [284]. This demonstrated that, evidently, the pore size should be bigger than the dimension of the protein. However, later studies showed that the most efficient adsorption occurred when the pore size was not much larger than the protein itself [285, 286]. The geometry of the pore structure, on the other hand, has an impact on the loading efficiency, but also on leaching and pore blocking effects. While 3-dimensional channels reduce the chances of leaching, this type of structures might have too small pores for large enzymes. In these cases, different materials, such as meso- or macroporous siliceous foams (MCF) have been used [287]. Another aspect to be considered is that the same forces which drive the adsorption, also promote the interaction of different enzyme molecules with each other. At the isoelectric point (see section 9.1.2), the repulsion between the proteins is minimized and the highest packing density can be achieved. However, a dense packing can sometimes hinder the enzymatic activity due to diffusion limitations. Similarly, the pH of the isoelectric point might not correspond to the optimum for the activity of the enzyme. A compromise between a good protein loading and sufficient spacing to retain the catalytic activity of the enzyme, could be the functionalization of the pore walls with selected molecules, in order to make the surface more hydrophilic or hydrophobic, according to the need, or even to introduce sites for covalent binding [283]. It is clear that an interplay of multiple factors determines the success of an immobilization protocol and that tailoring the experimental conditions to the system of interest is necessary and not trivial. In the following section, some pitfalls in the development of immobilization protocols directed to industrial applications will be briefly discussed.

9.1.4 Critical points in the design of enzyme immobilization protocols

Enzyme immobilization is intrinsically devoted to the development of new industrial technologies. However, scientists who are perfectly trained to find and solve the uncountable pitfalls of protocol optimization in a research lab, might not be familiar with other aspects concerning the profitable, industrial usage of the biocatalysts. It is quite obvious to think that the overall enzyme immobilization process should be as cheap as possible, but an inexpensive support or a simple protocol do not always, or necessarily, translate into a cost-effective industrial process. The economical assessment should always try to answer the question: do the potential benefits justify the costs of the immobilization procedure? For

instance, a support could be cheap but not guarantee a high enzyme loading capacity, which is often a primary requisite for a good industrial biocatalyst. On the other hand, a more expensive procedure could be justified if it enhances the enzyme activity and/or stability, which in turn will result in a higher production rate and longer bioreactor operativity. Elaborated and costly protocols might also be acceptable when very specific performances or properties of the biocatalyst are desired, such as low toxicity and low immune response in the production of biomedical goods.

Beside the economical aspect, the transition from lab to industrial scale faces numerous and non-trivial challenges. A simple step like the mixing of the enzyme with the support, which can be efficiently performed in a few seconds when dealing with milliliters of solution, can take considerably longer times when thousands of liters of the enzyme solution need to be mixed with hundreds of kg of solid support. For this reason, the use of a stable support, compatible with the characteristics of the bioreactor, is crucial. Not only the functional groups of the support should remain active during the initial adsorption phase, but also the particles of the support itself should remain intact for the whole operativity of the bioreactor. Rigid, fragile supports (*e.g.* porous glasses) might not be suited for mechanically stirred reactors; the breaking of the support particles might seriously alter the activity and/or the stability of the adsorbed enzyme, among other problems. Time can also be an issue if the immobilization protocol requires multiple quick steps, for the same reasons mentioned above.

The major purpose of the use of immobilized enzymes in industrial processes is the recovery of the biocatalyst or its retention in continuous-flow reactors. Therefore, one of the most important risks to be minimized is the enzyme release from its support. In case this happens, not only the contaminating enzyme will jeopardize the quality of the product, but the re-use of the biocatalyst will not be possible either. In the most common immobilization procedures based on physical adsorption, enzyme leaching is normally very well investigated at the initial conditions. However, not always the changes in the medium conditions during the reaction are taken into consideration. Especially for enzymes immobilized in porous materials, gradients of pH or ionic strength can be formed as the reaction proceeds, depending on the nature of the products. This can in turn alter the interaction equilibria of the initial immobilization conditions and cause the release of the enzyme in the late stages of the reaction. As already briefly mentioned in section 9.1.3, a solution to this problem could be the functionalization of the support with chemical groups that guarantee a stronger interaction with the enzyme. A recognized method is to functionalize the surface with glutaraldehyde to covalently bind the enzyme to the support. However, the covalent interaction is not the only

one to drive the immobilization process. Some enzyme molecules could still bind *via* adsorption forces and be subjected to the risks of enzyme release discussed above, therefore it is essential to control the efficiency of the covalent immobilization. Moreover, when working with a multimeric protein, it is important to check whether all the subunits are attached to the surface. If only one subunit is responsible for the immobilization, the other subunits might still be able to detach and contaminate the reaction medium, not to mention that this dissociation could cause the alteration or the total loss of the enzymatic activity itself.

In addition to a reliable enzyme retention, high production rates and yield are very desirable characteristics of an industrial biocatalyst. For this reason, steric hindrance or mass transfer resistance represent serious issues for an efficient performance of the immobilized enzyme. Quite obviously, the dimensions of the substrate should be smaller than the pore size of the support where the enzyme is immobilized. In many cases the substrate is a small molecule, but there can be reactions which employ large macromolecules as well; in this case, the use of a non-porous material might represent a solution. Another problem derives from the correct orientation of the enzyme once it is immobilized. If the active site is not easily accessible by the substrate, the efficiency of the enzymatic reaction might be lower than expected. To overcome this issue, a protocol which includes the control of the enzyme orientation upon immobilization could be used. Mass transfer occurs both from the bulk liquid medium to the biocatalyst particles and, locally, as a molecular diffusion within the porous material. The first one can be facilitated by efficient mixing, while the second process is independent of the external stirring. The ratio between the mass transfer and the reaction rate is critical; when the mass transfer is slower than the enzymatic reaction, concentration gradients of the substrate and the product are formed at the enzyme sites. Inhibition effects due to high local concentrations of the substrate or the product might result in a diminished catalytic efficiency. On the other hand, the accumulation of the substrate is not always a negative event. This is the case for co-immobilized enzymes in cascade reactions, where the accumulation of the product of the first enzyme triggers and promote the activity of the following one.

In this section, I discussed some of the most important pitfalls to consider when designing a new enzyme immobilization protocol. The list is non-exhaustive and many other factors have an impact on the success of the procedure. The interested reader is referred to [288] for a comprehensive and detailed treatment of the topic, of which this section was intended as a brief summary.

9.1.5 Immobilization of heme peroxidases

The model heme peroxidase from horseradish, HRP (Chapter 1, section 1.1.3), has been used for the development of numerous biosensing applications. Several biosensor designs have been proposed, relying on different immobilization methods and carrier typologies, which include, among others, mesoporous materials [289, 290], gold nanostructured thin films [291] and functionalized electrodes [292, 293]. The need for hydrogen peroxide addition in HRP-based biosensors represents a drawback because of the background current generated by H_2O_2 [290, 294]. To overcome this issue, Rahemi *et al.* have recently proposed a new hydrogen peroxide-free biosensor for phenol detection. The biosensor is based on the immobilization of HRP in mesoporous TiO_2 and it exploits the generation of reactive oxygen species (ROS) in the titania upon daylight irradiation, to activate the enzyme [295]. Another family of heme peroxidases which raised interest for its applicability in bioremediation processes is that of dye-decolorizing peroxidases (Chapter 1, section 1.1.4). In 2008, Shakeri and Shoda described the incorporation of a dye-decolorizing peroxidase from *Aspergillus oryzae* in two types of mesoporous silica for the scavenging of the toxic dye Remazol Brilliant Blue R. In addition to a clear dependency of the immobilization efficiency on pH, they also observed that the material with more anionic surface guaranteed the best retention of the enzyme [296]. More recently, in 2022, Ren *et al.* proposed a sophisticated immobilization protocol for a dye-decolorizing peroxidase from *Bacillus amyloliquefaciens* based on halloysite nanotubes (HNT) [297]. Halloysite is naturally-formed aluminosilicate with a hollow nanotubular structure. The tube wall is composed of two layers formed by arrays of siloxane groups (Si-O-Si) on the external surface, and aluminol groups (Al-OH), on the internal surface. In general, HNTs have an inner diameter of 5-20 nm, suited to accommodate biological macromolecules [298]. To obtain a good enzyme loading and to prevent leaching, Ren and colleagues needed to functionalize HNTs with adequate linkers. First, they coated the HNTs with chitosan, then they induced the aggregation of the coated HNTs in porous microspheres and finally they modified the latter with dopamine, a biomolecule which contains an abundance of catechol and amine functional groups, useful for the interaction with biomolecules. With this immobilization method, the authors observed a moderate increase in protein stability and activity, compared to the free enzyme. On the other hand, the activity of the immobilized enzyme dropped of ~ 29 % in the first re-use batch and to a minor extent in the following recycling tests; this diminished activity could be due, according to the authors, to the leaching of enzyme molecules adsorbed *via* non-covalent interactions [297]. As already discussed in Chapter 1, chlorite dismutases are very attractive for novel industrial applications [76]; however, to date, there are no examples in literature of the use of immobilized Clds. In the next sections, preliminary results on the incorporation of the chlorite dismutase from *Cyanothece* sp. PCC7425 (*C*Cld) (Chapter 1, section

1.1.5) in mesoporous titania and silica will be presented. In addition to that, the immobilization of HRP onto an ion-exchange resin will be described, to show some of the criticalities which can be encountered in the optimization of new protocols.

9.2 Experimental procedures

9.2.1 Incorporation of *C*Cld in silica and titania

9.2.1.1 Materials

For this experiment the materials were received from collaborators and used without further modifications. In brief, wild-type *C*Cld was expressed and purified as described in [201]. Mesoporous silica (SBA-15, pore diameter = 8 nm, surface = 710 m^2/g) was prepared as described in [299], while non-porous titania (P25, surface = 50 m^2/g) and mesoporous titania (Millennium PC500) were purchased from Sigma Aldrich. PC500 titania was further calcined as described in [300], to obtain a pore diameter of 8 nm and surface of 122 m^2/g.

9.2.1.2 Incorporation procedure

First, a 0.25 mg/mL (~5 μM) protein solution was prepared in 10 mM Na_2HPO_4/NaH_2PO_4 buffer, pH 7.0. The powders were prepared as follows: either 3 mg of SBA-15, 10 mg of P25 or 10 mg of PC500 were weighted in different 20 ml-glass vials. Then, 4 mL of protein solution was added to each vial and an additional control sample was prepared with 4 mL of solution in the absence of the carrier. All samples were sonicated for 30 seconds to dissolve the powders and remove possible aggregates. Finally, the samples were left shaking at 300 rpm, at room temperature, in the dark. UV-vis absorption spectra of all samples were recorded at time zero (t_0), 1 h, 2.5 h, 4 h, 6 h, 22 h and 46 h after the starting of the incorporation process. The sampling was performed as follows: 1 mL-aliquot was taken from each sample, transferred into a clean 1 mL-Eppendorf tube, and centrifugated to spin down the powder. In the case of control and SBA-15 samples, the aliquot was centrifugated 5 minutes at 10.000 rpm; while the P25 and PC500 aliquots were centrifugated 7 minutes at 10.000 rpm to guarantee a complete precipitation of the carrier. Then, the supernatant was transferred in a quartz cuvette for the UV-Vis measurement. After the measurement, the supernatant was placed again in the Eppendorf tube containing the powder; the aliquot was mixed well to resuspend the carrier material and it was transferred back in the vial with the remaining solution. UV-vis spectra were recorded using a Varian Cary 5E UV-Vis-NIR spectrometer. The extent of *C*Cld adsorption in the different carriers estimated by following the

decrease of the Soret band intensity at 404 nm in the supernatants at different time points. An overview of the procedure is depicted in **Figure 9.3**.

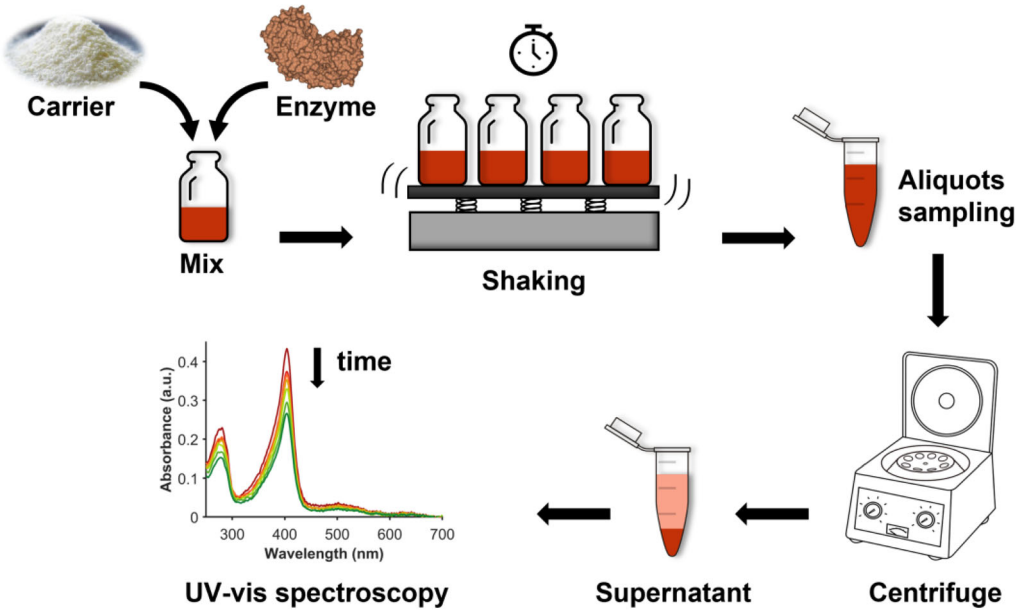

Figure 9.3 *Schematic representation of the procedure of chlorite dismutase incorporation in silica and titania carriers.*

9.2.2 Immobilization of HRP in Duolite® A568 resin.

Horseradish peroxidase (HRP) was purchased from Sigma Aldrich (Type VI-A, lyophilized) and used without further purification. Duolite® A568 resin was purchased from DuPont. First, the optimal starting protein concentration was assessed. To do so, HRP was dissolved in 10 mM Phosphate-buffered saline (PBS) buffer, pH 7.4, to obtain solutions at concentration of 0.5, 0.8, 1.0 and 2.0 μg/μL. The protein concentration was determined with a BCA (bicinchoninic acid) colorimetric assay kit from Thermo Fisher, which relies on the reduction of Cu^{2+} to Cu^{1+} by the protein in alkaline conditions and the subsequent spectrophotometric detection of the BCA-Cu^{1+} complex, whose amount is directly proportional to the concentration of protein in solution. This assay was employed to calculate both the initial concentration and the concentration of residual HRP in the supernatants after immobilization. For each immobilization condition, 50 mg of resin were weighted in a 1 mL-Eppendorf tube, then 500 μL of protein solution were added. The Eppendorf tubes were then incubated at room temperature, shaking at 600 rpm. At

selected time points (see Results section), the tubes were centrifugated for 5 min at 14.000 rpm and a small aliquot of the supernatant was taken for protein quantification with the BCA assay. Next, the optimal pH for immobilization was assessed. HRP solutions at pH values of 5.0, 6.0, 6.5, 7.0, 7.5 and 8.0 were prepared and used for another immobilization experiment, performed as described above. Once the best conditions in terms of concentration, pH, and time of contact of the protein with the carrier were determined, the immobilization was performed on a batch of Duolite® A568 previously activated with an acid-base treatment [282]. The efficiency of immobilization in the non-activated and in the activated resin was compared.

9.3 Results

9.3.1 Extent of *C*Cld incorporation in silica and titania

As described in Chapter 2, the concentration of a protein in solution can be obtained spectroscopically through the Lambert-Beer law (Eq. 2.1). In the case of heme-containing proteins, this method is particularly reliable due to the presence of specific absorption bands of the heme group, *i.e.* the Soret and the Q-bands. These allow the selective determination of the concentration of the protein of interest, rather than the total protein content, which might include contaminating species and/or heme-free apoprotein. The incorporation of a protein into porous materials (or on the surface of non-porous carriers) involves the transfer of the protein molecules from the bulk solution to the particles of the support. Therefore, in a successful incorporation process, the concentration of the protein in solution should decrease over time. We took advantage of this principle to assess the concentration of the residual *C*Cld in solution by UV-vis spectroscopy, taking supernatant aliquots at different time points from the start of the incorporation procedure. **Figure 9.4** shows the UV-Vis spectra of the *C*Cld alone (control), *C*Cld-SBA-15, *C*Cld-P25 and *C*Cld-PC500 systems taken at t_0, 1 h, 2.5 h, 4 h, 6 h, 22 h and 46 h after enzyme was placed in contact with the carrier material. The moderate decrease in the Soret band intensity in the control sample (**Figure 9.4**, top left), even after 46 h, shows that *C*Cld is reasonably stable in the selected experimental conditions (pH 7.0, room temperature), over a long period of time. The change in the relative intensities of the Soret and A_{280} absorption bands, which does not seem to have a clear trend over time, might be due to variations in the background signal, which in turn affected the correction of the baseline. In all the three *C*Cld-carrier systems, a more significant decrease in the Soret band is observed, with the SBA-15 sample showing the biggest change (**Figure 9.4**, top right). This suggests a partial

transfer of the enzyme molecules to the carrier particles. In the P25 and PC500 samples, strong absorption occurs between 250 and 300 nm (**Figure 9.4**, bottom panels), produced by the scattering of residual powder material in the supernatant, due to insufficient centrifugation during aliquot collection.

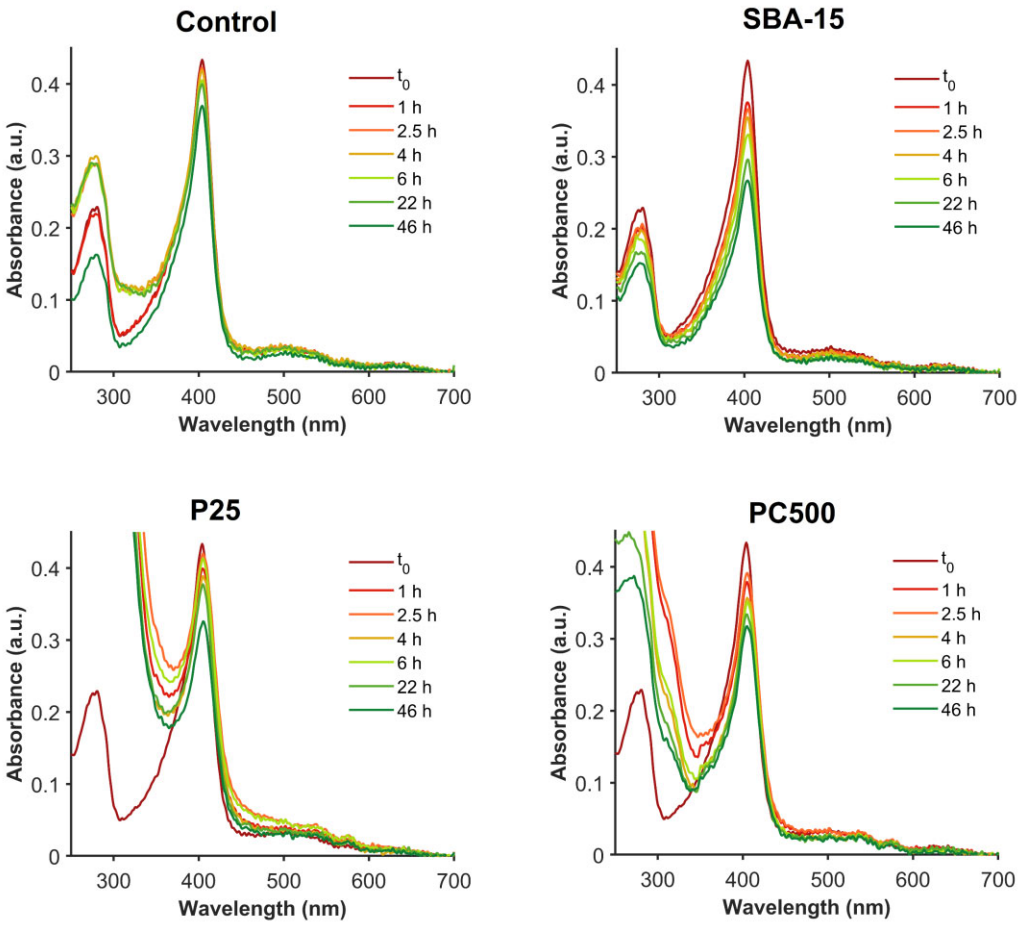

Figure 9.4 *UV-vis absorption spectra of different CCld samples in absence (control, top left) or in presence (SBA-15, P25 and PC500) of silica and titania supports for incorporation. The protein concentration was, in all cases, ~ 5 μM; the amount of the material used was 3 mg for SBA-15 and 10 mg for P25 and PC-500. Spectra were recorded at different time points, according to the figure legend. Aliquot sampling is described in the main text.*

A preliminary quantification of the incorporated *C*Cld was done by subtracting the amount of residual protein in solution from the initial concentration. The obtained values were then normalized to the amount of carrier used in each experiment. In the case of P25 and PC500 samples, the subtraction of the exponentially decaying 'tail' of the absorption band due to the scattering of residual titania was considered. However, because of the overlap with the Soret band, this data processing gave high uncertainty and the difference in the final calculated extent of protein adsorption in the material was negligible, compared to the unprocessed data. In **Figure 9.5**, the amount of incorporated *C*Cld is plotted against the experimental time. The adsorption curves (**Figure 9.5**, dashed lines) were fitted using the Elovich model [301], which describes chemical adsorption onto solid surfaces in heterogeneous systems. According to this model, the rate of adsorption decreases in time, with the increase of surface coverage. The Elovich equation is given by:

$$\frac{dq_t}{dt} = a\exp(-bq_t) \qquad \text{(Eq. 9.1)}$$

where q_t is the amount of protein adsorbed at time = t, a is the initial adsorption rate and b is the desorption constant. Assuming that $q_t = 0$ at $t = 0$, the equation can be integrated in the form:

$$q_t = \frac{1}{b}\ln(t + t_0) + \frac{1}{b}\ln(t_0) \qquad \text{(Eq. 9.2)}$$

where $t_0 = 1/ab$. If $t \gg t_0$, the equation can be rewritten as:

$$q_t = \frac{1}{b}\ln(ab) + \frac{1}{b}\ln(t) \qquad \text{(Eq. 9.3)}$$

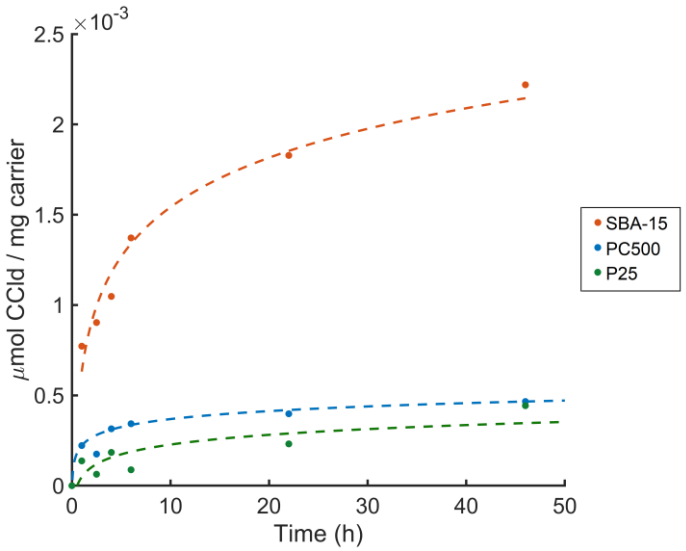

Figure 9.5 *Adsorption profile of wild-type CCld in SBA-15 (orange), PC500 (light blue) and P25 (green); dashed lines represent the fitting obtained with Eq. 9.3 (R^2 of 0.97, 0.94 and 0.64 for SBA-15, PC500 and P25, respectively). The amount of adsorbed protein (µmol) is normalized to the mg of carrier used in each experiment (3 mg SBA-15, 10 mg PC500 and P25).*

From the obtained curves, it is clear that the incorporation in SBA-15 was the most successful, highlighting the benefits of a highly ordered porous material, with extended surface area (see section 9.2.1.1). The fact that in both porous and non-porous titania, the adsorption efficiency was much lower than in SBA-15 can be adducted to their reduced surface area or a lower affinity of the protein for these materials, at least in the chosen experimental conditions.

9.3.2 Optimization of HRP immobilization on Duolite® A568

The development of an effective enzyme immobilization protocol requires the optimization of several parameters. In this work, the HRP was used as a model system for the design of an immobilization protocol based on ion-exchange, an established method for other industrial enzymes [281, 282]. These experiments were performed in the context of a short industrial internship in the biotech company ADM Biopolis in Valencia, Spain. The internship, programmed to be carried out between the end of February and beginning of March 2020, was

prematurely interrupted due to the COVID19 outbreak. For this reason, the experiments described below were not repeated more than once and it was not possible to estimate the experimental errors. Therefore, the reported outcomes need to be taken with caution.

Here, the focus was on obtaining the best immobilization conditions, rather than the characterization of the adsorption process. Therefore, the estimation of the immobilized HRP was performed on a final-point basis and normalized to the initial amount of HRP used in each experiment, to obtain a relative quantification. Three parameters were considered, namely the initial protein concentration, the pH of the medium and the pre-treatment of the resin (see section 9.2.2). The amount of adsorbed protein was determined as follows:

$$Adsorbed\ HRP\ (\%) = \frac{C_i - C_f}{C_i}\ \% \qquad \text{(Eq. 9.4)}$$

where C_i represents the initial protein concentration in solution, while C_f represents the concentration of the residual protein in the supernatant.

The first immobilization experiment was performed in PBS buffer, at pH 7.4 and it aimed at finding an optimal starting concentration of HRP. As shown in **Figure 9.6**, some variability in the extent of incorporation can appreciated within the first 30 minutes, but after 24 h the process reaches a plateau, with ~ 70 % of immobilized HRP in all the three tested conditions. The fact that the same amount of resin (50 mg) was used in the three conditions, indicates that the loading capacity of the material was not yet saturated and that other limiting factors were responsible for the observed results. Nevertheless, with an initial concentration of 0.8 μg/μL the highest amount of incorporated protein was obtained; therefore it was chosen for the following experiments.

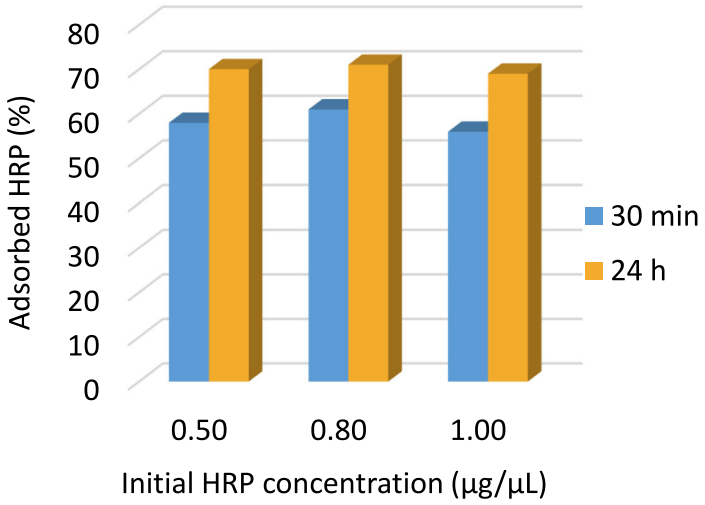

Figure 9.6 *Extent of HRP immobilization on Duolite® A568 (relative quantification), starting from different concentrations of the free enzyme in solution.*

Duolite A568® is a weak base anion-exchanger, therefore able to interact with negatively charged molecules [302]. For this reason, a better enzyme immobilization was expected to occur in a medium whose pH was higher than the isoelectric point of HRP. The latter was calculated with the Expasy ProtParam® tool on the sequence of the recombinant isozyme C (PDB code: 1H5A) and a theoretical value of 6.35 was obtained. **Figure 9.7** shows the influence of pH on the immobilization efficiency. At pH values below the isoelectric point or until ~ 0.4 pH units above, the efficiency of incorporation remained below 40 % after 24 h. On the other hand, at pH ≥ 7.5 the extent of HRP immobilization significantly increased, demonstrating the higher affinity of the negatively-charged protein towards the positively-charged resin. With an immobilization efficiency of ~ 80 % after 24 h, the pH of 7.5 was chosen for the next experiment.

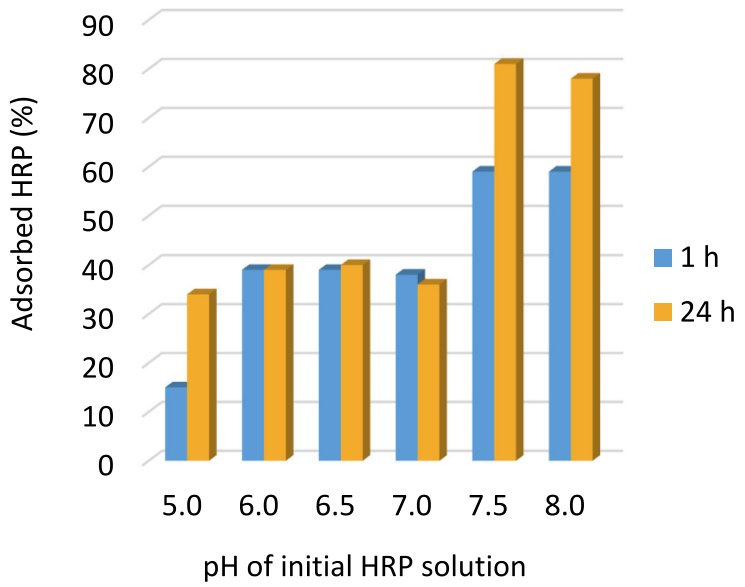

Figure 9.7 *Extent of HRP immobilization on Duolite® A568 (relative quantification) at different pH values. The initial concentration of the free enzyme in solution was of 0.8 µg/µL.*

The principle of ion-exchange is widely used in the science of protein purification. In this case, the resins are packed into columns which are routinely used to isolate different proteins, in subsequent experiments. For this reason, the *regeneration* procedure, at the end of each experiment, is an important step to guarantee the correct storage and re-usability of the resins. Depending on the chemical nature of the resin, the regeneration procedure might include several steps. In general, the procedure starts by washing the column with highly-concentrated salt solutions or strong acid (or base) to displace any fouling material attached to the functional groups of the resin. Then, a second incubation with a strong base (acid) is performed to re-balance the equilibrium between the functional groups and their counter-ions [303]. Similar to the regeneration procedure, a pre-treatment (*activation*) of Duolite® A568 was performed by first hydrating the resin with distilled water and then washing it with 1 M HCl and 1 M NaOH, following the procedure described in [282]. Next, the immobilization of HRP was carried out in parallel in non-activated and activated Duolite® A568, to evaluate the effect of the pre-treatment. The results shown in **Figure 9.8** demonstrate that the activation process was beneficial for the immobilization, with more than 90 % of adsorbed HRP after 16 h.

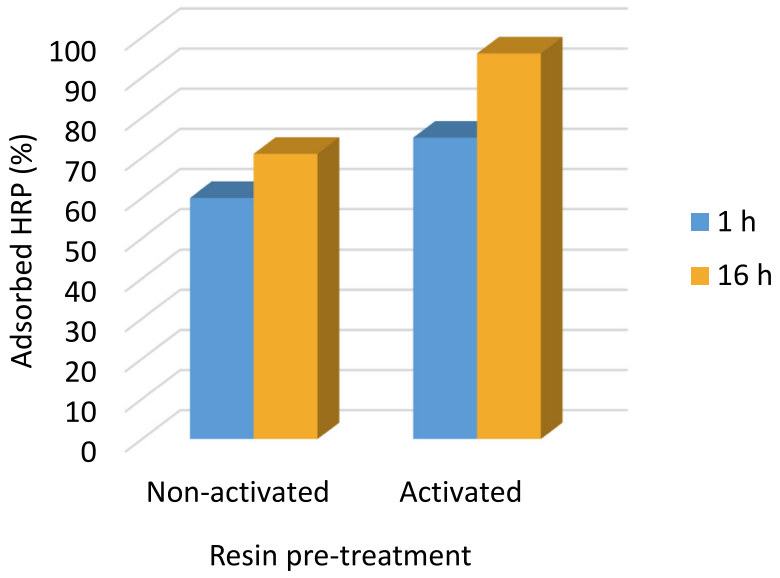

Figure 9.8 *Extent of HRP immobilization on Duolite® A568 (relative quantification) with and without activation pre-treatment. In this experiment the initial concentration of HRP in solution was of 0.8 µg/µL and the pH of the medium was 7.5.*

9.4 Discussion and conclusions

The incorporation of *C*Cld in (meso)porous materials might open new ways of exploiting this interesting biocatalyst for industrial applications. However, as extensively discussed in section 9.1, the development and optimization of a new enzyme immobilization protocol is not trivial. The results described in this Chapter are preliminary and presented as a proof-of-concept. In the conducted experiment, *C*Cld showed a better affinity for mesoporous silica SBA-15, rather than non-porous or porous titania, however it should be noted that the incorporation conditions were likely to be sub-optimal. In fact, the overall efficiency was very low ($\sim 2 \times 10^{-3}$ µmol *C*Cld / mg silica), indicating that many parameters still need to be optimized. To minimize denaturation effects over time, this initial incorporation experiment was carried out in *C*Cld storage buffer, at pH 7.0. This is above the theoretical isoelectric point of *C*Cld, *i.e.*, 5.88, as calculated with the Expasy ProtParam® tool; therefore, using a medium at this pH value should be considered in the future, to decrease the electrostatic repulsion between the protein molecules and increase the

interaction with the carrier. The use of different supports and/or their functionalization could also be considered. After obtaining a good protein loading on the carrier, structural and functional properties of the immobilized *C*Cld should be checked as the next step. The intrinsic paramagnetic nature of *C*Cld heme center allows investigations through EPR spectroscopy, which can give a first hint on the local structure of the active site. Nonetheless, additional studies on thermal stability, catalytic efficiency and re-usability of the enzyme should be performed as well.

The immobilization of HRP onto the ion-exchange resin Duolite® A568 described in this Chapter is an example of a possible approach to the optimization of different parameters. In this case, subsequent experiments were performed. The condition which gave the best result in first experiment was maintained in the next one, where another parameter was varied instead, and so on. This serial approach might be feasible in a small-scale experiment, where not many parameters need to be adjusted; however to optimize protocols which depend on a multitude of factors, an approach called Central Composite Design (CCD) is often used [304–306]. In CCD, several parallel experiments are performed, having just one parameter varied in each experiment, while all the other conditions are kept equal. Next, a statistical analysis is run to build a response surface and find the optimal values of the selected independent variables. Through this method it is possible to analyze the simultaneous influence of different parameters on a particular process. The presented experiments, however, were conducted within a didactic perspective in order to understand the major factors influencing immobilization by ion-exchange and a CCD analysis was not believed necessary at this stage. Given the promising results obtained with the right choice of pH and treatment of the carrier, the CCD approach could be taken in consideration to expand the set of experimental conditions to be tested and to investigate which of these factors might have an influence on the enzyme activity after immobilization.

In conclusion, the preliminary trials of enzyme immobilization presented in this Chapter demonstrate the importance of carefully choosing and testing different experimental conditions when developing a new immobilization protocol. The obtained results, although preliminary, suggest that the immobilization of the heme enzymes *C*Cld and HRP in (porous) inorganic materials and ion-exchange resin, respectively, is feasible and that it can be significantly improved by optimizing the experimental design. Further studies will be needed to obtain more efficient and reproducible immobilization protocols, which will hopefully unlock novel and exciting applications of these biocatalysts.

Chapter 10

Conclusions

10.1 Conclusions

Chlorite dismutases represent a group of recently discovered bacterial enzymes, generally recognized as a sub-family of heme peroxidases, and closely related to the family of the dye-decolorizing peroxidases. Surprisingly, none of the chlorite dismutases characterized so far, ever demonstrated a classic peroxidase activity. Their catalytic reaction, *i.e.* the decomposition of chlorite into chloride and molecular oxygen, has triggered the interest of numerous researchers for its biotechnological relevance and the involvement of an O-O bond formation, a rather unique reaction in the biological world. More than 25 years after the first description of a chlorite dismutase enzyme, the molecular determinants of their peculiar catalytic mechanism remain to be fully elucidated. This is most certainly due to the extremely fast turnover of these biocatalysts, which prevents a proper analysis of the intermediate states even with well-established techniques such as stopped-flow UV vis spectroscopy, generally sufficient to resolve transient species in the millisecond time range. A strong pH dependence of their enzymatic activity and a tendency to self-inactivate over time, make the understanding of chlorite dismutases even less obvious.

In this work, we investigated a representative of the clade II subdivision of chlorite dismutases, which until now counts lesser characterized members. EPR spectroscopy proved to be a powerful tool for the study of the paramagnetic ferric heme iron in the active site of chlorite dismutase, especially when flanked by other biochemical and biophysical techniques. With a site-directed mutagenesis approach, it was possible to gain insight into the role(s) of a conserved arginine which sits at the distal side of the heme iron, in an otherwise completely hydrophobic pocket. In previous studies, it was already proposed that this residue is catalytically important and flexible, being able to adopt different orientations with respect to the heme iron. We manipulated the arginine flexibility by exchanging its H-bonding partner glutamine, to either valine or glutamate. With a well-round combination of several spectroscopic methods, x-ray crystallography, activity, and calorimetry assays, we were able to determine the influence of the arginine flexibility on different enzyme properties, including catalytic efficiency and thermal stability. In this study, EPR spectroscopy provided evidence for the strong pH dependence of the active site spin state and how this was impacted by the H-bonds rearrangement in the heme proximity due to the inserted mutations.

We then focused our interest on the mechanism of substrate binding and the role of the conserved arginine on this step of the reaction cycle. To overcome the challenges of trapping the short-lived intermediates, our initial approach was that of using a substrate analogue, nitrite, to form a stable complex with chlorite dismutase. In this

part of the work, EPR spectroscopy played a fundamental role in the characterization of the low-spin complexes formed upon mixing nitrite with chlorite dismutases. While the flexibility of the arginine did not seem to strongly impact the EPR profile of the nitrite adducts, the substitution of this amino acid either with an alanine or a lysine, resulted in significant spectroscopic changes which correlate a with a dramatic decrease of the catalytic activity. Most interestingly, EPR suggested the occurrence of different binding modes of nitrite, denoted *O*-nitrito and *N*-nitro. These results, supported by crystal field theory and MD simulations, were then explored more into detail by means of HYSCORE experiments. To ease the interpretation of the complex nitrite-chlorite dismutase system, complementary HYSCORE experiments were performed on the nitrite-bound form of myoglobin, where the binding of nitrite is known to solely occur through the *O*-nitrito mode. The analysis of the nitrite-chlorite dismutase system confirmed the presence of at least one *O*-nitrito bound form and additional spectroscopic features have been tentatively assigned to a contribution from a *N*-nitro bound form. Even if the physiological relevance of nitrite binding to chlorite dismutase can be debated, these findings constitute a comprehensive spectroscopic investigation of the binding of nitrite to different heme proteins. This will hopefully provide the scientific community with a useful reference for the study of other nitrite-bound heme systems.

Rapid Freeze-Quench combined with EPR spectroscopy was chosen as a second approach to explore the reactivity of chlorite dismutases. RFQ-EPR aimed at characterizing the (paramagnetic) intermediate states observed by stopped-flow optical spectroscopy upon the reaction with either the chlorite or hypochlorite, whose features could not be unambiguously interpreted. The reaction with hypochlorite was expected to result in the formation of the so-called Compound I (Fe(IV) π-cation radical) according to stopped-flow experiments. However, RFQ-EPR revealed features of an amino acid radical, most likely due to migration of the radical from the heme porphyrin to a nearby residue. The reaction with the substrate chlorite did not provide additional information on the catalytically active intermediates, as the RFQ-EPR data only showed the presence of a chlorine dioxide radical, an off-pathway product whose strong features possibly covered underlying weak signals. These discrepancies between the stopped-flow and the RFQ-EPR findings draw the attention on the limitations of the latter technique. One issue is undoubtedly related to the concentrations needed to generate a detectable signal in EPR, which is at least two orders of magnitude higher than the concentrations used in stopped-flow UV-vis experiments. In our work, the use of highly concentrated reagents definitely pushed the time frame of the intermediates formation out of the range accessible by the instrumentation available in our lab. Compared to other systems described in literature, the commercial RFQ setup used in this work

suffered from a considerably long dead time (~ 50 ms), whose precise estimation required a long and resource-consuming calibration procedure.

In any case, in the light of the findings described in this work, it is possible now to remodel the catalytic pathways of *C*Cld, already introduced in Chapter 1 (**Scheme 1.2**). In the reaction with chlorite at pH optimum (~5.5), stopped-flow spectrophotometry experiments revealed the formation of Compound I, which remains dominant for all the duration of chlorite degradation. Conversely, at higher pH values, the dominant species is a ferryl species (Compound I*/Compound II). Further stopped-flow and RFQ-EPR experiments confirmed that the ferryl species corresponds to an amino-acid based radical species (Compound I*), which is the decay product of Compound I in absence of electron donors. This decay proved to be highly pH-dependent, being significantly faster at higher pH values. Altogether, these results suggest that Compound I is the catalytically relevant species at pH optimum and that the productive pathway of *C*Cld follows the heterolytic cleavage of chlorite with a subsequent rebound mechanism of ClO^- (**Scheme 10.1, Reactions 1, 2 and 3**). On the other hand, the pH-dependent decay of Compound I, which can be formed also by reacting *C*Cld with hypochlorite (**Scheme 10.1, Reaction 4**), results in the formation of Compound I*, where the radical most probably migrates to a tyrosine residue (**Scheme 10.1, Reaction 5**). RFQ-EPR provided additional evidence of the ability of Compound I to oxidize chlorite in a 1-electron process to produce chlorine dioxide, a side reaction which seems to be enhanced at higher concentrations of both the reagents (**Scheme 10.1, Reaction 6**). Finally, several sequential-mixing stopped-flow spectrophotometry measurements, as well as further CW-EPR experiments, demonstrated that serotonin can "rescue" the enzyme from its unproductive pathways, being able to act as 1-electron donor for both Compound I and Compound I* and to convert them back to the resting state (**Scheme 10.1, Reactions 7, 8 and 9**).

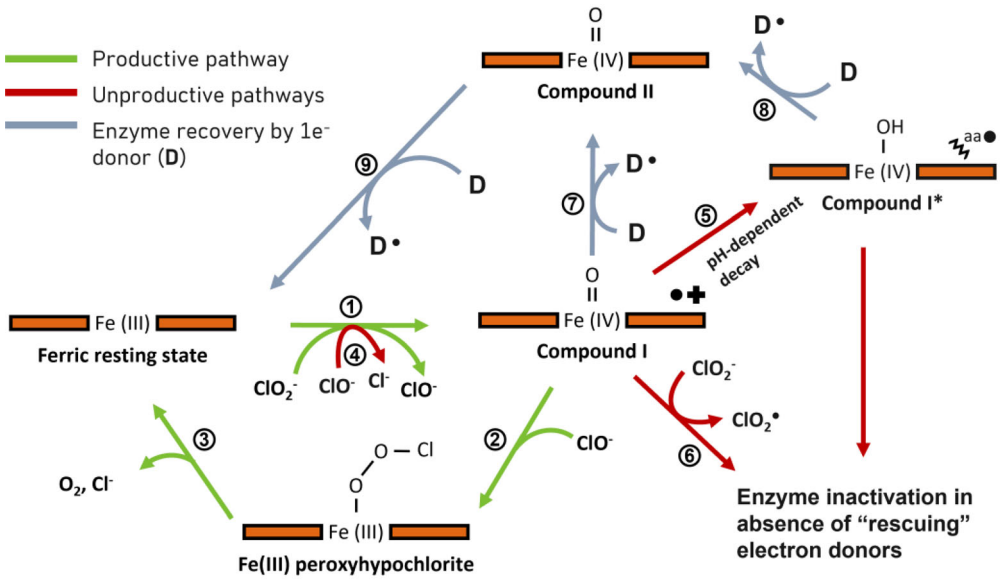

Scheme 10.1 Revisited scheme for *C*Cld reaction mechanism(s)

To resolve the nature of the short-lived intermediates, and thus confirm the proposed mechanisms, future research work might proceed in two parallel directions. On the one hand, the RFQ setup could be upgraded with home-built parts aiming at reducing its dead time. It can be thought of solutions to increase the speed jet of the reaction mixture sprayed on the surface of cryogenic bath, or to reduce the particles size and thus increase the freezing rate. A completely different freezing system could be also designed, taking inspiration from the solutions adopted by other research groups for their own home-made RFQ setups. On the other hand, it is possible to take advantage of the chlorite dismutase variants which show much slower reaction rates. In this case, there will be a chance of trapping the intermediate states over a longer time range. Anyway, questions remain open regarding the high selectivity of chlorite dismutases towards chlorite, despite their remarkable structural similarities with other heme peroxidases. Likewise, it remains to be determined the physiological role of chlorite dismutases in the organisms which do not possess a metabolism based on chlorate and perchlorate.

From the point of view of a possible biotechnological application of chlorite dismutases, some considerations have to be made. First, until a large-scale production of these enzymes is optimized, their applicability as industrial biocatalysts remains impracticable. Then, their sensitivity to pH and long-term

irreversible inactivation are issues to be considered. In this sense, providing the enzyme molecules with a "safer" microenvironment, such as the interieur of a porous material, might be of help. Enzyme immobilization was the focus of the last part of this project, which included preliminary experiments with the model system horseradish peroxidase and with the chlorite dismutase. Several experimental parameters such as pH, protein concentration and material pre-treatment were tuned to optimize the immobilization of horseradish peroxidase onto an ion-exchange resin. Differently, the incorporation of chlorite dismutase in different mesoporous and non-porous silica and titania was carried out in sub-optimal conditions and only presented as a proof-of-concept. Even if both experiments suggested the feasibility of immobilizing these two biocatalysts in different materials, extensive research will be needed in the future to develop a reliable and reproducible immobilization protocol. The structural and biochemical characterization of the immobilized enzymes, as well the evaluation of their catalytic activities will be a necessary continuation of the presented work in the view of developing novel industrial usages of these fascinating biomolecules.

10.2 Conclusies

Chlorietdismutasen vertegenwoordigen een groep recentelijk ontdekte bacteriële enzymen, die algemeen worden erkend als een sub-familie van heemperoxidases, en nauw verwant zijn aan de familie van de kleurstofontkleurende peroxidasen. Verrassend genoeg heeft geen van de tot nu toe gekarakteriseerde chlorietdismutasen ooit een peroxidase-activiteit aangetoond. Hun katalytische reactie, d.w.z. de afbraak van chloriet in chloride en moleculaire zuurstof, heeft de belangstelling gewekt van talrijke onderzoekers vanwege de biotechnologische relevantie ervan en de vorming van een O-O-binding, een vrij unieke reactie in de biologische wereld. Meer dan 25 jaar na de eerste beschrijving van een chlorietdismutase-enzym zijn de moleculaire stappen in hun unieke katalytische mechanisme nog steeds niet volledig opgehelderd. Dit is zeer zeker te wijten aan het extreem snelle verloop van de enzymatische reacties van deze biokatalysatoren, waardoor een goede analyse van de tussentoestanden onmogelijk is, zelfs met beproefde technieken zoals stop-flow UV-vispectroscopie, die over het algemeen voldoende zijn om transiënte moleculen in het milliseconden-tijdsbereik te resolveren. Een sterke pH-afhankelijkheid van hun enzymactiviteit en een neiging tot zelfinactivatie na verloop van tijd maken het nog minder vanzelfsprekend om inzicht te krijgen in de werking van chlorietdismutasen.

In dit werk onderzochten we een vertegenwoordiger van de clade-II onderverdeling van chlorietdismutasen, die tot nu toe minder gekarakteriseerd is. EPR-spectroscopie bleek een krachtig instrument voor de studie van het paramagnetische ferrisch heemijzer in de actieve site van chlorietdismutase, vooral wanneer dit wordt gecombineerd met andere biochemische en biofysische technieken. Met een gerichte mutagenese-aanpak kon inzicht worden verkregen in de rol(len) van het geconserveerd arginine dat zich aan de distale zijde van het heemijzer bevindt in een verder volledig hydrofobe omgeving. In eerdere studies werd al voorgesteld dat dit residu katalytisch belangrijk en flexibel is, omdat het verschillende oriëntaties ten opzichte van het heemijzer kan aannemen. Wij hebben de flexibiliteit van het arginine gemanipuleerd door zijn H-bindingspartner glutamine te vervangen door valine of glutamaat. Met een uitgebreide combinatie van verschillende spectroscopische methoden, X-stralenkristallografie, activiteits- en calorimetrietesten konden wij de invloed van de argininеflexibiliteit op verschillende enzymeigenschappen bepalen, waaronder katalytische efficiëntie en thermische stabiliteit. In dit onderzoek leverde EPR-spectroscopie het bewijs voor de sterke pH-afhankelijkheid van de spin-toestand van de actieve plaats en hoe deze werd beïnvloed door de herschikking van de H-bindingen in de nabijheid van het heem als gevolg van de ingevoegde mutaties.

Vervolgens werd het mechanisme van substraatbinding en de rol van het geconserveerde arginine in deze stap van de reactiecyclus verder onderzocht. Om de uitdagingen van het vangen van de kortlevende tussenproducten te omzeilen was onze eerste benadering die van het gebruik van een substraatanaloog, nitriet, om een stabiel complex te vormen met chlorietdismutase. In dit deel van het werk speelde EPR-spectroscopie een fundamentele rol bij de karakterisering van de lage-spin complexen die werden gevormd bij het mengen van nitriet met chlorietdismutasen. Terwijl de flexibiliteit van het arginine het EPR-profiel van de nitrietadducten niet sterk leek te beïnvloeden, resulteerde de vervanging van dit aminozuur door een alanine of een lysine in significante spectroscopische veranderingen die correleren met een dramatische afname van de katalytische activiteit. Zeer interessant is dat EPR het bestaan van verschillende bindingswijzen van nitriet suggereerde, aangeduid als O-nitrito en N-nitro. Deze resultaten, ondersteund door kristalveldtheorie en MD-simulaties, werden vervolgens nader onderzocht door middel van HYSCORE-experimenten. Om de interpretatie van het complexe nitriet-chlorietdismutase systeem te vergemakkelijken, werden aanvullende HYSCORE experimenten uitgevoerd op de nitrietgebonden vorm van myoglobine, waarvan bekend is dat de binding van nitriet uitsluitend plaatsvindt via de O-nitrito modus. De analyse van het nitriet-chlorietdismutase systeem bevestigde de aanwezigheid van ten minste één O-nitriet gebonden vorm en aanvullende spectroscopische signalen werden voorlopig toegewezen aan een

bijdrage van een N-nitro gebonden vorm. Hoewel de fysiologische relevantie van nitrietbinding aan chlorietdismutase kan worden betwist, vormen deze bevindingen spectroscopische data van de binding van nitriet aan verschillende heemeiwittende wetenschappelij, die de wetenschappelijke gemeenschap een nuttige referentie bieden voor de studie van andere nitrietgebonden heemsystemen.

Om de reactiviteit van chlorietdismutasen verder te onderzoeken, werd vervolgens gekozen voor een *Rapid Freeze-Quench* methode in combinatie met EPR-spectroscopie. RFQ-EPR had tot doel de (paramagnetische) tussentoestanden te karakteriseren die bij de reactie met chloriet of hypochloriet reeds werden waargenomen m.b.v. optische spectroscopie (*stop-flow*) en waarvan de signalen niet eenduidig konden worden geïnterpreteerd. De reactie met hypochloriet zou volgens de *stop-flow* experimenten resulteren in de vorming van de zogenaamde *Compound I* (Fe(IV) π-kation-radicaal). De RFQ-EPR spectra toonden echter de kenmerken van een aminozuurradicaal, waarschijnlijk door migratie van het radicaal van het heemporfyrine naar een nabijgelegen residu. De reactie met het substraat chloriet leverde geen aanvullende informatie op over de katalytisch actieve tussenproducten, aangezien de RFQ-EPR-spectra alleen de aanwezigheid aantoonden van een chloordioxideradicaal, een off-pathway product waarvan de sterke signalen mogelijk onderliggende zwakke EPR signalen dekten. Deze discrepanties tussen de stopped-flow en de RFQ-EPR bevindingen vestigen de aandacht op de beperkingen van laatstgenoemde techniek. Eén probleem houdt ongetwijfeld verband met de concentraties die nodig zijn om een detecteerbaar signaal te genereren bij EPR, die ten minste twee orden van grootte hoger zijn dan de concentraties die worden gebruikt bij de UV-vis-experimenten met *stop-flow* modus. In ons werk werden door het gebruik van sterk geconcentreerde reagentia de tussenproducten te snel gevormd om nog binnen het bereik van de in ons laboratorium beschikbare instrumenten te liggen. In vergelijking met andere in de literatuur beschreven systemen had de in dit werk gebruikte commerciële RFQ-opstelling een aanzienlijk lange dode tijd (~ 50 ms), waarvan de precieze schatting een extensieve en middelenverslindende kalibratieprocedure vereiste.

In elk geval is het nu, in het licht van de bevindingen beschreven in dit werk, mogelijk om de enzymatische reactiepaden van *C*Cld die reeds in Hoofdstuk 1 geïntroduceerd werden (**Schema 1.2**), opnieuw te modelleren. Stop-flow spectrofotometrie-experimenten toonden dat Compound I gevormd wordt bij de reactie van *C*Cld met chloriet bij optimale pH (~5,5). Deze vorm blijft dominant gedurende het volledige degradatieproces van chloriet. In tegenstelling daarmee is bij hogere pH-waarden de dominante vorm een ferrylvorm (Compound I*/ Compound II). Verdere stop-flow en RFQ-EPR-experimenten bevestigden dat deze

ferrylvorm overeenkomt met een vorm waarbij het radicaal zich op een aminozuur bevindt (Compound I*), wat het vervalproduct is van Compound I in afwezigheid van elektrondonoren. Dit verval bleek sterk pH-afhankelijk te zijn en was significant sneller bij hogere pH-waarden. De verschillende resultaten suggereren dat Compound I de katalytisch relevante vorm is bij de optimale pH en dat de productieve route van *C*Cld via de heterolytische splitsing van chloriet verloopt met een daaropvolgend mechanisme waarbij ClO^- terug gebonden wordt (**Schema 10.1**, **Reacties 1, 2 en 3**). Anderzijds resulteert het pH-afhankelijke verval van Compound I, dat ook kan worden gevormd door *C*Cld te laten reageren met hypochloriet (**Schema 10.1, Reactie 4**), in de vorming van Compound I*, waarbij het radicaal hoogstwaarschijnlijk migreert naar een tyrosineresidu (**Schema 10.1, Reactie 5**). RFQ-EPR leverde aanvullend bewijs voor het vermogen van Compound I om chloriet te oxideren in een 1-elektronproces om chloordioxide te produceren, een nevenreactie die lijkt te worden versterkt bij hogere concentraties van beide reagentia (**Schema 10.1, Reactie 6**). Ten slotte toonden verschillende stop-flow spectrofotometriemetingen met sequentieel mengen, evenals verdere CW-EPR experimenten, aan dat serotonine het enzym kan "redden" van zijn onproductieve paden, doordat het kan fungeren als 1-elektron-donor voor zowel Compound I als Compound I* en deze kan omzetten naar de rusttoestand (**Schema 10.1, Reacties 7, 8 en 9**).

Om de aard van de kortlevende tussenproducten te bepalen zou het toekomstige onderzoek in twee parallelle richtingen kunnen verlopen. Enerzijds zou de RFQ-opstelling kunnen worden verbeterd met zelfgebouwde onderdelen om de dode tijd te verminderen. Gedacht kan worden aan oplossingen om de snelheid van de straal van het reactiemengsel die op het oppervlak van het cryogene bad wordt gesproeid te verhogen, of om de deeltjes te verkleinen en zo de vriessnelheid te verhogen. Er zou ook een geheel ander vriessysteem kunnen worden ontworpen, waarbij inspiratie wordt geput uit de oplossingen die andere onderzoeksgroepen hebben gekozen voor hun eigen zelfgemaakte RFQ-opstellingen. Anderzijds is het mogelijk gebruik te maken van de varianten van chlorietdismutase die een veel tragere reactiesnelheid vertonen. In dat geval is er een kans dat de tussenliggende toestanden over een langere tijdspanne kunnen worden gevangen. Hoe dan ook blijven vragen open over de hoge selectiviteit van chlorietdismutasen t.a.v. chloriet, ondanks hun opmerkelijke structurele overeenkomsten met andere heemperoxidasen. Evenzo moet de fysiologische rol van chlorietdismutasen nog worden vastgesteld in organismen waarvan het metabolisme niet op chloraat of perchloraat gebaseerd is.

Wat betreft de mogelijke biotechnologische toepassing van chlorietdismutasen moeten enkele overwegingen worden gemaakt. Ten eerste blijft hun

toepasbaarheid als industriële biokatalysatoren onuitvoerbaar zolang de produktie van deze enzymen op grote schaal niet is geoptimaliseerd. Vervolgens moet rekening worden gehouden met hun gevoeligheid voor pH en onomkeerbare inactivatie op lange termijn. In die zin kan het nuttig zijn de enzymmoleculen een "veiligere" micro-omgeving te bieden, zoals in een poreus materiaal. Enzymimmobilisatie was de focus van het laatste deel van dit project, dat voorbereidende experimenten omvat met het modelsysteem mierikswortelperoxidase en met chlorietdismutase. Verschillende experimentele parameters zoals pH, eiwitconcentratie en materiaalvoorbehandeling werden afgestemd om de immobilisatie van mierikswortelperoxidase op een ionenuitwisselingshars te optimaliseren. De incorporatie van chlorietdismutase in verschillende mesoporeuze en niet-poreuze silica en titania werd uitgevoerd onder suboptimale omstandigheden en alleen getoond als *proof of concept*. Hoewel beide experimenten wezen op de haalbaarheid van immobilisatie van deze twee biokatalysatoren in verschillende materialen, zal in de toekomst uitgebreid onderzoek nodig zijn om een betrouwbaar en reproduceerbaar immobilisatieprotocol te ontwikkelen. De structurele en biochemische karakterisering van de geïmmobiliseerde enzymen, alsook de evaluatie van hun katalytische activiteiten zullen een noodzakelijke voortzetting zijn van het getoonde werk met het oog op de ontwikkeling van nieuwe industriële toepassingen van deze fascinerende biomoleculen.

10.3 Conclusiones

Las clorito-dismutasas representan un grupo de enzimas bacterianas de reciente descubrimiento, generalmente reconocidas como una subfamilia de las hemo peroxidasas y estrechamente relacionadas con la familia de las peroxidasas *dye-decolorizing peroxidases*. Sorprendentemente, ninguna de las clorito-dismutasas caracterizadas hasta ahora ha demostrado una actividad peroxidasa. Su reacción catalítica, es decir, la descomposición del clorito en cloruro y oxígeno molecular ha despertado el interés de numerosos investigadores por su relevancia biotecnológica y la implicación de la formación de un enlace O-O, una reacción bastante inusual en el mundo biológico. Más de 25 años después de la primera descripción de una enzima clorito-dismutasa, aún no se han establecido por completo los determinantes moleculares de su peculiar mecanismo catalítico. Ello se debe, con toda seguridad, al rapidísimo mecanismo de estos biocatalizadores, que impide un análisis adecuado de los estados intermedios incluso con técnicas bien establecidas como la espectroscopia de UV-vis de flujo detenido (*stopped-flow)*, generalmente suficientemente rápido para resolver especies transitorias en el rango temporal de

los milisegundos. Una fuerte dependencia del pH de su actividad enzimática y una tendencia a auto inactivarse con el tiempo, hacen que la comprensión de las clorito-dismutasas sea aún mas difícil.

En este trabajo hemos investigado un ejemplo representativo de la subdivisión *clade II* de las clorito-dismutasas, que hasta ahora cuenta con miembros menos caracterizados. La espectroscopia EPR ha demostrado ser una poderosa herramienta para el estudio del hierro férrico hemínico en el sitio activo de la clorito-dismutasa, especialmente cuando está apoyada por otras técnicas bioquímicas y biofísicas. Añadiendo, además, un enfoque de mutagénesis sitio-dirigida, fue posible comprender mejor la función de la arginina conservada que se encuentra en el lado distal del hemo, en un entorno que, por lo demás, es completamente hidrófobo. En estudios anteriores, ya se propuso que este residuo es catalíticamente importante y flexible, pudiendo adoptar diferentes conformaciones con respecto al hierro del grupo hemo. Manipulado la flexibilidad de la arginina mediante el cambio del residuo con el que está unido por un puente de hidrógeno, la glutamina, por valina o glutamato y usando una combinación de varios métodos espectroscópicos, cristalografía de rayos X, ensayos de actividad y calorimetría, pudimos determinar la influencia de la flexibilidad de la arginina en diferentes propiedades de la enzima, como la eficiencia catalítica y la estabilidad térmica. En este estudio, la espectroscopia EPR aportó pruebas de la fuerte dependencia del pH del estado de espín del sitio activo y de cómo éste se veía afectado por el reordenamiento de los puentes de hidrógeno en la proximidad del hemo debido a las mutaciones insertadas.

A continuación, centramos nuestro interés en el mecanismo de unión del sustrato y el papel de la arginina conservada en este paso del ciclo de reacción. Para superar las dificultades de atrapar los intermediarios reactivos, nuestro enfoque inicial consistió en utilizar un análogo del sustrato, el nitrito, para formar un complejo estable con la clorito-dismutasa. En esta parte del trabajo, la espectroscopia EPR desempeñó una función fundamental en la caracterización de los complejos de bajo espín formados al mezclar nitrito con clorito dismutasas. Mientras que la flexibilidad de la arginina no parecía tener un gran impacto en el espectro de EPR de los aductos de nitrito, la sustitución de este aminoácido por una alanina o una lisina provocaba cambios espectroscópicos significativos que se correlacionaron con una disminución drástica de la actividad catalítica. Y lo que es más interesante, la EPR sugirió la existencia de diferentes modos de unión del nitrito, denominados *O*-nitrito y *N*-nitro, en los que el análogo se une al hierro por del oxígeno o por el nitrógeno respectivamente. Estos resultados, apoyados por la teoría del campo cristalino y simulaciones MD, se exploraron más detalladamente mediante experimentos HYSCORE. Para facilitar la interpretación del complejo sistema

nitrito-clorito dismutasa, se realizaron experimentos HYSCORE complementarios con la proteína modelo mioglobina unida a nitrito, en la que se sabe que la unión del nitrito se produce únicamente a través del modo *O*-nitrito. El análisis del sistema nitrito-clorito dismutasa confirmó la presencia de al menos una forma unida *O*-nitrito y se han asignado provisionalmente huellas espectroscópicas adicionales a una contribución de una forma del tipo *N*-nitro. Aunque la relevancia fisiológica de la unión del nitrito a la clorito-dismutasa es discutible, estos resultados constituyen una investigación espectroscópica exhaustiva de la unión del nitrito a diferentes proteínas hemo. Es de esperar que esto proporcione a la comunidad científica una referencia útil para el estudio de otros sistemas hemo unidos a nitrito.

Se eligió la técnica de congelación rápida (*rapid freeze-quench)* combinada con espectroscopia de EPR como segundo enfoque para explorar la reactividad de las clorito-dismutasas. El objetivo de la RFQ-EPR era caracterizar los estados intermedios paramagnéticos observados mediante espectroscopia óptica de flujo detenido tras la reacción con el clorito o con el hipoclorito, y cuyas características no podían interpretarse de forma inequívoca. Se esperaba que la reacción con hipoclorito diera lugar a la formación del denominado *Compound I* (radical π-catiónico mas hemo-Fe(IV)) según los experimentos de flujo detenido. Sin embargo, la RFQ-EPR reveló rasgos de radical en un aminoácido, muy probablemente debido a la migración del radical desde la porfirina hemo a un residuo cercano. La reacción con el sustrato clorito no proporcionó información adicional sobre los productos intermedios catalíticamente activos, ya que los datos RFQ-EPR sólo mostraron la presencia de un radical de dióxido de cloro, un producto fuera de la ruta catalítica cuyas señales fuertes posiblemente cubren otras más débiles subyacentes. Estas discrepancias entre los resultados de flujo detenido y RFQ-EPR llaman la atención sobre las limitaciones de esta última técnica. Uno de los problemas está sin duda relacionado con las concentraciones necesarias para generar una señal detectable en la EPR, que es al menos dos órdenes de magnitud superior a las concentraciones utilizadas en los experimentos UV-vis de tipo *stopped-flow*. En nuestro trabajo, el uso de reactivos altamente concentrados llevó definitivamente el tiempo de formación de los intermedios fuera del rango accesible por la instrumentación disponible en nuestro laboratorio. En comparación con otros sistemas descritos en la bibliografía, la configuración RFQ comercial utilizada en este trabajo adolecía de un tiempo muerto considerablemente largo (~ 50 ms), cuya estimación precisa requería un procedimiento de calibración largo y que consumía muchos recursos.

En cualquier caso, a la luz de los hallazgos descritos en este trabajo, es posible ahora remodelar el mecanismo catalítico de *Cl*Cld introducido en el Capítulo 1 (**Esquema 1.2**). En la reacción con clorito a pH óptimo (~5.5), los experimentos de espectrofotometría de flujo detenido revelaron la formación del Compuesto I, que

domina en toda la duración de la degradación del clorito. Por el contrario, a valores de pH más altos, la especie dominante es una especie ferrílica (Compuesto I*/Compuesto II). Otros experimentos de flujo detenido y RFQ-EPR confirmaron que esta especia presenta un radical libre en un aminoácido (Compuesto I*), que es el producto de desintegración del Compuesto I en ausencia de donantes de electrones. Esta desintegración demostró ser altamente dependiente del pH, siendo significativamente más rápida a valores de pH más altos. En conjunto, estos resultados sugieren que el Compuesto I es la especie catalíticamente relevante a pH óptimo y que la vía productiva del *C*Cld sigue la escisión heterolítica del clorito siguiendo un posteriormente mecanismo de rebote del ClO^- (**Esquema 10.1**, **Reacciones 1, 2 y 3**). Por otra parte, la desintegración dependiente del pH del Compuesto I, que puede formarse también haciendo reaccionar *C*Cld con hipoclorito (**Esquema 10.1, Reacción 4**), da lugar a la formación del Compuesto I*, donde el radical migra muy probablemente a un residuo de tirosina (**Esquema 10.1, Reacción 5**). La RFQ-EPR proporcionó evidencias adicionales de la capacidad del compuesto I para oxidar el clorito en un proceso de transferencia de un electrón para producir dióxido de cloro, una reacción secundaria que parece potenciarse a concentraciones más altas de ambos reactivos (**Esquema 10.1, reacción 6**). Por último, varias mediciones de espectrofotometría de flujo detenido con mezcla secuencial, así como otros experimentos de CW-EPR, demostraron que la serotonina puede "rescatar" a la enzima de sus vías improductivas, pudiendo actuar como donante de un electrón tanto para el compuesto I como para el compuesto I* y devolver a la enzima al estado de reposo (**Esquema 10.1, reacciones 7, 8 y 9**).

Para resolver la naturaleza de los intermedios reactivos, los futuros trabajos de investigación podrían avanzar en dos direcciones paralelas. Por un lado, podría mejorarse la configuración RFQ con piezas de construcción propia con el objetivo de reducir su tiempo muerto. Se puede pensar en soluciones para aumentar la velocidad del chorro de la mezcla de reacción pulverizada sobre la superficie del baño criogénico, o para reducir el tamaño de las partículas y aumentar así la velocidad de congelación. También podría diseñarse un sistema de congelación completamente diferente, inspirándose en las soluciones adoptadas por otros grupos de investigación para sus propios montajes RFQ caseros. Por otra parte, es posible aprovechar las variantes de la clorito-dismutasa que muestran velocidades de reacción mucho más lentas. En este caso, existirá la posibilidad de atrapar los estados intermedios durante un intervalo de tiempo más largo. De todos modos, siguen abiertos los interrogantes sobre la alta selectividad de las clorito-dismutasas hacia el clorito, a pesar de sus notables similitudes estructurales con otras hemo peroxidasas. Asimismo, queda por determinar el papel fisiológico de las clorito-dismutasas en los organismos que no poseen un metabolismo basado en el clorato y el perclorato.

Desde el punto de vista de una posible aplicación biotecnológica de las clorito-dismutasas, hay que hacer algunas consideraciones. En primer lugar, hasta que no se optimice la producción a gran escala de estas enzimas, su aplicabilidad como biocatalizadores industriales seguirá siendo impracticable. Además, hay que tener en cuenta su sensibilidad al pH y su inactivación irreversible a largo plazo. En este sentido, podría ser útil proporcionar a las moléculas enzimáticas un microentorno "más seguro", como el interior de un material poroso. La inmovilización de enzimas fue el tema central de la última parte de este proyecto, que incluyó experimentos preliminares con el sistema modelo peroxidasa de rábano picante y con la clorito-dismutasa. Se ajustaron varios parámetros experimentales, como el pH, la concentración de proteínas y el pretratamiento del material, para optimizar la inmovilización de la *horseradish peroxidase* en una resina de intercambio iónico. Por otra parte, la incorporación de la clorito-dismutasa en diferentes sílices mesoporosas y no porosas y en titania se llevó a cabo en condiciones subóptimas y sólo se presentó como prueba de concepto. Aunque ambos experimentos sugirieron la viabilidad de la inmovilización de estos dos biocatalizadores en diferentes materiales, en el futuro será necesaria una amplia investigación para desarrollar un protocolo de inmovilización fiable y reproducible. La caracterización estructural y bioquímica de las enzimas inmovilizadas, así como la evaluación de sus actividades catalíticas, serán una continuación necesaria del trabajo presentado con vistas a desarrollar nuevos usos industriales de estas fascinantes biomoléculas.

Appendix A

Supplementary material Chapter 4

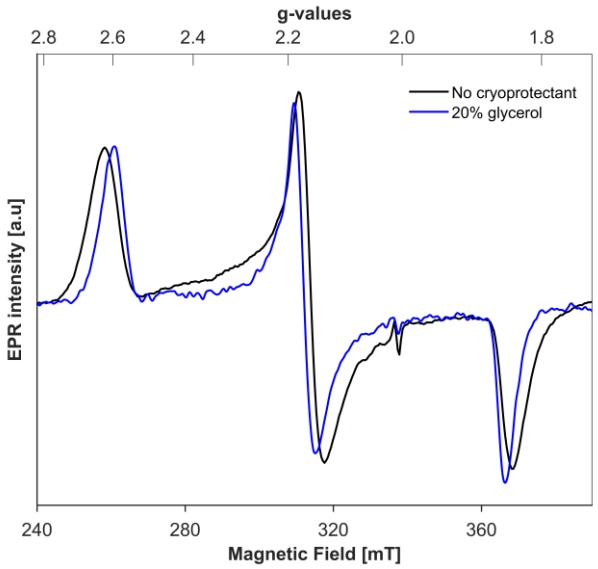

Figure A.1 *CW X-band EPR spectrum (low-spin region only) of myoglobin in glycine buffer 50 mM, without and with 20 % (v/v) of glycerol*

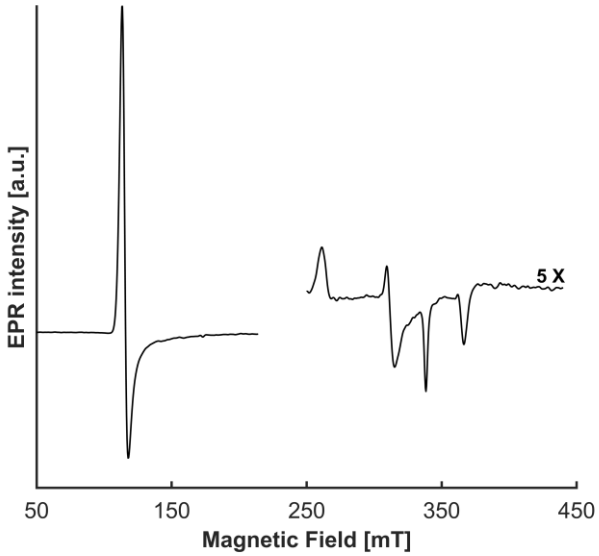

Figure A.2 *CW X-band EPR spectrum of myoglobin in carbonate-bicarbonate buffer 50 mM, in presence of 20 % (v/v) of glycerol. For clarity, the inset of the high-field region is 5x-magnified*

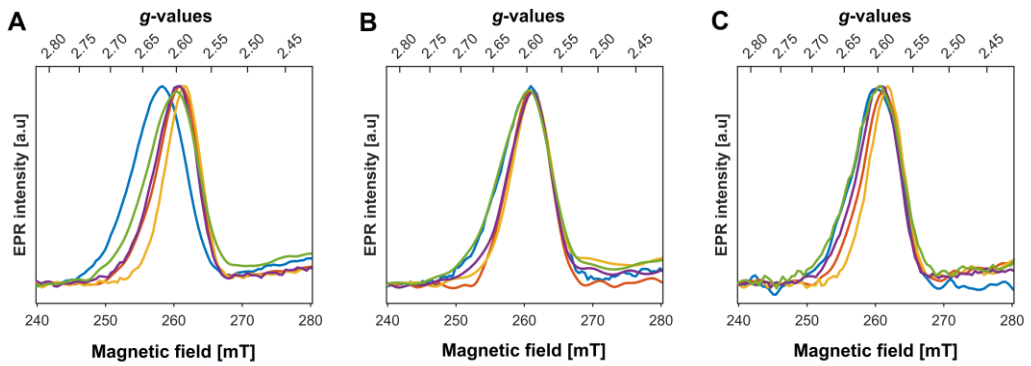

Figure A.3 *Details of the g_z feature of the OH-ligated LS of myoglobin samples prepared in* ***A)*** *glycine,* ***B)*** *CAPS and* ***C)*** *CHES buffer, respectively, in presence of different glassing agents. Spectra were normalized at the center of the line. Cyan: no cryoprotectant added; red: 20 % glycerol; dark yellow: 20 % ethylene glycol; purple: 0.36 M sucrose; green: 0.36 M trehalose*

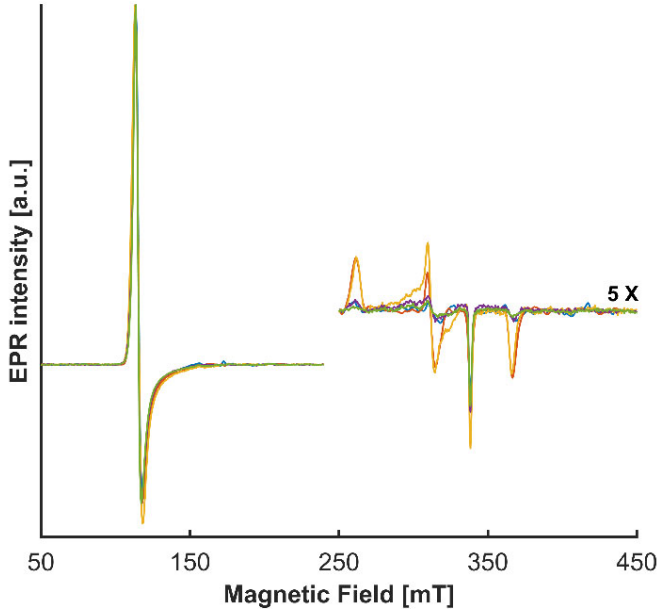

Figure A.4 *CW X-band EPR spectrum of myoglobin in carbonate-bicarbonate buffer 50 mM, in the presence of different cryoprotectants. Cyan: no cryoprotectant added; red: 20 % glycerol; dark yellow: 20 % ethylene glycol; purple: 0.36 M sucrose; green: 0.36 M trehalose. For clarity, the inset of the high-field region is 5x-magnified*

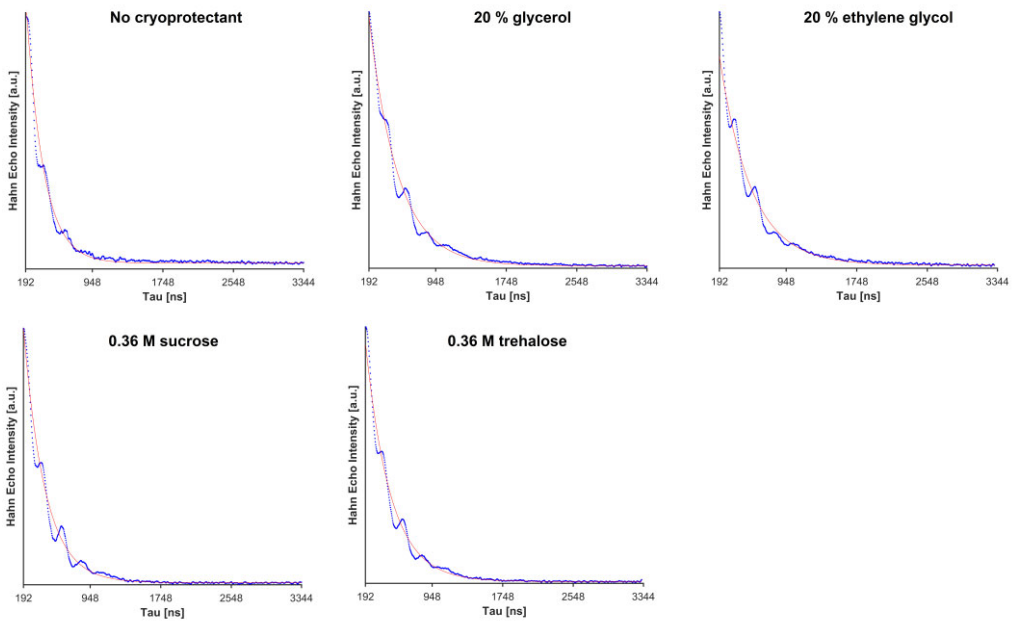

Figure A.5 *Exemplary curve-fitting of 2-pulse echo decay spectra at the gz position of myoglobin samples prepared in CAPS buffer with different cryoprotectants. Blue: experimental spectrum; red: fitted curve*

Cryoprotectant	T_m **(ns)**
None	205 ± 9
20 % glycerol	338 ± 8
20 % ethylene glycol	356 ± 15
0.36 M sucrose	251 ± 6
0.36 M trehalose	286 ± 5

Table A.1 *T_m values calculated from coefficient B of equation 4.1. Errors were estimated using a semi-empirical approach, taking into account the 95 % confidence interval of the fitting and T_m values obtained by performing the fitting on spectra with different starting points chosen arbitrarily within the first ~ 80 ns*

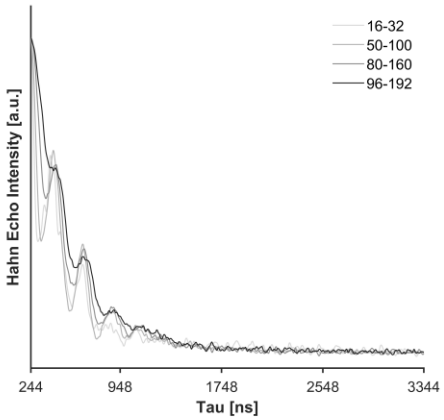

MW Pulses length, $t_{\pi/2}$ - t_{π} (ns)	T_m (ns)
16-32	332 ± 15
50-100	350 ± 17
80-160	331 ± 10
96-192	338 ± 8

Figure A.6 *X-band 2-pulse spin echo decay (left panel) and T_m values obtained from curve-fitting (right panel) of myoglobin samples prepared in CAPS buffer with 20 % (v/v) glycerol, measured at the g_z position with MW pulses of different length. Spectra were normalized at τ = 244 ns. Errors were estimated using a semi-empirical approach, taking into account the 95 % confidence interval of the fitting and T_m values obtained by performing the fitting on spectra with different starting points chosen arbitrarily within the first ~ 80 ns*

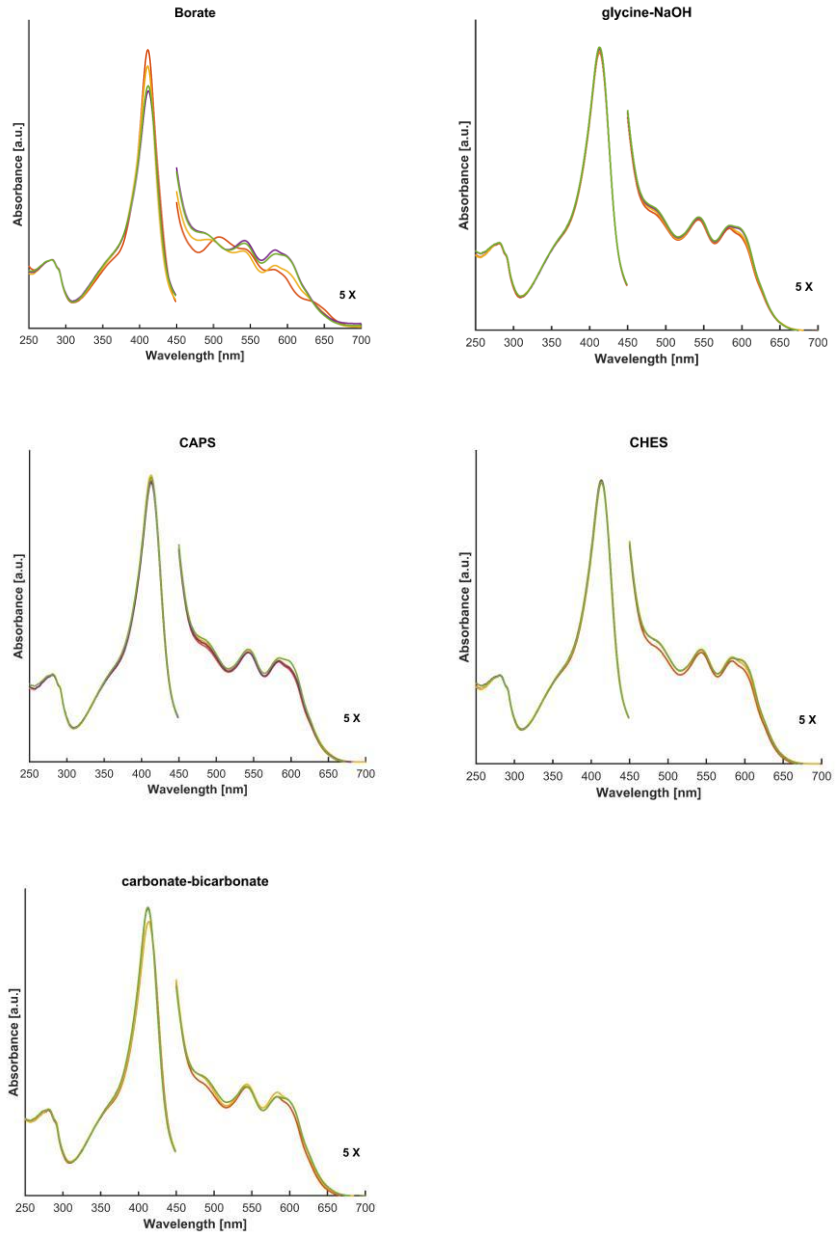

Figure A.7 *Optical spectra of myoglobin in different alkaline buffers at room temperature. Red: 20 % glycerol; dark yellow: 20 % ethylene glycol; purple: 0.36 M sucrose; green: 0.36 M trehalose. For clarity, spectra were normalised at λ = 280 nm and insets were 5x-magnified.*

Appendix B

Supplementary material Chapter 7

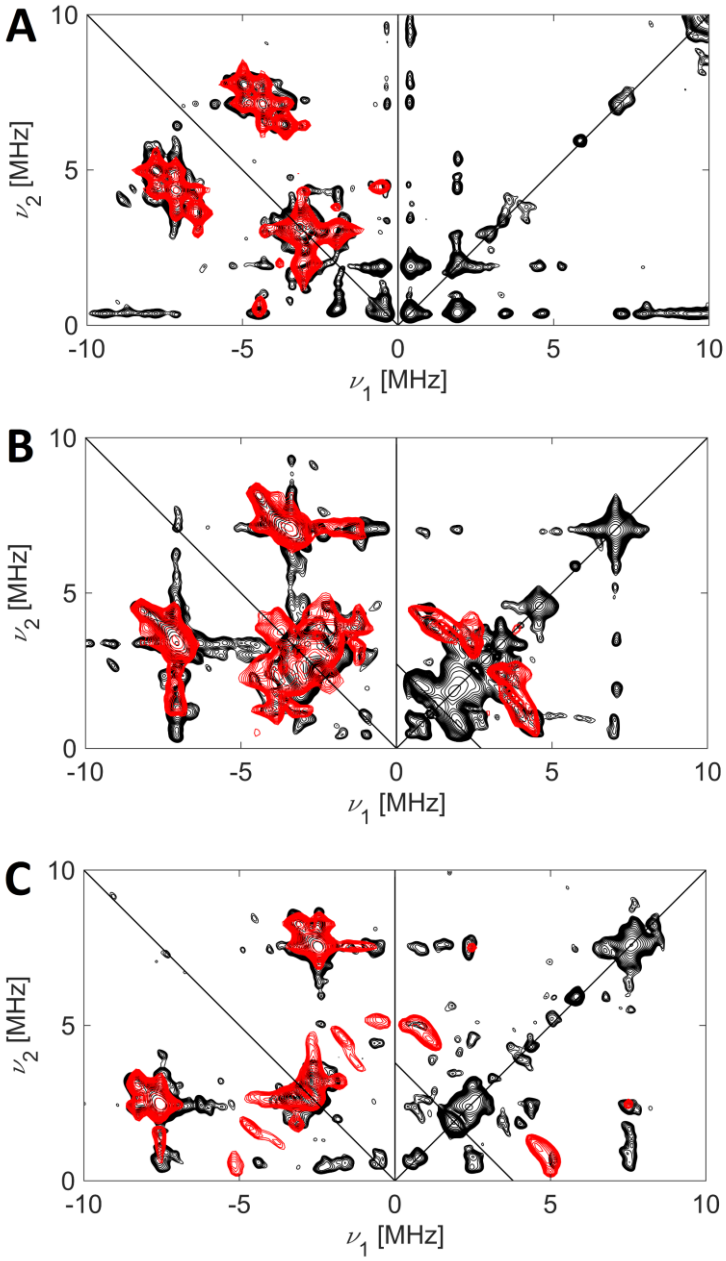

Figure B.1 *Experimental (black) and simulated (red) X-band HYSCORE spectra of 1 mM ferric horse heart myoglobin in presence of 500 mM of* $^{15}NO_2^-$*, recorded at the observer positions corresponding to* $g = g_z$ ***(A)***, $g = g_y$ ***(B)*** *and* $g = g_x$ ***(C)***, *respectively. The spectra are the sum of* τ *= 96, 176 and 208 ns, normalized to the noise level. The simulation includes the contributions of the heme and proximal histidine* ^{14}N *nuclei. The contribution of the weakly-coupled* ^{15}N *nucleus from nitrite was omitted and it is shown separately in* **Figure 7.5**

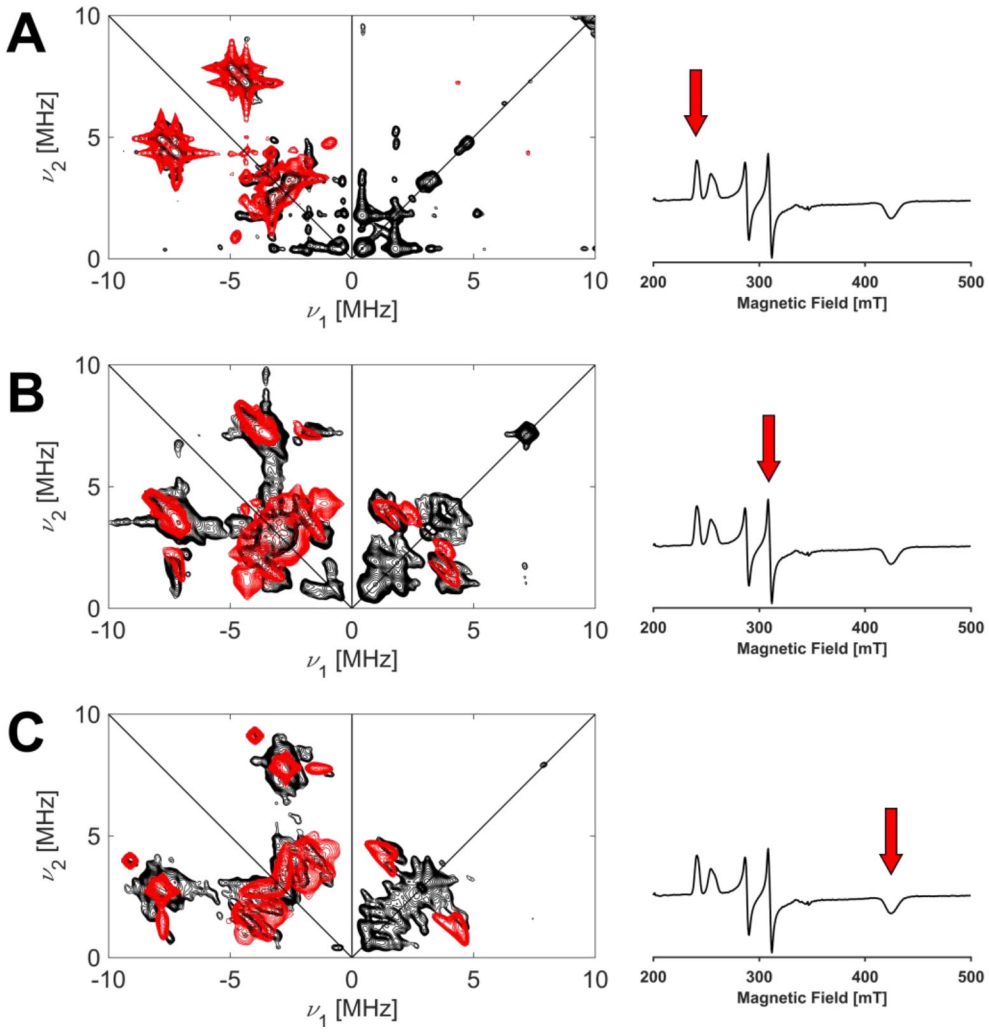

Figure B.2 *Experimental (black) and simulated (red) X-band HYSCORE spectra of 1 mM WT CCld in presence of 500 mM of* $^{15}NO_2^-$*, recorded at the observer positions corresponding to* $g = g_z(1)$ ***(A)***, $g = g_y(1)$ ***(B)*** *and* $g = g_x$ ***(C)****, respectively. The spectra are the sum of* τ *= 176 and 208 ns, normalized to the noise level. The simulation includes the contributions of the heme and proximal histidine* ^{14}N *nuclei. The contribution of the weakly-coupled* ^{15}N *nucleus from nitrite was omitted and it is shown separately in* **Figure 7.14**.

Appendix C

Side projects

Site-directed spin label (SDSL-) EPR for the study electrostatic coacervation and co-aggregation of alpha-synuclein and tau.

In collaboration with the group of Prof. Nunilo Cremades (Institute for Biocomputation and Physics of Complex Systems, University of Zaragoza), I performed several room-temperature continuous-wave EPR measurements of spin-labelled α-Synuclein, a protein well-known for its role in the development of neurodegenerative diseases. The project aimed at understanding the interaction between α-Synuclein and its partner Tau and the occurrence of liquid-liquid phase separation in presence of a crowder agent (PEG or dextran). The expected changes in the dynamics of the system were then followed by the analysis of the spin-label (TEMPOL) dynamics, covalently attached to α-Synuclein. The results of this collaboration have been published in Nature Communications (see "List of Publications" in the curriculum vitae).

Investigation of human myeloperoxidase (MPO) by continuous-wave EPR.

In collaboration with the group of Prof. Ange Mouithys from the Department of Physics at the University of Liege (BE), this project aimed at the identification of spin state or electronic configuration changes induced in the heme-containing human myeloperoxidase (MPO) by the interaction with selected drug molecules, such as a metabolite of the anti-inflammatory drug propofol (PPFQ) and 6-thioguanine, used as an anticancer drug.

Curriculum vitae

Education

2019 – 2023	**Joint PhD in Science / Biochemistry & Molecular Biology** University of Antwerp / University of Zaragoza Marie Skłodowska-Curie Actions Fellow
2016 - 2018	**Master of Science in Industrial Biotechnology** University of Modena and Reggio Emilia
2013 - 2016	**Bachelor of Science in Biotechnology** University of Bologna

Training

14/11/22 – 18/11/22	**Research visit at the Max Planck Institute for Chemical Energy Conversion** Mulheim an der Ruhr, Germany *High-frequency electron paramagnetic resonance of protein samples*
24/02/20 – 13/03/20	**Industrial internship at ADM Biopolis** Valencia, Spain *Training on enzyme immobilization*
1/10/19 – 29/11/19	**Research stay at the BOKU University of Vienna** Vienna, Austria *Production and purification of recombinant proteins, stopped-flow UV-vis spectroscopy; enzyme activity assays*

Summer schools

19/09/22 – 22/09/22	**4th PARACAT School** *"Electron Paramagnetic Resonance in Catalysis"* Athens, Greece
19/07/21 – 24/07/21	**3rd PARACAT School** *"Spectroscopic and computational methods towards molecular structure and reactivity"* Zaragoza, Spain
13/01/20 – 17/01/20	**2nd PARACAT School** *"Cardiff Winter School on Catalysis"* Cardiff, United Kingdom
18/11/19 – 25/11/19	**8th School of European Federation of EPR groups** *"Advanced EPR"* Brno, Czech Republic
14/07/19 - 20/07/19	**1st PARACAT School** *"Basics of Electron Paramagnetic Resonance (EPR) for applications in (bio)catalysis"* Antwerp, Belgium

List of publications

Schmidt, D., Falb, N., **Serra, I.**, Bellei, M., Pfanzagl, V., Hofbauer, S., van Doorslaer, S., Battistuzzi, G., Furtmüller, P. G., & Obinger, C. Compound I Formation and Reactivity in Dimeric Chlorite Dismutase: Impact of pH and the Dynamics of the Catalytic Arginine. *Biochemistry* 62, 3, 835–850 (2023).

Gracia P., Polanco D., Tarancón-Díez J., **Serra I.**, Bracci M. A., Oroz J., Laurents D. V., García I. and Cremades N. Molecular Mechanism for the Synchronized Electrostatic Coacervation and Amyloid Co-Aggregation of Alpha-Synuclein and Tau, *Nature Communications* 13, 4586 (2022).

Serra, I.**, Piccinini, D.**, Paradisi, A., Ciano, L., Bellei, M., Bortolotti, C. A., ... & Di Rocco, G. Activity and substrate specificity of lytic polysaccharide monooxygenases: An ATR FTIR-based sensitive assay tested on a novel species from Pseudomonas putida. *Protein Science*, *31*(3), 591-601 (2022).

*** Both authors contributed equally to this manuscript*

Serra I.**, Schmidt D.**, Pfanzagl V., Mlynek G., Hofbauer S., Djinovic-Carugo K., Furtmüller P.G., García Rubio I., Van Doorslaer S., and Obinger C. Impact of the dynamics of the catalytic arginine on nitrite and chlorite binding by dimeric chlorite dismutase. *Journal of Inorganic Biochemistry* 227, 111689 (2022).

*** Both authors contributed equally to this manuscript*

Serra I., García Rubio I. and Van Doorslaer S., Pitfalls in sample preparation of metalloproteins for low-temperature EPR – the example of alkaline myoglobin. *Applied Magnetic Resonance* 53, 1105–1119. Part of a collection: Klaus Möbius and Kev Salikhov: on the Occasion of Their 85th Birthdays (2021).

Schmidt, D.;** **Serra, I.**;** Mlynek, G.; Pfanzagl, V.; Hofbauer, S.; Furtmüller, P. G.; Djinović-Carugo, K.; Van Doorslaer, S.; Obinger, C. Arresting the catalytic arginine in chlorite dismutases – Impact on heme coordination, thermal stability and catalysis. *Biochemistry* 60, 8, 621–634 (2021).

*** Both authors contributed equally to this manuscript*

Bracci, M.; Bruzzese P. C.; Famulari, A.; Fioco, D.; Guidetti, A.; Liao Y.- K.; Podvorica, L.; Rezayi, S. F.; **Serra, I.**; Thangavel, K. Paramagnetic Species in Catalysis Research: A Unified Approach Towards (the role of EPR in) Heterogeneous, Homogeneous and Enzyme Catalysis. In *Electron Paramagnetic Resonance: Volume 27*; Chechik, Victor; Murphy, D. M.; Bode, Bela E, Ed.; Royal Society of Chemistry: London pp. 1 – 46 (2020).

Awards

2nd jury award and public award of the 'PRESS>>SPEAK' competition organized by the University of Antwerp, for the writing of a short text about own research topic, addressed to a general public.

Bibliography

[1] M. Sánchez, L. Sabio, N. Gálvez, M. Capdevila, and J.M. Dominguez-Vera (2017) "Iron chemistry at the service of life". *IUBMB Life*, 69:382–388

[2] A.W. Munro, H.M. Girvan, K.J. McLean, M.R. Cheesman, and D. Leys (2009) "Heme and Hemoproteins". In: Warren MJ, Smith AG (eds) "Tetrapyrroles: Birth, Life and Death". Springer, New York, pp 160–183

[3] H. Fischer, H. Orth, and A. Stern (1937) "Die Chemie des Pyrrols". Akademische Verlagsgesellschaft, Leipzig

[4] J.A. Shelnutt, X.Z. Song, J.G. Ma, S.L. Jia, W. Jentzen, et al (1998) "Nonplanar porphyrins and their significance in proteins". *Chemical Society Reviews*, 27:31–41

[5] G.H. Loew and D.L. Harris (2000) "Role of the Heme Active Site and Protein Environment in Structure, Spectra, and Function of the Cytochrome P450s". *Chemical Reviews*, 100:407–419

[6] M. Sundaramoorthy, J. Terner, and T.L. Poulos (1995) "The crystal structure of chloroperoxidase: a heme peroxidase-cytochrome P450 functional hybrid". *Structure*, 3:1367–1378

[7] T.O. Fischmann, A. Hruza, X. da Niu, J.D. Fossetta, C.A. Lunn, et al (1999) "Structural characterization of nitric oxide synthase isoforms reveals striking active-site conservation". *Nature Structural Biology*, 6:233–242

[8] T. Burmester and T. Hankeln (2014) "Function and evolution of vertebrate globins". *Acta Physiologica*, 211:501–514

[9] H. Wajcman, L. Kiger, and M.C. Marden (2009) "Structure and function evolution in the superfamily of globins". *Comptes Rendus - Biologies*, 332:273–282

[10] S.N. Vinogradov and L. Moens (2008) "Diversity of globin function: Enzymatic, transport, storage, and sensing". *Journal of Biological Chemistry*, 283:8773–8777

[11] R.M. Roat-Malone (2007) "Iron-Containing Proteins and Enzymes". In: "Bioinorganic Chemistry". pp 343–476

[12] U. Flögel, M.W. Merx, A. Gödecke, U.K.M. Decking, and J. Rgen Schrader (2001) "Myoglobin: A scavenger of bioactive NO". *Proceedings of the National Academy of Sciences*, 98:735–740

[13] U.B. Hendgen-Cotta, M.W. Merx, S. Shiva, J. Schmitz, S. Becher, et al (2008) "Nitrite reductase activity of myoglobin regulates respiration and cellular viability in myocardial ischemia-reperfusion injury". *Proceedings of the National Academy of Sciences*, 105:10256–10261

[14] J.S. Olson and G.N. Phillips (1997) "Myoglobin discriminates between O2, NO, and CO by electrostatic interactions with the bound ligand". *Journal of Biological Inorganic Chemistry*, 2:544–552

[15] C. Slebodnick and J.A. Ibers (1997) "Myoglobin models and steric origins of the discrimination between O2 and CO". *Journal of Biological Inorganic Chemistry*, 2:521–525

[16] D.M. Copeland, A.S. Soares, A.H. West, and G.B. Richter-Addo (2006) "Crystal structures of the nitrite and nitric oxide complexes of horse heart myoglobin". *Journal of Inorganic Biochemistry*, 100:1413–1425

[17] J. Yi, J. Heinecke, H. Tan, P.C. Ford, and G.B. Richter-Addo (2009) "The distal pocket histidine residue in horse heart myoglobin directs the O-binding mode of nitrite to the heme iron". *Journal of the American Chemical Society*, 131:18119–18128

[18] M. Zámocký and C. Obinger (2010) "Molecular phylogeny of heme peroxidases". In: "Biocatalysis Based on Heme Peroxidases: Peroxidases as Potential Industrial Biocatalysts". Springer Berlin Heidelberg, pp 7–35

[19] M. Zámocký, S. Hofbauer, I. Schaffner, B. Gasselhuber, A. Nicolussi, et al (2015) "Independent evolution of four heme peroxidase superfamilies". *Archives of Biochemistry and Biophysics*, 574:108–119

[20] L.A. Planche (1810) "Note sur la sophistication de la résine de jalap et sur les moyens de la reconnaître". *Bulletin de Pharmacie*, 2:578–580

[21] F.W. Krainer and A. Glieder (2015) "An updated view on horseradish peroxidases: recombinant production and biotechnological applications". *Applied Microbiology and Biotechnology*, 99:1611–1625

[22] B.L. Clement Markert and F. Moller (1959) "Multiple Forms of enzymes: tissue, ontogenetic, and species specific patterns". *Proceedings of the National Academy of Sciences*, 45:753–763

[23] M.C. Hoyle (1977) "High Resolution of Peroxidase-Indoleacetic Acid Oxidase Isoenzymes from Horseradish by Isoelectric Focusing". *Plant Physiology*, 60:787–793

[24] G.I. Berglund, G.H. Carlsson, A.T. Smith, H. Szöke, A. Henriksen, et al (2002) "The catalytic pathway of horseradish peroxidase at high resolution". *Nature*, 417:463–468

[25] A.T. Smith, N. Santama, S. Daceys, M.E. Robert, C. Bray, et al (1990) "Expression of a Synthetic Gene for Horseradish Peroxidase C in Escherichia coli and Folding and Activation of the Recombinant Enzyme with Ca2+ and Heme*". *Journal of Biological Chemistry*, 265:13335–13343

[26] N.C. Veitch (2004) "Horseradish peroxidase: A modern view of a classic enzyme". *Phytochemistry*, 65:249–259

[27] M. Ayala and E. Torres (2016) "Peroxidases as Potential Industrial Biocatalysts". In: "Heme Peroxidases". The Royal Society of Chemistry, pp 309–333

[28] R.L. Osborne, G.M. Raner, L.P. Hager, and J.H. Dawson (2006) "C. fumago chloroperoxidase is also a dehaloperoxidase: Oxidative dehalogenation of halophenols". *Journal of the American Chemical Society*, 128:1036–1037

[29] B. Goblirsch, R.C. Kurker, B.R. Streit, C.M. Wilmot, and J.L. Dubois (2011) "Chlorite dismutases, DyPs, and EfeB: 3 microbial heme enzyme families comprise the CDE structural superfamily". *Journal of Molecular Biology*, 408:379–398

[30] A. Sturm, A. Schierhorn, U. Lindenstrauss, H. Lilie, and T. Brüser (2006) "YcdB from Escherichia coli reveals a novel class of Tat-dependently translocated hemoproteins". *Journal of Biological Chemistry*, 281:13972–13978

[31] S. Lé Toffé, G. Heuck, P. Delepelaire, N. Lange, and C. Cile Wandersman (2009) "Bacteria capture iron from heme by keeping tetrapyrrol skeleton intact". *Proceedings of the National Academy of Sciences* , 106:11719–11724

[32] S. Hofbauer, V. Pfanzagl, H. Michlits, D. Schmidt, C. Obinger, et al (2021) "Understanding molecular enzymology of porphyrin-binding α + β barrel proteins - One fold, multiple functions". *Biochimica et Biophysica Acta (Proteins and Proteomics)*, 1869:140536

[33] S.J. Kim and M. Shoda (1999) "Decolorization of molasses and a dye by a newly isolated strain of the fungus Geotrichum candidum Dec 1". *Biotechnology and Bioengineering*, 62:114–119

[34] T. Yoshida and Y. Sugano (2015) "A structural and functional perspective of DyP-type peroxidase family". *Archives of Biochemistry and Biophysics*, 574:49–55

[35] Y. Sugano and T. Yoshida (2021) "Dyp-type peroxidases: Recent advances and perspectives". *International Journal of Molecular Sciences*, 22:5556–5571

[36] B. Westereng, D. Cannella, J. Wittrup Agger, H. Jørgensen, M. Larsen Andersen, et al (2015) "Enzymatic cellulose oxidation is linked to lignin by long-range electron transfer". *Scientific Reports*, 5:18561

[37] K. Nys, P.G. Furtmüller, C. Obinger, S. van Doorslaer, and V. Pfanzagl (2021) "On the Track of Long-Range Electron Transfer in B-Type Dye-Decolorizing Peroxidases: Identification of a Tyrosyl Radical by Computational Prediction and Electron Paramagnetic Resonance Spectroscopy". *Biochemistry*, 60:1226–1241

[38] R. Shrestha, X. Chen, K.X. Ramyar, Z. Hayati, E.A. Carlson, et al (2016) "Identification of surface-Exposed protein radicals and a substrate oxidation site in a-Class dye-Decolorizing peroxidase from thermomonospora curvata". *ACS Catalysis*, 6:8036–8047

[39] Y. Sugano, Y. Matsushima, K. Tsuchiya, H. Aoki, M. Hirai, et al (2009) "Degradation pathway of an anthraquinone dye catalyzed by a unique peroxidase DyP from Thanatephorus cucumeris Dec 1". *Biodegradation*, 20:433–440

[40] M. Scheibner, B. Hülsdau, K. Zelena, M. Nimtz, L. de Boer, et al (2008) "Novel peroxidases of Marasmius scorodonius degrade β-carotene". *Applied Microbiology and Biotechnology*, 77:1241–1250

[41] K. Sugawara, E. Igeta, Y. Amano, M. Hyuga, and Y. Sugano (2019) "Degradation of antifungal anthraquinone compounds is a probable physiological role of DyP secreted by Bjerkandera adusta". *AMB Express*, 9:56

[42] F.A. Riyadi, A.A. Tahir, N. Yusof, N.S.A. Sabri, M.J.M.M. Noor, et al (2020) "Enzymatic and genetic characterization of lignin depolymerization by Streptomyces sp. S6 isolated from a tropical environment". *Scientific Reports*, 10:7813

[43] M. Sahinkaya, D.N. Colak, A. Ozer, S. Canakci, I. Deniz, et al (2019) "Cloning, characterization and paper pulp applications of a newly isolated DyP type peroxidase from Rhodococcus sp. T1". *Molecular Biology Reports*, 46:569–580

[44] H. Contreras, M.S. Joens, L.M. McMath, V.P. Le, M. v. Tullius, et al (2014) "Characterization of a Mycobacterium tuberculosis nanocompartment and its potential cargo proteins". *Journal of Biological Chemistry*, 289:18279–18289

[45] C.G. van Ginkel, G.B. Rikken, A.G.M. Kroon, and S.W.M. Kengen (1996) "Purification and characterization of chlorite dismutase: A novel oxygen-generating enzyme". *Archives of Microbiology*, 166:321–326

[46] N. Bardiya and J.H. Bae (2011) "Dissimilatory perchlorate reduction: A review". *Microbiological Research*, 166:237–254

[47] J.D. Coates and L.A. Achenbach (2004) "Microbial perchlorate reduction: Rocket-fuelled metabolism". *Nature Reviews Microbiology*, 2:569–580

[48] P.L. Hagedoorn, D.C. de Geus, and W.R. Hagen (2002) "Spectroscopic characterization and ligand-binding properties of chlorite dismutase from the chlorate respiring bacterial strain GR-1". *European Journal of Biochemistry*, 269:4905–4911

[49] K. Stenklo, H. Danielsson Thorell, H. Bergius, R. Aasa, and T. Nilsson (2001) "Chlorite dismutase from Ideonella dechloratans". *Journal of Biological Inorganic Chemistry*, 6:601–607

[50] B.R. Streit and J.L. DuBois (2008) "Chemical and steady-state kinetic analyses of a heterologously expressed heme dependent chlorite dismutase". *Biochemistry*, 47:5271–5280

[51] F. Mehboob, A.F.M. Wolterink, A.J. Vermeulen, B. Jiang, P.L. Hagedoorn, et al (2009) "Purification and characterization of a chlorite dismutase from Pseudomonas chloritidismutans". *FEMS Microbiology Letters*, 293:115–121

[52] F. Maixner, M. Wagner, S. Lücker, E. Pelletier, S. Schmitz-Esser, et al (2008) "Environmental genomics reveals a functional chlorite dismutase in the nitrite-oxidizing bacterium “Candidatus Nitrospira defluvii”". *Environmental Microbiology*, 10:3043–3056

[53] G. Mlynek, B. Sjöblom, J. Kostan, S. Füreder, F. Maixner, et al (2011) "Unexpected diversity of chlorite dismutases: A catalytically efficient dimeric enzyme from Nitrobacter winogradskyi". *Journal of Bacteriology*, 193:2408–2417

[54] I. Schaffner, S. Hofbauer, M. Krutzler, K.F. Pirker, M. Bellei, et al (2015) "Dimeric chlorite dismutase from the nitrogen-fixing cyanobacterium Cyanothece sp. PCC7425". *Molecular Microbiology*, 96:1053–1068

[55] I. Schaffner, G. Mlynek, N. Flego, D. Pühringer, J. Libiseller-Egger, et al (2017) "Molecular Mechanism of Enzymatic Chlorite Detoxification: Insights from Structural and Kinetic Studies". *ACS Catalysis*, 7:7962–7976

[56] J. Kostan, B. Sjöblom, F. Maixner, G. Mlynek, P.G. Furtmüller, et al (2010) "Structural and functional characterisation of the chlorite dismutase from the nitrite-oxidizing bacterium " Candidatus Nitrospira defluvii": Identification of a catalytically important amino acid residue". *Journal of Structural Biology*, 172:331–342

[57] S. Hofbauer, K. Gysel, M. Bellei, A. Hagmüller, I. Schaffner, et al (2014) "Manipulating conserved heme cavity residues of chlorite dismutase: Effect on structure, redox chemistry, and reactivity". *Biochemistry*, 53:77–89

[58] B. Blanc, J.A. Mayfield, C.A. McDonald, G.S. Lukat-Rodgers, K.R. Rodgers, et al (2012) "Understanding how the distal environment directs reactivity in chlorite dismutase: Spectroscopy and reactivity of Arg183 Mutants". *Biochemistry*, 51:1895–1910

[59] D.C. de Geus, E.A.J. Thomassen, P.L. Hagedoorn, N.S. Pannu, E. van Duijn, et al (2009) "Crystal Structure of Chlorite Dismutase, a Detoxifying Enzyme Producing Molecular Oxygen". *Journal of Molecular Biology*, 387:192–206

[60] B.R. Goblirsch, B.R. Streit, J.L. DuBois, and C.M. Wilmot (2010) "Structural features promoting dioxygen production by Dechloromonas aromatica chlorite dismutase". *Journal of Biological Inorganic Chemistry*, 15:879–888

[61] A. De Schutter, H.D. Correia, D.M. Freire, M.G. Rivas, A. Rizzi, et al (2015) "Ligand Binding to Chlorite Dismutase from Magnetospirillum sp.". *Journal of Physical Chemistry B*, 119:13859–13869

[62] K.F. Ettwig, M.K. Butler, D. le Paslier, E. Pelletier, S. Mangenot, et al (2010) "Nitrite-driven anaerobic methane oxidation by oxygenic bacteria". *Nature*, 464:543–548

[63] A.Q. Lee, B.R. Streit, M.J. Zdilla, M. Abu-Omar, and J.L. Dubois (2008) "Mechanism of and exquisite selectivity for O-O bond formation by the heme-dependent chlorite dismutase". *Proceedings of the National Academy of Sciences*, 105:15654–15659

[64] J.A. Mayfield, B. Blanc, K.R. Rodgers, G.S. Lukat-Rodgers, and J.L. Dubois (2013) "Peroxidase-type reactions suggest a heterolytic/nucleophilic o-o

joining mechanism in the heme-dependent chlorite dismutase". *Biochemistry*, 52:6982–6994

[65] S. Hofbauer, C. Gruber, K.F. Pirker, A. Sündermann, I. Schaffner, et al (2014) "Transiently produced hypochlorite is responsible for the irreversible inhibition of chlorite dismutase". *Biochemistry*, 53:3145–3157

[66] S. Sun, Z.S. Li, and S.L. Chen (2014) "A dominant homolytic O-Cl bond cleavage with low-spin triplet-state Fe(IV)=O formed is revealed in the mechanism of heme-dependent chlorite dismutase". *Dalton Transactions*, 43:973–981

[67] S. Hofbauer, V. Pfanzagl, H. Michlits, D. Schmidt, C. Obinger, et al (2021) "Understanding molecular enzymology of porphyrin-binding α + β barrel proteins - One fold, multiple functions". Biochim Biophys Acta Proteins Proteom 1869

[68] P.T. Anastas and E.S. Beach (2009) "Changing the Course of Chemistry". In: "Green Chemistry Education". American Chemical Society, Washington D.C., pp 1–18

[69] P.T. Anastas and J.C. Warner (1998) "Green Chemistry: Theory and Practice". Oxford University Press

[70] M. v. Arbige, J.K. Shetty, and G.K. Chotani (2019) "Industrial Enzymology: The Next Chapter". *Trends in Biotechnology*, 37:1355–1366

[71] A.D. McNaught and A. Wilkinson (1997) "IUPAC. Compendium of Chemical Terminology". In: "The Gold Book", 2nd ed. Blackwell Scientific Publications, Oxford

[72] S. Hofbauer, I. Schaffner, P.G. Furtmüller, and C. Obinger (2014) "Chlorite dismutases - a heme enzyme family for use in bioremediation and generation of molecular oxygen". *Biotechnology Journal*, 9:461–473

[73] K.C. Mobilia, J.M. Hutchison, and J.L. Zilles (2017) "Characterizing isozymes of chlorite dismutase for water treatment". *Frontiers in Microbiology*, 8:2423

[74] C.G. van Ginkel, A.G.M. Kroon, and R.J. van Wijk (1999) "Process for the degradation of chlorite". In: "U.S. Patent No. 5,891,339". U.S. Patent and Trademark Office, Washington, DC

[75] H. Ueno, K. Oishi, Y. Sayato, and K. Nakamuro (2000) "Oxidative Cell Damage in Kat-Sod Assay of Oxyhalides as Inorganic Disinfection By-Products and Their Occurrence by Ozonation". *Archives of Environmental Contamination and Toxicology*, 38:1–6

[76] O. Wang and J.D. Coates (2017) "Biotechnological applications of microbial (Per)chlorate reduction". *Microorganisms*, 5:76

[77] J.D. Coates (2020) "Recombinantly engineered cells expressing chlorite dismutase and methods for using same in cell culture". In: "U.S. Patent No. 10,724,010". U.S. Patent and Trademark Office, Washington, DC

[78] A.L. Markhard, J.G. Mccoy, T.-L. To, and V.K. Mootha (2022) "A genetically encoded system for oxygen generation in living cells". *Proceedings of the National Academy of Sciences*, 119:43

[79] J.M. Berg, J.L. Tymoczko, G.J. Gatto, and L. Stryer (2019) "Biochemistry", 9th ed. W. H. Freeman and Company, New York

[80] K. Rajagopal (2012) "Recombinant DNA Technology and Genetic Engineering". Tata McGraw-Hill

[81] W.L. Carroll (1993) "Introduction to recombinant-DNA technology". *The American Journal of Clinical Nutrition*, 58:249–258

[82] G.L. Rosano and E.A. Ceccarelli (2014) "Recombinant protein expression in Escherichia coli: Advances and challenges". *Frontiers in Microbiology*, 5:172

[83] F.X. Schmid (2001) "Biological Macromolecules: UV-visible Spectrophotometry". In: "Encyclopedia of Life Science". Macmillan Publishers Ltd

[84] A.R. Goldfarb and L.J. Saidel (1951) "Ultraviolet absorption spectra of proteins". *Science*, 114:156–157

[85] M. Gouterman (1978) "Optical spectra and electronic structure of porphyrins and related rings". In: "The porphyrins". Academic Press

[86] G.R. Schokbaum and S. Lo (1972) "Interaction of Peroxidases with Aromatic Peracids and Alkyl peroxides". *The Journal of Biological Chemistry*, 247:3353–3360

[87] R. Wever and H. Plat (1981) "Spectral properties of myeloperoxidase and its ligand complexes". *Biochimica et Biophysica Acta*, 661:235–239

[88] V. Pfanzagl, K. Nys, M. Bellei, H. Michlits, G. Mlynek, et al (2018) "Roles of distal aspartate and arginine of B-class dye-decolorizing peroxidase in heterolytic hydrogen peroxide cleavage". *Journal of Biological Chemistry*, 293:14823–14838

[89] R.M. Roat-Malone (2007) "Bioinorganic chemistry", 2nd ed. John Wiley & Sons, Inc.

[90] E. Carter, V. Chechik, and D. Murphy (2016) "Electron Paramagnetic Resonance". Oxford University Press, Oxford, UK

[91] J.A. Weil and J.R. Bolton (2006) "Electron Paramagnetic Resonance: Elementary Theory and Practical Applications", 2nd ed. John Wiley & Sons

[92] D. Goldfarb and S. Stoll (2018) "EPR Spectroscopy: Fundamentals and methods". John Wiley & Sons Ltd

[93] E. Zavoisky (1945) "Spin-magnetic resonance in paramagnetics". *Journal of Physics USSR*, 9:211–245

[94] R.C. Bray (1961) "Sudden Freezing as a Technique for the Study of Rapid Reactions". *Biochemical Journal*, 81:189

[95] R.J. Appleyard, W.A. Shuttleworth, and J.N.S. Evans (1994) "Time-Resolved Solid-state NMR Spectroscopy of 5-Enolpyruvylshikimate-3-phosphate Synthase". *Biochemistry*, 33:6812–6821

[96] D.P. Ballou and G.A. Palmer (1974) "Rapid Mixing and Sampling Techniques in Biochemistry". *Analytical chemistry*, 48:9

[97] A. Ivancich, | Hélène, M. Jouve, B. Sartor, and J. Gaillard (1997) "EPR Investigation of Compound I in Proteus mirabilis and Bovine Liver Catalases: Formation of Porphyrin and Tyrosyl Radical Intermediates". *Biochemistry*, 36:9356–9364

[98] N. Ravi, J.M. Bollinger, L. Boi, H. Huynh, D.E. Edmondson, et al (1994) "Mechanism of Assembly of the Tyrosyl Radical-Diiron(111) Cofactor of E. Coli Ribonucleotide Reductase. 1. Mossbauer Characterization of the Diferric Radical Precursor". *J Am Chem SOC*, 116:8007–8014

[99] S. Oellerich, E. Bill, and P. Hildebrandt (2000) "Freeze-Quench Resonance Raman and Electron Paramagnetic Resonance Spectroscopy for Studying Enzyme Kinetics: Application to Azide Binding to Myoglobin". *Applied Spectroscopy*, 54:1480–1484

[100] M. Tanaka, K. Matsuura, S. Yoshioka, S. Takahashi, K. Ishimori, et al (2003) "Activation of hydrogen peroxide in horseradish peroxidase occurs within ~200 μs observed by a new freeze-quench device". *Biophysical Journal*, 84:1998–2004

[101] Y. Lin, G.J. Gerfen, D.L. Rousseau, and S.R. Yeh (2003) "Ultrafast Microfluidic Mixer and Freeze-Quenching Device". *Analytical Chemistry*, 75:5381–5386

[102] A. v. Cherepanov and S. de Vries (2004) "Microsecond freeze-hyperquenching: Development of a new ultrafast micro-mixing and sampling technology and application to enzyme catalysis". *Biochimica et Biophysica Acta - Bioenergetics*, 1656:1–31

[103] V. Schünemann, F. Lendzian, C. Jung, J. Contzen, A.L. Barra, et al (2004) "Tyrosine radical formation in the reaction of wild type and mutant cytochrome P450cam with peroxy acids: A multifrequency EPR study of intermediates on the millisecond time scale". *Journal of Biological Chemistry*, 279:10919–10930

[104] J. Manzerova, V. Krymov, and G.J. Gerfen (2011) "Investigating the intermediates in the reaction of ribonucleoside triphosphate reductase from

Lactobacillus leichmannii: An application of HF EPR-RFQ technology". *Journal of Magnetic Resonance*, 213:32–45

[105] R. Kaufmann, I. Yadid, and D. Goldfarb (2013) "A novel microfluidic rapid freeze-quench device for trapping reactions intermediates for high field EPR analysis". *Journal of Magnetic Resonance*, 230:220–226

[106] BioLogic "Mix & Freeze accessory For SFM-X000 user's manual v. 1.6"

[107] R. Pievo, B. Angerstein, A.J. Fielding, C. Koch, I. Feussner, et al (2013) "A rapid freeze-quench setup for multi-frequency EPR spectroscopy of enzymatic reactions". *ChemPhysChem*, 14:4094–4101

[108] F. Nami, P. Gast, and E.J.J. Groenen (2016) "Rapid Freeze-Quench EPR Spectroscopy: Improved Collection of Frozen Particles". *Applied Magnetic Resonance*, 47:643–653

[109] U.T. Bornscheuer, G.W. Huisman, R.J. Kazlauskas, S. Lutz, J.C. Moore, et al (2012) "Engineering the third wave of biocatalysis". *Nature*, 485:185–194

[110] S. Wenda, S. Illner, A. Mell, and U. Kragl (2011) "Industrial biotechnology—the future of green chemistry?". *Green Chemistry*, 13:3007–3047

[111] M. Paoli, J. Marles-Wright, and A. Smith (2002) "Structure-Function Relationships in Heme-Proteins". *DNA AND CELL BIOLOGY*, 21:271–280

[112] R.A. Marcus (1956) "On the theory of oxidation-reduction reactions involving electron transfer". *The Journal of Chemical Physics*, 24:966–978

[113] S.K. Chapman, S. Daft, and A.W. Munro (1997) "Heme: The Most Versatile Redox Centre in Biology?". In: "Structure and Bonding". Springer Verlag Berlin Heidelberg

[114] T.L. Poulos (2014) "Heme enzyme structure and function". *Chemical Reviews*, 114:3919–3962

[115] I. Serra, D. Schmidt, V. Pfanzagl, G. Mlynek, S. Hofbauer, et al (2022) "Impact of the dynamics of the catalytic arginine on nitrite and chlorite binding by dimeric chlorite dismutase". *Journal of Inorganic Biochemistry*, 227:111689

[116] P.C.E. Moody and E.L. Raven (2018) "The Nature and Reactivity of Ferryl Heme in Compounds I and II". *Accounts of Chemical Research*, 51:427–435

[117] P. Atkins and T. Overton (2009) "Shriver & Atkins' Inorganic Chemistry", 5th ed. Oxford University Press

[118] F. Trandafir, P. Heerdt, M. Fittipaldp, E. Vinck, S. Dewilde, et al (2007) "Applied Magnetic Resonance Studying High-Spin Ferric Heme Proteins by Pulsed EPR Spectroscopy: Analysis of the Ferric Form of the E7Q Mutant of Human Neuroglobin". *Applied Magnetic Resonance*, 31:553–572

[119] W.R. Hagen (2006) "EPR spectroscopy as a probe of metal centres in biological systems". *Dalton Transactions*, 4415–4434

[120] Hendrich Michael P and Debrunner Peter G (1988) "EPR Spectra of Quintet Ferrous Myoglobin and a Model Heme Compound". *Journal of Magnetic Resonance*, 78:133–141

[121] M.P. Hendrich and P.G. Debrunner (1989) "Integer-spin electron paramagnetic resonance of iron proteins". *Biophysical Journal*, 56:489–506

[122] P.J. Alonso, J.I. Martínez, and I. García-Rubio (2007) "The study of the ground state Kramers doublet of low-spin heminic system revisited. A comprehensive description of the EPR and Mössbauer spectra". *Coordination Chemistry Reviews*, 251:12–24

[123] C.P.S. Taylor (1977) "The EPR of low spin heme complexes Relation of the τ2g hole model to the directional properties of the g tensor, and a new method for calculating the ligand field parameters". *BBA - Protein Structure*, 491:137–148

[124] W.E. Blumberg and J. Peisach (1971) "Low—Spin Compounds of Heme Proteins". In: "Bioinorganic Chemistry". American Chemical Society, Washington DC, pp 271–291

[125] C. Aldag, I.A. Gromov, I. García-Rubio, K. von Koenig, I. Schlichting, et al (2009) "Probing the role of the proximal heme ligand in cytochrome P450cam by recombinant incorporation of selenocysteine". *Proceedings of the National Academy of Sciences of the United States of America*, 106:5481–5486

[126] G. Zoppellaro, K.L. Bren, A.A. Ensign, E. Harbitz, R. Kaur, et al (2009) "Studies of ferric heme proteins with highly anisotropic/highly axial low spin (S = 1/2) electron paramagnetic resonance signals with bis-histidine and histidine-methionine axial iron coordination". *Biopolymers - Peptide Science Section*, 91:1064–1082

[127] E.L. Raven and B. Dunford (2016) "Heme peroxidases". Royal Society of Chemistry, Cambridge

[128] X. Huang and J.T. Groves (2018) "Oxygen Activation and Radical Transformations in Heme Proteins and Metalloporphyrins". *Chemical Reviews*, 118:2491–2553

[129] R. Rutter, L.P. Hager, H. Dhonau, M. Hendrich, M. Valentine, et al (1984) "Chloroperoxidase Compound I: Electron Paramagnetic Resonance and Mössbauer Studies". *Biochemistry*, 23:6809–6816

[130] C.E. Schulz, P.W. Devaney, H. Winkler+, P.G. Debrunner, N. Doan, et al (1979) "Horseradish peroxidase Compound I: Evidence for spin coupling between the heme iron and a “free” radical". *FEBS Letters*, 103:102–105

[131] J. Rittle and M.T. Green (2010) "Cytochrome P450 Compound I: Capture, Characterization, and C-H Bond Activation Kinetics". *Science*, 330:933–937

[132] A. Bencini and D. Gatteschi (1990) "Electron Paramagnetic Resonance of Exchange Coupled Systems". Springer-Verlag

[133] J.C. Schöneboom, F. Neese, and W. Thiel (2005) "Toward identification of the compound I reactive intermediate in cytochrome P450 chemistry: A QM/MM study of its EPR and mössbauer parameters". *Journal of the American Chemical Society*, 127:5840–5853

[134] B.J. Lawrence, S.S. Eaton, and G.R. Eaton (2006) "Distance Measurements in Biological Systems by EPR". Springer US, Boston

[135] A.L.P. Houseman, P.E. Doan, D.B. Goodin, and B.M. Hoffman (1993) "Comprehensive Explanation of the Anomalous EPR Spectra of Wild-Type and Mutant Cytochrome c Peroxidase Compound ES". *Biochemistry*, 32:4430–4443

[136] K.D. Miner, T.D. Pfister, P. Hosseinzadeh, N. Karaduman, L.J. Donald, et al (2014) "Identifying the elusive sites of tyrosyl radicals in cytochrome c peroxidase: Implications for oxidation of substrates bound at a site remote from the heme". *Biochemistry*, 53:3781–3789

[137] F.J. Ruiz-Dueñas, R. Pogni, M. Morales, S. Giansanti, M.J. Mate, et al (2009) "Protein radicals in fungal versatile peroxidase: Catalytic tryptophan radical in both compound I and compound II and studies on W164Y, W164H, and W164S variants". *Journal of Biological Chemistry*, 284:7986–7994

[138] D. Dolphin (1978) "The porphyrins", 7th ed. Elsevier

[139] M. Alfonso-Prieto, P. Vidossich, and C. Rovira (2012) "The reaction mechanisms of heme catalases: An atomistic view by ab initio molecular dynamics". *Archives of Biochemistry and Biophysics*, 525:121–130

[140] S.H. Kim, R. Perera, L.P. Hager, J.H. Dawson, and B.M. Hoffman (2006) "Rapid freeze-quench ENDOR study of chloroperoxidase compound I: The site of the radical". *Journal of the American Chemical Society*, 128:5598–5599

[141] R. Davydov, T.M. Makris, V. Kofman, D.E. Werst, S.G. Sligar, et al (2001) "Hydroxylation of camphor by reduced oxy-cytochrome p450cam: Mechanistic implications of EPR and ENDOR studies of catalytic intermediates in native and mutant enzymes". *Journal of the American Chemical Society*, 123:1403–1415

[142] M.J. Benecky, J.E. Frew, N. Scowen, P. Jones, and B.M. Hoffman (1993) "EPR and ENDOR Detection of Compound I from Micrococcus lysodeikticus Catalase1". *Biochemistry*, 32:11929–11933

[143] J.E. Roberts, B.M. Hoffman, R. Rutter, and L.P. Hager (1981) "Electron-Nuclear Double Resonance of Horseradish Peroxidase Compound I". *The Journal of Biological Chemistry*, 256:2118–2121

[144] J.E. Roberts and B.M. Hoffman (1981) "17O ENDOR of Horseradish Peroxidase Compound I". *Journal of American Chemical Society*, 103:7654

[145] R. Pogni, C. Teutloff, F. Lendzian, and R. Basosi (2007) "Applied Magnetic Resonance Tryptophan Radicals as Reaction Intermediates in Versatile Peroxidases: Multifrequency EPR, ENDOR and Density Functional Theory Studies". *Appl Magn Reson*, 31:509–526

[146] C. Bernini, R. Pogni, F.J. Ruiz-Dueñas, A.T. Martínez, R. Basosi, et al (2011) "EPR parameters of amino acid radicals in P. eryngii versatile peroxidase and its W164Y variant computed at the QM/MM level". *Physical Chemistry Chemical Physics*, 13:5078–5098

[147] S. Hofbauer, M. Bellei, A. Sündermann, K.F. Pirker, A. Hagmüller, et al (2012) "Redox thermodynamics of high-spin and low-spin forms of chlorite dismutases with diverse subunit and oligomeric structures". *Biochemistry*, 51:9501–9512

[148] A.I. Celis, Z. Geeraerts, D. Ngmenterebo, M.M. Machovina, R.C. Kurker, et al (2015) "A dimeric chlorite dismutase exhibits O2-generating activity and acts as a chlorite antioxidant in Klebsiella pneumoniae MGH 78578". *Biochemistry*, 54:434–446

[149] Z. Geeraerts, O.R. Stiller, G.S. Lukat-Rodgers, and K.R. Rodgers (2022) "Roles of High-Valent Hemes and pH Dependence in Halite Decomposition Catalyzed by Chlorite Dismutase from *Dechloromonas aromatica*". *ACS Catalysis*, 12:8641–8657

[150] D. Schmidt, N. Falb, I. Serra, M. Bellei, V. Pfanzagl, et al (2023) "Compound I Formation and Reactivity in Dimeric Chlorite Dismutase: Impact of pH and the Dynamics of the Catalytic Arginine". *Biochemistry*, 62:835–850

[151] J. Püschmann, D. Mahor, D.C. de Geus, M.J.F. Strampraad, B. Srour, et al (2021) "Unique Biradical Intermediate in the Mechanism of the Heme Enzyme Chlorite Dismutase". *ACS Catalysis*, 11:14533–14544

[152] M. Tamura and H. Hiroshi (1972) "Optical and magnetic measurements of horseradish peroxidase III. Electron Paramagnetic Resonance studies at liquid-hydrogen and liquid-helium temperatures". *Biochimica et biophysica acta*, 284:20–29

[153] G.R. Schonbaum (1973) "New Complexes of Peroxidases with Hydroxamic Acids, Hydrazides, and Amides". *The Journal of Biological Chemistry*, 248:502–511

[154] J.S. Leigh, M.M. Maltempo, P.I. Ohlsson, and K.G. Paul (1975) "Optical, NMR and EPR properties of horseradish peroxidase and its donor complexes". *FEBS Letters*, 51:304–308

[155] M.M. Maltempo, P.I. Ohlsson, K.G. Paul, L. Petersson, and A. Ehrenberg (1979) "Electron Paramagnetic Resonance Analyses of Horseradish Peroxidase in Situ and after Purification?". *ACS Biochemistry*, 18:2935–2941

[156] B.D. Howes, C.B. Schiødt, K.G. Welinder, M.P. Marzocchi, J.G. Ma, et al (1999) "The quantum mixed-spin heme state of barley peroxidase: A paradigm for class III peroxidases". *Biophysical Journal*, 77:478–492

[157] J.N. Roberts, R. Singh, J.C. Grigg, M.E.P. Murphy, T.D.H. Bugg, et al (2011) "Characterization of dye-decolorizing peroxidases from rhodococcus jostii RHA1". *Biochemistry*, 50:5108–5119

[158] D. Linde, R. Pogni, M. Cañellas, F. Lucas, V. Guallar, et al (2015) "Catalytic surface radical in dye-decolorizing peroxidase: A computational, spectroscopic and site-directed mutagenesis study". *Biochemical Journal*, 466:253–262

[159] A. Rai, J.P. Klare, P.Y.A. Reinke, F. Englmaier, J. Fohrer, et al (2021) "Structural and biochemical characterization of a dye-decolorizing peroxidase from dictyostelium discoideum". *International Journal of Molecular Sciences*, 22:6265

[160] E. Strittmatter, K. Serrer, C. Liers, R. Ullrich, M. Hofrichter, et al (2015) "The toolbox of Auricularia auricula-judae dye-decolorizing peroxidase - Identification of three new potential substrate-interaction sites". *Archives of Biochemistry and Biophysics*, 574:75–85

[161] M.C. Baratto, A. Sinicropi, D. Linde, V. Sáez-Jiménez, L. Sorace, et al (2015) "Redox-Active Sites in Auricularia auricula-judae Dye-Decolorizing Peroxidase and Several Directed Variants: A Multifrequency EPR Study". *Journal of Physical Chemistry B*, 119:13583–13592

[162] R. Shrestha, X. Chen, K.X. Ramyar, Z. Hayati, E.A. Carlson, et al (2016) "Identification of surface-Exposed protein radicals and a substrate oxidation site in a-Class dye-Decolorizing peroxidase from thermomonospora curvata". *ACS Catalysis*, 6:8036–8047

[163] L. Li, T. Wang, T. Chen, W. Huang, Y. Zhang, et al (2021) "Revealing two important tryptophan residues with completely different roles in a dye-decolorizing peroxidase from Irpex lacteus F17". *Biotechnology for Biofuels*, 14:128

[164] W.B. Mims and J. Peisach (1981) "Electron Spin Echo Spectroscopy and the Study of Metalloproteins". In: Berliner LJ, Reuben J (eds) "Biological Magnetic Resonance". Plenum Press, New York, pp 213–263

[165] J. Dubochet, M. Adrian, J.-J. Chang, J. Lepault, and A.W. McDowall (1987) "Cryoelectron Microscopy of Vitrified Specimens". In: "Cryotechniques in Biological Electron Microscopy". pp 114–131

[166] P. Brüggeller and E. Mayer (1980) "Complete vitrification in pure liquid water and dilute aqueous solutions". *Nature*, 288:569–571

[167] D. Russell S. (1992) "Physical methods for chemists", 2nd ed. Scientific Publishers

[168] A.R. Bizzarri and S. Cannistraro (1993) "Solvent modulation of the structural heterogeneity in FeIII myoglobin samples: a low temperature EPR investigation". *European Biophysics Journal*, 22:259–267

[169] J.R. Brender, S. Kishimoto, G.R. Eaton, S.S. Eaton, Y. Saida, et al (2021) "Trehalose as an alternative to glycerol as a glassing agent for in vivo DNP MRI". *Magnetic Resonance in Medicine*, 85:42–48

[170] P.M.A. Gadsby, J. Peterson, N. Foote, C. Greenwood, and A.J. Thomson (1987) "Identification of the ligand-exchange process in the alkaline transition of horse heart cytochrome c". *Biochemical Journal*, 246:43–54

[171] T. Yonetani and H. Anni (1987) "Yeast cytochrome c peroxidase. Coordination and spin states of heme prosthetic group.". *Journal of Biological Chemistry*, 262:9547–9554

[172] G. Smulevich, A.R. Mantini, A.M. English, and J.M. Mauro (1989) "Effects of Temperature and Glycerol on the Resonance Raman Spectra of Cytochrome c Peroxidase and Selected Mutants". *Biochemistry*, 28:5058–5064

[173] J.H.A. Nugent (2001) "Photoreducible high spin iron electron paramagnetic resonance signals in dark-adapted Photosystem II: are they oxidised non-haem iron formed from interaction of oxygen with PSII electron acceptors?". *Biochimica et Biophysica Acta*, 1504:288–298

[174] C.J. Halkides, C.T. Farrar, and D.J. Singel (1998) "The Effects of Cryoprotection on the Structure and Activity of p21 ras: Implications for Electron Spin-Echo Envelope Modulation Spectroscopy". *Journal of Magnetic Resonance*, 134:142–153

[175] E.R. Georgieva, A.S. Roy, V.M. Grigoryants, P.P. Borbat, K.A. Earle, et al (2012) "Effect of freezing conditions on distances and their distributions derived from Double Electron Electron Resonance (DEER): A study of doubly-spin-labeled T4 lysozyme". *Journal of Magnetic Resonance*, 216:69–77

[176] C.G. Hoogstraten and R. David Britt (2002) "Water counting: Quantitating the hydration level of paramagnetic metal ions bound to nucleotides and nucleic acids". *RNA*, 8:252–260

[177] B. Garcia-Moreno (2009) "Adaptations of proteins to cellular and subcellular pH". *Journal of Biology*, 8:98

[178] D.A. Svistunenko, M.A. Sharpe, P. Nicholls, C. Blenkinsop, N.A. Davies, et al (2000) "The pH dependence of naturally occurring low-spin forms of methaemoglobin and metmyoglobin: An EPR study". *Biochemical Journal*, 351:595–605

[179] F.P. Nicoletti, J.P. Bustamante, E. Droghetti, B.D. Howes, M. Fittipaldi, et al (2014) "Interplay of the H-bond donor-acceptor role of the distal residues in hydroxyl ligand stabilization of Thermobifida fusca truncated hemoglobin". *Biochemistry*, 53:8021–8030

[180] D.L. Brautigan, B.A. Feinberg, B.M. Hoffman, E. Margoliash, J. Peisach, et al (1977) "Multiple low spin forms of the cytochrome c ferrihemochrome". *The Journal of biological chemistry*, 252:574–582

[181] B.R. Streit, B. Blanc, G.S. Lukat-Rodgers, K.R. Rodgers, and J.L. Dubois (2010) "How active-site protonation state influences the reactivity and ligation of the heme in chlorite dismutase". *Journal of the American Chemical Society*, 132:5711–5724

[182] P. George and G. Hanania (1952) "The ionization of acidic metmyoglobin.". *The Biochemical journal*, 52:517–523

[183] M. Brunori, G. Amiconi, E. Antonini, J. Wyman, R. Zito, et al (1968) "The transition between “acid” and “alkaline” ferric heme proteins". *Biochimica et Biophysica Acta (BBA) - Protein Structure*, 154:315–322

[184] D.A. Svistunenko, B.J. Reeder, M.M. Wankasi, R.L. Silaghi-Dumitrescu, C.E. Cooper, et al (2007) "Reaction of Aplysia limacina metmyoglobin with hydrogen peroxide". *Dalton Transactions*, 840–850

[185] O. Baffa, O.R. Nascimento, and M. Tabak (1985) "The acid-alkaline transition of a sea turtle myoglobin: coexistence at high pH of high- and low-spin forms". *Biochimica et Biophysica Acta (BBA) - Protein Structure*, 832:63–68

[186] W.J. Bowen (1949) "The absorption spectra and extinction coefficients of myoglobin". *The Journal of Biological Chemistry*, 179:235–245

[187] E. Antonini and M. Brunori (1972) "Hemoglobin and Myoglobin in Their Reactions with Ligands". North-Holland publishing Co., Amsterdam, The Netherlands

[188] S. Stoll and A. Schweiger (2006) "EasySpin, a comprehensive software package for spectral simulation and analysis in EPR". *Journal of Magnetic Resonance*, 178:42–55

[189] L. Tofani, A. Feis, R.E. Snoke, D. Berti, P. Baglioni, et al (2004) "Spectroscopic and interfacial properties of myoglobin/surfactant complexes". *Biophysical Journal*, 87:1186–1195

[190] W.A. Eaton and R.M. Hochstrasser (1968) "Single-crystal spectra of ferrimyoglobin complexes in polarized light". *The Journal of Chemical Physics*, 49:985–995

[191] A.Z. Halimehjani, H. Gholami, and M.R. Saidi (2012) "Boric acid/glycerol as an efficient catalyst for regioselective epoxide ring opening by aromatic amines in water". *Green Chemistry Letters and Reviews*, 5:1–5

[192] C. Mukhopadhyay, A. Datta, and R.J. Butcher (2009) "Highly efficient one-pot, three-component Mannich reaction catalysed by boric acid and glycerol in water with major “syn” diastereoselectivity". *Tetrahedron Letters*, 50:4246–4250

[193] Y. Orii and M. Morita (1977) "Measurement of the pH of Frozen Buffer Solutions by Using pH Indicators". *Journal of Biochemistry*, 81:163–168

[194] D.L. Williams-Smith, R.C. Bray, M.J. Barber, A.D. Tsopanakis, and S.P. Vincent (1977) "Changes in Apparent pH on Freezing Aqueous Buffer Solutions and their Relevance to Biochemical Electron-Paramagnetic-Resonance Spectroscopy"

[195] N. Le Breton, J.J. Wright, A.J.Y. Jones, E. Salvadori, H.R. Bridges, et al (2017) "Using Hyperfine Electron Paramagnetic Resonance Spectroscopy to Define the Proton-Coupled Electron Transfer Reaction at Fe-S Cluster N2 in Respiratory Complex i". *Journal of the American Chemical Society*, 139:16319–16326

[196] L. Veselý, B. Susrisweta, and D. Heger (2021) "Making good’s buffers good for freezing: The acidity changes and their elimination via mixing with sodium phosphate". *International Journal of Pharmaceutics*, 593:120128

[197] M.J. O’Neil (2013) "The Merck index : an encyclopedia of chemicals, drugs, and biologicals.", 15th ed. Royal Society of Chemistry

[198] D. Schubert (2011) "Kirk-Othmer Encyclopedia of Chemical Technology". Wiley, New York

[199] P. Bernal-Bayard, L. Puerto-Galán, I. Yruela, I. García-Rubio, C. Castell, et al (2017) "The photosynthetic cytochrome c 550 from the diatom Phaeodactylum tricornutum". *Photosynthesis Research*, 133:273–287

[200] I. Schaffner, S. Hofbauer, M. Krutzler, K.F. Pirker, P.G. Furtmüller, et al (2015) "Mechanism of chlorite degradation to chloride and dioxygen by the enzyme chlorite dismutase". Arch Biochem Biophys 574:18–26

[201] D. Schmidt, I. Serra, G. Mlynek, V. Pfanzagl, S. Hofbauer, et al (2021) "Arresting the Catalytic Arginine in Chlorite Dismutases: Impact on Heme Coordination, Thermal Stability, and Catalysis". *Biochemistry*, 60:621–634

[202] S. Hofbauer, K. Gysel, G. Mlynek, J. Kostan, A. Hagmüller, et al (2012) "Impact of subunit and oligomeric structure on the thermal and conformational stability of chlorite dismutases". *Biochimica et Biophysica Acta - Proteins and Proteomics*, 1824:1031–1038

[203] T. Yonetani, D.F. Wilson, and B. Seamonds (1966) "Studies on Cytochrome c Peroxidase". *Biological Chemistry*, 241:5347–5352

[204] B.A. Wittenberg, L. Kampa, J.B. Wittenberg, W.E. Blumberg, and J. Peisach (1968) "The Electronic Structure of Protoheme Proteins. An electron paramagnetic resonance and optical study of cytochrome c peroxidase and its derivatives". *Journal of Biological Chemistry*, 243:1863–1870

[205] L. Tilleman, F. Germani, S. de Henau, S. Helbo, F. Desmet, et al (2015) "A globin domain in a neuronal transmembrane receptor of Caenorhabditis elegans and Ascaris suum: Molecular modeling and functional properties". *Journal of Biological Chemistry*, 290:10336–10352

[206] F.P. Nicoletti, E. Droghetti, B.D. Howes, J.P. Bustamante, A. Bonamore, et al (2013) "H-bonding networks of the distal residues and water molecules in the active site of Thermobifida fusca hemoglobin". *Biochimica et Biophysica Acta - Proteins and Proteomics*, 1834:1901–1909

[207] W.E. Blumberg (1981) "The study of hemoglobin by electron paramagnetic resonance spectroscopy". In: "Methods in Enzymology". pp 312–329

[208] H. Danielsson Thorell, N.H. Beyer, N.H.H. Heegaard, M.O.¨ Hman, and T. Nilsson (2004) "Comparison of native and recombinant chlorite dismutase from Ideonella dechloratans". *European Journal of Biochemistry*, 271:3539–3546

[209] S. Van Doorslaer, M. van den Bosch, L. Tilleman, and S. Dewilde (2015) "EPR Analysis of Imidazole Binding to Methanosarcina acetivorans Protoglobin". *Applied Magnetic Resonance*, 46:421–433

[210] D.M. Freire, M.G. Rivas, A.M. Dias, A.T. Lopes, C. Costa, et al (2015) "The homopentameric chlorite dismutase from Magnetospirillum sp.". *Journal of Inorganic Biochemistry*, 151:1–9

[211] A. Sündermann, M.M. Reif, S. Hofbauer, C. Obinger, and C. Oostenbrink (2014) "Investigation of ion binding in chlorite dismutases by means of molecular dynamics simulations". *Biochemistry*, 53:4869–4879

[212] J.O. Lundberg, E. Weitzberg, and M.T. Gladwin (2008) "The nitrate-nitrite-nitric oxide pathway in physiology and therapeutics". Nat Rev Drug Discov 7:156–167

[213] J.S. Griffith and L.E. Orgel (1957) "Ligand-field theory". *Quarterly Reviews, Chemical Society*, 11:381–393

[214] R. Sgammato, N. Van Brempt, R. Aerts, S. Van Doorslaer, S. Dewilde, et al (2023) " Interaction of nitrite with ferric protoglobin from Methanosarcina acetivorans – an interesting model for spectroscopic studies of the haem–ligand interaction ". *Dalton Transactions*, 52:2976–2987

[215] L.J. Young and L.M. Siegel (1988) "On the reaction of ferric heme proteins with nitrite and sulfite". *Biochemistry*, 27:2790–2800

[216] R. Silaghi-Dumitrescu, D.A. Svistunenko, D. Cioloboc, C. Bischin, F. Scurtu, et al (2014) "Nitrite binding to globins: Linkage isomerism, EPR silence and reductive chemistry". *Nitric Oxide - Biology and Chemistry*, 42:32–39

[217] C. He, H. Ogata, and M. Knipp (2010) "Formation of the complex of nitrite with the ferriheme b β-barrel proteins nitrophorin 4 and nitrophorin 7". *Biochemistry*, 49:5841–5851

[218] C. He, H. Ogata, and W. Lubitz (2016) "Elucidation of the heme active site electronic structure affecting the unprecedented nitrite dismutase activity of the ferriheme b proteins, the nitrophorins". *Chemical Science*, 7:5332–5340

[219] B.I. Goetz, H.W. Shields, S. Basu, P. Wang, S.B. King, et al (2010) "An electron paramagnetic resonance study of the affinity of nitrite for methemoglobin". *Nitric Oxide - Biology and Chemistry*, 22:149–154

[220] J. Yi, M.K. Safo, and G.B. Richter-Addo (2008) "The nitrite anion binds to human hemoglobin via the uncommon O-nitrito mode". *Biochemistry*, 47:8247–8249

[221] D.E. Schwab, J.S. Stamler, and D.J. Singel (2010) "EPR spectroscopy of nitrite complexes of methemoglobin". *Inorganic Chemistry*, 49:6330–6337

[222] M. Ubbink, A.P. Campos, M. Teixeira, N.I. Hunt, H.A.O. Hill, et al (1994) "Characterization of mutant Met100Lys of cytochrome c-550 from Thiobacillus versutus with lysine-histidine heme ligation.". *Biochemistry*, 33:10051–10059

[223] G.G. Silkstone, C.E. Cooper, D. Svistunenko, and M.T. Wilson (2005) "EPR and optical spectroscopic studies of Met80X mutants of yeast ferricytochrome c. models for intermediates in the alkaline transition". *Journal of the American Chemical Society*, 127:92–99

[224] F.I. Rosell, J.C. Ferrer, and A. Grant Mauk (1936) "Proton-Linked Protein Conformational Switching: Definition of the Alkaline Conformational Transition of Yeast Iso-1-ferricytochrome c". *Journal of American Society*, 285:11234–11245

[225] E.A. Johnson, M.M. Russo, D.B. Nye, J.L. Schlessman, and J.T.J. Lecomte (2018) "Lysine as a heme iron ligand: A property common to three truncated hemoglobins from Chlamydomonas reinhardtii". *Biochimica et Biophysica Acta - General Subjects*, 1862:2660–2673

[226] J.E. Martinez Grundman, L. Julió Plana, J.L. Schlessman, L. Capece, D.A. Estrin, et al (2021) "Control of distal lysine coordination in a monomeric hemoglobin: A role for heme peripheral interactions". *Journal of Inorganic Biochemistry*, 219:111437

[227] A. Butler and J. Moffett (2009) "Saltpetre in early and medieval Chinese medicine". *Asian Medicine*, 5:173–185

[228] L.B. Maia and J.J.G. Moura (2014) "How biology handles nitrite". *Chemical Reviews*, 114:5273–5357

[229] A. Dejam, C.J. Hunter, A.N. Schechter, and M.T. Gladwin (2004) "Emerging role of nitrite in human biology". *Blood Cells, Molecules, and Diseases*, 32:423–429

[230] M.T. Gladwin, A.N. Schechter, D.B. Kim-Shapiro, R.P. Patel, N. Hogg, et al (2006) "The emerging biology of the nitrite anion". *Nature Chemical Biology*, 1:308–314

[231] R. SoRelle (1998) "Nobel Prize Awarded to Scientists for Nitric Oxide Discoveries". *Circulation*, 98:2365–2366

[232] K. Cosby, K.S. Partovi, J.H. Crawford, R.P. Patel, C.D. Reiter, et al (2003) "Nitrite reduction to nitric oxide by deoxyhemoglobin vasodilates the human circulation". *Nature Medicine*, 9:1498–1505

[233] M.T. Gladwin and D.B. Kim-Shapiro (2008) "The functional nitrite reductase activity of the heme-globins". *Blood*, 112:2636–2647

[234] T.M. Millar, C.R. Stevens, N. Benjamin, R. Eisenthal, R. Harrison, et al (1998) "Xanthine oxidoreductase catalyses the reduction of nitrates and nitrite to nitric oxide under hypoxic conditions". *FEBS Letters*, 427:225–228

[235] M.L. Brennan, W. Wu, X. Fu, Z. Shen, W. Song, et al (2002) "A tale of two controversies. Defining both the role of peroxidases in nitrotyrosine formation in vivo using eosinophil peroxidase and myeloperoxidase-deficient mice, and the nature of peroxidase-generated reactive nitrogen species". *Journal of Biological Chemistry*, 277:17415–17427

[236] J.P. Eiserich, M. Hristova, C.E. Cross, A. Daniel Jones, B. Freeman, et al (1998) "Formation of nitric oxide-derived inflammatory oxidants by myeloperoxidase in neutrophils". *Nature*, 391:393–397

[237] O. Einsle, A. Messerschmidt, P. Stach, G.P. Bourenkov, H.D. Bartunik, et al (1999) "Structure of cytochrome c nitrite reductase". *Nature*, 400:476–480

[238] S. Nakano, M. Takahashi, A. Sakamoto, H. Morikawa, and K. Katayanagi (2012) "X-ray crystal structure of a mutant assimilatory nitrite reductase that shows sulfite reductase-like activity". *Chemistry and Biodiversity*, 9:1989–1999

[239] F.A. Walker (2005) "Nitric oxide interaction with insect nitrophorins and thoughts on the electron configuration of the {FeNO}6 complex". *Journal of Inorganic Biochemistry*, 99:216–236

[240] D.E. Champagne, R.H. Nussenzveig, and J.M.C. Ribeiro (1995) "Purification, Partial Characterization, and Cloning of Nitric Oxide-carrying Heme Proteins (Nitrophorins) from Salivary Glands of the Blood-sucking Insect Rhodnius prolixus*". *The Journal of Biological Chemistry*, 270:8691–8695

[241] C. He, H. Ogata, and M. Knipp (2012) "Insertion of an H-Bonding Residue into the Distal Pocket of the Ferriheme Protein Nitrophorin 4: Effect on Nitrite-Iron Coordination and Nitrite Disproportionation". *Chemistry and Biodiversity*, 9:1761–1775

[242] J.L. Zweier, A. Samouilov, and P. Kuppusamy (1999) "Non-enzymatic nitric oxide synthesis in biological systems". *Biochimica et biophysica acta*, 1411:250–262

[243] P. Ascenzi, A. Pesce, M. Nardini, M. Bolognesi, C. Ciaccio, et al (2013) "Reductive nitrosylation of Methanosarcina acetivorans protoglobin: A comparative study". *Biochemical and Biophysical Research Communications*, 430:1301–1305

[244] N. Van Brempt, R. Sgammato, Q. Beirinckx, D. Hammerschmid, F. Sobott, et al (2023) "The effect of pH and nitrite on the haem pocket of GLB-33, a globin-coupled neuronal transmembrane receptor of Caenorhabditis elegans". *Biochimica et Biophysica Acta (Proteins and Proteomics)*, 1871:140913

[245] L. Tilleman, F. Germani, S. De Henau, S. Helbo, F. Desmet, et al (2015) "A globin domain in a neuronal transmembrane receptor of Caenorhabditis elegans and Ascaris suum: Molecular modeling and functional properties". *Journal of Biological Chemistry*, 290:10336–10352

[246] A. (Arthur) Schweiger and Gunnar. Jeschke (2001) "Principles of pulse electron paramagnetic resonance". Oxford University Press

[247] E. Vinck and S. Van Doorslaer (2004) "Analysing low-spin ferric complexes using pulse EPR techniques: A structure determination of bis (4-methylimidazole) (tetraphenylporphyrinato)iron(III)". *Physical Chemistry Chemical Physics*, 6:5324–5330

[248] I. García-Rubio, J.I. Martínez, R. Picorel, I. Yruela, and P.J. Alonso (2003) "HYSCORE Spectroscopy in the Cytochrome b559 of the Photosystem II Reaction Center". *Journal of the American Chemical Society*, 125:15846–15854

[249] S. Van Doorslaer, M. van den Bosch, L. Tilleman, and S. Dewilde (2015) "EPR Analysis of Imidazole Binding to Methanosarcina acetivorans Protoglobin". *Applied Magnetic Resonance*, 46:421–433

[250] C.P. Scholes, K.M. Falkowski, S. Chen, and J. Bank (1986) "Electron Nuclear Double Resonance (ENDOR) of Bis(imidazole)-Ligated Low-Spin Ferric Heme Systems". *Journal of American Chemical Society*, 108:1660–1671

[251] C.F. Mulks, C.P. Scholes, L.L.C. Dickinson, and A. Lapidot (1979) "Electron Nuclear Double Resonance from High-and Low-Spin Ferric Hemoglobins and Myoglobins". *Journal of he American Chemical Society*, 101:1645–1654

[252] R.S. Magliozzo and J. Peisacht (1993) "Evaluation of Nitrogen Nuclear Hyperfine and Quadrupole Coupling Parameters for the Proximal Imidazole in Myoglobin-Azide,-Cyanide, and-Mercaptoethanol Complexes by Electron Spin Echo Envelope Modulation Spectroscopy". *Biochemistry*, 32:8446–8456

[253] H.L. Flanagan and D.J. Singel (1987) "Analysis of 14N ESEEM patterns of randomly oriented solids". *The Journal of Chemical Physics*, 87:5606–5616

[254] R. Ikeda, M. Mikami, D. Nakamura, and M. Kubo (1969) "Nuclear Quadrupole Resonance of Nitrogen in Sodium Nitrite". *Journal of magnetic resonance*, 1:211–220

[255] J. Kubišta, D.A. Kolářová, V. Shestivska, K. Sovová, and P. Španěl (2020) "14N NQR Quantification of Sodium Nitrite and Urotropin Using Singular Spectrum Analysis (SSA) for Data Filtering". *Applied Magnetic Resonance*, 51:449–460

[256] A.I. Ioanitescu, S. Van Doorslaer, S. Dewilde, B. Endeward, and L. Moens (2007) "Probing the heme-pocket structure of the paramagnetic forms of cytoglobin and a distal histidine mutant using electron paramagnetic resonance". *Molecular Physics*, 105:2073–2086

[257] M. Sundararajan and F. Neese (2015) "Distal Histidine Modulates the Unusual O-Binding of Nitrite to Myoglobin: Evidence from the Quantum Chemical Analysis of EPR Parameters". *Inorganic Chemistry*, 54:7209–7217

[258] P.A. Williams, V. Fulop, E.F. Garman, N.F.W. Saunders, S.J. Ferguson, et al (1997) "Haem-ligand switching during catalysis in crystals of a nitrogen-cycle enzyme". *Letters to Nature*, 389:406–412

[259] O. Einsle, A. Messerschmidt, R. Huber, P.M.H. Kroneck, and F. Neese (2002) "Mechanism of the six-electron reduction of nitrite to ammonia by cytochrome c nitrite reductase". *Journal of the American Chemical Society*, 124:11737–11745

[260] K.M. Polyakov, K.M. Boyko, T. V. Tikhonova, A. Slutsky, A.N. Antipov, et al (2009) "High-Resolution Structural Analysis of a Novel Octaheme Cytochrome c Nitrite Reductase from the Haloalkaliphilic Bacterium Thioalkalivibrio nitratireducens". *Journal of Molecular Biology*, 389:846–862

[261] C.L. French, S. Yaun, L.A. Baldwin, D.A. Leonard, X.Q. Zhao, et al (1995) "Potency Ranking of Methemoglobin-forming Agents". *Journal of applied toxicology*, 15:167–174

[262] E.G. Hrycay, J.-&e Gustafsson, M. Ingelman-Sundberg, and L. Ernster (1975) "Sodium periodate, sodium chlorite, and organic hydroperoxides as hydroxylating agents in hepatic microsomal steroid hydroxylation reactions catalyzed by cytochrome P-450". *FEBS Letters*, 56:161–165

[263] C. Jakopitsch, H. Spalteholz, P.G. Furtmüller, J. Arnhold, and C. Obinger (2008) "Mechanism of reaction of horseradish peroxidase with chlorite and chlorine dioxide". *Journal of Inorganic Biochemistry*, 102:293–302

[264] C. Jakopitsch, K.F. Pirker, J. Flemmig, S. Hofbauer, D. Schlorke, et al (2014) "Mechanism of reaction of chlorite with mammalian heme peroxidases". *Journal of Inorganic Biochemistry*, 135:10–19

[265] J. Arnhold, E. Monzani, P.G. Furtmüller, M. Zederbauer, L. Casella, et al (2006) "Kinetics and thermodynamics of halide and nitrite oxidation by mammalian heme peroxidases". *European Journal of Inorganic Chemistry*, 3801–3811

[266] Paul Georg Furtmüller, Ursula Burner, Walter Jantschko, Günther Regelsberger, and Christian Obinger (2000) "The reactivity of myeloperoxidase compound I formed with hypochlorous acid". *Redox Report*, 5:173–178

[267] M. Bracci, S. Van Doorslaer, and I. García-Rubio (2020) "EPR of Compound I: An Illustrated Revision of the Theoretical Model". *Applied Magnetic Resonance*, 51:1559–1589

[268] C.A. McDowell, P. Raghunathan, and J.C. Tait (1973) "Electron spin resonance of chlorine dioxide in inert matrices at 4.2°K". *The Journal of Chemical Physics*, 59:5858–5867

[269] J.A.R. Coope, C.L. Gardner, C.A. McDowell, and A.I. Pelman (1971) "Electron spin resonance study of ClO2 and Cl2- adsorbed on zeolites". *Molecular Physics*, 21:1043–1055

[270] C.E.E. Schulz, P.W.W. Devaney, H. Winkler, P.G.G. Debrunner, N. Doan, et al (1979) "Horseradish peroxidase compound I: evidence for spin coupling between the heme iron and a “free” radical". *FEBS Letters*, 103:102–105

[271] A.K. Chaplin, T.M. Chicano, B. v. Hampshire, M.T. Wilson, M.A. Hough, et al (2019) "An Aromatic Dyad Motif in Dye Decolourising Peroxidases Has Implications for Free Radical Formation and Catalysis". *Chemistry - A European Journal*, 25:6141–6153

[272] W. Jantschko, P.G. Furtmüller, M. Allegra, M.A. Livrea, C. Jakopitsch, et al (2002) "Redox intermediates of plant and mammalian peroxidases: A comparative transient-kinetic study of their reactivity toward indole derivatives". *Archives of Biochemistry and Biophysics*, 398:12–22

[273] F. Lendzian (2005) "Structure and interactions of amino acid radicals in class I ribonucleotide reductase studied by ENDOR and high-field EPR spectroscopy". *Biochimica et Biophysica Acta - Bioenergetics*, 1707:67–90

[274] A. Ivancich, P. Dorlet, D.B. Goodin, and S. Un (2001) "Multifrequency high-field EPR study of the tryptophanyl and tyrosyl radical intermediates in wild-type and the W191G mutant of cytochrome c peroxidase". *Journal of the American Chemical Society*, 123:5050–5058

[275] A. Ivancich, C. Jakopitsch, M. Auer, S. Un, and C. Obinger (2003) "Protein-Based Radicals in the Catalase-Peroxidase of Synechocystis PCC6803: A Multifrequency EPR Investigation of Wild-Type and Variants on the Environment of the Heme Active Site". *Journal of American Chemical Society*, 125:14093–14102

[276] M.I. Awad, A. Denggerile, and T. Ohsaka (2004) "Electroreduction of Peroxyacetic Acid at Gold Electrode in Aqueous Media". *Journal of The Electrochemical Society*, 151:E358

[277] C.S. Furman and D.W. Margerum (1998) "Mechanism of Chlorine Dioxide and Chlorate Ion Formation from the Reaction of Hypobromous Acid and Chlorite Ion". *Inorganic Chemistry*, 37:4321–4327

[278] T. Chibata, T. Tosa, and T. Shibatani (1992) "The industrial production of optically active compounds by immobilized biocatalysts". In: Collins AN, Sheldrake GN, Crosby J (eds) "Chirality in industry - The commercial manufacture and application of optically active compounds". Wiley & sons Ltd, Chichester, England, pp 351–371

[279] R.A. Sheldon (2007) "Enzyme immobilization: The quest for optimum performance". *Advanced Synthesis and Catalysis*, 349:1289–1307

[280] R.P. Vaz and E.X.F. Filho (2019) "Ion Exchange Chromatography for Enzyme Immobilization". In: "Applications of Ion Exchange Materials in Biomedical Industries". Springer International Publishing, pp 13–27

[281] C. Huitron and J. Limon-Lason (1978) "Immobilization of Glucose Isomerase to Ion-Exchange Materials". *Biotechnology and Bioengineering*, 20:1377–1391

[282] C.Z. Guidini, J. Fischer, L.N.S. Santana, V.L. Cardoso, and E.J. Ribeiro (2010) "Immobilization of Aspergillus oryzae β-galactosidase in ion exchange resins by combined ionic-binding method and cross-linking". *Biochemical Engineering Journal*, 52:137–143

[283] D.I. Fried, F.J. Brieler, and M. Fröba (2013) "Designing Inorganic Porous Materials for Enzyme Adsorption and Applications in Biocatalysis". *ChemCatChem*, 5:862–884

[284] B.: Enzymatic, J.F. Diaz, and K.J. Balkus (1996) "Enzyme immobilization in MCM-41 molecular sieve". *Journal of Molecular Catalysis B: Enzymatic*, 2:11–126

[285] H. Takahashi, B. Li, T. Sasaki, C. Miyazaki, T. Kajino, et al (2000) "Catalytic activity in organic solvents and stability of immobilized enzymes depend on the pore size and surface characteristics of mesoporous silica". *Chemistry of Materials*, 12:3301–3305

[286] J. Aburto, M. Ayala, I. Bustos-Jaimes, C. Montiel, E. Terrés, et al (2005) "Stability and catalytic properties of chloroperoxidase immobilized on SBA-16 mesoporous materials". *Microporous and Mesoporous Materials*, 83:193–200

[287] W. Guo, H. Bi, L. Qiao, J. Wan, K. Qian, et al (2011) "Characterization of efficient proteolysis by trypsin loaded macroporous silica". *Molecular BioSystems*, 7:2890–2898

[288] J.M. Bolivar, J.M. Woodley, and R. Fernandez-Lafuente (2022) "Is enzyme immobilization a mature discipline? Some critical considerations to capitalize on the benefits of immobilization". *Chemical Society Reviews*, 51:6251–6290

[289] Z. Dai, X. Xu, L. Wu, and H. Ju (2005) "Detection of trace phenol based on mesoporous silica derived tyrosinase-peroxidase biosensor". *Electroanalysis*, 17:1571–1577

[290] V. Rahemi, S. Trashin, Z. Hafideddine, V. Meynen, S. Van Doorslaer, et al (2019) "Enzymatic sensor for phenols based on titanium dioxide generating surface confined ROS after treatment with H2O2". *Sensors and Actuators, B: Chemical*, 283:343–348

[291] C. Qiu, T. Chen, X. Wang, Y. Li, and H. Ma (2013) "Application of horseradish peroxidase modified nanostructured Au thin films for the amperometric detection of 4-chlorophenol". *Colloids and Surfaces B: Biointerfaces*, 103:129–135

[292] M.A. Alonso-Lomillo, O. Domínguez-Renedo, A. Hernández-Martín, and M.J. Arcos-Martínez (2009) "Horseradish peroxidase covalent grafting onto screen-printed carbon electrodes for levetiracetam chronoamperometric determination". *Analytical Biochemistry*, 395:86–90

[293] K. Radhapyari, P. Kotoky, and R. Khan (2013) "Detection of anticancer drug tamoxifen using biosensor based on polyaniline probe modified with horseradish peroxidase". *Materials Science and Engineering C*, 33:583–587

[294] S. Trashin, V. Rahemi, K. Ramji, L. Neven, S.M. Gorun, et al (2017) "Singlet oxygen-based electrosensing by molecular photosensitizers". *Nature Communications*, 8:1610

[295] V. Rahemi, S. Trashin, Z. Hafideddine, S. Van Doorslaer, V. Meynen, et al (2020) "Amperometric Flow-Injection Analysis of Phenols Induced by Reactive Oxygen Species Generated under Daylight Irradiation of Titania Impregnated with Horseradish Peroxidase". *Analytical Chemistry*, 92:3643–3649

[296] M. Shakeri and M. Shoda (2008) "Decolorization of an anthraquinone dye by the recombinant dye-decolorizing peroxidase (rDyP) immobilized on mesoporous materials". *Journal of Molecular Catalysis B: Enzymatic*, 54:42–49

[297] J. Ren, J. Huo, Q. Wang, Z. Liu, S. Li, et al (2022) "Characteristics of immobilized dye-decolorizing peroxidase from Bacillus amyloliquefaciens and application to the bioremediation of dyeing effluent". *Biochemical Engineering Journal*, 182:108430

[298] C. Chao, B. Zhang, R. Zhai, X. Xiang, J. Liu, et al (2014) "Natural nanotube-based biomimetic porous microspheres for significantly enhanced biomolecule immobilization". *ACS Sustainable Chemistry and Engineering*, 2:396–403

[299] V. Chaudhary and S. Sharma (2017) "An overview of ordered mesoporous material SBA-15: synthesis, functionalization and application in oxidation reactions". *Journal of Porous Materials*, 24:741–749

[300] S. Loreto, H. Vanrompay, M. Mertens, S. Bals, and V. Meynen (2018) "The Influence of Acids on Tuning the Pore Size of Mesoporous TiO2 Templated by Non-Ionic Block Copolymers". *European Journal of Inorganic Chemistry*, 2018:62–65

[301] F.C. Wu, R.L. Tseng, and R.S. Juang (2009) "Characteristics of Elovich equation used for the analysis of adsorption kinetics in dye-chitosan systems". *Chemical Engineering Journal*, 150:366–373

[302] DuPont (2023) "DuPont™ Duolite™ A568"

[303] J.-C. Janson (2011) "Protein purification. Principles, High resolution Methods, and Applications", 3rd ed. John Wiley & sons. Inc., Hoboken, New Jersey

[304] C. Pizarro, M.A. Fernández-Torroba, C. Benito, and J.M. González-Sáiz (1997) "Optimization by experimental design of polyacrylamide gel composition as support for enzyme immobilization by entrapment". *Biotechnology and Bioengineering*, 53:497–506

[305] M. Wolf and A.T. Paulino (2019) "Full-factorial central composite rotational design for the immobilization of lactase in natural polysaccharide-based hydrogels and hydrolysis of lactose". *International Journal of Biological Macromolecules*, 135:986–997

[306] M. Talat, A.K. Singh, and O.N. Srivastava (2011) "Optimization of process variables by central composite design for the immobilization of urease enzyme on functionalized gold nanoparticles for various applications". *Bioprocess and Biosystems Engineering*, 34:647–657